MULTI-WAVELENGTH STUDIES OF AGN FEEDBACK AND NON-THERMAL EMISSION IN GALAXY CLUSTERS AND GROUPS

DISSERTATION

zur Erlangung des Doktorgrades
an der Fakultät für Mathematik, Informatik und Naturwissenschaften
Fachereich Physik
der Universität Hamburg

vorgelegt von

THOMAS PASINI

Hamburg
2022

Eidesstattliche Versicherung

Hiermit versichere ich an Eides statt, die vorliegende Dissertationsschrift selbst verfasst und keine anderen als die angegebenen Hilfsmittel und Quellen benutzt zu haben.

Hamburg, den 12.05.2022

Thomas Pasini

Gutachter der Dissertation:	Prof. Dr. Marcus Brüggen A/Prof. Dr. Francesco de Gasperin
Zusammensetzung der Prüfungskommission:	Prof. Dr. Jochen Liske A/Prof. Dr. Marcus Brüggen Prof. Dr. Francesco de Gasperin Prof. Dr. Robi Barenjee Prof. Dr. Peter Hauschildt
Vorsitzender der Prüfungskommission:	Prof. Dr. Jochen Liske
Datum der Disputation:	24.08.2022
Vorsitzender des Fach-Promotionsausschusses PHYSIK:	Prof. Dr. Wolfgang J. Parak
Leiter des Fachbereichs PHYSIK:	Prof. Dr. Günter H. W. Sigl
Dekan der Fakultät MIN:	Prof. Dr. Heinrich Graener

To my family,
and to Giulia.

"May your heart
be your guiding key."

Zusammenfassung

Galaxienhaufen und -gruppen sind massereiche Strukturen, die sich als letztes in der Entwicklungsgeschichte unseres Universums formten. Als solche spielt ihre Entstehung und Entwicklung eine Schlüsselrolle im Verständnis der Strukturbildung und der kosmologischen Parameter. In den letzten zwei Jahrzehnten hat sich herausgestellt, dass Galaxienhaufen nicht den Vorhersagen von Modellen entsprechen, die lediglich gravitative Prozesse berücksichtigen. Skalierungsrelationen und Beobachtungen zeigen, dass eine nicht-gravitative Erwärmung erforderlich ist, um zu erklären, warum beispielsweise das heiße Plasma, das die Galaxienhaufen und -gruppen durchdringt, nicht auf niedrige Temperaturen abkühlt. Immer mehr Hinweise legen nahe, dass Rückkopplungsmechanismen aktiver galaktischer Nuklei (AGN) eine Erklärung dafür liefern: Das zentrale schwarze Loch speist sich aus Gas, welches aus einer heißeren Phase abkühlt, und erzeugt seinerseits Stoßwellen und Wärme, die die Strahlungsverluste des heißen Plasmas abschwächen.

Es gibt noch viel über die Rückkopplung von AGN zu verstehen. Derzeit ist nicht klar, ob die relative Position des AGN und der Kühlregion des Haufens relevante Auswirkungen auf diesen Arbeitszyklus haben kann. Liegt der AGN außerhalb der Kühlregion (oder ist von dieser versetzt), kann sich das schwarze Loch möglicherweise nicht aus kaltem Gas speisen, und der AGN kann seine Umgebung nicht effizient genug aufheizen, um Strahlungsverluste zu unterdrücken. Während die Detektion von Spuren der Rückkopplung, wie z. B. Stoßwellen und Blasen in massereichen Galaxienhaufen, leichter geworden ist, fehlt es noch an Untersuchungen der Rückkopplung von AGN im unteren Massenbereich von Galaxiengruppen, hauptsächlich wegen ihrer geringeren Oberflächenhelligkeit und Ausdehnung. Auch ist es wichtig, die Rolle der Rückkopplung zu verstehen, wenn es um die Eigenschaften der Heimatgalaxien von AGN geht. Die Simulation von Rückkopplung muss die Merkmale, die wir in Galaxienhaufen und -gruppen beobachten, reproduzieren können. Desweiteren kann die AGN-Rückkopplung auch eine wichtige Rolle bei der Herstellung geeigneter Bedingungen für ausgedehnte Radioemission spielen, die durch die Beschleunigung kosmischer Strahlung auf Skalen von Galaxienhaufen erzeugt wird und die in gestörten Systemen häufig von Radio-Interferometern wie LOFAR beobachtet wird.

Während meiner Doktorarbeit habe ich Galaxienhaufen untersucht, in denen der Punkt maximaler Kühlung von der Position des AGN versetzt ist. Zudem habe ich die AGN-Rückkopplung in Galaxiengruppen mit geringer Masse untersucht. Dabei habe ich Beobachtungen von mehreren Teleskopen in verschiedenen Bereichen des elektromagnetischen Spektrums sowie Himmelsdurchmusterungen der neuen Generation von eROSITA (Röntgen) und LOFAR (Radio) genutzt. Zusammen bilden sie eine große Stichprobe von Systemen mit einer noch nie dagewesenen Fülle von Multi-Wellenlängen-Daten. Ich habe Werkzeuge entwickelt, um Daten zu kalibrieren und zu analysieren, vor allem im Röntgen- und Radiofrequenzbereich. Diese Daten habe ich kombiniert, um einen besseren Einblick in die Wirkung der AGN-Rückkopplung in Haufen und Gruppen zu erhalten. Ich habe statistische Methoden sowie Simulationen benutzt, um die Wechselwirkung zwischen dem hei0en Plasma in Galaxienhaufen und der nicht-thermischen Emission von zentralen Radiogalaxien zu studieren. Zuletzt habe ich eine Software entwickelt, um sehr niedrig-frequente (54 MHz)

Radiodaten von LOFAR zu kalibrieren und habe dies angewandt auf den interessantesten Galaxienhaufen im HETDEX Feld, Abell 1550 (A1550).

Wir haben Hinweise darauf gefunden, dass Galaxienhaufen und -gruppen einer ähnlichen Korrelation zwischen der Röntgenleuchtkraft des heißen Plasmas und der Radioleistung des zentralen AGN folgen. Darüber hinaus haben wir gezeigt, dass Galaxien in der Nähe des Haufen-/Gruppenzentrums mit höherer Wahrscheinlichkeit einen radiolauten AGN beherbergen, da sie das Reservoir an kaltem Gas leicht anzapfen können, während Galaxien außerhalb des Zentrums auf eher episodische Auslöser wie Verschmelzungen angewiesen sein könnten. Wir haben keine Korrelation zwischen der Ausdehnung der zentralen Radiogalaie und der Dichte des Galaxienhaufen gefunden, was ein Hinweis darauf sein könnte, das andere Faktoren, wie Alter oder Leistung der Quelle wichtiger sein könnte. In Systemen mit begrenzten Abständen (< 50 kpc) zwischen dem AGN und dem Ort höchster Abkühlung haben wir festgestellt, dass der AGN-Arbeitszyklus nicht unterbrochen wird und dass das Schwappen des Gases einen weiteren Versatz mit dem warmen Gas, das aus der heißen Phase abkühlt, hervorrufen kann. Schließlich haben wir eine der ersten Niederfrequenz-Beobachtungen (54 MHz) von LOFAR analysiert, bei der wir den gestörten Galaxienhaufen Abell 1550 untersucht und mehrere diffuse Emissionsquellen mit stark unterschiedlichen Eigenschaften gefunden haben, die wahrscheinlich durch die Beschleunigung kosmischer Strahlung mit verschiedenen Beschleunigungsmechanismen entstanden sind.

Ich habe meine Ergebnisse in fünf, im Peer-Review-Verfahren veröffentlichten Erstautor-Publikationen zusammengefasst, die ich hier vorstelle. Zusammenfassend gewährt meine Dissertation neue Einblicke in AGN Rückkopplung in Galaxienhaufen und -gruppen. Außerdem habe ich die Möglichkeiten von LOFAR bei ultra-tiefen Frequenzen erkundet, um diffuse, nicht-thermische Emission in Galaxienhaufen zu untersuchen.

Abstract

Galaxy clusters and groups are the latest, more massive structures to have formed in our Universe. As such, their birth and evolution provides key information to understand structure formation and constrain cosmology. In the last two decades, it has become clear that galaxy clusters deviate from the predictions of models which incorporate only gravitational processes. Scaling relations and observational constrains demonstrate that non-gravitational heating is required to explain why, for example, the hot plasma permeating clusters and groups is not cooling to low temperatures. Increasing evidence points indeed to Active Galactic Nuclei (AGN) feedback as an explanation for these features: the central BH feeds from gas which is cooling down from an hotter phase, and in turn produces shocks and induce heating which quench the radiative losses of the hot plasma.

There is still much to understand about AGN feedback. It is currently not clear whether the relative position of the AGN and of the cluster cooling region can have relevant effects on this duty cycle. It is possible that, if the AGN lies outside of (or is offset from) the cooling region, the BH might not be able to feed from cold gas, and the AGN not able to heat its surroundings efficiently enough to quench radiative losses. Furthermore, while it has become relatively easy to detect feedback features (e.g. shocks, bubbles) in massive clusters, investigations of AGN feedback in the lower mass range of galaxy groups are still lacking, mainly because of their low surface brightness and smaller dimension. It is also essential to understand the role of feedback when it comes to the properties of AGN optical hosts, and to model feedback prescriptions in our simulations in a way in which they can reproduce the features we observe in clusters and groups. Finally, feedback can also have a relevant role on setting the necessary conditions to power the extended radio emission produced by the acceleration of Cosmic Rays (CR) on cluster scales, which is being frequently observed in disturbed systems by low-frequency interferometers such as LOFAR.

During my PhD, I have studied clusters which show offsets between the peak of the cooling and the AGN, as well as investigated feedback in the low-mass regime of galaxy groups. In doing that, I have exploited observations by multiple instruments, in different bands of the electromagnetic spectrum, as well as new-generation surveys provided by eROSITA (X-ray) and LOFAR (radio), which together provide large sample of systems with an unprecedented wealth of multi-wavelength data available. I have learnt and developed tools to calibrate and analyse data, mainly at X-ray and radio frequencies, and combined them to get a new, unexplored perspective of how AGN feedback acts in clusters and groups. I have exploited statistical methods and simulations to study the interplay between the hot plasma permeating clusters and the non-thermal emission by central radio galaxies. Finally, we have developed a pipeline to properly calibrate LOFAR ultra low-frequency (54 MHz) observations, applying it to one of the most interesting galaxy clusters in the HETDEX sky field, Abell 1550 (A1550).

We have found evidence that clusters and groups follow a similar correlation between X-ray luminosity of the hot plasma and radio power of the central AGN. The correlation becomes tighter when we compare the total energy output from the AGN (which the radio power is a proxy of) to the X-ray luminosity, and apparently holds for both relaxed and

disturbed systems. We showed that galaxies close to the cluster/group center are more likely to host a radio-loud AGN, since they can easily tap into the cold gas reservoir, while outer galaxies might rely on more episodic triggers, such as mergers. We found no apparent correlation between the extent of central radio galaxy and the density of the host group/cluster, suggesting that other factors, such as the age and radio power of the source, might be more dominant. In systems with limited offsets (< 50 kpc) between AGN and cooling peak, we determined that the duty cycle is not broken, and that gas sloshing can induce further offsets with the warm gas which is cooling out from the hot phase. Finally, we have analysed one of the first ultra low-frequency observations provided by LOFAR, studying the disturbed galaxy cluster A1550 and finding multiple diffuse emission sources with surprisingly heterogeneous properties, which are likely produced by different cosmic-ray acceleration mechanisms. I have gathered all my findings into 5 first-author, peer-reviewed publications, which I present here.

In summary, my thesis provides new insights into the current knowledge of AGN feedback in clusters and groups, and explores the potentiality of LOFAR ultra low-frequency observations to detect and investigate diffuse, non-thermal emission in galaxy clusters.

List of publications

This thesis is based on (but does not include all of) the following publications, which I have led as first author or took part to as co-author:

First author:

1. **T. Pasini**, H. W. Edler, M. Brüggen, F. de Gasperin, A. Botteon, K. Rajpurohit, R. J. van Weeren, F. Gastaldello, M. Gaspari, G. Brunetti, V. Cuciti, C. Nanci, G. di Gennaro, M. Rossetti, D. Dallacasa, D. N. Hoang, and C. J. Riseley: *Particle re-acceleration and diffuse radio sources in the galaxy cluster Abell 1550.* Accepted by A&A, June 2022. Pasini et al. 2022b
2. **T. Pasini**, M. Brüggen, D. N. Hoang, V. Ghirardini, E. Bulbul, M. Klein, A. Liu, T. W. Shimwell, M. J. Hardcastle, W. L. Williams, A. Botteon, F. Gastaldello, R. J. van Weeren, A. Merloni, F. de Gasperin, Y. E. Bahar, F. Pacaud, and M. Ramos-Ceja: *The eROSITA Final Equatorial-Depth Survey (eFEDS): LOFAR view of brightest cluster galaxies and AGN feedback.* A&A, 661A, 13P, May 2022. Pasini et al. 2022a
3. **T. Pasini**, A. Finoguenov, M. Brüggen, M. Gaspari, F. de Gasperin, and G. Gozaliasl: *Radio galaxies in galaxy groups: kinematics, scaling relations, and AGN feedback.* MNRAS, 505, 2628, August 2021. Pasini et al. 2021b
4. **T. Pasini**, M. Gitti, F. Brighenti, E. O'Sullivan, F. Gastaldello, F. Temi, and S. L. Hamer: *A First Chandra View of the Cool Core Cluster A1668: Offset Cooling and AGN Feedback Cycle.* ApJ, 911, 66, April 2021. Pasini et al. 2021a
5. **T. Pasini**, M. Brüggen, F. de Gasperin, L. Bîrzan, E. O'Sullivan, A. Finoguenov, M. Jarvis, M. Gitti, F. Brighenti, I. H. Whittam, J. D. Collier, I. Heywood, and G. Gozaliasl: *The relation between the diffuse X-ray luminosity and the radio power of the central AGN in galaxy groups.* MNRAS, 497, 2163, September 2020. Pasini et al. 2020
6. **T. Pasini**, M. Gitti, F. Brighenti, P. Temi, A. Amblard, S. L. Hamer, S. Ettori, E. O'Sullivan and F. Gastaldello: *A BCG with Offset Cooling: Is the AGN Feedback Cycle Broken in A2495?* ApJ, 885, 111, November 2019. Pasini et al. 2019

Co-author:

1. E. Bulbul, A. Liu, **T. Pasini** et al. : *The eROSITA Final Equatorial-Depth Survey (eFEDS): Galaxy Clusters and Groups in Disguise.* A&A, 661A, 10B, May 2022.
2. M. Brienza, L. Lovisari, K. Rajpurohit et al. : *The galaxy group NGC 507: newly detected AGN remnant plasma transported by sloshing.* A&A, 661A, 92B, May 2022.
3. T. W. Shimwell, M. J. Hardcastle, C. Tasse et al. : *The LOFAR Two-metre Sky Survey. V. Second data release.* A&A, 659, A1, March 2022.

Contents

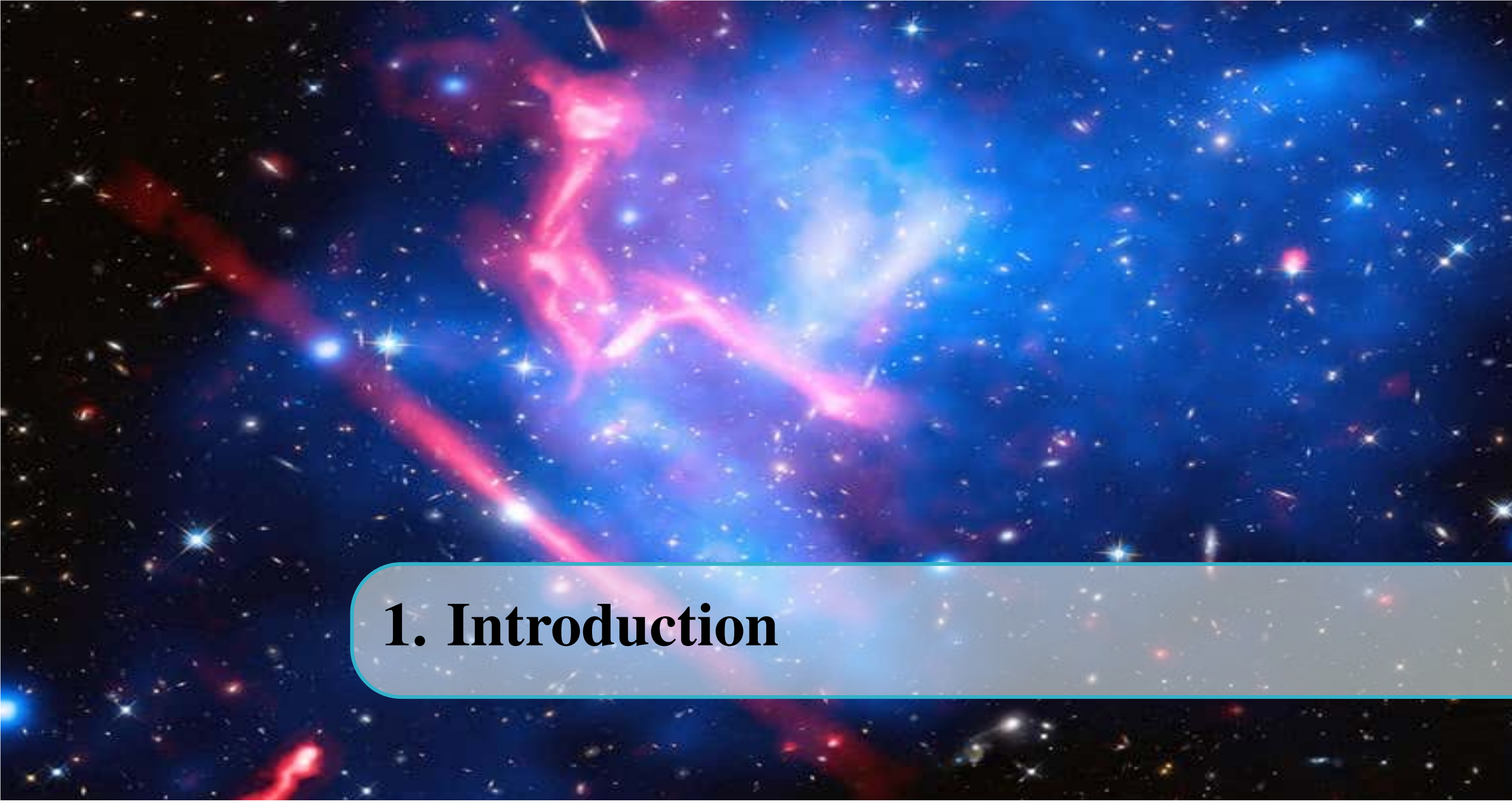

1. Introduction

In the last century, our understanding of how the Universe works has undergone an extraordinary evolution. It was only in the 1920s that Edwin Hubble observed the first extra-galactic object: before that, astronomers could not prove that the extent of the Universe was larger than the Milky Way. Furthermore, in that historical period astrophysics was restricted to the optical band of the electromagnetic spectrum. In 1932, Karl Jansky discovered emission in the radio band (wavelength 1 cm $\leq \lambda \leq$ 10 m) from an extraterrestrial source. This event marked the birth of radio astronomy, which quickly progressed after World War II thanks to the evolution of modern antennas and radars.

From those years, technological developments have allowed us to extend our observations to all the frequencies of the electromagnetic spectrum. Optical telescopes easily reach sub-arcsecond resolution, X-ray and Infrared (IR) emission is observed through space telescopes orbiting around the Earth, while radio astronomy has developed interferometers which combine signal from multiple antennas spread among the whole planet, reaching uprecedented resolution in this band. As of today, the combination of multi-wavelength data from different instruments is widely used to reach a better understanding of astrophysical processes. The scale of the Universe does not include only stars anymore: we are able to detect thousands of millions of galaxies. Furthermore, galaxies are often grouped in clusters, and we are starting to comprehend that galaxies and clusters are distributed across a giant filamentary structure, which is known as the Cosmic Web (see Fig. 1.1), that likely permeates the whole Universe. It is around these giant filaments, which are constituted by agglomerates of gravitationally-attracted matter, that galaxy clusters have merged over time, slowly building the Universe that we observe today. Therefore, galaxy clusters can act as cosmological laboratories: first, their numerical density as a function of the redshift is highly sensitive to cosmology. Furthermore, they trace primordial Dark Matter (DM) perturbations, and their mass function also provide key information to constrain the state equation of Dark Energy.

In galaxy clusters we observe emission from almost all the frequencies of the electromagnetic spectrum. While IR and optical emission mainly originates from interstellar dust and stars within the galaxies hosted in clusters, X-ray emission permeates the whole extent of these systems. Radio detections usually come from Supernova Remnants (SNR) and Active Galactic Nuclei (AGN) hosted in the core of galaxies, but we also observe emission not associated to discrete objects, and that can extend through the whole cluster. The physical processes from which these different kinds of emission originate affect and interact with each other, altering the evolution of galaxy clusters.

In this thesis, we will mainly focus on the connections between the thermal X-ray emission and the non-thermal radio emission in galaxy clusters and groups, which are both strictly related to feedback, turbulence and particle acceleration processes. In the next sections of this chapter we will introduce galaxy clusters and groups, as well as the main properties of their thermal and non-thermal emission. We will also discuss the current understanding of feedback processes, from the point of view of, both, observations and simulations. Finally, we provide a layout of the motivation of this thesis and of the questions that we will try to address, as well as a summary of the next chapters.

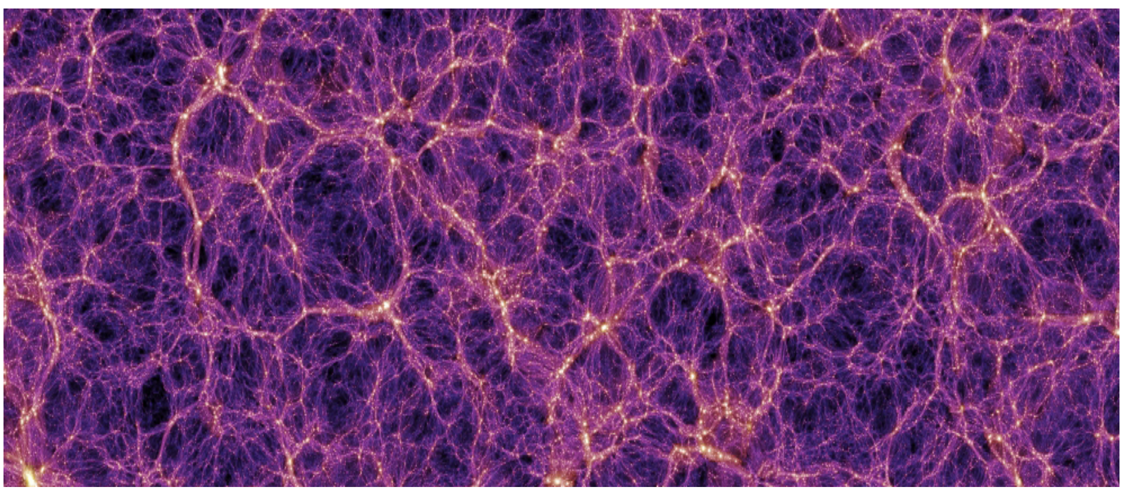

Figure 1.1: The bright filaments of matters and large voids which constitute the Cosmic Web. The image is from the Millennium Simulation (Springel et al., 2006).

1.1 Galaxy clusters and groups

Galaxy clusters are the largest and more massive virialised structures in the Universe, capable to host more than a thousand galaxies and often reaching extents of 1-2 Mpc. They are located at the nodes of the filamentary structure known as Cosmic Web, and are formed through mergers and mass accretion of smaller groups and clumps. DM represents $\sim$80% of the total mass of a cluster, which is usually of the order of $\sim 10^{14}$ - 10^{15} $M_{\odot}$. Galaxies and baryons constitute the remaining $\sim$20%, with baryons mostly ($\sim$90%) in the form of a hot plasma (Intra-Cluster Medium, hereafter ICM), that fills the space in-between galaxies, while the remaining 10% is locked up in stars within galaxies (Lin et al., 2003). Given the masses and velocities ($\sim$ 2000 km s^{-1}) in play during cluster mergers, these processes are among the most energetic in the Universe, reaching energies of the order of $E = \frac{1}{2}Mv^2 \sim 10^{64}$ erg (Markevitch et al., 1999).

The presence of gas in clusters is easily explained by hierarchical structure formation models, with warm baryons swept towards the cluster together with collapsing DM, and then heated to $\sim 10^7$ - 10^8 K by accretion shocks and adiabatic compression (see also McNamara and Nulsen 2012). Therefore, the ICM shows thermal emission in the form of Bremsstrahlung (due to Coulomb collisions of electrons and ions) and line emission, which are observable in the X-ray band (e.g. Fig. 1.2) with luminosity range $L_X \sim 10^{43} - 10^{45}$ erg s^{-1} and emissivity $J_X(T) \propto n^2$, where n is the ICM density. The primary components of this plasma are hydrogen and helium, ionized because of the high temperature. They are mixed with heavier elements at $\sim$1/3 of the solar metal abundance (Arnaud et al., 1992).

Figure 1.2: X-ray (XMM-Newton) and optical (SDSS) view of the Coma Cluster (Sanders et al., 2020). Colorised is the Bremsstrahlung emission from the ICM.

It is well-known that structure formation operates as a bottom-up process: matter collects to build stars and galaxies, while galaxies attract each other forming groups. Therefore, clusters are the latest structures to be formed. The building blocks of galaxy clusters are galaxy groups that, with masses ranging from $\sim 10^{13}$ M$_\odot$ to $\sim 10^{14}$ M$_\odot$, lie at the peak of the mass density in the current Universe (see e.g. review by Eckert et al. 2021). Although groups usually show lower gas fractions and flatter entropy profiles (Finoguenov et al., 2005; Voit et al., 2005), it is yet not clear where the physical separation between galaxy clusters and groups lies, or if it even exists beyond the obvious differences in mass and gravitational potential. Observations have shown that very similar processes take place in clusters and groups. Nevertheless, such processes could produce different consequences on the environment, precisely because of the mass difference. We will return on this in the next sections.

Groups, intended as the lowest-mass clusters, are the repositories of the majority of baryons and host more than half of all galaxies (Eke et al., 2006). As such, to understand the formation and evolution of galaxies, it is necessary to comprehend the processes undergoing in galaxy clusters and groups. The large scale structure of the Universe agrees fairly well with the ΛCDM model[1] (Spergel et al., 2007; Vikhlinin et al., 2009; Allen et al., 2011). However, additional physics is needed to explain the distribution and numbers of baryons detected in galaxies and clusters (Bregman, 2007). Models incorporating radiative cooling and gravitational heating alone fail to reproduce the observed amount of cold gas and stars, leading to overcooling of the gas and, consequently, to mismatches in terms of star content (i.e. too many young stars), galaxy luminosities and colors (McNamara and Nulsen, 2012). A contribution from non-gravitational energy is therefore required to quench star formation and reproduce the observed stellar mass function.

1.2 Cluster classification and the cooling flow problem

One of the most used classifications of galaxy clusters and groups is based on their dynamical state and distinguishes them into merging and relaxed, with the latters mostly being cool cores (see below). While in relaxed clusters massive galaxies, usually ellipticals, are often observed to lie close to the centre because of dynamical friction, in merging clusters the galaxy distribution does not follow this behaviour, since friction did not have the time to play its role yet. Mergers can also produce turbulent motions, shocks and heat the cluster gas, and a fraction of their energy is channelled into the acceleration of cosmic rays (CR) and amplification of pre-existing magnetic fields (Brunetti and Jones, 2014). This leads to the formation of diffuse non-thermal radio emission, such as giant halos and relics, that are observed only in merging clusters. We will discuss this in more detail in Sec. 1.4.

On the other hand, cool-core clusters usually show a peak of surface brightness in the centre. Their X-ray morphology often has a roundish, symmetrical shape, and their surface brightness profile is well-described by the so-called double-β Model (Cavaliere and Fusco-Femiano, 1976a), assuming that the gas is multiphase (see also Fig. 1.3):

$$\Sigma_X(r) = \sum \Sigma_{X,i}(0)\left[1+\left(\frac{r}{r_{c,i}}\right)^2\right]^{\frac{1}{2}-3\beta}, \tag{1.1}$$

[1]Hereafter, we assume $\Omega_\Lambda = 0.7$ and $\Omega_\mathrm{m} = 0.3$ unless explicited otherwise.

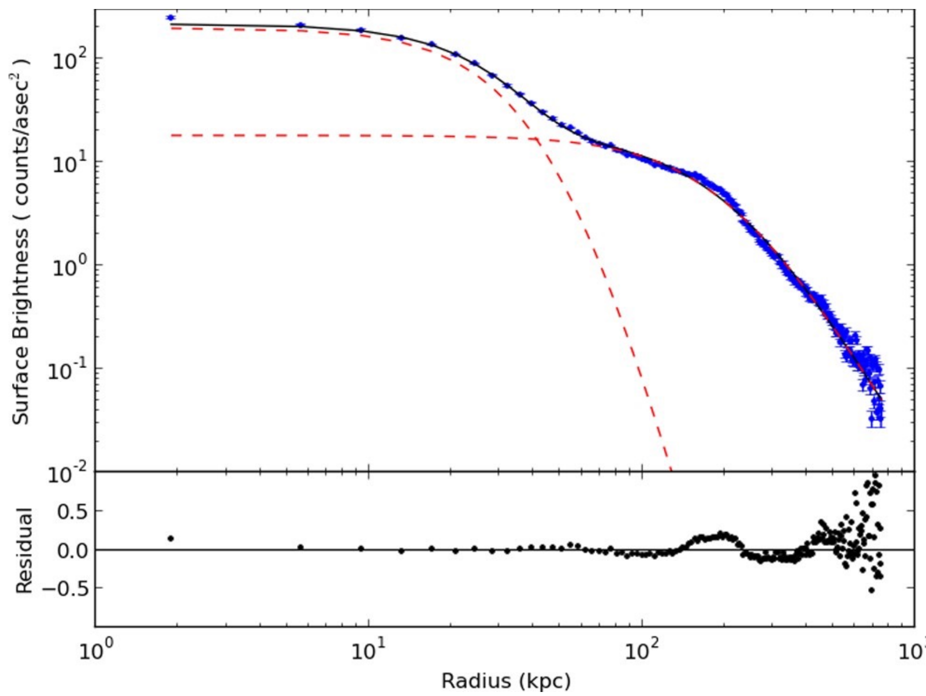

Figure 1.3: Surface brightness profile of MS 0735.6+7421 fitted with a double-β Model (Vantyghem et al., 2014). The red, dashed lines show the two components of the model.

where $\beta \sim 0.75$ (Arnaud, 2009) is defined as the ratio between the kinetic energy of galaxies and the thermal energy of the gas. The name 'cool core' is due to a visible drop in the cluster temperature inside $\sim 0.1 R_{500}$[2]. Such particular feature is a consequence of the cooling of the ICM, that proceeds faster where the density is higher, as in the cluster centre. More in details, the cooling time of the ICM can be estimated as:

$$t_{\text{cool}} = \frac{H}{\Lambda(T) n_e n_p} = \frac{\gamma}{\gamma - 1} \frac{kT(r)}{\mu X n_e(r) \Lambda(T)}, \tag{1.2}$$

where γ=5/3 is the adiabatic index, H is the enthalpy, $X \sim 0.71$ is the hydrogen mass fraction, and $\Lambda(T)$ is the cooling function, defined as the bolometric power emitted as thermal radiation by the plasma, normalised by the emission measure $\dot{\varepsilon}_X = n_e n_H V$, with V being the volume.

From early studies of cool cores, it was predicted that the cooling of the ICM, especially at the cluster centre where the density is higher, would lead to the formation of a so-called *cooling flow*. As the ICM in the centre cools off, its entropy decreases and it gets compressed by the surrounding gas, producing an inflow towards the core. Therefore, the density increases and the cooling becomes more and more relevant, with the gas temperature rapidly reaching $T < 10^4$K and condensing onto central galaxies. The hot ICM, previously lying out of the cluster core, replenishes the condensed gas, finally resulting in a steady

[2] The radius at which the density is 500 times the critical density of the Universe at that redshift.

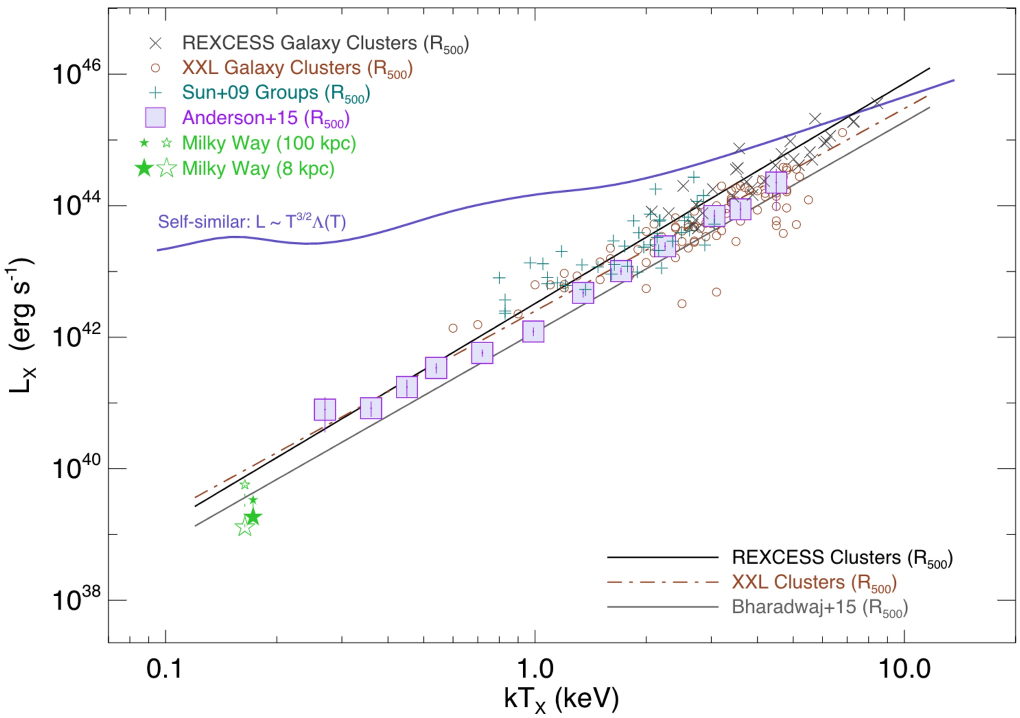

Figure 1.4: Observed correlations between the X-ray luminosity and the ICM temperature for samples of galaxy clusters, groups and the Milky Way. The purple line shows the scaling relation which would be produced by only considering gravitational heating. The image is from Donahue and Voit (2022).

cooling flow which was initially predicted to show rates of $\sim$1000 $M_\odot$ yr^{-1} (Fabian, 1994). This is commonly known as the *standard cooling flow model*.

In the late 90s, with the advent of new-generation X-ray telescopes such as *Chandra* and XMM-Newton, it became clear that observations did not match such models. The observed rates of star formation in clusters central galaxies (Brightest Cluster Galaxy, BCG) and strength of line emission in the cores were only 1-10% of those predicted by the cooling flow model (Peterson and Fabian, 2006), and the temperature was observed to never drop below $\sim T_{\rm vir}/3$ (Molendi and Pizzolato, 2001; Peterson et al., 2001), with $T_{\rm vir}$ being the virial temperature, defined as the temperature at which a gravitationally bound system would satisfy the virial theorem. This effect came to be known as the *cooling flow problem*.

It was then proposed that some heating source was probably compensating for the radiative losses of the ICM. This also provided a possible solution for the long-standing problem of the deviation from self-similar relations which has been observed in clusters and groups. As a matter of fact, while one of the earliest findings of X-ray surveys implied strong scaling relations between X-ray luminosity, mass and temperature of clusters, models incorporating only gravitational heating were not able to reproduce such correlations (see Fig. 1.4). On the other hand, non-gravitational processes are able to account for these differences (Donahue and Voit, 2022).

As of today, feedback from central AGN constitutes the most likely solution to the cooling flow problem. In fact, BCGs in cool-core clusters and groups usually host radio loud AGN (Mittal et al., 2009; Sabater et al., 2019), even though this trend seems to become relatively weaker moving to the group regime (Bharadwaj et al., 2014a, 2015b). Observations have shown that the central AGN often interacts with the surrounding environment, producing visible effects on the ICM and on the whole cluster, that will be the subject of Sec. 1.3.

1.3 AGN feedback in galaxy clusters

Evidence for feedback

One of the challenges of the current cosmological model is to explain why so few baryons have condensed into stars (Cole, 1991; White and Frenk, 1991a). Simulations which incorporate only gravitational heating and radiative cooling predict that more than 20% of baryons should lie into galaxies, while we only observe ∼10% in stars (Balogh et al.,

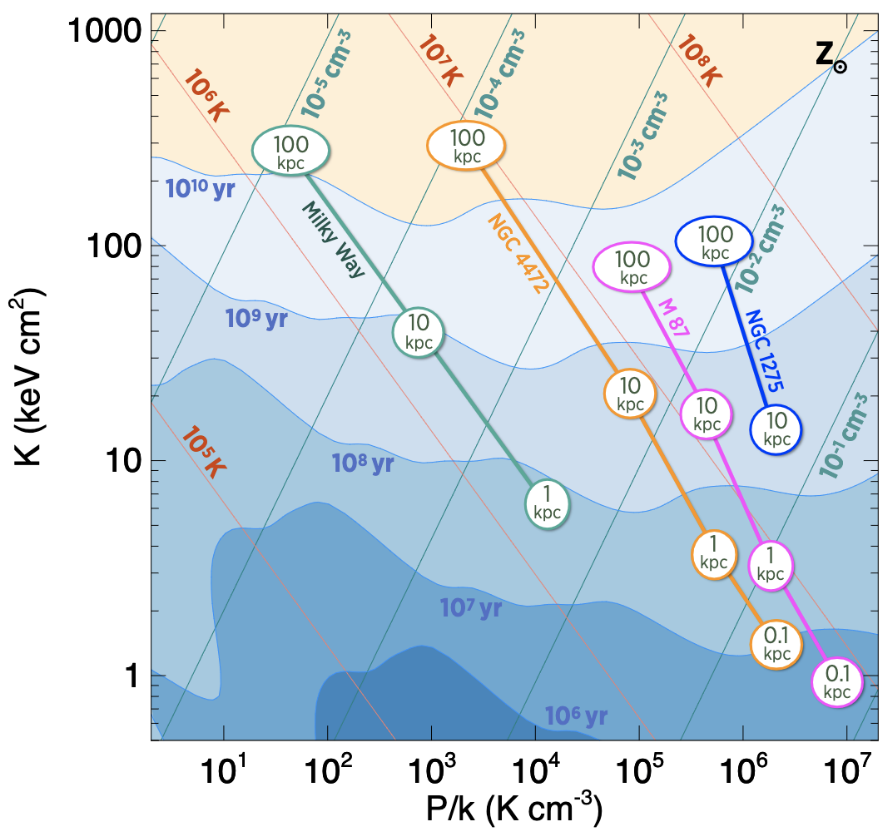

Figure 1.5: ICM entropy vs. pressure in 4 galaxies with different properties: a star-forming galaxy within a massive cluster (NGC 1275 in Perseus), a low star-formation galaxy in a small cluster (M87 in Virgo), an elliptical, satellite galaxy with no star formation (NGC 4472 in Virgo) and the Milky Way. Red, diagonal lines represent lines of constant temperature, while cyan, diagonal ones represent lines of constant density. Blue contours represent constant cooling times. All 4 systems reach cooling times shorter than 10^9 yr at the same distance of ∼ 10 kpc from the corresponding center. The figure is from Donahue and Voit (2022).

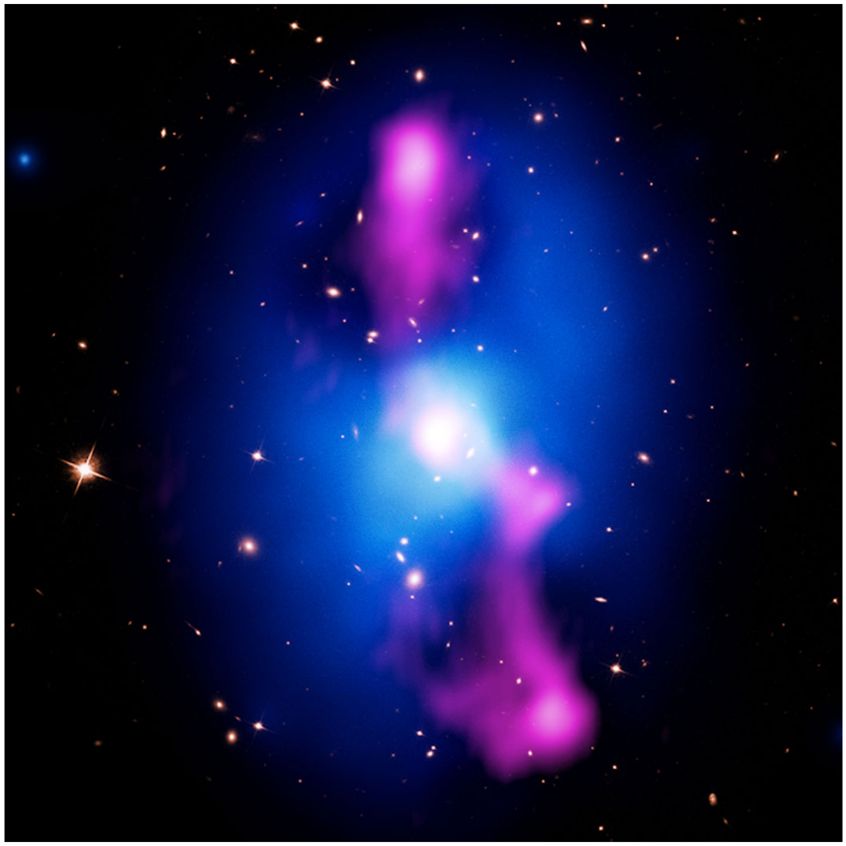

Figure 1.6: *Chandra* X-ray (blue) and Very Large Array (VLA) radio (red) observation of the galaxy cluster MS0735+7421 (McNamara et al., 2005). The radio lobes clearly fill the giant cavities. The image physical size is 800x800 kpc.

2001). The remaining fraction is found in the ICM, at temperatures much higher than those initially predicted by models, and which prevent baryons to form stars. Furthermore, the ICM in different systems is observed to reach a cooling time shorter than $\sim 10^9$ yr always at distances of ~ 10 kpc from the center, regardless of the mass, gas density and temperature: we see this behaviour from spiral to ellipticals, from groups to clusters (see Fig. 1.5). This evidence pointed to some kind of heating source that could supply for the radiative losses of the hot plasma. One of the first proposed solution involved Supernovae, which show energetics ($E \sim 10^{62}$ erg) comparable to that needed to quench cooling (Narayan and Medvedev, 2001). However, the timescale and energy supply of Supernovae are too short compared to cooling, which is a continuous process that last for several Gyr. Mergers were also investigated as a promising source of heating: sloshing, i.e. an oscillation of the gas within the cluster potential which is usually triggered by mergers, can mix hot gas from the outskirts with the cold gas in the core, preventing a significant cooling flow (ZuHone et al., 2010). Nevertheless, mergers are again too episodic to sustain the steady radiative losses of the ICM.

In the early 2000s, an increasing number of X-ray observations of galaxy clusters and groups, mostly performed with the unprecedented resolution of *Chandra*, started to detect disturbances in the ICM such as shocks, cold fronts (discontinuities between colder and warmer gas clouds) and ripples (Fabian et al., 2006; Markevitch and Vikhlinin, 2007; Gastaldello et al., 2009; Ghizzardi et al., 2010). The passage of a shock, produced by the expansion of the radio galaxy through the ICM, compresses and heats the gas. For this reason, it was pointed out that this kind of non-gravitational processes could provide a possible solution to the cooling flow problem. As discussed in Eckert et al. (2021), the shock energy can be as large as 10^{55} - 10^{61} erg (Liu et al., 2019b), which is often comparable to the amount needed to quench ICM radiative losses. However, a single shock, because of its episodic and transient nature, fails to compensate for the radiative losses due to cooling. Nevertheless, the amount of heating provided by multiple shocks becomes relevant and is able to quench cooling inside the inner cluster core (McNamara and Nulsen, 2012).

The conclusive solution to the cooling flow problem came from the discovery of *cavities*, X-ray surface brightness depressions that are usually found to be spatially coincident with the lobes of the central radio galaxy (e.g. (McNamara et al., 2000; Bîrzan et al., 2004; Rafferty et al., 2006)). Observations of such bubbles mostly came from clusters (Fig. 1.6), since their relatively high surface brightness compared to groups makes the detection of ICM depressions easier (McNamara et al., 2005; Nulsen et al., 2005). Cavities have been interpreted as regions of low-density relativistic plasma produced by the displacement of the ICM caused by the expansion of the AGN radio lobes through the medium, which translates into heating. AGN are powered by matter accreting onto the central SuperMassive Black Hole (SMBH, see also Sec. 1.4). The released energy is of the order of $E_{\rm BH} = \varepsilon M c^2 \sim 10^{62}$ erg for a SMBH of $\sim 10^9 M_\odot$ with efficiency $\varepsilon \sim 0.1$, which is consistent with those needed to quench radiative cooling.

Cavities are produced by the AGN lobes excavating though the ICM. Therefore, heating is thought to occur through dissipation of the cavity enthalpy, other than shocks produced by the outburst. The energy required to excavate a cavity is the sum of the work done to displace the ICM and the internal energy of the radio lobes:

$$H = E_{\rm int} + pV = \frac{\gamma}{\gamma - 1} pV, \tag{1.3}$$

with p being the ICM pressure in an undisturbed region close to the cavity, V the cavity volume (equal to the volume of the displaced ICM) and γ is the ratio of the specific heats of the plasma filling the cavities. For a relativistic plasma, $\gamma = 4/3$ and $H = 4pV$. The range of enthalpies ($\sim 10^{56}$ - 10^{61} erg) typically found for cavities is very similar to the energy estimated for shocks, suggesting that the two processes could provide a comparable contribution to heating (Forman et al., 2017). Potential uncertainties include projection effects, that can lead to underestimate the size of the cavity, and systematic errors when determining the thermodynamical properties of the ICM.

To assess whether the radiative losses from cooling can be counterbalanced by AGN heating, an estimate of the cavity age is required. This can be done using three different methods. The age can be assumed to be equal to the *sound-crossing* time $t_s = R/c_s$, i.e. the time required to reach the current position R of the cavity at the speed of sound c_s.

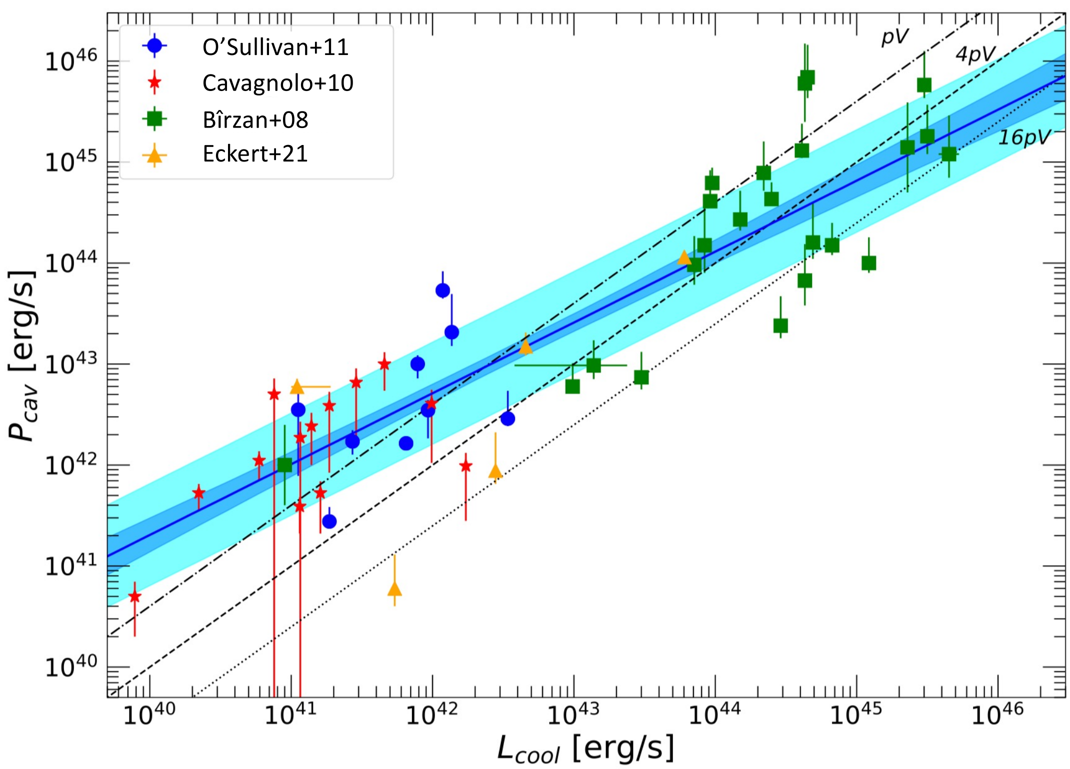

Figure 1.7: Correlation between cooling luminosity of the ICM (x-axis) and cavity power (y-axis), estimated as the ratio between $4pV$ and cavity age (Eckert et al., 2021). The cavity power acts as proxy for the heating provided by AGN outflows. The blue line shows the best fit using a power law relation. The uncertainty is indicated by the blue area, while cyan indicates the intrinsic scatter around the relation.

An alternative way is the *refill* time $t_{\rm ref} = \sqrt{r/g}$, i.e. the time required for the gas to refill the volume displaced by the formation of the cavity, with r being the cavity radius and $g = GM(< R)/R^2$ the gravitational acceleration at distance R. Since cavities do not usually travel at sound speed, a good compromise between these two methods is the *buoyancy* time $t_{\rm buoy} = R/v_T$, the time required for the cavity to rise buoyantly to its current position. Here, $v_T = 1/\sqrt{SC/2gV}$ is the buoyancy velocity, with S being the cavity cross-section and $C = 0 = 75$ the drag efficiency. These three estimates usually agree within a factor of 2, providing cavity ages of the order of 10^7 yr (Rafferty et al., 2006).

Dividing the enthalpy for the age provides an estimate of the *cavity power*, a proxy for the total feedback from the AGN. This is often found to be comparable to the energy needed to quench ICM cooling (see Bîrzan et al. 2004 for a detailed description of the methods). In fact, the mean power of the outbursts of the central AGN shows a relatively strong correlation with the amount of radiative losses due to cooling (Fig. 1.7) (Bîrzan et al., 2004; Nulsen et al., 2007). The existence of such tight link constitutes an unprecedented support for AGN feedback as a solution to the cooling flow problem in clusters.

Therefore, the emerging picture is that outflows from the central AGN create bubbles and drive weak ($\mathscr{M} \sim 1-2$) shocks, heating the ICM and also inducing gas and metals

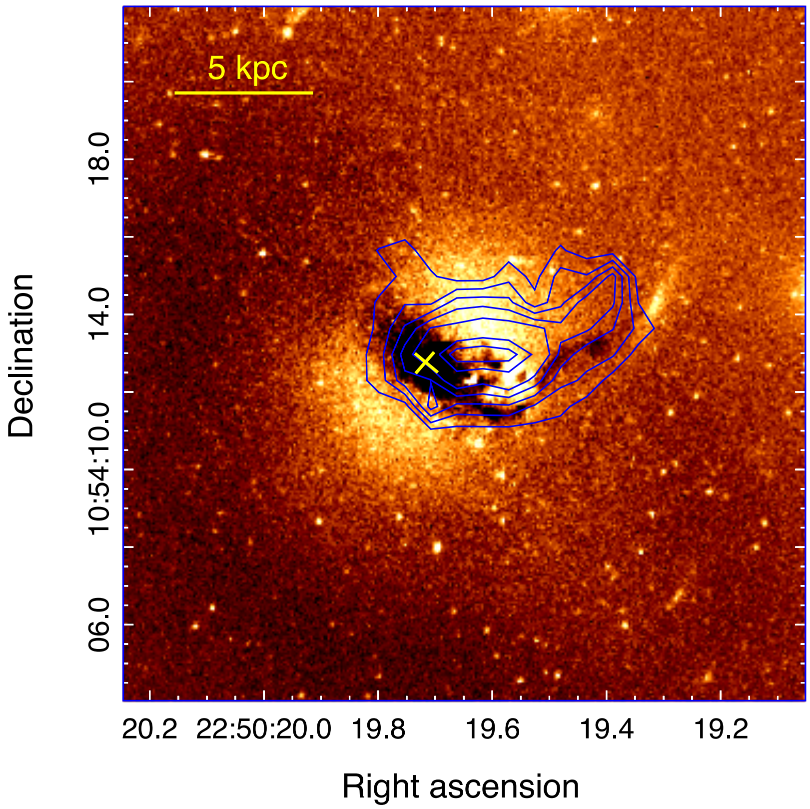

Figure 1.8: Dust (colored in black) and Hα emission (blue contours) in front of the BCG of the galaxy cluster A2495 (Pasini et al., 2019). The yellow cross is the BCG optical center.

circulation across several hundreds of kpc (Ettori et al., 2013). The same outflows are powered by cold gas accreting onto the SMBH: the availability of dense, cold gas translates into outbursts, which in turn translate into mechanical heating through shocks and bubbles. Heating prevents the gas from further cooling, and as a consequence this leads to less heating, and with time to replenish the fuel of cold gas for the SMBH. This is known as the *AGN duty cycle*.

In some cases, cavities are observed to be surrounded by bright shells of gas, which are cooler than the surrounding ICM (McNamara et al., 2000; Blanton et al., 2001, 2003). The weak shocks produced by AGN outbursts may also contain a fraction of the heating energy, even though they are often hard to observe. Nevertheless, there are a few cases in which relatively strong, large-scale shocks have been observed, such as Hydra A (Nulsen et al., 2005) and MS0735+7421 (McNamara et al., 2005). When such powerful outbursts happen, AGN feedback becomes relevant not only in the central region, but is likely able to affect the global properties of the ICM. These events are observed only in 10% of all known cool cores. Therefore, they should occur in a similar fraction of time across the lifetime of a cluster (Gitti et al., 2012). This is in agreement with simulations, which predict that the majority of the heating required to quench cooling over the lifetime of a cluster is provided by rare, powerful outbursts (Nipoti and Binney, 2005).

Finally, it is important to assess the consequences of AGN feedback not only on the ICM, but also on the galaxy population. Since feedback mostly affects the cluster core, the evolution of BCGs strongly depends on the AGN duty cycle. One of the most striking evidence of ongoing cooling is the presence of warm, line-emitting gas at the center of clusters, close to BCGs. This is revelead by line emission from ionised and/or molecular gas (e.g., Crawford et al., 1999; McDonald et al., 2014; Hamer et al., 2016). The strength of such line emission, mostly Hα, correlates with the presence of ICM (Edge, 2001; Hogan et al., 2017b; Pulido et al., 2018), suggesting that the warm gas is cooling out of the hot phase of the ICM, albeit at rates of $\sim 1\%$ with respect to those predicted by classical cooling flow models. The availability of cold gas close to the BCG location could also help to explain why these galaxies sometimes show ongoing star formation (McDonald et al., 2018). Furthermore, in some cases a minor merger can trigger sloshing, which can in turn make the cluster gas oscillate. In undisturbed objects, the BCG and the cooling peak are usually found at the center, where the bottom of the potential well lies. However, sloshing can move the gas and bring the peak away from the BCG (Haarsma et al., 2010; Hamer et al., 2012; Barbosa et al., 2018). With cooling not centered on the BCG anymore, the availability of fuel for the SMBH becomes more limited. It is currently not clear whether this can have consequences, or even break, the AGN duty cycle. Pasini et al. (2019) have recently investigated one of these cases in the galaxy cluster A2495, where they observed a $\sim$10 kpc offset between the BCG and the X-ray peak, as well as two putative generations of cavities. They concluded that the offset does not break the link between heating and cooling, likely because the offset is too small to prevent mechanical heating. Nevertheless, it is essential to assess the frequency of these offsets, and to investigate whether in some cases they can have consequences on the AGN duty cycle.

The impact of AGN feedback in galaxy groups

The observation of cavities, that has rapidly become a widely accepted method to investigate AGN feedback, requires a combination of resolution and flux sensitivity that is hard to achieve, even in galaxy clusters. Nevertheless, bubbles have also been observed in closeby elliptical galaxy (e.g. Forman et al. 2005) and groups (e.g. Cavagnolo et al. 2010; O'Sullivan et al. 2017). We remind to Eckert et al. (2021) for an up-to-date list of all groups in which X-ray brightness depressions have been detected. Similarly to galaxy clusters, we observe deviation from self-similar scaling relations, even though the gas fraction is usually lower compared to most clusters (see also Sun et al. 2009). It is speculated that, albeit AGN outflows and mechanical feedback through bubbles and weak shocks are still observed in groups, these processes could act in a more gentle way compared to cluster. On the other hand, it is likely that strong outbursts would be easily able to disrupt the environment (Gaspari et al., 2011).

Recently, Randall et al. (2015) have presented a $\sim$650 ks *Chandra* observation of the galaxy group NGC5813. The resulting images (Fig. 1.9) show an unprecedented (at least in the group regime) number of cavities, shocks and ripples. It was clearly shown that the ICM gets re-heated through the passage of shock fronts, caused by outbursts of the central AGN, suggesting that feedback produces relevant effects also in galaxy groups. In fact,

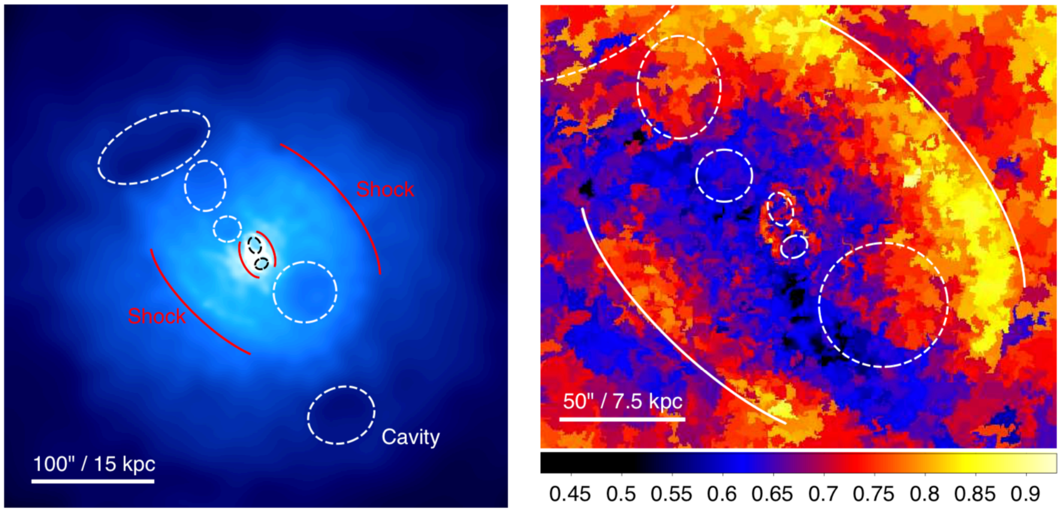

Figure 1.9: *Left*: Adaptively smoothed 0.5-2 keV *Chandra* image of the galaxy group NGC5813. Detected cavities and shocks are marked. *Right*: Temperature map of NGC5813. The re-heating of the ICM through the passage of shocks is clearly visibile. Images are from Kim et al. 2019.

its impact on groups could actually be stronger than in clusters since, given the shallower gravitational potential, even a relatively small energy injection could eject gas from the group (Giodini et al., 2010), explaining the lower gas fractions cited above. Simulations by Gaspari et al. (2011) seem to confirm that AGN feedback in groups may act differently than in clusters: not through strong, episodic outbursts, but rather via a gentle, but persistent heating characterised by subsonic outflows.

McCarthy et al. (2010) showed that, by including feedback from BH in cosmological hydrodynamical simulations, it is possible to reproduce fairly well the same thermodynamical profiles, gas and stellar fractions and Star Formation Rates (SFR) that are observed in real galaxy groups. Understanding how feedback operates in the group regime could also be of particular interest because their different environments compared to clusters could translate into significant dissimilarities in the impact of this process.

Nevertheless, X-ray observations of groups deep enough to allow to perform analyses of shocks and cavities are hardly feasible, apart from closeby systems, because of their low surface brightness and small dimension (i.e. high definition required to resolve ICM structures). Radio observations offer an alternative and cheaper way to assess AGN feedback in the low-mass regime. In radio sources, a fraction of the total energy provided by the AGN has been radiated away, while a much larger fraction is stored into the lobes and a similar amount has been dissipated into the ICM during the expansion of the lobes. Therefore, the radio power as measured from observations is a proxy for the total amount of feedback from the AGN, that can then be compared to the raditive losses. The link between radio power and total energy (i.e. *kinetic* luminosity) has been widely studied (Willott et al., 1999; Cavagnolo et al., 2010; Smolčić et al., 2017; Hardcastle et al., 2019) with the aim to determine their best-fit relation (Fig. 1.10). This implies to identify cavities on a relatively

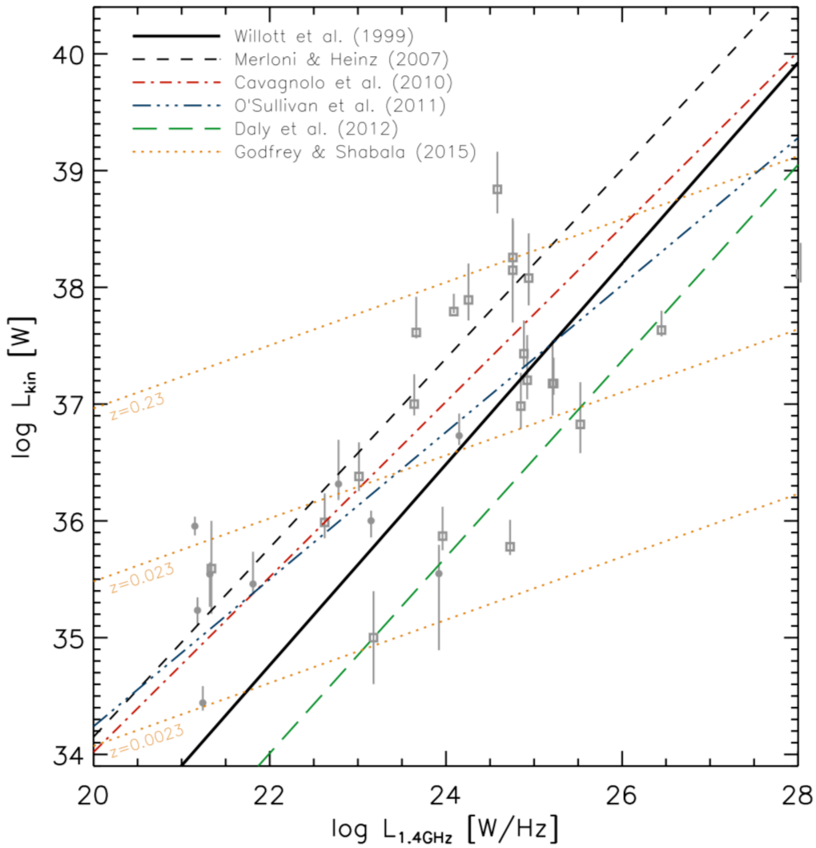

Figure 1.10: Compilation of kinetic luminosity (y-axis) vs. 1.4 GHz luminosity (x-axis) scaling relations from the literature (see legend, Smolčić et al. 2017). Plotted data are from Bîrzan et al. (2004) and O'Sullivan et al. (2011a).

large number of systems, which allows to associate the cavity power to the radio luminosity and extract the underlying scaling relation. This can then be used to determine the kinetic luminosity in objects for which deep X-ray observations are not feasible. Theoretical models that involve assumptions on radio source age and environment can also be used to predict such link. This approach comes at a cost, since both scaling relations and theoretical models can lead to relevant uncertainties when estimating the kinetic luminosity and, in turn, its relation to the cooling of the ICM. We will return on this throughout this thesis.

The role of simulations

Together with observations, numerical simulations also started to investigate if AGN feedback, in the form of mechanical heating through shocks and bubbles, could provide enough heating to quench the ICM radiative losses. Brüggen and Kaiser (2002) employed hydrodynamical simulations to show that cavities, inflated by central AGN, can increase the cooling time and reduce the amount of cold gas. Brüggen (2003) provided more insights into this, proving that bubbles are able to uplift cold gas from the center. The uplifted material can then appear around cavities as bright rims with low temperature. This was found to be

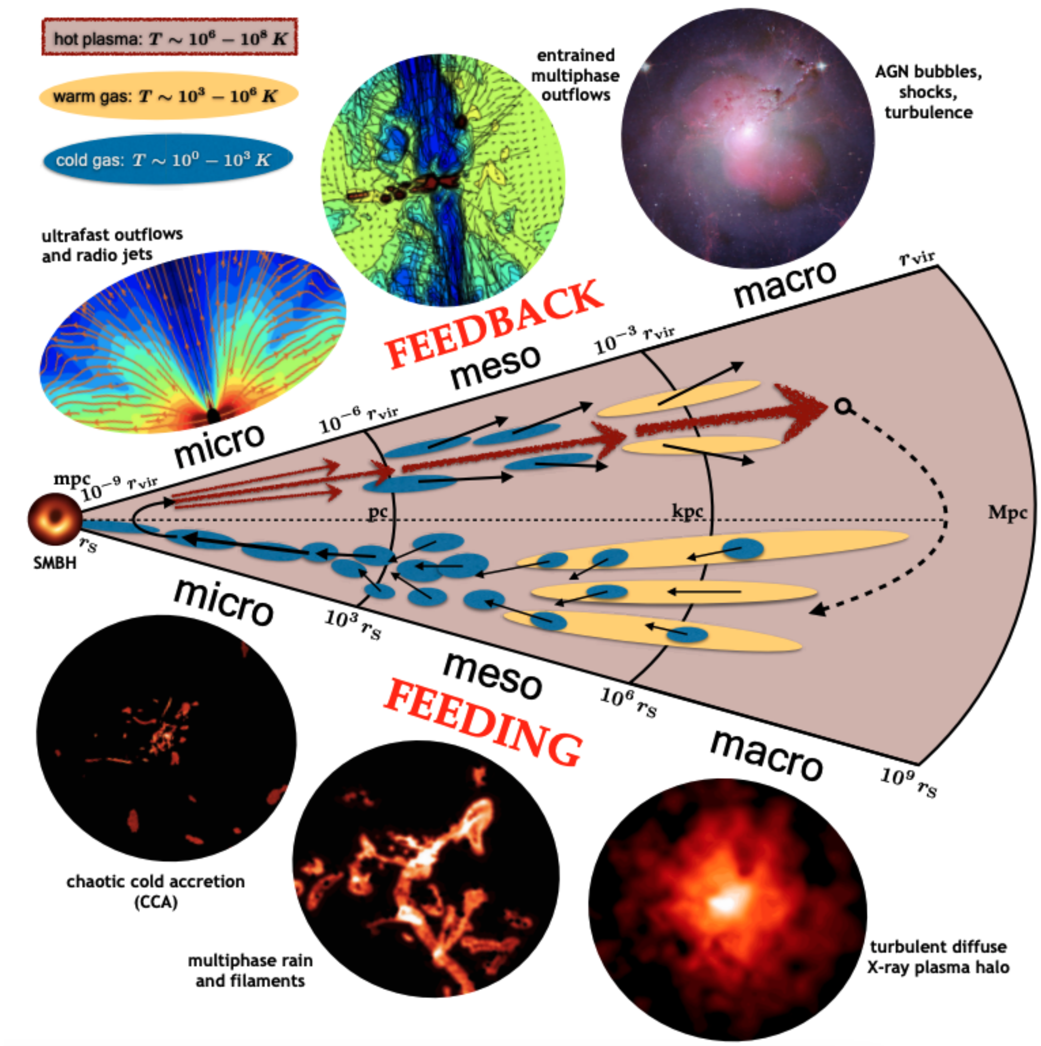

Figure 1.11: The different scales of the AGN feeding-feedback process. The figure is adapted from Gaspari et al. (2020).

consistent with X-ray observations, which sometimes show low-entropy gas around cavities (e.g., McNamara et al., 2000; Blanton et al., 2003).

With all the evidence converging towards AGN feedback as a solution to the long-lasting cooling flow problem, numerical simulations turned to study how the accretion onto the SMBH works, and how the energy injection occur in clusters and groups. Until two decades ago, Bondi accretion (Bondi, 1952) was assumed to describe the accretion mode in most astrophysical environments. Nevertheless, Bondi theory relies on assumptions which are found to be inadequate, or at least unrealistic. The flow is assumed to be steady, adiabatic, spherically simmetric and undisturbed. Furthermore, it does not account for magnetic fields and feedback processes.

Gaspari et al. (2013) relaxed this assumptions using 3D simulations of an elliptical galaxy embedded within a hot halo. They found that the accretion does not follow Bondi's assumption, but it is rather chaotic and cold. Non-linear thermal instabilities lead to condensation of cold clouds, which decouple from the hot phase of the ICM when the ratio between the cooling time and the *free-fall* time $t_{\rm ff} = \sqrt{2R^3/GM}$ approaches $t_{\rm cool}/t_{\rm ff} \leq 10$. These clouds then 'rain' onto the SMBH. The continuous collisions between clouds and filaments quench the angular momentum, boosting the accretion.

With time, *Chaotic Cold Accretion* (CCA) was found to be consistent with observations. For example, CCA predicts flat X-ray temperature profiles at the cluster center, which have been observed in most cool-core systems (Gaspari, 2016). Furthermore, the timescale of this process is consistent with what is needed to prevent significant cooling of the ICM, and it is able to preserve the cool-core appearance of the cluster, preventing both overcooling and overheating. Finally, Gaspari and Sądowski (2017) linked the micro- ($\sim$pc) and macro- ($\sim$kpc to Mpc) scales of AGN feedback (see Fig. 1.11), providing a unified model which accounts for, both, the physics of feeding and that of feedback.

Although CCA still shows some flaws that needs to be completely understood, like predicting accretion rates which are too high compared to observations, as of today it provides the best description of the accretion mode in ellipticals, groups and clusters. Nevertheless, there are multiple questions that still need to be addressed, for example:

- What is the frequency of cold vs. hot accretion in galaxy clusters?
- How are feeding and feedback linked on the micro scales close to the SMBH?
- How is the feedback energy deposited within the ICM?
- Does the AGN duty cycle hold over the entire Hubble time?

Answering these and many others (see also Gaspari et al., 2020) will be the next step forward to reach a more complete understanding of feedback. Thanks to the increasing availability of multi-wavelength observations of galaxy clusters and groups, in the next future it will also be possible to test cold accretion modes on large samples of objects. This will help to better constrain our models, and to eventually discover outlier systems. In particular, CCA needs to be able to reproduce the observed clusters and groups scaling relations. In this thesis, I will investigate more deeply into this in Chapter 5.

1.4 Non-thermal emission in clusters and groups

Radio galaxies

Radio galaxies are galaxies characterised by radio emission driven by $\sim$kpc to Mpc scale jets (see left panel of Fig. 1.12). The central engine is an accreting SMBH, with masses usually in the range 10^7-$10^9\ M_\odot$. Due to angular momentum conservation of the infalling matter, an accretion disk forms around the SMBH. Here, the mass-energy conversion is highly efficient, going up to 10% (Fabian, 1999). The activity of the SMBH is observable in the radio band in the form of synchrotron emission, which indicates that relativistic particles are being accelerated in the presence of magnetic fields. The energy density of radiating electrons can be written as:

$$U = kJ(\nu)B^{-\frac{p+1}{2}} + \frac{B^2}{2\mu_0}, \tag{1.4}$$

with $J(\nu)$ being the volume emissivity, B the magnetic field, p the electron energy index and k a constant which incorporates other physical constants, the observing frequency and the integral over electron energies (see also Hardcastle and Croston 2020 for more details). The minimum-energy condition from Eq. 1.4, which strongly depends on B, is close to equipartition $U_e = U_B$, in which the energy density of electrons and of the magnetic field are equal. Such minimum usually corresponds to total energies $\sim 10^{54}$ J, indicating that the energy budget is likely higher for any deviation from the minimum-energy condition.

Synchrotron spectra of radio galaxies are well-described by a power-law in the form $S(\nu) \propto \nu^{\alpha}$, with $S(\nu)$ being the flux density at a given frequency ν, and α being the spectral index. More relativistic electrons lose energy faster, translating into a steeper spectral index, that can therefore be useful to assess the radiative age of the electron population. Typical spectral indeces of radio galaxies are $\sim$-0.7 – -0.8. Their extent can go from a few kpc to $\sim$Mpc scale (Giant Radio Galaxies, GRG), and most exhibit a roughly symmetrical, double-lobed shape centered on the optical host of the AGN, identified as the core. Some of them show small regions ($\sim$kpc) of enhanced surface brightness close to the lobe edges, referred to as hotspots. Their spectral index is usually flatter, suggesting the presence of a younger electron population.

The most frequently used classification of radio galaxies was introduced by Fanaroff and Riley (1974) and makes use of their radio power and morphology. Above $P_{1.4\mathrm{GHz}} \sim 10^{24.5}$ W Hz^{-1}, they usually show bright hotspots, well-separated lobes and collimated jets. Such *edge-brightened* sources are referred to as *FRII*. Below this luminosity threshold, hotspots are often absent or weak, there is a bright core and lobes are asymmetrical, extended and often in contact with the central source. Such *edge-darkened* sources are referred to as *FRI*.

While it is possible to find FRI- and FRII-like radio galaxies at the centre of galaxy clusters, multiple evidence suggests that the vast majority have amorphous structures, often without collimated jets (Burns, 1990; Owen et al., 1985). On the other hand, moving to the group regime, where the ICM density is lower, it is easier to find large sources (Mack et al., 1998; Subrahmanyan et al., 2008; Cantwell et al., 2020). In a number of cases (e.g. Owen and Rudnick, 1976; O'Dea and Owen, 1985), the jets and tails of radio galaxies are observed to be bented, likely because they are left behind while the host galaxy moves through the cluster environment. Low-frequency observations have also shown extended, low-surface brightness lobes which are possibly associated to previous outbursts of the AGN (e.g. Owen et al., 2000; de Gasperin et al., 2012).

To enable any kind of physical interpretation for radio galaxies, it has been (and it still is) essential to be able to match them to their optical counterpart, i.e. the host galaxy. This requires the combination of radio and optical images with resolution high enough to prevent blending of multiple sources. Studying the properties of optical counterparts reveals interesting features: first of all, the vast majority of the hosts are early-type (i.e. elliptical) galaxies (see also Hardcastle and Croston 2020). Nevertheless, AGN can be also observed in spirals (e.g., Heesen et al., 2022).

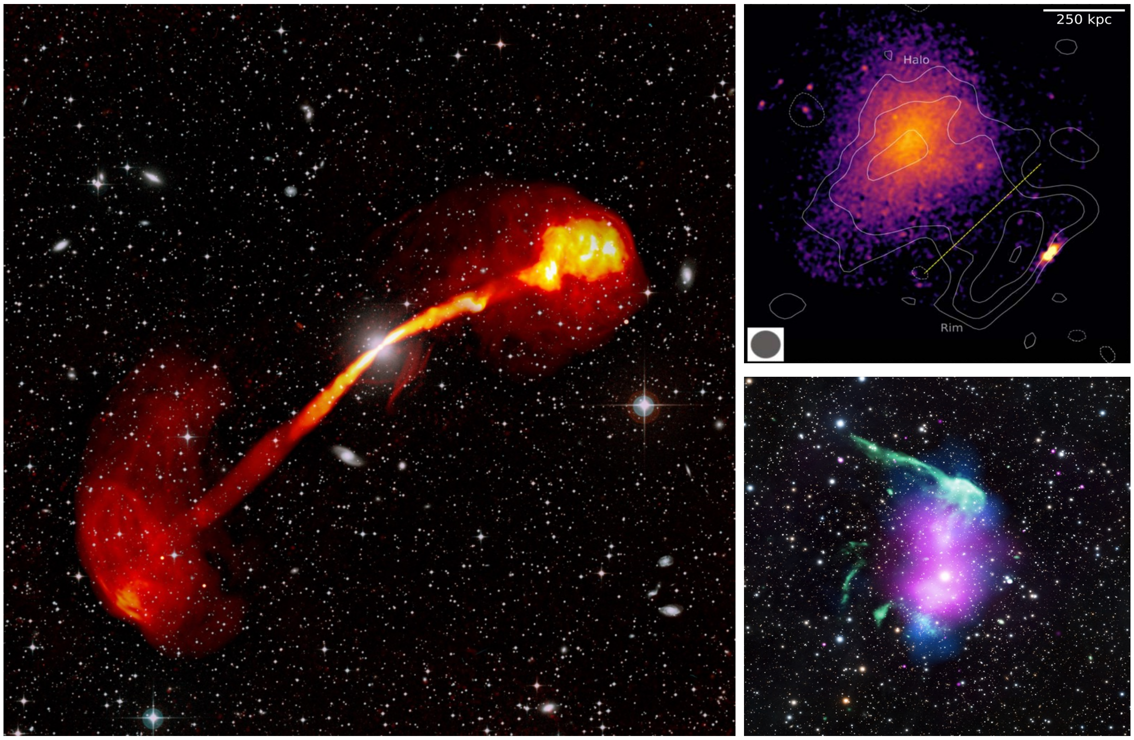

Figure 1.12: *Left*: Radio galaxy at 1.4 GHz as detected by the MeerKAT telescope (Condon et al., 2021). *Top right*: Radio halo (white contours) detected at 144 MHz by the LOw Frequency ARray (LOFAR) in the galaxy cluster PSZ2G145.92-12.53 (Botteon et al., 2021). The X-ray emission by XMM-Newton in the 0.5-2 keV band is colorised. The beam is shown on the bottom left. *Bottom right*: Toothbrush radio relic (cyan) observed by LOFAR (van Weeren et al., 2016; Rajpurohit et al., 2020).

Diffuse emission

As briefly discussed above, in merging clusters it is not rare to detect diffuse radio emission extending from $\sim$ hundreds kpc up to $\sim$1-2 Mpc, which is not directly associated to galaxies (e.g. Willson, 1970). These sources are produced when cosmic-ray electrons are re-accelerated to $\sim$GeV energies in the presence of pre-existing magnetic fields frozen in the ICM (Brunetti and Jones, 2014; van Weeren et al., 2019). Since this is synchrotron emission, we observe a power-law spectrum, similarly to radio galaxies, even though spectral indices are usually steeper ($\alpha < -1$).

In galaxy clusters the typical lifespan of relativistic electrons is of the order of $\sim 10^8$ yr (van Weeren et al., 2011). This can be estimated by combining the radiative losses by synchrotron and Inverse Compton (IC):

$$t = 3.2 \times 10^{10} \frac{B^{0.5}}{B^2 + B_{\text{CMB}}^2} [(1+z)\nu]^{-0.5}, \tag{1.5}$$

with t being the particle age in years, B the cluster magnetic field, $B_{\text{CMB}} = 3.25(1+z)^2$ the equivalent magnetic field of the CMB, z the redshift and ν the observing frequency in MHz. Given the extents typically observed for diffuse radio emission, this age is much shorter than the time required to transport radiating electrons within the cluster volume, that is estimated to be $\sim$10 times higher. This is known as the *slow diffusion problem*, and poses that CR electrons producing diffuse emission need to be continuously re-accelerated, otherwise we would not be able to detect them. Throughout the years, multiple acceleration mechanisms were proposed and tested with observations. To date, different processes are associated to different kinds of diffuse emission, which will be discussed in the next sections.

Radio Halos

Radio halos (RH) are typically centered in the central region of clusters (Cassano et al., 2010), and extend up to $\sim$ 1-2 Mpc (top-right panel of Fig. 1.12). They show a steep spectral index ($\alpha \sim$ -1.3, Giovannini et al. 2009; Feretti et al. 2012), that is observed to be relatively constant across the whole structure. RH often exhibit a roundish morphology, but filamentary structures have also been detected sometimes (van Weeren et al., 2017; Botteon et al., 2020a). Such morphology is often observed to follow the same distribution of the ICM, suggesting a possible link of RH with the thermal gas (Govoni et al., 2001; Rajpurohit et al., 2018; Bruno et al., 2021; Rajpurohit et al., 2021). They usually show no or low polarisation, even though this is probably the consequence of beam depolarisation due to low angular resolution.

It is observed that more massive clusters usually host more powerful halos (e.g. Cassano et al., 2013; Botteon et al., 2022). The correlation (see Fig. 1.13) shows a relatively large scatter, which has been recently shown to be, at least in part, due to different merging histories of the host clusters (Cuciti et al., 2021). RH are almost exclusively observed in disturbed clusters: in the sample of 75 clusters by Cuciti et al. (2021), 90% of halos are found in merging systems. This has allowed to link the formation of such structures with the dynamical state of the host. To date, the re-acceleration of electrons producing RH is associated with large-scale MagnetoHydroDynamic (MHD) turbulence produced by mergers (Brunetti and Jones, 2014; Cassano et al., 2010). Such turbulence, transferred to lower scales, translate into electrons scattering because of inhomogeneities in the magnetic field (i.e. second-order Fermi processes), and subsequently getting re-accelerated. Nevertheless, this is not enough to accelerate electrons from the cluster thermal pool, therefore requiring the existence of a population of mildly-relativistic particles. Other than turbulence (primary or leptonic models), hadronic (or secondary) models predict that halos could be generated when secondary electrons are produced by hadronic collisions between thermal and CR protons (e.g. Pfrommer et al., 2008).

Thanks to the increasing surface brightness sensitivity of interferometers, radio halos with significantly steep spectra ($\alpha > 1.6$) are being discovered (e.g. Brunetti et al., 2008; Macario et al., 2010; Bonafede et al., 2012; Wilber et al., 2018; Bruno et al., 2021; Duchesne et al., 2022). While Ultra-Steep Spectrum Radio Halos (USSRH) are predicted from leptonic models, hadronic models struggle to explain their origin. Furthermore, γ-ray emission is also expected from hadronic collisions, which has not been observed yet. Currently, this evidence suggests that primary models do a better job in explaining the nature of radio halos.

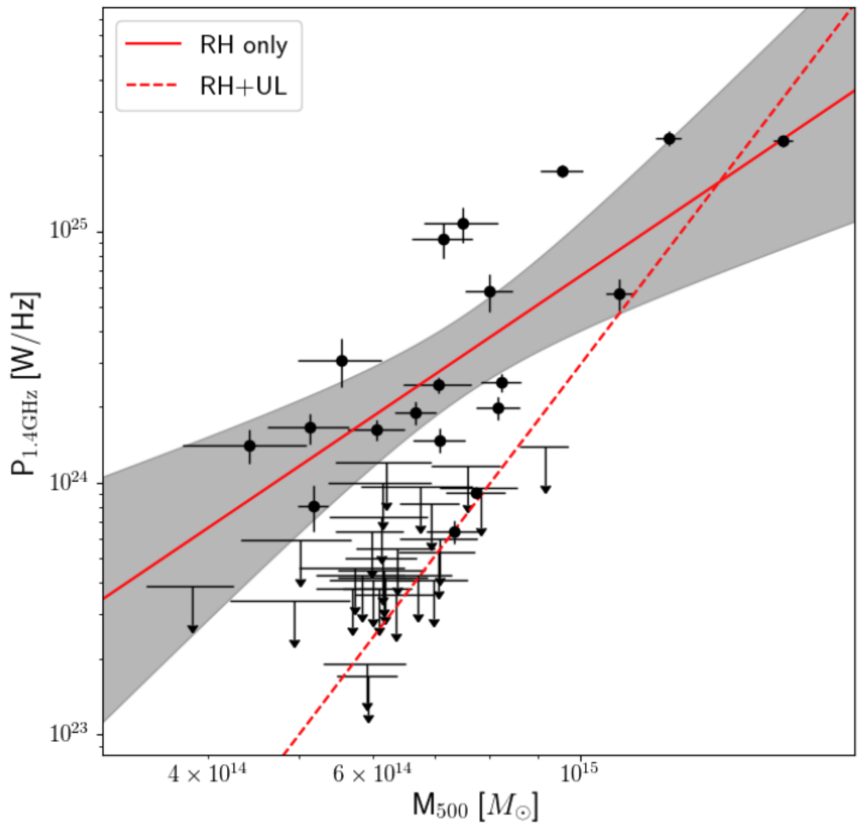

Figure 1.13: Radio power at 1.4 GHz vs. M_{500} for the sample of galaxy cluster radio halos studied in Cuciti et al. (2021). Downward arrows denote upper limits, i.e. clusters with no halo detection.

Radio Relics and fossil radio sources

Contrary to radio halos, relics are located at the edge of the cluster environment (bottom-right panel of Fig. 1.12), have elongated shape and their extent ranges from ∼500 kpc up to ∼Mpc (Vazza et al., 2012). Recently, high-resolution observations have also detected filamentary structures within relics (Di Gennaro et al., 2018; Rajpurohit et al., 2020; de Gasperin et al., 2022; Rajpurohit et al., 2022b). They trace electrons that are being re-accelerated by ICM shock waves with relatively low ($\mathscr{M} < 3$) Mach numbers (Finoguenov et al., 2010; Akamatsu et al., 2013; Botteon et al., 2016), as they are observed to be co-spatial with shocks detected through X-ray observations. Relatively large polarisation (up ∼70% at 1.4 GHz, Ensslin et al. 1998; Bonafede et al. 2014; de Gasperin et al. 2022) is often detected in relics, that usually show a clear gradient of spectral index, steeper in the direction of the cluster centre and flatter moving towards the outskirts. Correlations are known between their extent, the integrated spectral index and the radio power (van Weeren et al., 2009a; Bonafede et al., 2012; de Gasperin et al., 2014).

The formation of these structures is attributed to Diffusive Shock Acceleration (DSA), in which electrons get accelerated diffusively at the shock location (Ensslin et al., 1998; Roettiger et al., 1999). As they scatter because of magnetic inhomogeneities, they cross

Figure 1.14: *Left*: LOFAR 144 MHz and Chandra 0.5-2 keV images of the radio phoenix in the galaxy cluster A2034 (Shimwell et al., 2016). *Right*: Optical (SDSS), radio (LOFAR) and X-ray (Chandra) images of the GReET observed in A1033 (de Gasperin et al., 2017).

back and forward across the shock front, gaining energy at every crossing and eventually producing a power-law distribution. However, this mechanism can be rather inefficient in accelerating electrons from the thermal pool (Vazza and Brüggen, 2014; Vazza et al., 2016; Botteon et al., 2020a; Brüggen and Vazza, 2020a), suggesting that a population of midly-relativistic electrons could already exist prior to DSA processes. It has recently been suggested that such electrons could be provided by tails and lobes of radio galaxies (van Weeren et al., 2017; Stuardi et al., 2019).

Due to synchrotron and IC losses, relativistic electrons at higher frequency lose energy faster. Old, faint populations of electrons can sometimes be revived through re-acceleration mechanisms such as adiabatic compression (Enßlin and Gopal-Krishna, 2001). Indeed, low-frequency observations have revealed the presence of ultra-steep sources tracing AGN radio plasma (Fig. 1.14), often referred to as radio phoenices (Kempner and David, 2004), in which the steep index is due to electrons energy losses (Clarke et al., 2013; de Gasperin et al., 2015a; Mandal et al., 2019). Phoenices can show different morphology, and usually have extents up to $\sim$500 kpc. They are not exclusively observed in disturbed systems, suggesting that mergers could not be necessary for their formation.

All currently known radio halos and relics have been detected in galaxy clusters with $M > 10^{14} M_{\odot}$ (van Weeren et al., 2019). On the other hand, diffuse emission in the galaxy group mass regime has never been observed yet. There could be multiple reasons for this dearth of data. Mergers in galaxy groups could be not strong enough to trigger the turbulences and shocks required to re-accelerate seed electrons. The limited surface brightness sensitivity of most radio telescopes and interferometers could even prevent us from detecting diffuse emission in groups.

Finally, in a few cases revived tails of radio galaxies (labelled Gently Re-Energised Tails, GReETs) have also been detected, showing a flatter spectrum with respect to phoenices. This is the case of A1033 (de Gasperin et al., 2017), in which a $\sim$500 kpc long tail was found to exhibit an almost flat spectral index across its whole extent. Since it is unlikely, for a shock, to be able to re-accelerate all these electrons at the same time, second-order Fermi processes were invoked (van Weeren et al., 2019) to explain GReETs. This mechanism is so gentle that it barely compensate for the electron radiative losses, leading to the flat spectral index distribution.

According to these models, extremely low-frequency observations are expected to detect an increasing number of sources undergoing similar re-accleeration mechanisms (e.g., Cuciti et al., 2018; Botteon et al., 2021; Ignesti et al., 2022; Brienza et al., 2022), as well as bridges connecting RH and relics to the AGN plasma. We will return on this in Chapter 6.

Magnetic fields in galaxy clusters

It is been known for a long time that galaxy clusters and groups are embedded within magnetic fields with $B \sim \mu G$ (e.g., Jaffe, 1977; Carilli and Taylor, 2002). Large et al. (1959) discovered a radio source in the Coma cluster which was later (Willson, 1970) classified as the first cluster radio halo (see Sec. 1.4). The presence of large-scale synchrotron emission indicated the presence of a magnetic field of $\sim 2\mu G$ (if in equipartition) which permeated the whole cluster.

It quickly became clear that magnetic fields are obiquitus in galaxy clusters (Klein and Fletcher, 2015), and scientists started to look for methods to accurately measure their strength. One of the most successful makes use of the Faraday rotation, i.e. the rotation of the polarisation plane when a polarised radiation crosses a magnetised medium. Such rotation is proportional to the medium density, which can be estimated through observations, and to the magnetic field. An alternative method is to use equipartition, i.e. assuming that the contribution of relativistic particles and magnetic field to the total energy of a synchrotron source is equal (Feretti et al., 2012). Finally, it is in theory possible to derive constraints on magnetic fields by comparing radio and X-ray emission at energy > 10 keV, which is mainly produced by Inverse Compton (IC) scattering between ICM and CMB photons. However, cluster emission is faint and hard to detect at high energy.

The strength of magnetic fields seems to decrease as the distance from the cluster centre decreases (Bonafede et al., 2010). Although this looks in contrast with observations of radio diffuse emission in the cluster outskirts (see Sec. 1.4), the contribution of shocks may lead to amplify magnetic fields through adiabatic compression (Brüggen, 2013). Recently, simulations by Chadayammuri et al. (2022) showed that amplification can be observed by Faraday rotation measures.

There is still a lot to understand about magnetic fields in galaxy clusters. Their origin, for instance, is still unknown, albeit different hypotheses have been proposed. It is likely that magnetic field seeds already existed in the primordial Universe, which have then grown during expansion. These seeds could have either been generated during inflation, and therefore be observable in the CMB spectrum, or by AGN and galactic winds at $z \sim 2-3$

(see Subramanian 2016 for a review).

1.5 Aims and outline of this thesis

This thesis is composed by the research I have conducted in my three years of PhD. The main focus of the first two years is on AGN feedback in galaxy clusters and groups, with an eye on large samples and, especially, the low-mass regime, which has been hardly investigated before. To this end, I have vastly employed new-generation radio surveys of the sky, led by interferometers such as LOFAR and MeerKAT, and X-ray space telescopes such as *Chandra* and the newly-launched eROSITA. The combination of high-resolution and high-sensitivity multi-wavelength data, as well as the coordination with optical telescopes, allowed us to build samples of galaxy clusters and groups for which we were able to locate the central radio galaxy, often associated with the BCG. We were therefore in possess of a wealth of X-ray (ICM emission), radio (from the central AGN) and optical (BCG) observations which would have been hard to imagine even just ten years ago. This data was then used to investigate the mechanisms of AGN feedback in a way that was hardly possible before.

Finally, in my last year of PhD I focused instead on diffuse emission in galaxy clusters as seen by the lowest frequency allowed by LOFAR, 54 MHz. Given the technical complications of observing the sky at this frequency, the observations provided by LOFAR are unprecedented, and allow us to explore a previously poorly-studied frequency regime. This will provide more constrains on the re-acceleration processes which we think might explain the different kinds of extended sources observed in disturbed systems. To this end, while to-date I am still working on a publication which will focus on all the galaxy clusters observed at 54 MHz in the HETDEX sky field, I have selected one among the most interesting systems in this field, A1550, to show the capabilities of LOFAR. I have combined data at different frequencies, finding a plethora of different kinds of diffuse emission, such as a steep-spectrum radio halo, a relic, a phoenix, and possibly a re-accelerated radio tail. All these sources were studied, also with the aid of X-ray observations, to understand the mechanisms that produce them. In the next future, I will lead a further publication which applies the same kind of analysis on all HETDEX clusters.

The questions that this thesis aims to address are the following:

- How does feedback act in galaxy clusters in which the AGN has been offset from the center of the cooling region?
- How do AGN feedback mechanisms act in the lower-mass regime of galaxy groups? What happens when we extend the analysis on large samples of clusters and groups?
- What are the differences, in terms of kinematic properties, between galaxies hosting radio emission and not in galaxy groups? Does AGN feedback play a role in this picture?

- Does the link between central AGN and ICM hold even in disturbed galaxy clusters? If yes, what keeps this link alive?
- What can we learn from 54 MHz observations of galaxy clusters? Can we better constrain re-acceleration mechanisms by combining them with other multi-frequency data?

I have gathered and published my results in 5 scientific, peer-reviewed journal articles, which are discussed from Chapter 2 to Chapter 6 of this thesis:

1. T. Pasini, M. Gitti, F. Brighenti, E. O'Sullivan, F. Gastaldello, F. Temi, and S. L. Hamer: *A First Chandra View of the Cool Core Cluster A1668: Offset Cooling and AGN Feedback Cycle.* ApJ, 911, 66, April 2021.
2. T. Pasini, M. Brüggen, F. de Gasperin, L. Bîrzan, E. O'Sullivan, A. Finoguenov, M. Jarvis, M. Gitti, F. Brighenti, I. H. Whittam, J. D. Collier, I. Heywood, and G. Gozaliasl: *The relation between the diffuse X-ray luminosity and the radio power of the central AGN in galaxy groups.* MNRAS, 497, 2163, September 2020.
3. T. Pasini, M. Brüggen, D. N. Hoang, V. Ghirardini, E. Bulbul, M. Klein, A. Liu, T. W. Shimwell, M. J. Hardcastle, W. L. Williams, A. Botteon, F. Gastaldello, R. J. van Weeren, A. Merloni, F. de Gasperin, Y. E. Bahar, F. Pacaud, and M. Ramos-Ceja: *The eROSITA Final Equatorial-Depth Survey (eFEDS): LOFAR view of brightest cluster galaxies and AGN feedback.* A&A, 661A, 13P, May 2022.
4. T. Pasini, A. Finoguenov, M. Brüggen, M. Gaspari, F. de Gasperin, and G. Gozaliasl: *Radio galaxies in galaxy groups: kinematics, scaling relations, and AGN feedback.* MNRAS, 505, 2628, August 2021.
5. T. Pasini, H. W. Edler, M. Brüggen, F. de Gasperin, A. Botteon, K. Rajpurohit, R. J. van Weeren, F. Gastaldello, M. Gaspari, G. Brunetti, V. Cuciti, C. Nanci, G. di Gennaro, M. Rossetti, D. Dallacasa, D. N. Hoang, and C. J. Riseley: *Particle re-acceleration and diffuse radio sources in the galaxy cluster Abell 1550.* Accepted by A&A, June 2022.

The chapters are not in chronological order (i.e. publication year order), but gathered in a way that best allows the reader to reach a good comprehension of the topics. Chapter 2 discusses the work published in Pasini et al. (2021b), in which we combined radio, X-ray and optical observations of the cool-core galaxy cluster A1668 to study feedback processes and to investigate whether offsets between the central AGN, the ICM cooling peak and the Hα gas can break the AGN duty cycle. Chapter 3 discusses the work published in Pasini et al. (2020), in which we built a sample of 247 galaxy groups observed at radio (VLA+MeerKAT) and X-ray (*Chandra*) wavelengths in the COSMOS sky field. We then investigated correlations between the hot gas and the central AGN, with the aim of assessing how feedback operates in the lower-mass regime of galaxy groups. Chapter 4 discusses the work published in Pasini et al. (2022a), in which we applied the same kind of analysis previously performed on the COSMOS sample, on a much larger sample of 542 galaxy clusters and groups observed by LOFAR and the new-generation X-ray telescope eROSITA in the eFEDS field. We investigated the balance between the ICM radiative losses and the heating provided by the central AGN, classifying our systems into relaxed or disturbed based on their dinamical state, providing new information on the feedback processes in play. Chapter 5 discusses the work published in Pasini et al. (2021a), in which we investigate the kinematics of a large sample of 998 COSMOS spectroscopic galaxies, distributed among 79 galaxy groups, finding significant differences between those hosting radio emission and those which are radio quiet. We then put our results in context with the current picture of AGN feedback. Finally, Chapter 6 discusses the work published in Pasini et al. (2022b), shifting the focus from AGN feedback to diffuse emission in galaxy clusters: we use multi-frequency radio observations, as well as *Chandra* data, to study the different kinds of extended emission detected in A1550, with the aim of providing new insights into re-acceleration processes at low frequency. This publication will be soon followed by a complete census of the diffuse emission observed at 54 MHz in all HETDEX galaxy clusters. As a conclusion of this thesis, Chapter 7 put all these results in context with the above scientific topics and issues, also including an eye on next-future projects that could help us to further address the open questions in the field.

2. AGN feedback and offsets in A1668

A first Chandra view of the cool core cluster A1668: offset cooling and AGN feedback cycle

T. Pasini, M. Gitti., F. Brighenti et al. *Astrophysical Journal*, 911, 66 (2021)

Abstract. *We present a multi-wavelength analysis of the galaxy cluster A1668, performed by means of new EVLA and Chandra observations and archival Hα data. The radio images exhibit a small central source (∼14 kpc at 1.4 GHz) with $L_{1.4\,GHz}$ ∼$6 \cdot 10^{23}$ W Hz^{-1}. The mean spectral index between 1.4 GHz and 5 GHz is ∼ -1, consistent with the usual indices found in BCGs. The cooling region extends for 40 kpc, with bolometric X-ray luminosity $L_{cool} = 1.9 \pm 0.1 \cdot 10^{43}$ erg s^{-1}. We detect an offset of ∼ 6 kpc between the cluster BCG and the X-ray peak, and another offset of ∼ 7.6 kpc between the Hα and the X-ray peaks. We discuss possible causes for these offsets, which suggest that the coolest gas is not condensing directly from the lowest-entropy gas. In particular, we argue that the cool ICM was drawn out from the core by sloshing, whereas the Hα filaments were pushed aside from the expanding radio galaxy lobes. We detect two putative X-ray cavities, spatially associated to the west radio lobe (cavity A) and to the east radio lobe (cavity B). The cavity power and age of the system are $P_{cav} \sim 9 \times 10^{42}$ erg s^{-1} and t_{age} ∼5.2 Myr, respectively. Evaluating the position of A1668 in the cooling luminosity-cavity power parameter space, we find that the AGN energy injection is currently consistent within the scatter of the relationship, suggesting that offset cooling is likely not breaking the AGN feedback cycle.*

2.1 Introduction

In the last two decades, our understanding of the evolution of cool core galaxy clusters has led to a picture in which the cooling of the *Intra-Cluster Medium* (ICM), the cold gas accreting onto the *Brightest Cluster Galaxy* (BCG), and the feedback from the central radio source give birth to a tightly-connected cycle, known as Active Galactic Nuclei (AGN) feedback loop (for reviews see e.g. McNamara and Nulsen, 2007; Gitti et al., 2012; McNamara and Nulsen, 2012; Fabian, 2012; Soker, 2016). Multi-wavelength data provide strong evidences of this cycle: cavities in the ICM, revealed through deep X-ray observations and induced by the jets of the central radio galaxy (e.g., McNamara et al., 2000; Bîrzan et al., 2004; Clarke et al., 2004; Fabian et al., 2006; Gentile et al., 2007), cold fronts (e.g., Fabian et al., 2006; Markevitch and Vikhlinin, 2007; Gastaldello et al., 2009; Ghizzardi et al., 2010), optical line emission (Crawford et al., 1999; McDonald et al., 2010; Hamer et al., 2016) and dust filaments (Van Dokkum and Franx, 1995; Laine et al., 2003) indicate an extremely complex and dynamical environment, whose physical processes are still to be completely understood.

Recently, a number of studies have revealed strong links between the central BCG, the X-ray core and the cluster dynamics (Sanderson et al., 2009; Hudson et al., 2010; Rossetti et al., 2016). In particular, spatial offsets between the BCG, the Hα line emission and the X-ray emission peak (e.g. Haarsma et al., 2010; Hamer et al., 2012, 2016; Barbosa et al., 2018) suggest that ICM sloshing and offset cooling, together with the AGN, can have a significant influence on the cluster evolution. Indeed, all these elements affect the activity of the central Supermassive Black Hole (SMBH) through motions of the gas, that could be able to regulate the cavity production and, consequently, the feedback cycle, since the ICM oscillates back and forth with respect to the central SMBH.

This was recently discussed in Pasini et al. (2019) for the cool core cluster A2495. Spatial offsets have been observed in this cluster, with the X-ray peak being separated by $\sim$ 6 kpc from the BCG and $\sim$ 4 kpc from the Hα line emission peak. The analysis presented by the authors on two putative systems of X-ray cavities, hinted at in the shallow ($\sim$ 8 ks) *Chandra* observation, suggests that even if cooling is not depositing gas onto the BCG core, the coupling between the AGN power output and the cooling rate is still consistent with the observed distribution for cluster samples. In a forthcoming publication we will present the detailed analysis of the deeper *Chandra* observations of A2495, recently allocated ($\sim$ 130 ks, P.I. Gitti[1]), which will be key to probe the presence of two pairs of ICM cavities and test the proposed scenario that the feeding-feedback cycle is not broken.

A1668 was selected, along with A2495, from the ROSAT Brightest Cluster Sample (BCS; Ebeling et al. 1998) by choosing objects with X-ray fluxes greater than 10^{-11} erg cm^{-2} s^{-1} and, among these, by selecting those characterized by $\log L_{H\alpha} > 40$ from the catalogue of Crawford et al. (1999). Of the obtained sample of 13 objects, A2495 and A1668 still lacked *Chandra* observations, that were obtained jointly with new VLA data (P.I. Gitti[2]). Pasini et al. (2019) have presented the results for A2495, making also use of Hα line emission data and *Hubble Space Telescope* (HST) archival images. In this work we combine the A1668 VLA and *Chandra* new observations in order to study the interactions between the radio source hosted in the BCG and the ICM. As well as for A2495, we included Hα

[1]Proposal Number 22800391
[2]Proposal Number 12800143

Frequency	Number of spw	Channels	Bandwith	Array	Total exposure time
5 GHz (C BAND)	2 (4832 MHz - 4960 MHz)	64	128 MHz	B	3h59m21s
1.4 GHz (L BAND)	2 (1264 MHz - 1392 MHz)	64	128 MHz	A	2h59m28s

Table 2.1: Radio observations properties (project code SC0143, P.I. M. Gitti).

line emission data from Hamer et al. (2016); on the other hand, no HST data are available for this cluster.

A1668 was previously observed in the radio band by TGSS (TIFR GMRT Sky Survey), which gives an estimate for the 150 MHz flux density of 1589± 159 mJy; Hogan et al. (2015) performed a 5 GHz radio analysis (the data they used are not the same presented in this work), estimating a flux density of 21.0 ± 0.1 mJy. A1668 was recently included by Bîrzan et al. (2020) in their sample of systems observed at 150 MHz by the LOw Frequency ARray (LOFAR, van Haarlem et al. 2013), showing the presence of large radio lobes, each extending for more than 50 kpc, and estimating a total flux density of 1.83 ± 0.44 Jy, consistent with TGSS.

Richness-based estimate of the mass provided values of $M_{200} \simeq 1.66{\cdot}10^{14}$ $M_\odot$ (Andreon, 2016) and $M_{2500} = 3.9 \pm^{0.8}_{0.7} \cdot 10^{13}$ $M_\odot$ (Pulido et al., 2018). The cluster's BCG, IC4130, shows a Star Formation Rate (SFR), estimated from extinction-corrected Hα luminosity obtained from long-slit observations, of SFR = 2.5 ± 0.3 $M_\odot$ yr^{-1} (Pulido et al., 2018), and extends for $\sim$ 85 kpc (diameter at the isophotal level of 25 mag/arcsec^2 in the B-band, Makarov et al. 2014). [3] Edwards et al. (2009) also presented IFU observations of the Hα emission close to the BCG, finding a clear velocity gradient from positive values north of the centre to negative values at the south. They also argued that the line emitting gas is likely not at rest with respect to the BCG.

In this work, we adopt a ΛCDM cosmology with H_0 = 73 km s^{-1} Mpc^{-1}, $\Omega_M = 1 - \Omega_\Lambda$ = 0.3. The BCG redshift is z = 0.06355 (Hamer et al., 2016) and the luminosity distance is 273.7 Mpc, leading to a conversion of 1 arcsec = 1.173 kpc.

2.2 Radio analysis

Observations and data reduction

IC4130, the BCG of A1668, was observed with the EVLA on 2011 June 17th in the 1.4 GHz band, and on 2011 March 9th in the 5 GHz band, in A and B configurations respectively. Details of the observations are shown in Table 2.1.

The sources J1331+3030 (3C286) and J1327+2210 were used for both the observations as flux and phase calibrators, respectively. The data reduction was performed using the NRAO Common Astronomy Software Applications package (CASA, version 5.3), applying the standard calibration procedure after carrying out an accurate editing of the visibilities with the CASA task `FLAGDATA`. We removed about 6% of the target visibilities at 5 GHz, whereas at 1.4 GHz the data were highly contaminated by Radio Frequence Interferences

[3] HyperLEDA catalog.

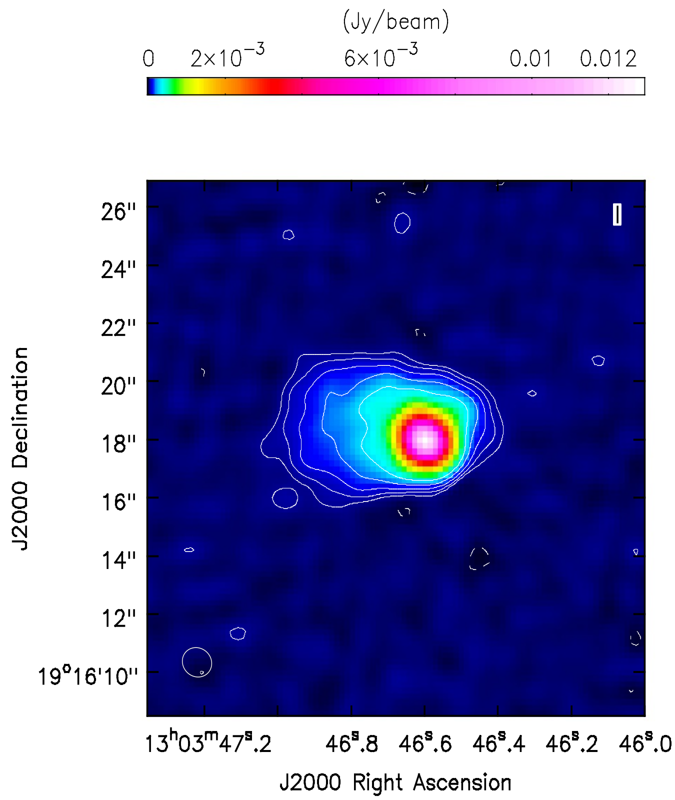

Figure 2.1: 5 GHz VLA map (ROBUST 0) of the radio source hosted in IC4130, the BCG of A1668. The resolution is 1.14” × 1.00”, with a rms noise of 6 μJy beam^{-1}. Contours are at -3,3,6,12,24,48 · rms. The source flux density is 19.9 ± 1.0 mJy. The bottom-left white ellipse represents the beam.

(RFI), thus producing a visibility loss of $\sim$ 40%.

We applied the standard imaging procedure, making use of the `CLEAN` task on a 7” × 7” region centered on the radio source. We took into account the sky curvature by setting the `gridmode=WIDEFIELD` parameter and used a two-terms approximation of the spectral model exploiting the MS-MFFS algorithm (Rau and Cornwell, 2011).

Results

We produced total intensity radio maps by setting `weighting = BRIGGS`, corresponding to `ROBUST 0`. This baseline weighting provides the best compromise between angular resolution (determined by long baselines) and sensitivity to extended emission (provided by short baselines). The uncertainty on the flux density measurements is 5%, estimated from the amplitude calibration errors.

At 5 GHz (Fig. 2.1), the radio source exhibits a total flux density of 19.9 ± 1.0 mJy, consistent with Hogan et al. (2015), that corresponds to a luminosity of $L_{5\,\mathrm{GHz}} = (1.8 \pm 0.1) \cdot 10^{23}$ W Hz^{-1}. The rms noise is 6 μJy beam^{-1}. The source stretches Eastwards for $\sim$ 11 kpc, with a minor axis of $\sim$ 5.7 kpc. There are no visible hints of larger emission up to the scale we are sensitive to (60 kpc with the VLA B configuration at 5 GHz). The

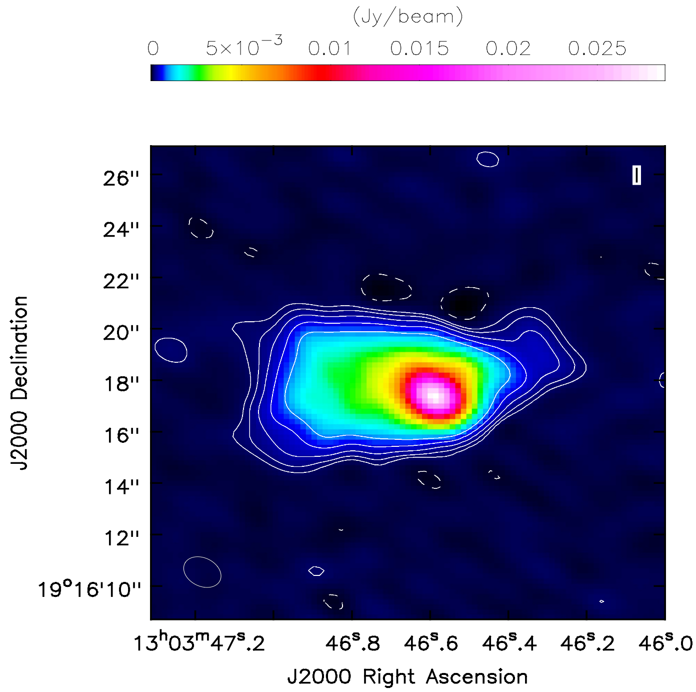

Figure 2.2: 1.4 GHz VLA map (ROBUST 0) of the radio source hosted in IC4130. The resolution is 1.44" × 1.08", with a rms noise of 17 μJy beam^{-1}. Contours are at -3,3,6,12,24,48 · rms. The source flux density is 70.2 ± 3.5 mJy. The bottom-left white ellipse represents the beam.

Band	Flux density [mJy]	rms [μJy beam^{-1}]	beam [arcsec]	Luminosity [10^{22} W Hz^{-1}]	Volume [kpc^3]	Brightness Temperature [K]	Equipartition Field [μG]
5 GHz	19.9 ± 1.0	6	1.14x1.00	16.8 ± 0.8	185 ± 22	39.6 ± 10.4	8.7 ± 0.1
1.4 GHz	70.2 ± 3.5	17	1.44x1.08	59.1 ± 2.9	359 ± 30	1129.3 ± 241.2	10.3 ± 0.1

Table 2.2: Radio properties of A1668 in the two bands observed. The axes of the radio galaxy are a = 10.9 ± 1.3, b = 5.7 ± 1.3 for the 5 GHz map and a = 14.0 ± 1.3, b = 7.1 ± 1.3 for the 1.4 GHz map. The flux density is estimated within 3σ contours, while for the volume we assumed a prolate elissoid shape.

equipartition magnetic field was estimated following the method described in Feretti and Giovannini (2008), finding H_{eq}(5 GHz) = 8.7 ± 0.1 μG.

The 1.4 GHz map (ROBUST 0, Fig. 2.2) shows no significant differences with respect to the 5 GHz emission. The source flux density is 70.2 ± 3.5 mJy and the rms is ∼ 17 μJy beam^{-1}. The radio source scale is slightly larger (∼ 14 kpc for the major axis, ∼ 7 kpc for the minor axis), with a more developed west lobe; again, we did not detect any hint of larger scale emission up to our sensitivity scale (70 kpc with VLA A configuration at 1.4 GHz). Some cool core clusters show diffuse emission in the form of radio mini-halos (e.g., Gitti et al., 2004; Govoni et al., 2009; Giacintucci et al., 2014). Giacintucci et al. (2017) define for mini-halos a minimum radius of 50 kpc since, at smaller radii, diffusion and other transport mechanisms are plausibly able to spread the relativistic electrons from the central AGN within their synchrotron radiative cooling time. In Fig. 2.1 and Fig. 2.2, the radio emission is coincident with the optical BCG, and the small scale suggests that it can all

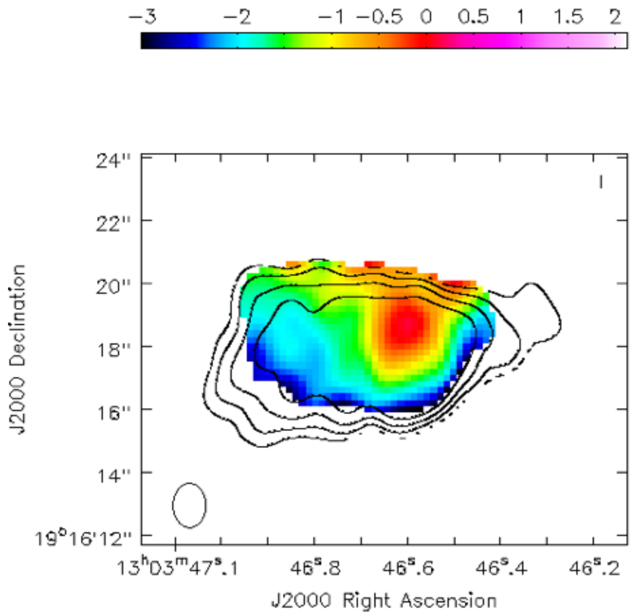

Figure 2.3: Spectral index map between 5 GHz and 1.4 GHz of the radio source hosted in IC4130. Contours are the same as Fig. 2.2, and typical errors range from $\Delta\alpha \simeq 0.1$ for the inner and $\Delta\alpha \simeq 0.5$ for the outer regions.

be accounted to the AGN/radio galaxy. It is possible that diffuse emission larger than our sensitivity scale exists; however, given the extended double-lobe morphology of the LOFAR 150 MHz image presented in Bîrzan et al. (2020), the presence of a mini-halo in A1668 looks unlikely. The equipartition field is H_{eq}(1.4 GHz) = 10.3 $\pm$ 0.1 μG. Radio properties can be found in Table 2.2.

The radio source hosted in the centre of A1668 can be classified as a FRI galaxy, as demonstrated by both the morphology (asimmetric lobes, no hotspots) and the 1.4 GHz luminosity ($L_{1.4\,\mathrm{GHz}} = (6.3 \pm 0.3) \cdot 10^{23}$ W Hz^{-1}), that place IC4130 in the 70$^{\mathrm{th}}$ percentile of the BCG radio luminosity function presented in Hogan et al. (2015).

Spectral index map

The synchrotron spectrum follows a power law $S_\nu \propto \nu^\alpha$, where α is the spectral index. The spectral index map (Fig. 2.3) was generated using the CASA task `IMMATH`, combining 1.4 GHz and 5 GHz maps produced with matched `weighting=UNIFORM` (to enhance the resolution), `UVRANGE=6.5-152` , and a resolution of 1.4” $\times$ 1.0”. The `UVRANGE` was set in order to be sensitive to the same baselines (thus, physical scales) for both observations.

Table 2.3 lists the peak, the extended and the total radio emission flux densities at 5 and 1.4 GHz, together with the estimated spectral index between the two frequencies. The radio core exhibits a flat index ($\alpha \simeq 0$), as expected from optical thick regions where the radiation is self-absorbed. Moving towards the outskirt the spectrum becomes steeper, reaching $\alpha \simeq -2.5$ in the outermost part. The mean index is -0.99$\pm$ 0.06, consistent with the typical values found in BCGs (Hogan et al., 2015). Table 2.3 summarizes the spectral

Region	$S_C \pm \Delta S_C$ [mJy]	$S_L \pm \Delta S_L$ [mJy]	$\alpha \pm \Delta\alpha$
Peak	7.5 $\pm$ 0.4	17.6 $\pm$ 0.9	-0.67 $\pm$ 0.06
Extended	12.4$\pm$ 0.6	52.6 $\pm$ 2.6	-1.13 $\pm$0.05
Total	19.9 $\pm$ 1.0	70.2 $\pm$ 3.5	-0.99 $\pm$ 0.06

Table 2.3: The first column shows the flux density values at 5 GHz (C band), while the second displays the 1.4 GHz (L band) values. The third column presents the corrispondent spectral index values. The extended flux density was estimated as the difference between the total and the peak fluxes.

index properties.

2.3 X-ray Analysis

Observation and data reduction

A1668 was observed with the *Chandra Advanced CCD Imaging Spectrometer* (ACIS), with the focal point on the S3 CCD, in cycle 12 (ObsID 12877, P.I. Gitti) for a total exposure of $\sim$ 10 ks. Data were reprocessed with CIAO 4.9 (Fruscione et al., 2006) using CALDB 4.2.1. We ran the `Chandra_repro` script to perform the standard calibration process. After background flare removal, we used the `Blanksky` template files, filtered and normalized to the count rate of the source in the hard X-ray band (9-12 keV), in order to subtract the background. The final exposure time is 9979 s, with roughly $\sim$ 6800 net counts in a 100" ($\sim$ 120 kpc radius region (0.5-2 keV) centered on the cluster.

Point sources were identified and removed using the CIAO task `WAVDETECT`. Making use of optical catalogues, we found that no astrometry correction was necessary. Unless otherwise stated, the reported errors are at 68 % confidence level (1 σ).

Results

Surface Brightness Profile

In Fig. 2.4 we show the smoothed 0.5-2 keV image of A1668. The ICM exhibits a roughly circular and regular morphology on large scales (> 30" $\sim$ 35 kpc), while the cluster core shows a region with enhanced emission in the NE-SW direction. Using the tool `SHERPA` (Freeman et al., 2001), a surface brightness profile was produced from a background-subtracted, exposure-corrected image, making use of 2"-width concentric annuli centered on the X-ray peak. The profile was then fitted with a single β-Model (Cavaliere and Fusco-Femiano, 1976b) over the external 30"-100" (35-120 kpc) interval, in order to exclude the whole core region[4]. The result of the fit (χ^2/DoF $\sim$ 1.71) and its extrapolation to the core region is represented with the blue line in Fig 2.5. The best-fit values are: core radius `r0`=10.0 $\pm^{0.7}_{0.4}$ arcsec ($\sim$ 11.8 kpc), `beta`=0.43 $\pm^{0.04}_{0.02}$ and central surface brightness `ampl`=0.64 $\pm^{0.10}_{0.04}$ counts s^{-1} cm^{-2} sr^{-1}.

[4]The assumption of 30", that was already justifiable through visual inspection, will be furtherly supported, in Sec. 2.3, by the estimate of the cooling radius

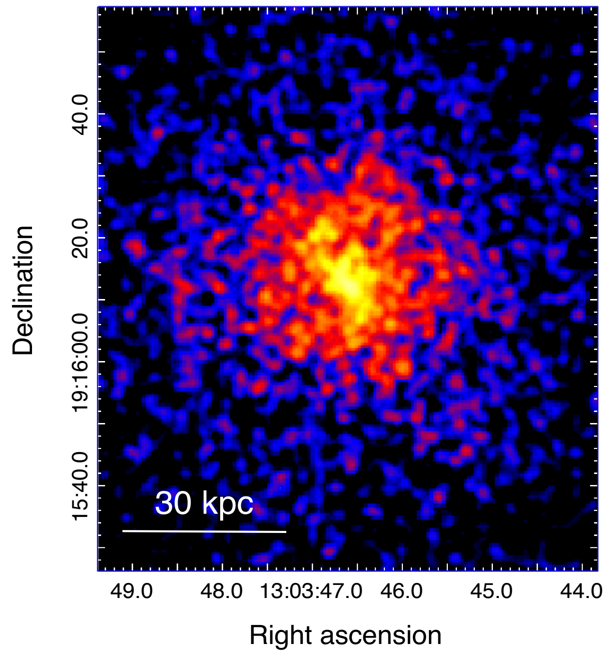

Figure 2.4: Chandra image of A1668 in the 0.5-2 keV band, smoothed with a gaussian filter with a 3 pixel radius.

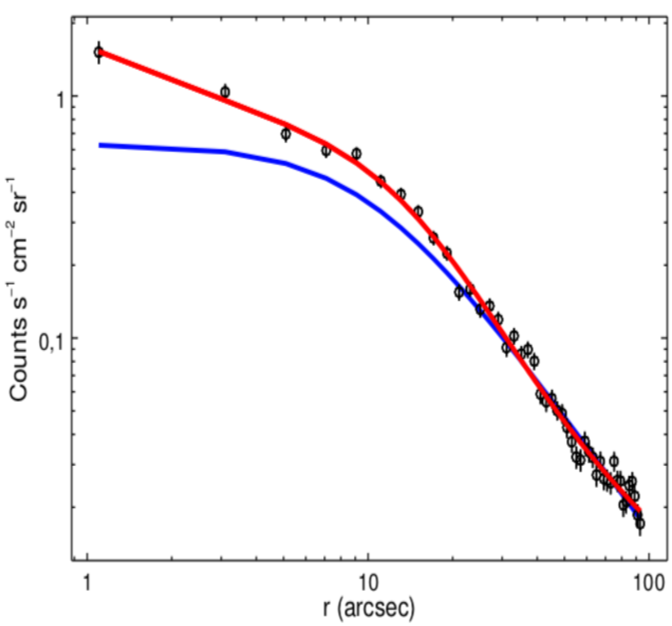

Figure 2.5: 0.5-2 keV radial surface brightness profile of A1668. The blue line represents the single β-Model fit performed in the external 30"-100" interval and extrapolated to the center, while the red line is the double β-Model fit performed on every radius.

r_{min}-r_{max} [arcsec]	r_{min}-r_{max} [kpc]	Counts	kT $\pm\sigma_{kT}$ [keV]	χ^2/DoF
0 - 12	0 - 14	1346 (99.6 %)	$1.74 \pm^{0.15}_{0.08}$	45/42
12 - 21	14 - 25	1274 (99.1 %)	$2.09 \pm^{0.33}_{0.16}$	62/47
21 - 33	25 - 35	1328 (97.8 %)	$2.84 \pm^{0.39}_{0.36}$	68/52
33 - 45	35 - 53	1111 (96.9 %)	$3.65 \pm^{0.66}_{0.51}$	60/50
45 - 60	53 - 70	1101 (93.8 %)	$4.05 \pm^{0.90}_{0.66}$	78/58
60 - 75	70 - 88	947 (91.2 %)	$3.39 \pm^{0.81}_{0.54}$	123/61
75 - 90	88 - 106	1006 (89.2 %)	$3.51 \pm^{0.75}_{0.55}$	98/64

Table 2.4: Fit results for the projected analysis. The first and second columns show the lower and upper limits of the extraction rings in arcsec and kpc, while the third column represents the number of source photons coming from each ring, with the percentage indicating their number compared to the total photons of the same region. In the last two columns we report the values of kT, with associated errors, and the χ^2/ DoF.

The central brightness excess with respect to the β-Model is a strong indication of the presence of a cool core in A1668, as we expected from the selection criteria described in Sec. 6.1. This will also be confirmed by the spectral analysis (see Sec 2.3). We therefore fitted the same profile on the entire radial range with a double β-Model (Mohr et al., 1999; LaRoque et al., 2006), represented with the red line in Fig. 2.5 (χ^2/DoF $\sim$ 1.49), which provides a better description of the real trend; we found $\mathtt{r0}_1$=15.6 $\pm^{4.2}_{2.7}$ arcsec ($\sim$ 18.3 kpc), $\mathtt{beta}_1$=0.67 $\pm^{0.14}_{0.08}$ and $\mathtt{ampl}_1$= 0.59 $\pm^{0.11}_{0.14}$ counts s^{-1} cm^{-2} sr^{-1} for the first and $\mathtt{r0}_2$=0.64 $\pm^{0.32}_{0.76}$ arcsec, $\mathtt{beta}_2$=0.42 $\pm^{0.02}_{0.01}$ and $\mathtt{ampl}_2$=1.78 $\pm^{0.75}_{3.07}$ counts s^{-1} cm^{-2} sr^{-1} for the second β-Model.

Spectral Analysis

Spectra were extracted with the CIAO task `specextract` in the 0.5-7 keV band; the extraction was made from a series of concentric rings centered on the X-ray peak. Each region contains at least $\sim$ 1000 net counts. Background spectra were also extracted from the `Blanksky` files of each region. We individually fitted every spectrum via `Xspec` (Arnaud, 1996, vv.12.9.1) using a `phabs*apec` model, approximating an absorbed, collisionally-ionized diffuse gas. The redshift was fixed at z=0.06355 and the hydrogen column density was fixed at $N_H = 2.20 \cdot 10^{20}$ cm^{-2} (estimated from Kalberla et al. 2005). The normalization parameter and the temperature kT were left free to vary. The observation was too shallow to allow us to fit metallicity, which was instead kept fixed at a value of 0.3 $Z_\odot$[5,6]. Note that these fits do not take in to account projection effects. The best-fitting parameters are listed in Table 2.4. The projected temperature profile of A1668 is shown in blue in Fig 2.6.

Projection effects were then taken into account extracting spectra from concentric rings centered on the X-ray peak, containing more than 1500 counts, and fitting them with a `projct*phabs*apec` model. Temperature and normalization were left free to vary, while column density, redshift and abundance were frozen at the same values of the projected analysis above. Results are listed in Table 2.5. The deprojected temperature profile of the

[5] This value was assumed after we tried to leave the metallicity free to vary. However, errorbars were too large to keep it thawed.

[6] The exploited abundance table is from Anders and Grevesse (1989)

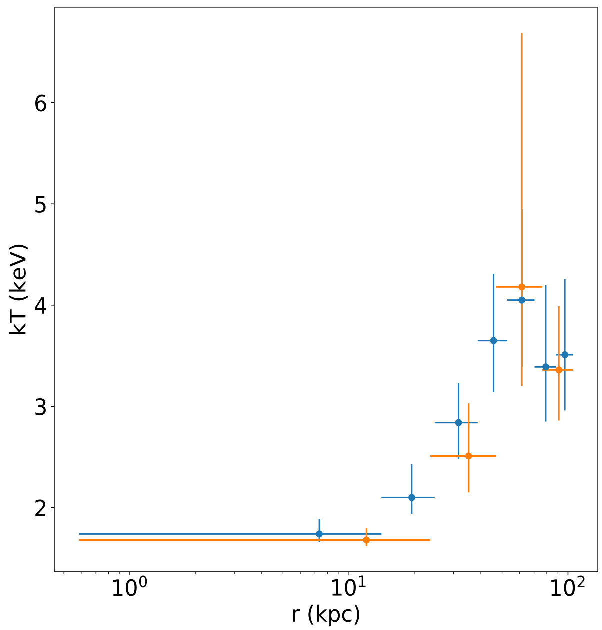

Figure 2.6: Projected (blue) and deprojected (yellow) temperature profile of A1668. Bars in the x-axis represent the range of the extraction rings, while in the y-axis are the errors for the temperature values.

cluster is shown in black in Fig. 2.6.

Following the same method described in Pasini et al. (2019)[7], we estimated the electronic density as :

$$n_e = \sqrt{10^{14}\left(\frac{4\pi \cdot N(r) \cdot [D_A \cdot (1+z)]^2}{0.82 \cdot V}\right)} \tag{2.1}$$

where N(r) is the `apec` normalization of the deprojected model, V is the shell volume and D_A is the angular distance of the source, estimated as $D_A = D_L/(1+z)^2$. Table 2.5 lists

[7]Note the typo in Eq. 4 of that paper

$r_{\min}$-$r_{\max}$ [arcsec]	$r_{\min}$-$r_{\max}$ [kpc]	Counts	kT [keV]	N(r) (10^{-4})	Electronic Density [10^{-2} cm^{-3}]	Pressure [10^{-11} dy cm^{-2}]	Entropy [keV cm^2]	t_{cool} [Gyr]
0 - 20	0 - 23.5	2506 (99.4 %)	$1.68 \pm^{0.12}_{0.06}$	$10.3 \pm^{0.6}_{0.6}$	$2.67 \pm^{0.01}_{0.01}$	$13.4 \pm^{1.1}_{0.4}$	$19.5 \pm^{0.5}_{0.2}$	$1.4 \pm^{0.1}_{0.1}$
20 - 40	23.5 - 46.9	2162(97.4 %)	$2.51 \pm^{0.52}_{0.36}$	$12.5 \pm^{0.8}_{0.8}$	$1.07 \pm^{0.01}_{0.01}$	$7.7 \pm^{1.4}_{1.0}$	$51.8 \pm^{2.0}_{1.4}$	$4.3 \pm^{0.6}_{0.6}$
40 - 65	46.9 - 76.2	1862 (93.7 %)	$4.18 \pm^{2.51}_{0.98}$	$8.1 \pm^{0.8}_{0.8}$	$0.44 \pm^{0.01}_{0.01}$	$7.5 \pm^{5.1}_{2.4}$	$219.9 \pm^{24.5}_{11.3}$	$15.8 \pm^{5.2}_{5.1}$
65 - 90	76.2 - 105.5	1653 (89.1 %)	$3.36 \pm^{0.63}_{0.50}$	$16.9 \pm^{0.9}_{0.9}$	$0.44 \pm^{0.01}_{0.01}$	$4.2 \pm^{0.7}_{0.6}$	$120.7 \pm^{3.5}_{3.0}$	$11.7 \pm^{1.7}_{1.8}$

Table 2.5: Fit results for the deprojected analysis. The first two columns report the limits of the annular regions and the number of source photons from each ring, with the percentage indicating their number compared to the total photons of the same region. The remaining columns report temperature, normalization factor, electronic density, pressure, entropy and cooling time. The fit gives χ^2/DoF = 1.46.

the density values for each ring, with the results showed in Fig. 2.7.

Making use of the deprojected temperature and density values, we can derive the cooling time, the pressure and the entropy for each bin. Table 2.5 presents the pressure values, calculated as $p = 1.83 n_e kT$, while the entropy, that was estimated as $S = kTn_e^{-2/3}$, is presented in Fig. 2.8.

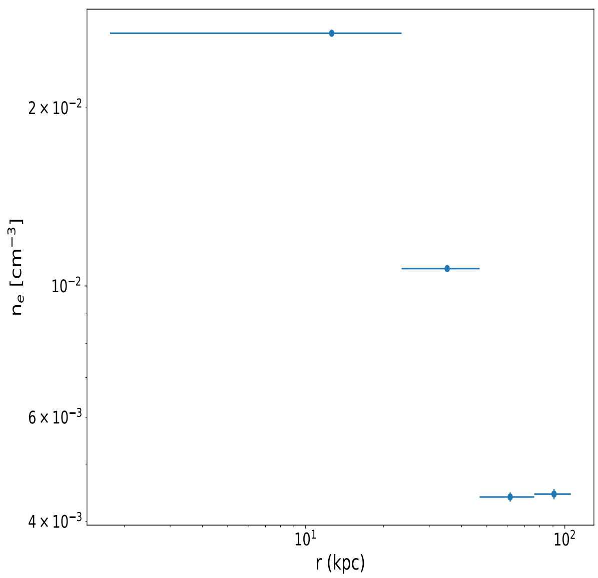

Figure 2.7: Density radial profile of A1668 derived from the deprojected analysis. Each bin defines an extraction region.

The cooling time is defined as:

$$t_{\text{cool}} = \frac{H}{\Lambda(T) n_e n_p} = \frac{\gamma}{\gamma - 1} \frac{kT(r)}{\mu X n_e(r) \Lambda(T)} \tag{2.2}$$

where γ=5/3 is the adiabatic index, H is the enthalpy, $\mu \simeq 0.61$ is the molecular weight for a fully ionized plasma, X $\simeq 0.71$ is the hydrogen mass fraction and $\Lambda(T)$ is the cooling function (Sutherland and Dopita, 1993). Results are listed in Table 2.5, while the cooling time radial profile is shown in Fig. 2.9.

We thus estimated the cooling radius of the cluster, i.e. the radius within which the ICM cooling is efficient, assuming $t_{\text{age}} \sim 7.7$ Gyr, corresponding to the look-back time at z=1, as an upper limit for the cluster age. Consequently, the intersection between the profile best fit (blue line) and t_{age} (red line) defines the cooling radius of A1668, being $r_{\text{cool}} \approx 34" \approx 40$ kpc.

The bolometric X-ray luminosity emitted within this radius was estimated by extracting a spectrum from an annular region centered on the X-ray peak with r = r_{cool}. Projection effects were taken into account by using a second annular region with internal radius coincident with

r_{cool} and external radius ~ 100". By fitting both spectra with a `projct*phabs*apec` model, the bolometric luminosity inside the cooling region results $L_{\text{cool}} = 1.9 \pm 0.1 \cdot 10^{43}$ erg s^{-1}. Assuming a steady state cooling flow model, the *Mass Deposition Rate* of the cooling flow of A1668 can be estimated as:

$$\dot{\mathrm{M}} \simeq \frac{2}{5}\frac{\mu m_p}{kT} \cdot L_{\text{cool}} \tag{2.3}$$

In this way, we obtain $\dot{\mathrm{M}} \simeq 29.6 \pm 1.6$ M$_\odot$ yr^{-1}.

As a different approach, we performed a further fit of the spectrum of the cooling region with a `phabs*(apec + mkcflow)` model, where the `apec` component approximates the ICM emission along the line of sight outside of the cooling region, while `mkcflow` is a multiphase component reproducing a cooling flow-like emission inside the cooling radius. As above, the abundance was fixed at 0.3 Z$_\odot$, while the temperature of the `apec` model was left free to vary and bounded to the `high temperature` parameter of `mkcflow`. Redshift and absorbing column density were fixed at the Galactic values (see above), while the `low temperature` parameter of `mkcflow` was fixed at the lowest possible value, ~ 0.1 keV. The fit gives χ^2/DoF = 105/100 and provides an upper limit of $\dot{\mathrm{M}} < 5$ M$_\odot$ yr^{-1}. The bolometric luminosity associated to the `mkcflow` model is $\mathrm{L}_{\text{mkcflow}} = 3.2 \pm 0.1 \cdot 10^{41}$ erg s^{-1}. The difference between the two estimates of the mass deposition rate reflects the *Cooling Flow (CF) problem*: observed mass deposition rates do not match expectations from the standard CF model, and heating contribution, likely produced by the central AGN, is required to balance the ICM radiative losses.

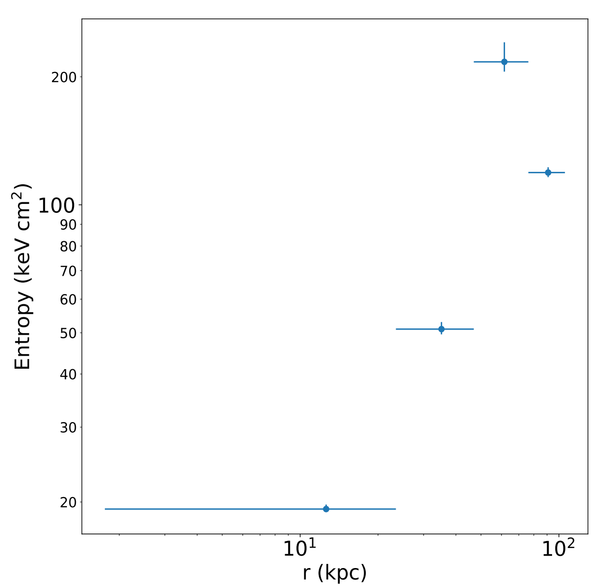

Figure 2.8: Entropy radial profile of A1668 derived from the deprojected analysis. Each bin defines an extraction region.

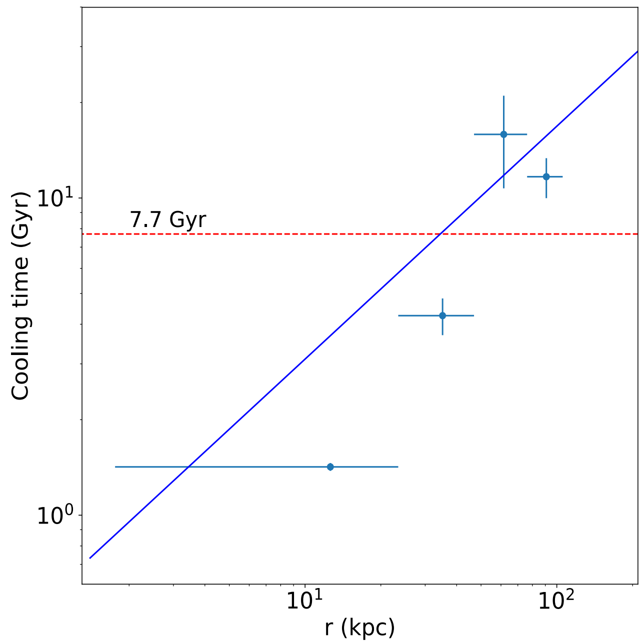

Figure 2.9: Cooling time profile of A1668. Each bin defines an extraction region. The blue line represents the best-fit function $f(x)=(0.57\pm0.99)x^{0.73\pm0.43}$, while the red line is t_{age} = 7.7 Gyr.

2.4 Discussion

Radio-X-ray combined analysis

In order to investigate the interactions between the cooling ICM and the BCG, we overlaid the 1.4 GHz radio contours on the X-ray 0.5-2 keV cluster image. Since we are interested in the core region, in Fig. 2.10 we show the resulting image, zoomed in the central 30×30 kpc.

The cluster X-ray cool core exhibits an elliptical nuclear region. Exploiting optical catalogues, we found that the radio galaxy is coincident with the BCG nuclear region, as expected. The emission centroid of the large-scale X-ray emission (RA=$13^h03^m43.6^s$, DEC=$+19°16^m17.4^s$), defined as the center of the isophotes, lies within this region, too. On the other hand, the X-ray peak (RA=$13^h03^m46.6^s$, DEC=$+19°16^m12.2^s$), is found to the south of the nucleus of the BCG, exhibiting a significant offset of $\sim$ 5.2”, corresponding to $\sim$ 6 kpc.

In order to check for the possible presence of a field point-source that could bias the detection of the X-ray peak, we extracted a spectrum from a $\sim$ 4” circular region centered on the peak, and fitted it with two models: `phabs*apec` and `phabs*(apec+powerlaw)`. The first fit gave χ^2/DoF $\sim$ 78/79, while for the second χ^2/DoF $\sim$ 71/77; the F-stat method was then applied in order to check if the addition of the `powerlaw` component provided a significant improvement of the fit. We obtained an F-value of 3.4 and p=0.035,

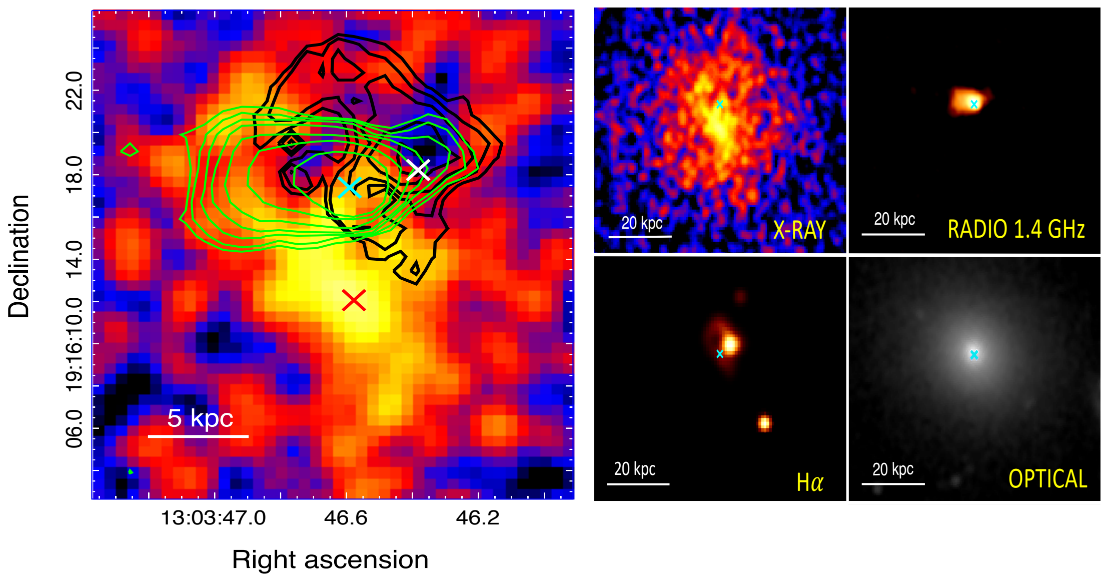

Figure 2.10: *Left Panel*: 1.4 GHz radio (green) and Hα (black) contours overlaid on the 0.5-2 keV X-ray image, zoomed towards the cluster centre. The cyan cross represents the X-ray emission centroid, coincident with the BCG centre; the red and white crosses are the X-ray and Hα peaks, respectively. *Right Panel*: From left to right, from top to bottom: 0.5-2 keV, 1.4 GHz, Hα and optical (SDSS) images of A1668. All images are centered on the X-ray peak. The cyan cross represents the BCG.

correspondent to a null hypothesis probability of 1-p=0.965. This suggests that the addition of the point-source emission component is not statistically significant. As a further check, we looked for possible point-sources in high energy, optical and infrared catalogues, as well as in a harder band (4-7 keV) X-ray image; however, we did not detect any point source coincident with the X-ray peak. We thus conclude that the peak detection is likely not biased, and therefore the offset is real.

This is analogous with what was found in A2495, that presents a similar-scale offset between these two components, and with a number of recent works that found the same feature in other clusters (e.g., Sanderson et al., 2009; Haarsma et al., 2010; Hudson et al., 2010; Rossetti et al., 2016, and others; for a brief review of the state-of-the-art literature about BCG/cool core offsets, see Pasini et al., 2019). We will return on this in Sec. 2.4.

A two-dimensional temperature map is often used in order to further investigate on the cluster structure and its thermodynamical state, but the small number of photons prevents us from producing such map. We also estimated the *softness ratio* as (S-H)/(S+H), where S and H are the number of counts in the soft (0.5-2 keV) and hard (2-7 keV) band, respectively. However, the statistics are still too poor and errors are too large to draw any conclusion from such analysis.

Hα analysis

The presence of optical line emitting nebulae in galaxy clusters is linked to the thermodynamical conditions of the cluster core; observational studies (e.g., Cavagnolo et al., 2008;

McNamara et al., 2016) have argued that such warm structures are only found if the central ($\sim$ 10 kpc) entropy falls below 30 keV cm^2 or, alternatively, when $t_{cool}/t_{ff} < 10$-20 (Voit et al., 2015), where $t_{ff} = \sqrt{2R^3/GM}$ is the *freefall* time. The estimated entropy within the central bin of our spectral analysis ($r < 23.5$ kpc, Table 2.5) is $\sim$ 19.5 keV cm^2, thus satisfying the criterion for the presence of such nebulae in A1668. Hamer et al. (2016) presented *VIMOS* observations of the Hα line emission of a sample of 73 BCGs, including A1668, whose image is shown in Fig. 2.11.

The Hα structure presents a rather compact shape, extending for $\sim$ 9" ($\sim$ 10.6 kpc). Its total luminosity is $L_{H\alpha} = 3.85 \pm 0.30 \cdot 10^{40}$ erg s^{-1}[8], and Hamer et al. (2016) classified it as a quiescent object, showing a simple, centrally-concentrated morphology[9]. To better visualize the interplay of the three components, in Fig. 2.10 we also overlay the Hα contours on the X-ray 0.5-2 keV image.

The line emission lies entirely within the BCG, but although it is also within the cool core as defined from the cooling time profile, it only overlaps one end of the bright X-ray ridge. This highlights a difference with A2495, in which the Hα structure connects the galaxy with the X-ray peak, and with other systems (e.g., Bayer-Kim et al., 2002; Hamer et al., 2012, 2016), in which the line emission seems to be mostly associated to the cooling ICM, rather than to the BCG.

A significant offset of $\sim$ 6.5" ($\sim$ 7.6 kpc) is present between the Hα (*RA*=13^{h}03^{m}46.4^s, *DEC*=+19°16^{m}18.1^s) and the X-ray peaks. The same feature, albeit smaller, was found in A2495 by Pasini et al. (2019); offsets between these two peaks were also detected in A1795 (Crawford et al., 2005) and in a number of systems by Hamer et al. (2016). We will return on this in Sec. 2.4.

As described in more details in Hamer et al. (2012), the ratio of the Hα plume extent and the total velocity gradient of the warm gas provides an estimate of the projected offset timescale. Pasini et al. (2019) showed that, for A2495, such timescale is comparable to the age difference between two putative cavity pairs, suggesting that, for systems where the BCG oscillates back and forth through the cooling region, this measure could be a good indicator for the AGN cycle intermittency. In A1668, the Hα structure extends for D'$\sim$ 7.7" from the BCG centre, corresponding to $\sim$ 9 kpc, and shows a very smooth velocity gradient from East to West. We measured a velocity difference of $\sim$ +500 km s^{-1} between the gas at the BCG centre and that at the tail of the Hα structure. This indicates a projected timescale of T'= D'/V $\sim$ 18 Myr. In order to correct for the projection effects we assumed a most likely inclination of $\sim$ 60 °, with a range of 30-75 ° (Hamer et al., 2012); the corrected timescale can thus be estimated with T = T' $\times$ cos(i)/sen(i), with i being the inclination. We obtained in this way an offset timescale of $\sim$ 10.4 Myr, with an upper and lower limit of $\sim$ 31.2 and $\sim$ 4.8 Myr, respectively; this is consistent with the value of $\sim$ 13 Myr estimated for A2495, suggesting that the cold gas dynamics in the two systems are similar, and that the timescale of AGN feedback intermittency is comparable.

[8] This estimate differs from Pulido et al. (2018) since it is not extinction-corrected and is obtained from IFU observations.

[9] The morphology looks slightly different when compared to Edwards et al. (2009), whose IFU image shows a somehow better 'resolved' shape.

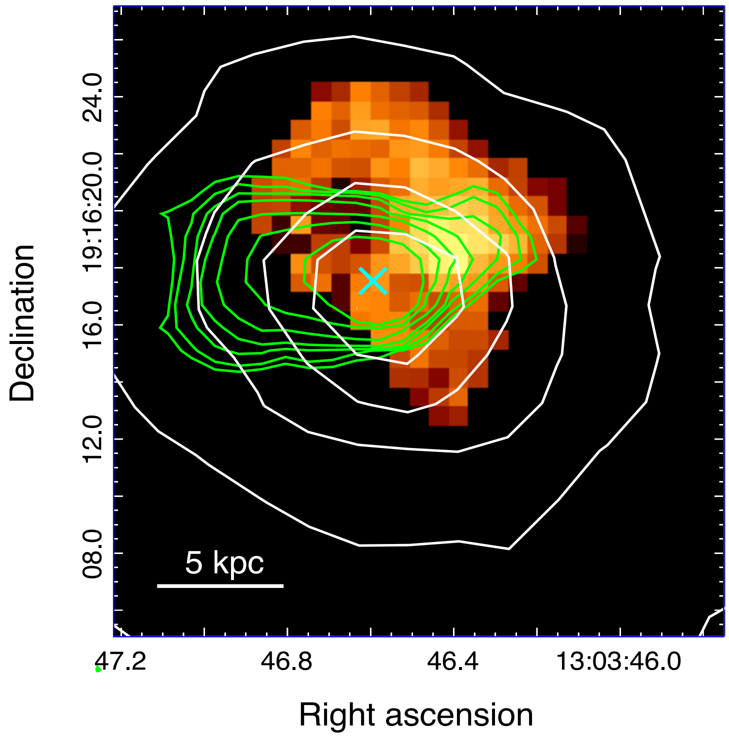

Figure 2.11: 1.4 GHz radio (green) contours overlaid on the *VIMOS* Hα image (Hamer et al., 2016). The mean seeing is 1.21", and the map units are in 10^{-16} erg s^{-1} cm^{-2} Å. The white contours are the optical isophotes from SDSS. The cyan cross represents the radio galaxy centre, coincident with the BCG core.

One can also estimate the mass of the warm gas by assuming that it is optically thin:

$$M_{\mathrm{H}\alpha} \simeq L_{\mathrm{H}\alpha} \frac{4\mu m_p}{n_{\mathrm{H}\alpha}\varepsilon_{\mathrm{H}\alpha}} \tag{2.4}$$

where $\varepsilon_{\mathrm{H}\alpha} \sim 3.3 \cdot 10^{-25}$ erg cm^3 s^{-1} is the Hα line emissivity, while $n_{\mathrm{H}\alpha}$ is obtained assuming pressure equilibrium with the local ICM:

$$n_{\mathrm{H}\alpha} T_{\mathrm{H}\alpha} \simeq n_{\mathrm{ICM}} T_{\mathrm{ICM}} \tag{2.5}$$

where $T_{\mathrm{H}\alpha} \sim 10^4$ K, T_{ICM} is the first value reported in Tab. 2.4 ($\sim$ 1.74 keV, since the Hα structure is located within the first spectral bin), while $n_{\mathrm{ICM}} \sim 1.83 n_e$, where n_e is the electronic density reported in the first row of Tab. 2.5. In this way, we obtain $M_{\mathrm{H}\alpha} \sim (2.4 \pm 0.2) \cdot 10^6$ M$_\odot$.

The [SII]$_\lambda$6716/[SII]$_\lambda$6731 line ratio provides an independent estimate of the density of the ionised gas and is measured in Hamer et al. 2016 (Appendix F) as 1.21±0.2. Assuming case B reionisation and a temperature of 10^4 K, this gives an electron density of $n_{e,\mathrm{H}\alpha}$ =350 ± 270 cm^{-3} which corresponds to a total density of $n_{\mathrm{H}\alpha}$=640 ± 495 cm^{-3}. These values are comparable, within the (large) uncertainties, with the value of $n_{\mathrm{H}\alpha}$=100 $\pm\frac{8}{3}$ cm^{-3} derived from Eq. 2.5. It is important to consider the impact of the assumed ionised gas temperature ($T_{\mathrm{H}\alpha}$) on the two measurements though. A lower $T_{\mathrm{H}\alpha}$ would result in a higher $n_{e,\mathrm{H}\alpha}$

from Eq. 2.5 but a lower $n_{e,\mathrm{H}\alpha}$ from the $[\mathrm{SII}]_\lambda 6716/[\mathrm{SII}]_\lambda 6731$ line ratio measurement, while a higher $T_{\mathrm{H}\alpha}$ would have the opposite effect on both measurements. The VIMOS data from (Hamer et al., 2016) are not sensitive enough to provide a reliable estimate of $T_{\mathrm{H}\alpha}$ for Abell 1668, but deep observations of other objects have found upper limits to $T_{\mathrm{H}\alpha}$ that are much lower than expected (e.g. $T_{\mathrm{H}\alpha} < 5685\,\mathrm{K}$ in the Centaurus cluster, Hamer et al. 2019). Assuming $T_{\mathrm{H}\alpha} = 5000\,\mathrm{K}$, we find $n_e = 230 \pm 180\,\mathrm{cm}^{-3}$ and $n_{\mathrm{H}\alpha}$=$420 \pm 330\,\mathrm{cm}^{-3}$ from the [SII] ratio and $n_{\mathrm{H}\alpha}$=$200 \pm^{16}_{6}\,\mathrm{cm}^{-3}$ derived from Eq. 2.5, indicating that the two measurements are consistent within the limits of the available data and assumed values.

Putative cavities and AGN feedback cycle

From the 0.5-2 keV X-ray image (see Fig. 2.12) it is possible to identify a number of ICM surface brightness depressions. The present observation is very shallow ($\sim$ 10 ks), thus the reader shall be warned about the significance of these deficits, that could possibly be artifacts. However, we focused our attention on three of these features (showed in Fig. 2.12) that, due to their position, could possibly represent real ICM cavities. One of them (A) lies within the radio galaxy West lobe; another surface brightness depression (B) is detected in the radio galaxy East lobe, while a symmetrical (with respect to the X-ray peak), similar-shaped brightness depression (C), is found at the opposite side of the cluster core, not associated with the radio galaxy. It is noteworthy to mention that cavity A is also coincident with the Hα line emission peak.

To investigate on these features, we estimated their significance as $\mathrm{N_M}$-$\mathrm{N_C}/\sqrt{\mathrm{N_M}+\mathrm{N_C}}$, where $\mathrm{N_M}$ and $\mathrm{N_C}$ are the number of counts in regions of equal area close to the candidate cavity and within the cavity, respectively. The number of counts is different depending on the size of the elliptical region chosen to cover the putative cavity and, as previously stated, the current observation requires us to be cautious, since the shape and extent of the depression observed 'by eye' can slightly change using different color scales. For this reason, the upper and lower limits for the dimensions of these regions were estimated by varying the axes of the ellipse until reaching a significance of 2σ and 3σ, respectively. The assumed 'true' size of the bubble is the mean between these two limits. Cavity A exhibits a circular shape, with a diameter of 4.8 $\pm$ 0.6 kpc, while cavity B is more elliptical, with a major axis of 5.2 $\pm$ 0.4 kpc and a minor axis of 3.0 $\pm$ 0.3 kpc. On the other hand, the brightness deficit related to candidate cavity C is less enhanced and, in order to reach the desired significances, requires the size to be larger than the observed depression. Therefore, in the following analysis we will only discuss candidate cavities A and B, while cavity C will not be considered. Following the method described in Bîrzan et al. (2004), we determined the cavity power:

$$P_{\mathrm{cav}} = \frac{E_{\mathrm{cav}}}{t_{\mathrm{cav}}} = \frac{4pV}{t_{\mathrm{cav}}} \tag{2.6}$$

where t_{cav} is the age of the cavity, calculated as $t_{\mathrm{cav}} = R/c_s$, with R being the cavity distance from the BCG center, p is the pressure at the distance of the cavity, V is the cavity volume and c_s is the sound velocity. The volume was estimated assuming an oblate

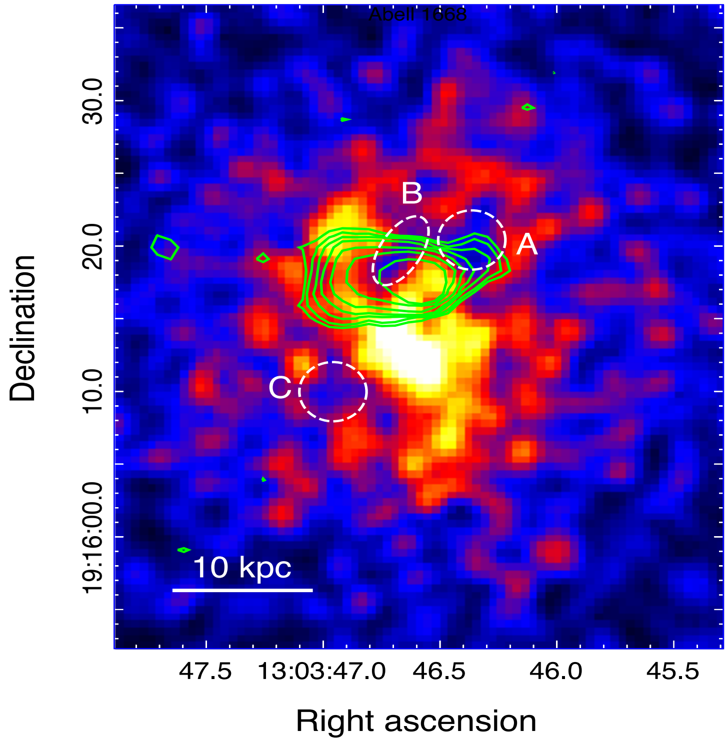

Figure 2.12: 0.5 - 7 keV image showing three surface brightness depressions: A and B lie in the west and east lobes of the radio galaxy, respectively, while C is found at the opposite side of the core. Overlaid are the 1.4 GHz contours.

elipsoidal shape for both cavities, while for pressure and temperature we assumed the values listed in Table 2.5 corresponding to the annular bin the cavities lie in.

We obtained the same age for both cavities: t_{cav} = 5.2 $\pm$0.7 Myr. This leads to $P_{cav,\,A}$ = 5.1 $\pm$2.6 $\cdot$ 10^{42} erg s^{-1} for cavity A, and $P_{cav,\,B}$ = 3.8 $\pm$1.4 $\cdot$ 10^{42} erg s^{-1} for cavity B. The age is consistent with the offset timescale estimated in Sec. 2.4. Finally, we compared the estimated values of P_{cav} (in the hypothesis that the cavities are real) and L_{cool} with the typical distribution observed for cool core clusters (Bîrzan et al., 2017). The result is presented in Fig. 2.13.

The L_{cool}-P_{cav} relationship in A1668 is consistent within the scatter of the expected distribution, despite being on its lower edge. The detected offsets, therefore, do not seem to affect the feeding-feedback cycle, that is still maintained. The same result was found in A2495, where the two cavity systems (i.e., the AGN) have enough energy to balance the radiative losses within the cooling region. We then argue that small offsets are not able to break the AGN feeding-feedback cycle.

Offsets, cooling and Hα emission: are sloshing and AGN activity shaping the core of A1668?

As described in the previous sections, the core of A1668 contains a complex set of structures whose origin is not immediately clear. It is worth reiterating that the available *Chandra* data

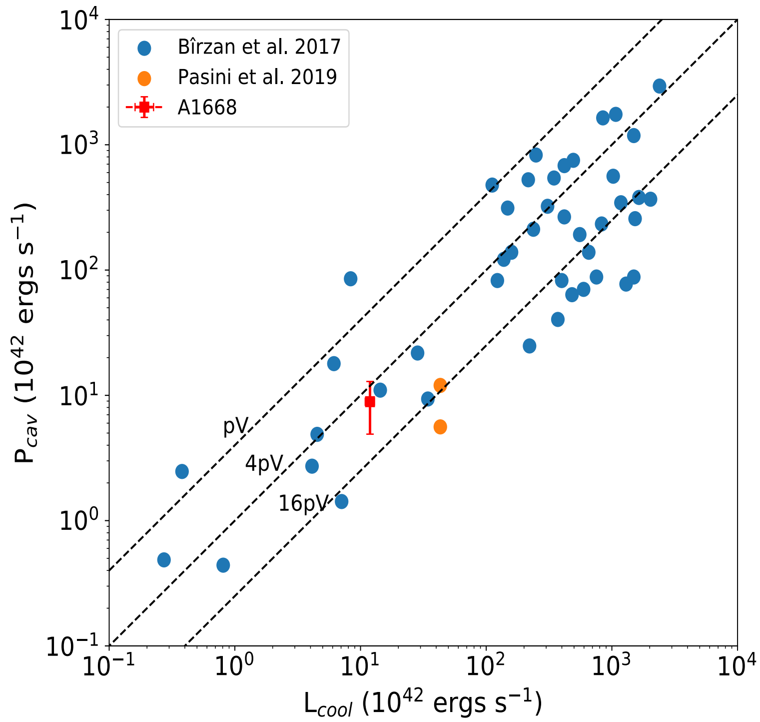

Figure 2.13: Blue points are the data from Bîrzan et al. (2017), the orange ones are the values for A2495 (Pasini et al., 2019), while red represents the cavity system detected in A1668. Dashed lines represent, from left to right, $P_{cav} = L_{cool}$ assuming pV, $4pV$ or $16pV$ as the deposited energy.

is only a snapshot, providing somewhat limited information on the ICM. It should also be remembered that all of the structures we observe are contained within the central ~ 20 kpc, inside the stellar body of the BCG.

The offsets between the peaks of the radio, X-ray and Hα emission raise the question of how these components came to be separated. The peak of emission from the hot ICM lies not in the BCG nucleus, but $\sim$6 kpc to the south. The radio emission is reasonably evenly distributed Eastwards and Westwards with respect to the nucleus, but the Hα peaks in the region of the west radio jet/lobe, extending around the western half of the radio structure and overlapping the optical centroid of the BCG.

We suggest a qualitative scenario which might explain the relative morphologies of the different components. At some point in the past, A1668 may have been a relaxed cluster with a cool core. In that core, centred on the BCG, gas had begun to cool and condense out of the ICM, forming the kind of filamentary Hα nebula observed in other cool core cluster. The small velocity gradient in the Hα emission is consistent with such an origin. At that stage, A1668 underwent a minor merger, which caused the core to begin sloshing, oscillating around the centre of the cluster gravitational potential. Sloshing motions in the plane of the sky are typically visible as a spiral pattern in the ICM, but if the plane of motion is aligned along the line of sight, the motions produce pairs of nested cold fronts, and the cool ICM gas drawn out from the core can appear as a tail to one side of the BCG. Our *Chandra* observation is too short for fronts to be visible, but we do see the tail: the ridge structure.

At this stage, cooling (and Hα emission) would still have been centred in the core of the BCG. About 5 Myr ago ($\sim$ cavity age), sufficient cooled material reached the central SMBH to trigger an outburst. This produced the radio jets/lobes we observe, and as these expanded they pushed aside the pre-existing Hα filaments and hotter ICM gas. This produced a correlated Hα/radio morphology, with much of the Hα wrapped around the west jet/lobe. It also disrupted the centre of the cool core, reducing the X-ray surface brightness as a large part of the volume in the core of the BCG was filled by the radio lobes, producing the apparent cavities in the ICM. This brings us to the current situation, where the brightest X-ray emission is in the tail to the south of the BCG nucleus.

The expansion timescale of the radio lobes is only a few 10^6 yr. This is very short compared to typical sloshing timescales. The hot ICM oscillates with sloshing timescale given by $t_{\rm slosh} = 2\pi/\omega_{\rm BV}$ where $\omega_{\rm BV} = \Omega_K \left(\frac{1}{\gamma}\frac{d\ln S}{d\ln r}\right)^{1/2}$. Here $d$ls$S$/$d$ln$r$ is the logarithmic entropy gradient, Ω_K=$\sqrt{GM/r^3}$ and γ=5/3 for the ionized ICM plasma. We also know that the free-fall time in the cluster is $t_{\rm ff} = \sqrt{2r/g}$. Our *Chandra* data are not sufficient to accurately model the mass profile, but we know that the stellar velocity dispersion, σ_*, in the inner regions of the BCG will follow the gravitational potential, so that $t_{\rm ff} \simeq r/\sigma_*$ (Voit et al., 2015). We can therefore approximate $\omega_{\rm BV}$ as $\frac{1}{t_{ff}}\sqrt{\frac{6}{5}\frac{d\ln S}{d\ln r}}$.

Our data do not allow the calculation of the entropy profile on scales $r \lesssim 25$ kpc (Fig. 2.8), thus we use the average slope $d\ln S/d\ln r = 0.67$ given by Hogan et al. (2017b) (see also Panagoulia et al. 2014). This returns $t_{\rm slosh} \sim 7t_{\rm ff}$. We do not know the scale of the sloshing, but it must be greater than the length of the X-ray tail ($\sim$16 kpc). Based on the measured σ_*=226$\pm$7 km s^{-1} (Pulido et al., 2018), at 16 kpc $t_{\rm ff}$=70 Myr, and thus $t_{\rm slosh}$ may be as much as $\sim$ 490 Myr. As expected this is considerably longer than the AGN expansion timescale, confirming that if sloshing is occurring, it cannot yet have affected the structure of the radio lobes.

As argued by Olivares et al. (2019), the fact that filamentary nebulae in cool core clusters generally lack a significant velocity gradient indicates that the cool Hα or CO-emitting gas they contain is at least partially tied to the surrounding ICM. It is unclear how the different phases are connected, but it has been suggested that the denser material may be enveloped by many diffuse layers of warmer gas (Li et al., 2018), or threaded through by magnetic fields (McCourt et al., 2015), either of which could increase drag forces. We would thus expect the Hα emission to trace the regions in which gas has most recently cooled from the ICM, after modification by the expanding radio lobes. If the inflation of cavities has disrupted the cooling region, we might expect the locus of any future cooling to be at the new X-ray peak of surface brightness, source of the BCG nucleus. However, the lack of Hα emission at that location suggests that cooling there is slower than it was near the BCG core, and that no reservoir of cooled material has yet built up at that location.

This scenario is of course speculative, given the constraints available from the data. Several aspects are uncertain. All, part or none of the Hα emitting gas might have formed as a result of the AGN outburst, with the expanding lobes triggering condensation (e.g., Qiu et al., 2020). If the cluster is sloshing, we cannot know the scale or alignment of the motion without deeper data. However, our scenario explains several basic facts: the radio and Hα emission are correlated because the radio has at least partly determined the morphology of the Hα-emitting gas. The X-ray offset is the result of sloshing, which has not affected the radio sources or Hα because the radio source expansion timescale is short compared to the sloshing timescale. The BCG is no longer the centre of ICM cooling because the AGN has pushed aside the dense gas which fuelled the outburst.

The scenario also makes testable predictions. If the cluster is sloshing, we should expect deeper *Chandra* data to reveal nested cold fronts, and the X-ray ridge should contain relatively cool, high abundance gas. Deeper imaging should also allow us to more accurately measure the morphology of any cavities, which should be correlated with the rado jets and lobes. Higher resolution radio data may be required to make this comparison. Lastly, we might expect higher resolution Hα imaging to reveal complex structure in the cooled material, consistent with a filamentary nebula disturbed by an AGN outburst.

Alternative explanations for the origin of the Hα emission and spatial offsets

An alternative hypothesis that could explain the observed displacement of the Hα emission is cooling *in situ*, perhaps stimulated by the same AGN outburst which originated the X-ray cavities. Inhomogeneous cooling scenarios in clusters have been the object of a long, lively debate (see early reviews by Fabian et al. 1991; Fabian 1994, and references therein). Nowadays, many lines of evidence suggest that hot gas cools at a (mean) low rate and in a spatially distributed fashion, when the ISM/ICM conditions are appropriate (see Hogan et al. 2017b; Pulido et al. 2018; Lakhchaura et al. 2018 for a quantitative discussion). The primary trigger of this localized cooling (that is, the origin of thermally unstable perturbations) might be turbulence (e.g. Chaotic Cold Accretion, CCA, see Gaspari et al., 2012, 2013; Voit et al., 2015), lifting of low entropy gas by X-ray cavities (Revaz et al., 2008; Brighenti et al., 2015) or the sloshing itself.

CCA implies the trigger of thermal instabilities, that is favoured by a central ($\leq$ 10 kpc) cooling time $t_{\rm cool} \sim 1$ Gyr (Hogan et al., 2017a; Pulido et al., 2018), or by $t_{\rm cool}/t_{ff} \leq 10-20$ (Voit et al., 2015). It is easier to ensue at the position of the X-ray peak, but it can be triggered wherever these conditions are respected. Therefore, the displacement observed for the Hα gas could be the result of CCA detached from the emission peak. CCA at the current position of the peak could still be happening, but it could have not built yet enough material to be detected in Hα. However, given the available X-ray observation, we are not in a position to accurately estimate the cooling time in the central region of the cluster.

We can explore in some more detail the scenario where the warm gas derives from a cool component of the ICM, originally located close to the nucleus of the BCG, uplifted by the cavities and then cooled to 10^4 K. Following Archimedes' principle, cavities can lift an amount of gas equal to their displacement, though simulations suggest that the maximum amount is only ~50% of this value (Pope et al., 2010). This corresponds to $M_{\rm uplift} = 9 \cdot$

10^6 $M_\odot$ for cavity A, and M_{uplift} = $3 \cdot 10^6$ $M_\odot$ for cavity B. The mass of the Hα plume is lower ($M_{H\alpha} \sim 2.4 \cdot 10^6$ $M_\odot$, see Sec. 2.4). However, given the state-of-the-art correlation between $L_{H\alpha}$ and molecular gas mass M_{mol} (see e.g., Edge, 2001; Salomé and Combes, 2003; Pulido et al., 2018), that is usually found to be co-spatial with Hα, we would expect to have $M_{mol} \sim 10^9$ $M_\odot$ (lower than the upper limit 1.5×10^9 $M_\odot$ quoted by Salomé and Combes 2003). The total amount of gas would therefore be too large for the cavities to uplift and this, along with the radio/Hα morphology, would imply the need for an earlier cycle of AGN jet activity if uplift is responsible.

The observed Hα line emission could also be the remnant of the ISM of a gas-rich galaxy which merged with the BCG. To test this hypothesis, we examined SDSS and DSS optical images and catalogs in order to check whether a member galaxy could be interacting with the BCG. However, the closest system lies more than 40 kpc away from the BCG, not showing any hint of interplay. Therefore, the merging hypothesis looks unlikely with the current data.

Finally, the warm gas could originate from the stellar mass loss in the BCG (Mathews, 1990; Li et al., 2019). With a total B-band luminosity $L_B \sim 1.3 \times 10^{11}$ $L_{B,\odot}$ (Makarov et al., 2014) and a stellar mass to ratio for an old population $(M/L_B) \sim 7$ (e.g., Maraston, 2005), the expected mass loss rate is $\dot{M}_* \sim 1.35$ $M_\odot$/yr (Mathews, 1989). Thus, the observed amount of emission line gas can be accumulated in less than 2 Myr. However, the displacement with respect to the BCG center and its filamentary and disturbed distribution (Edwards et al., 2009; Hamer et al., 2016) are not easily accounted for by this scenario.

2.5 Conclusions

We performed a multi-wavelength analysis of the cool core cluster A1668, by means of new radio (EVLA) and X-ray (*Chandra*) observations and of Hα line emission data from Hamer et al. (2016). The results can be summarized as follows:

- The radio analysis at 1.4 ($L_{1.4\,GHz} \sim 6 \cdot 10^{23}$ W Hz^{-1}) and 5 GHz ($L_{5\,GHz} \sim 2 \cdot 10^{23}$ W Hz^{-1}) shows a small ($\sim$ 11 -14 kpc) and elongated FRI radio galaxy, with no hints of larger scale emission at these frequencies. The mean spectral index is $\alpha = 0.99 \pm 0.06$, consistent with the usual values found in BCGs.
- The X-ray analysis confirms the classification of A1668 as a cool core cluster, with a cooling radius of $\sim$ 40 kpc inside which we estimate a bolometric luminosity $L_{cool} \sim 1.9 \cdot 10^{43}$ erg s^{-1}.
- The multi-wavelength analysis reveals two spatial offsets, with the first of $\sim$ 6 kpc being between the BCG nucleus and the X-ray peak, while the second of $\sim$ 7.6 kpc between the Hα and the X-ray peaks. This is similar to what was found in another similar cluster, A2495, with two offsets of 6 and 4 kpc, respectively (Pasini et al., 2019). The compact Hα emission structure extends for $\sim$ 11 kpc and is mostly co-spatial with the BCG, unlike A2495, where the line emission seems to be linked to the cluster cool core, rather than to the central galaxy.

- We identify three X-ray surface brightness depressions, one of them (A) coincident with the west radio lobe and with the Hα peak, another one (B) lying within the east radio lobe, while the third one (C) being more uncertain. For the system of cavities A and B we determine an age of $\sim$ 5.2 Myr. The L_{cool}-P_{cav} estimates for A1668 are in agreement with the relationship observed for other systems (e.g., Bîrzan et al., 2017), suggesting that the detected offsets are not able to break the AGN feeding-feedback cycle.
- Finally, we discuss possible explanations for the multiphase gas and for the displacements observed in the core of A1668. We propose that, initially, all the components were spatially coincident in the cluster cool core. Sloshing was likely triggered by a minor merger, causing some of the cool gas around the BCG to be drawn out into a tail that we now observe as an X-ray ridge structure. On the other hand, the densest, most rapidly cooling gas, still in and around the BCG core, condensed out to form the Hα nebula. About 5 million years ago, the condensed material fuelled the central SMBH, triggering the outburst that produced the observed radio jets/lobes. The expansion of the lobes finally pushed aside the Hα nebula and the hot ICM, disrupting the cool core centre. Alternative explanations for the misplacement of the Hα emission include cooling *in situ* through thermal instabilities, uplift from the cavities, reminiscence from a past merger with a gas-rich galaxy, or stellar mass loss from the BCG, although the last three look unlikely (see Sec. 2.4).

Acknowledgements. *We thank the referee for thoughtful comments and suggestions, which have significantly improved the presentation of our results. TP is supported by the BMBF Verbundforschung under grant number 50OR1906. E.O'S. ackonwledges support for this work from the National Aeronautics and Space Administration through Chandra Award Number G07-18162X issued by the Chandra X-ray Center, which is operated by the Smithsonian Astrophysical Observatory for and on behalf of the National Aeronautics Space Administration under contract NAS8-03060. Based on observations made with ESO Telescopes at the La Silla or Paranal Observatories under programme ID 080.A-0224 and 082.B-0671. The National Radio Astronomy Observatory is a facility of the National Science Foundation operated under cooperative agreement by Associated Universities, Inc.*

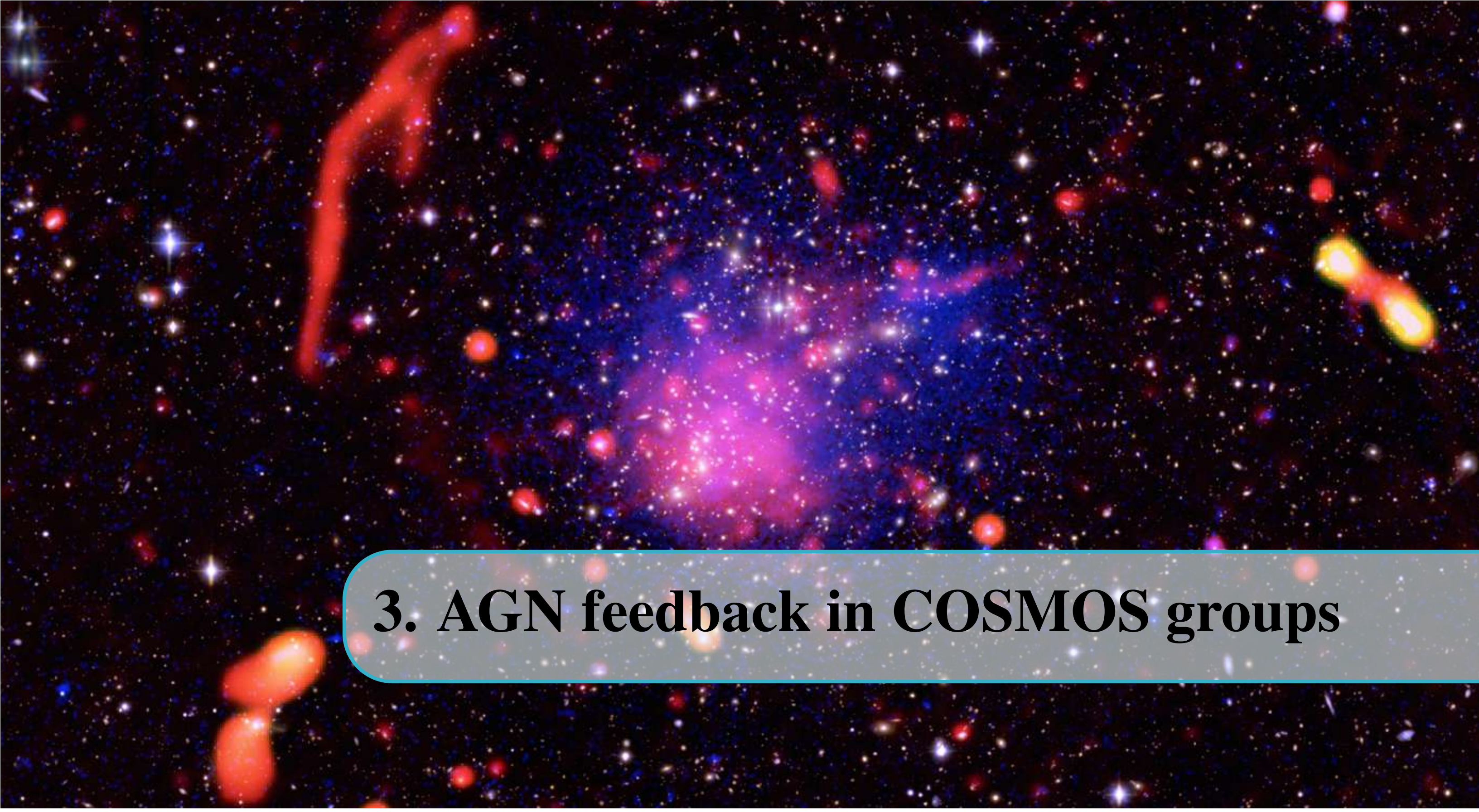

3. AGN feedback in COSMOS groups

The relation between the diffuse X-ray luminosity and the radio power of the central AGN in galaxy groups

T. Pasini, M. Brüggen., F. de Gasperin et al. MNRAS, 497, 2163 (2020)

Abstract. *Our understanding of how AGN feedback operates in galaxy clusters has improved in recent years owing to large efforts in multi-wavelength observations and hydrodynamical simulations. However, it is much less clear how feedback operates in galaxy groups, which have shallower gravitational potentials. In this work, using very deep VLA and new MeerKAT observations from the MIGHTEE survey, we compiled a sample of 247 X-ray selected galaxy groups detected in the COSMOS field. We have studied the relation between the X-ray emission of the intra-group medium and the 1.4 GHz radio emission of the central radio galaxy. For comparison, we have also built a control sample of 142 galaxy clusters using ROSAT and NVSS data. We find that clusters and groups follow the same correlation between X-ray and radio emission. Large radio galaxies hosted in the centres of groups and merging clusters increase the scatter of the distribution. Using statistical tests and Monte-Carlo simulations, we show that the correlation is not dominated by biases or selection effects. We also find that galaxy groups are more likely than clusters to host large radio galaxies, perhaps owing to the lower ambient gas density or a more efficient accretion mode. In these groups, radiative cooling of the ICM could be less suppressed by AGN heating. We conclude that the feedback processes that operate in galaxy clusters are also effective in groups.*

3.1 Introduction

Over the past years, deep observations performed by both *Chandra* and *XMM-Newton* have led the way for a better understanding of the X-ray emission produced by the Intra-Cluster Medium (ICM), its consequent cooling and how this links to structure formation. Particularly, multi-wavelength studies based on the combination of X-ray and radio observations have shown that the ICM and the Active Galactic Nucleus (AGN) usually hosted in the Brightest Cluster Galaxy (BCG) are part of a tight cycle in which the cooling of the hot ($\sim 10^7$ K) ICM is regulated by the mechanical feedback provided by the AGN itself (see e.g. reviews by McNamara and Nulsen 2012; Gitti et al. 2012). In this scenario, AGN jets and outflows produce shock waves and cold fronts (McNamara et al., 2000; Fabian et al., 2006) and inflate bubbles in the ICM, known as X-ray cavities, that can be used to assess the AGN mechanical power (Bîrzan et al., 2004; Rafferty et al., 2006), establishing a tight feedback cycle with the diffuse gas. The impact of the AGN could be even stronger in galaxy groups, where the gravitational potential is shallower. Here, even a relatively small energy injection could eject gas from the group itself (Giodini et al., 2010). It has been suggested that AGN feedback could thus set apart galaxy clusters from groups, especially in terms of their baryonic properties (Jetha et al., 2007), albeit there is still no universal agreement in the distinction between these objects.

Therefore galaxy groups, that are the repositories of the majority of baryons and host more than half of all galaxies (Eke et al., 2006), are key in order to reach a complete understanding of the AGN feedback cycle and of how it is able to influence the evolution of galaxies and their environments (e.g., Giacintucci et al., 2011). However, X-ray observations of galaxy groups are relatively difficult since most of them lie at the lower sensitivity limit of the current generation of instruments. This normally prevents us from reaching the combination of signal-to-noise ratio and resolution required to perform the same type of analysis that is usually applied to galaxy clusters (see e.g., Willis et al. 2005). Nonetheless, there are numerous studies of galaxy groups that make use of either deep observations, and/or low-redshift samples. O'Sullivan et al. (2017) presented an optically-selected, statistically complete sample of 53 low-redshift galaxy groups (Complete Local Volume Groups Sample, CLoGS), for which they were able to perform a detailed X-ray analysis. They classified groups into cool-cores and non cool-cores and studied the central radio galaxy (Kolokythas et al., 2018), finding that $\sim 92\%$ of their groups' dominant galaxies host radio sources. Other studies are based on estimating the scaling relations between observables such as temperature, luminosity, entropy and mass (e.g., Lovisari et al., 2015). Bharadwaj et al. (2014a) estimated the central cooling time (CCT; see Sec. 3.4 for a definition) in a sample of galaxy groups and found that the fractions of strong (CCT < 1 Gyr), weak ($1 <$ CCT < 7.7 Gyr), and non cool-cores (CCT > 7.7 Gyr) were similar to those in galaxy clusters. They also found that BGGs (Brightest Group Galaxies) in their galaxy groups may have a higher stellar mass than BCGs in clusters.

Simulations by Gaspari et al. (2011) showed that AGN feedback may be more persistent and delicate in galaxy groups than in galaxy clusters. A small number of deep observations of single, local objects also detected cavities and shocks (e.g., Nulsen et al., 2005; Gitti et al., 2010; Randall et al., 2015; Forman et al., 2017), allowing investigations of the balance between the AGN energy injection and the gas cooling. X-ray cavities were also recently observed by Bîrzan et al. (2020) in a sample of 42 systems, of which 17 are groups or ellipticals.

Ineson et al. (2013, 2015) performed a study of the interactions between AGN and their environment in a sample of radio-loud AGN in clusters and groups. They found a correlation between the X-ray emission from the intra-group medium and the 151 MHz power of the central radio source. They also argued that such a correlation could arise from AGN in a phase of radiatively-inefficient accretion (Low Excitation Radio Galaxies, or LERGs), while High Excitation Radio Galaxies (HERGs) stand out of the distribution and show higher radio powers. The origin of such a relation is not obvious. In fact, X-ray emission in clusters and groups is mostly due to line emission and Bremsstrahlung, that consequently allow the ICM to cool from high ($\sim 10^7$ K) temperatures. The time scale of such radiative losses is thus strongly dependent on the distance of the diffuse gas from the cluster (or group) core, varying from less than 1 Gyr in the centre of the strongest cool-cores to $\sim$ few Gyrs moving towards the outskirts. On the other hand, Nipoti and Binney (2005) suggested that the AGN power output could act in cycles of $\sim 10^8$ yr. Hence, the time scales of these two processes are usually significantly different. However, O'Sullivan et al. (2017) found that groups typically show shorter cooling time at a given radius when compared to clusters, due to the high cooling efficiency of line emission at kT < 2 keV.

Here, we study the relationship between the X-ray emission from the intra-group medium and the radio emission from the radio galaxy hosted in the centre of a large (N = 247) sample of X-ray detected galaxy groups in the 2 deg^2 of the COSMOS field (RA = $10^h00^m28.6^s$, DEC = +02°$12^m21.0^s$, J2000). This field was chosen as it offers a unique combination of deep and multi-wavelength data. In order to account for the faintness of groups, we make use of the deepest observations and catalogs.

This paper is organized as follows: in Sec. 3.2, we explain how we built the catalog and we describe its main properties. In Sec. 6.2, we compare the groups with a sample of galaxy clusters and explore the correlation between the X-ray and the radio emission exploiting statistical tests and a Monte-Carlo simulation. In Sec. 3.4, we discuss the physical implications of our results and put them into context. In Sec. 6.5, we draw the conclusions. Throughout this paper, we adopt a fiducial ΛCDM cosmological model with $H_0 = 71$ km s^{-1} Mpc^{-1}, $\Omega_\Lambda = 0.7$ and $\Omega_M = 0.3$.

3.2 The samples

Construction of the group sample

Gozaliasl et al. (2019) presented a catalog of 247 X-ray-selected galaxy groups in the COSMOS field, obtained combining all available *Chandra* and *XMM-Newton* observations, in the redshift range (spectroscopic for 183 groups, photometric for the remaining 64) $0.08 \leq z \leq 1.75$ and with luminosities in the $0.1-2.4$ keV band ranging from $\sim 10^{41}$ to $\sim 10^{44}$ erg s^{-1}. The flux limit of the sample is $\sim 3 \cdot 10^{-16}$ erg s^{-1} cm^{-2}. Setting a search radius of 30” from the groups' centre (assumed as coincident with the X-ray peak) and a

Image	Beam [arcsec]	Sensitivity [μJy/beam]
VLA-COSMOS Deep	2.5 x 2.5	12
MIGHTEE high-resolution	4.7 x 4.2	8.6
MIGHTEE low-resolution	9 x 7.4	4.1
NVSS	45 x 45	450

Table 3.1: Properties of the 1.4 GHz images exploited for the detection of central radio sources in the group sample (see Sec. 3.2) and in the cluster sample (see Sec. 3.2).

redshift threshold of $\Delta z = 0.02$, we cross-matched this sample with the VLA-COSMOS Deep Survey at 1.4 GHz (rms $\sim$ 12 μJy beam^{-1}, beam = 2.5"x 2.5", Schinnerer et al. 2010), to look for the radio galaxy hosted in the centre of every group. We chose to use VLA-COSMOS to get the highest resolution available. At the mean redshift of our sample ($z \sim 0.7$), the largest visible angular scale at this frequency corresponds to $\sim$ 450 kpc. The results were then inspected visually, exploiting COSMOS optical catalogs, to check the bounty of the cross-match. We found that, out of the 136 groups for which BGG properties are available, only in 41 ($\sim$ 30%) the detected radio source is hosted in the BGG. This is consistent with recent works that observed offsets between the optical dominant galaxy and the X-ray peak. Gozaliasl et al. (2019) found that only 30% of BGGs in COSMOS are closer to the X-ray peak than 0.1R$_{200}$, and that the peak is often not located at the bottom of the potential well, where the dominant galaxy usually lie. We will return on this in Sec. 3.2.

Groups showing no central radio emission were then further inspected exploiting new, deep MeerKAT observations of COSMOS that are part of the MIGHTEE survey (The MeerKAT International GHz Tiered Extragalactic Exploration, Jarvis et al. 2016, Heywood et al. in prep.). For these MIGHTEE COSMOS Early Science images, the thermal noise component, measured from the circular polarization images (Stokes V), is 2.2 μJy/beam in the image with 9"x 7.4"resolution, and 7.5 μJy/beam in the 4.7"x 4.2"resolution image. However, in the map centre the "noise" will appear to be higher due to the contribution from confusion (faint background sources below the formal noise limit). We obtain an estimate of this thermal-plus-confusion noise by subtracting the model of the sky obtained by the PyBDSF source finder (Mohan and Rafferty, 2015a)[1] and generating a RMS map of the image from this residual product using the same software. The mean RMS value over the inner 20"x 20"region (where the primary beam attenuation is approximately negligible) is then measured. For the MIGHTEE COSMOS Early Science map this measurement is 4.1 μJy/beam in the 9"x 7.4"image, and 8.6 μJy/beam in the 4.7"x 4.2"resolution image. The properties of all the radio images are summarized in Table 3.1.

Our final sample (hereafter referred to as group sample) consists of 174 (155 detected by both VLA and MIGHTEE and 19 only by MIGHTEE) objects for which we have redshifts and both the X-ray emission (flux, luminosity, R$_{200}$) and the radio emission (flux density, luminosity, largest linear size) from the central radio galaxy, plus 73 groups for which the

[1]https://github.com/darafferty/PyBDSF

	Total	VLA + MIGHTEE	MIGHTEE
Detections	174	155	19
Upper limits	73		$> 3\sigma$
Resolved	55	50	5
Unresolved	119	119	14

Table 3.2: Composition of the group sample. In a sample of 247 galaxy groups, we observed a central radio source in 174 of them. 155 are detected by both VLA-COSMOS and MIGHTEE, while 19 only by MIGHTEE. Among the 155 VLA+MIGHTEE detections, 55 are resolved, while 119 remain unresolved. Among the 19 MIGHTEE-only detections, 5 are resolved and 14 remain unresolved.

central source was undetected in the radio band. These are thus treated as 3σ upper limits, with σ being the rms noise of the MIGHTEE low-resolution observation. The largest linear size is defined as the linear size of the major axis of a source, and we will hereafter refer to it as LLS. The 1.4 GHz luminosity was estimated as:

$$L_{1.4\mathrm{GHz}} = S_{1.4} 4\pi D_{\mathrm{L}}^2 (1+z)^{-\alpha} \tag{3.1}$$

where $S_{1.4}$ is the flux at 1.4 GHz, D_L is the luminosity distance at redshift z and α is the spectral index, that was assumed ~ 0.6, since this is the mean synchrotron index usually observed in radio galaxies.

The group sample was further divided into groups with *resolved* and *unresolved* radio galaxies, following the same criteria presented in Schinnerer et al. (2007) and Schinnerer et al. (2010). This classification is based on the assumption that the ratio between integrated and peak flux density gives a measure of the spatial extent of a source in comparison to the size of the synthesized beam(see Sec. 6.2 and appendix of Schinnerer et al. 2010 for more details). We find that $\sim 32\%$ (55 objects) of the sample show well-resolved radio sources, while for the remaining $\sim 68\%$ (119 objects) we only have upper limits on the LLS. Exploiting MIGHTEE images, we found that no sources are spatially unextended due to VLA lacking surface brightness sensitivity. Table 3.2 summarizes the composition of the sample; all the properties of the objects are listed in Table 4, described in Appendix .1 and available as online material.

Characteristics of the group sample

Fig. 3.1 shows the redshift and mass (M_{200}, the mass within the radius corresponding to 200 times the critical density) distributions of the group sample. The redshift distribution of resolved and unresolved radio sources show a similar behaviour: we detect both resolved, high-redshift and unresolved, low-redshift radio galaxies. The masses of most groups, estimated via the L_X - M_{200} correlation (Leauthaud et al., 2010), lie within $\sim 10^{13}$ and $\sim 10^{14}$ $M_\odot$.

In Fig. 3.2 we show the X-ray and radio luminosity distribution functions of the group sample. The X-ray distribution function suggests that there is no significant difference in the intra-group medium emission between groups with resolved and unresolved radio galaxies. However, the 1.4 GHz function shows that resolved radio sources are able to reach higher

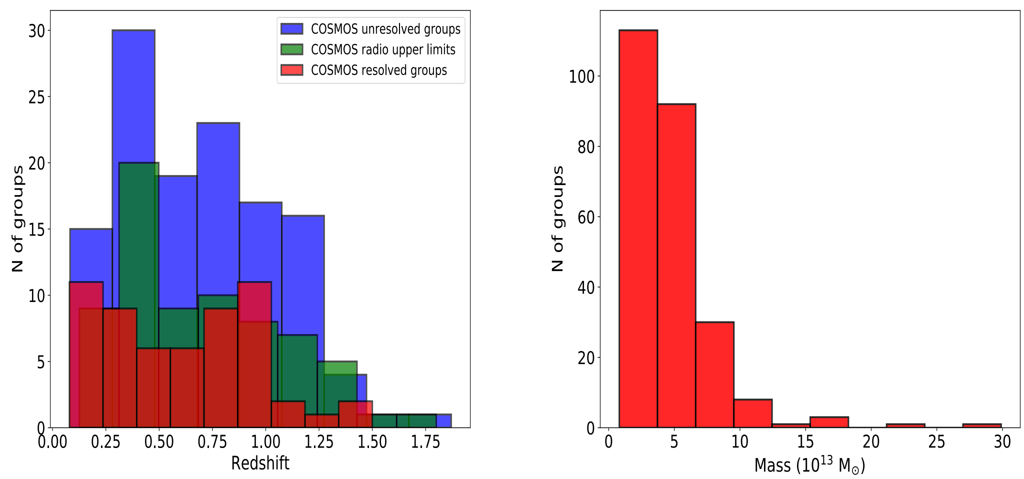

Figure 3.1: *Top Panel*: Histogram showing the redshift distribution of the group sample, classified into objects with resolved (red) and unresolved (blue) radio galaxies and radio upper limits (green). *Bottom Panel*: Mass (M_{200}) distribution of the group sample. The mass was estimated through the L_X - M_{200} correlation by Leauthaud et al. (2010).

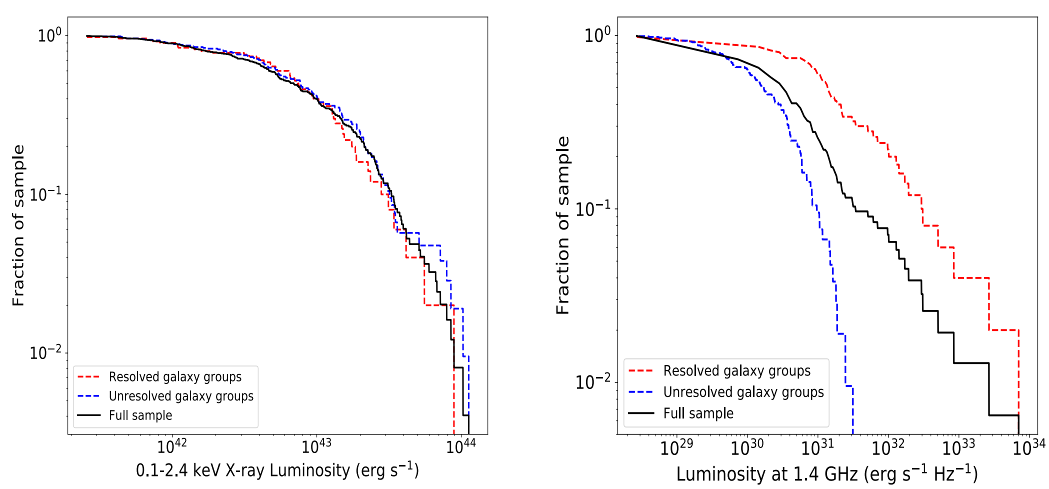

Figure 3.2: *Top Panel*: X-ray luminosity distribution function for the group sample in the 0.1-2.4 keV band. The red line denotes groups hosting resolved VLA radio sources, the blue line unresolved ones, while the black line represents the full sample. *Bottom Panel*: 1.4 GHz luminosity distribution function for the group sample. The red line denotes groups hosting resolved VLA radio sources, the blue line unresolved ones, while the black line represents the full sample.

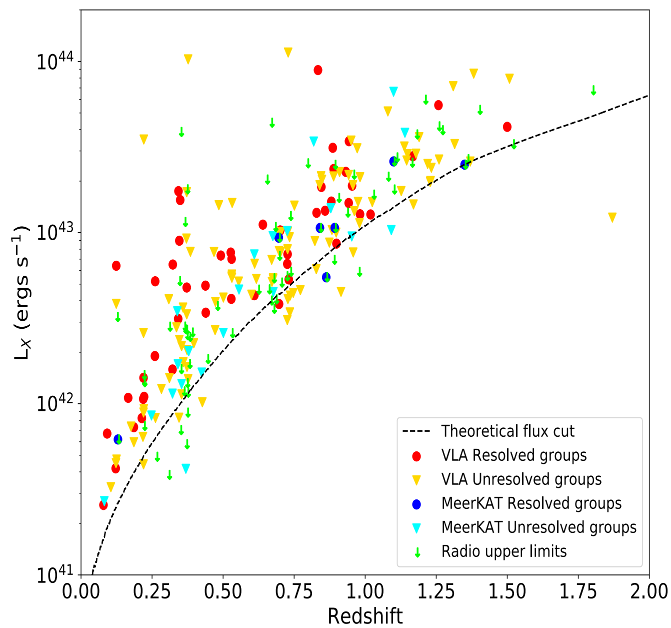

Figure 3.3: Malmquist bias for the group sample: X-ray luminosity in the 0.1-2.4 keV band vs. redshift. Circles and triangles represent groups hosting resolved and unresolved radio sources, respectively. Green arrows denote upper limits in the radio band. The dashed line represents the theoretical cutoff of the flux-limited sample, produced assuming a surface brightness of $\sim 10^{-15}$ erg s^{-1} cm^{-2} arcmin^{-2} in the 0.5-2 keV band in a circle with a radius of 32", which corresponds to the construction of the COSMOS catalog. Some objects lie under the cutoff, since in some of the COSMOS regions the X-ray sensitivity was higher due to different sky coverages.

powers at these frequencies, while unresolved radio galaxies exhibit a break between 10^{31} and 10^{32} erg s^{-1} Hz^{-1}. We also note that the radio distribution function of our groups' sources spans the same luminosity range as BCGs in clusters (e.g., Hogan et al., 2015; Yuan et al., 2016), despite the different environments.

Since our sample is flux-limited, it shows the typical Malmquist bias displayed in Fig. 3.3. At low redshifts we have mostly low X-ray luminosity objects, while groups with high luminosities are rarer. As we move to higher redshifts, we start to see more powerful groups, while weak objects disappear due to their faintness. The fact that the distribution is not perfectly aligned with the curve is likely due to how the X-ray catalog was produced. Combining multiple observations, performed with different instruments and different sky coverage, can lead to different flux sensitivities. We will return to this issue in Sec. 3.3.

A control sample of galaxy clusters

We constructed a sample of galaxy clusters in order to compare it to our main sample of groups. The *ROSAT* Brightest Cluster Sample (BCS, Ebeling et al. 1998) is a 90% flux-complete sample of 201 galaxy clusters in the Northern hemisphere with $z \leq 0.3$, that

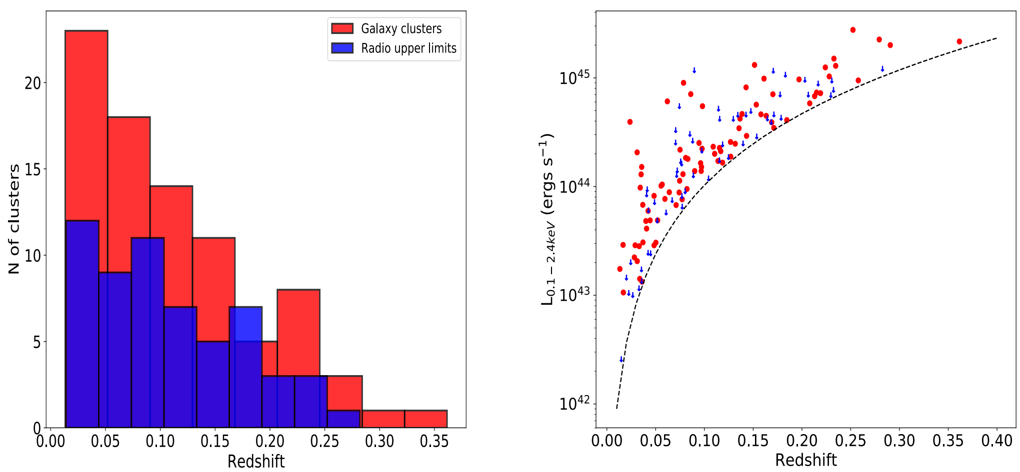

Figure 3.4: *Top Panel*: Histogram showing the redshift distribution of the cluster sample. *Bottom Panel*: X-ray luminosity vs. redshift for the cluster sample. The dashed line represents the theoretical flux cut.

reaches a flux limit of $4.4 \cdot 10^{-12}$ erg s^{-1} cm^{-2} in the 0.1-2.4 keV band. Crawford et al. (1999) presented the optical BCG position for 165 of the BCS clusters. We cross-matched it with the NRAO VLA Sky Survey (NVSS, Condon et al. 1998) in order to find the corresponding radio galaxy, using the same criteria discussed in Sec. 3.2. NVSS has a lower resolution when compared to both VLA-COSMOS and MIGHTEE, but it still provides good estimates of the properties of the radio sources we are interested in (e.g., flux density). The survey is produced with VLA in D configuration, resulting in a largest visible angular scale at 1.4 GHz of 970"that, at the mean redshift of the CS, corresponds to $\sim$ 2500 kpc. The final catalog (hereafter referred to as cluster sample) consists of 84 galaxy clusters for which we have the same measurements (ICM X-ray luminosity, radio power of the central source, redshift, LLS) as for the group sample, and 58 objects for which we only have upper limits for the radio emission from the central galaxy.

We then exploited the red sequence members of the CODEX cluster sample (Finoguenov et al., 2019) to calculate the fraction of radio galaxies that are BCGs. In clusters, 85 $\pm$ 6% of the central radio galaxies coincide with the BCG. This is different in galaxy groups, where only $\sim$ 30% of the central radio sources are hosted by the BGG. In most objects, the X-ray peak should represent a good indicator of the center. Smolčić et al. (2011) found that, in their sample of groups, radio galaxies are in fact always found next to the X-ray peak, justifying our approach. However, Gozaliasl et al. (2019, 2020) showed that BGGs defined within R_{200} have a broad distribution of their group-centric radii, and also show kinematics not well matched to that of simulated central galaxies. It might be that radio sources provide a better identification for central galaxies. This possibility needs to be investigated through multi-wavelength observations and by performing a thorough study of the dynamical properties of central radio galaxies, and will be the subject of a future work.

The top panel of Fig. 3.4 shows the redshift distribution for the cluster sample. The

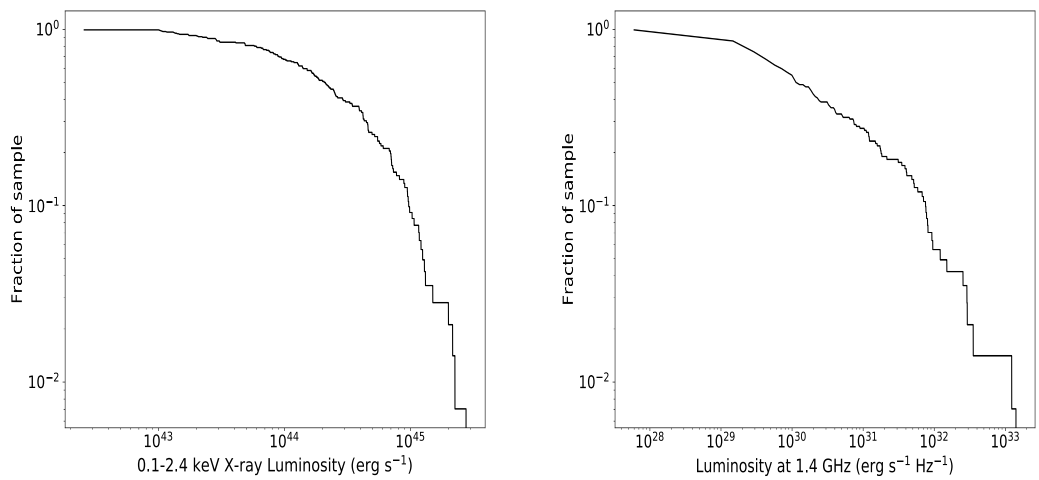

Figure 3.5: *Top Panel*: X-ray luminosity distribution function for the cluster sample in the 0.1-2.4 keV band. *Bottom Panel*: 1.4 GHz luminosity distribution function for the cluster sample.

redshift range is much narrower than the group sample, with most clusters lying at $z \leq 0.15$ and only a few objects reaching $z \sim 0.35$. On the other hand, the bottom panel shows the Malmquist bias. The sensitivity of the X-ray observations of the cluster sample is uniform for all the objects, leading to a smoother distribution with respect to the group sample.

Fig. 3.5 shows the X-ray and radio luminosity distribution for the cluster sample. While the X-ray luminosity of groups never exceeds $\sim 10^{44}$ erg s^{-1}, clusters are able to reach $\sim 5 \cdot 10^{45}$ erg s^{-1}. On the other hand, the 1.4 GHz power of clusters stops at $\sim 10^{33}$ erg s^{-1} Hz^{-1}, while radio sources hosted in groups can, in some cases, be 10 times more powerful. We will discuss this in more depth in the following sections.

3.3 Analysis

In the following, we will focus on the relationship between log(P$_{1.4GHz}$) vs log(L$_X$) for groups and clusters, where P$_{1.4GHz}$ is the 1.4 GHz power of the central radio source and L$_X$ is the X-ray luminosity of the intra-group/cluster medium.

Correlation between X-ray and radio luminosity

In Fig. 3.6 we show the 1.4 GHz luminosity of the radio galaxy vs. the X-ray luminosity from the intra-group medium for every group, where the sizes of symbols are proportional to the LLS and colour denotes redshift. The upper limits in the radio band are represented by down-sided arrows.

Groups hosting unresolved radio galaxies follow a narrow distribution (see squares in Fig. 3.6) that suggests a possible connection between radio and X-ray luminosities, with higher intra-group medium emission corresponding to higher power coming from the central radio source. However, groups hosting big radio galaxies (up to ~ 600 kpc, see also Fig. 3.7)

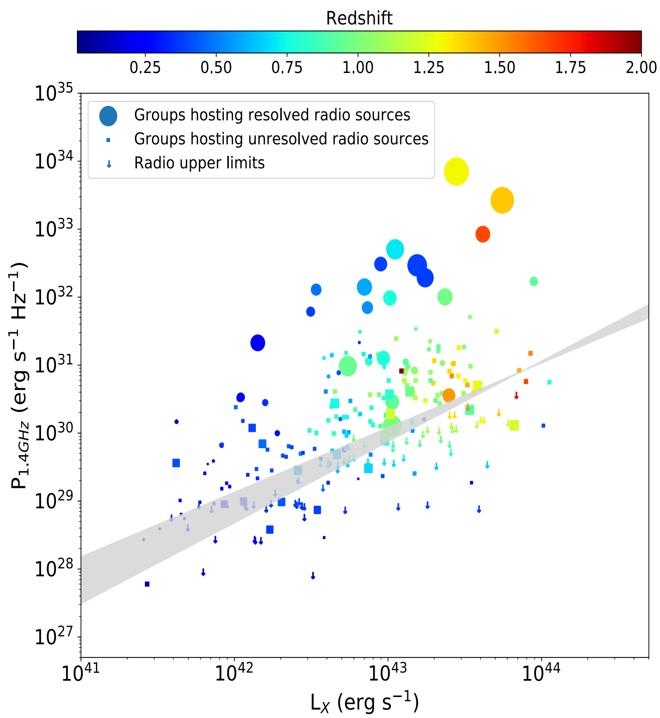

Figure 3.6: 1.4 GHz luminosity of the central radio galaxy vs. intra-group medium X-ray luminosity in the 0.1-2.4 keV band for the group sample. The points are sized by the radio LLS and colorized for the redshift. Down arrows denote MIGHTEE radio upper limits. The grey area represents the best fit: $\log L_{\rm R}$ = (1.07 $\pm$ 0.12) $\cdot \log L_{\rm X}$ - (15.90 $\pm$ 5.13).

Sample	N	τ/σ	p
Galaxy groups	247	5.04	< 0.0001
Galaxy groups, no res. groups	197	3.94	< 0.0001
Galaxy groups, uniform flux cut	175	4.16	< 0.0001
Galaxy clusters	142	2.99	0.0028
Full sample	389	6.66	< 0.0001
Full sample, no res. groups	339	8.84	< 0.0001

Table 3.3: Results of the partial correlation Kendall's τ test in the presence of a correlation with a third factor. N is the sample size, τ is the partial correlation statistic, σ is the standard deviation, while p represents the probability under the null hypothesis that the correlation is produced by the dependence on redshift.

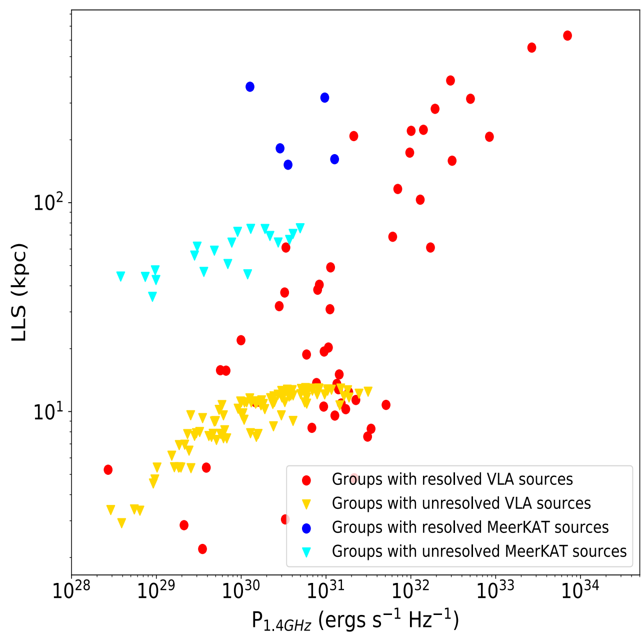

Figure 3.7: Largest Linear Size (LLS) vs. radio power at 1.4 GHz of the central radio galaxies for the group sample. Circles represent groups hosting resolved sources, while triangles are unresolved ones. For the latter class, the upper limits on the LLS were estimated as 1.5θ, with θ being the resolutions of the VLA ($\sim$ 2.5") and MeerKAT ($\sim$ 9") observations.

with higher radio luminosities broaden the distribution. This is consistent with what we have previously argued from the radio distribution function (Fig. 3.2), in which the function for resolved objects is able to reach $\sim 10^{34}$ erg s^{-1} Hz^{-1}, while unresolved radio sources never go above $\sim 10^{31}$ erg s^{-1} Hz^{-1}.

As discussed above, the Malmquist bias is able to produce spurious correlations when two luminosities in different bands are compared. In order to test for Malmquist bias, we used the partial correlation Kendall τ test (Akritas and Siebert, 1996), as in Ineson et al. (2015). This allows us to look for correlations between radio and X-ray luminosities in the presence of upper limits and a dependence on redshift. The results, with the null hypothesis being that the correlation is produced by the dependence on redshift, are presented in Table 3.3.

We found a strong correlation for the group sample, estimating $p < 0.0001$, with p being the null hypothesis probability. However, as discussed in Sec. 3.3, the X-ray minimum sensitivity used to build the catalog is not constant across the entire COSMOS field. Especially at low fluxes, there is the chance that this could lead to ambiguous results. To address this issue, we applied a further, uniform flux cut at $5 \cdot 10^{-15}$ erg s^{-1} cm^{-2}, and repeated the test for this subsample. We still find $p < 0.0001$, supporting the hypothesis that there is a intrinsic correlation between X-ray and radio luminosities. We also performed the

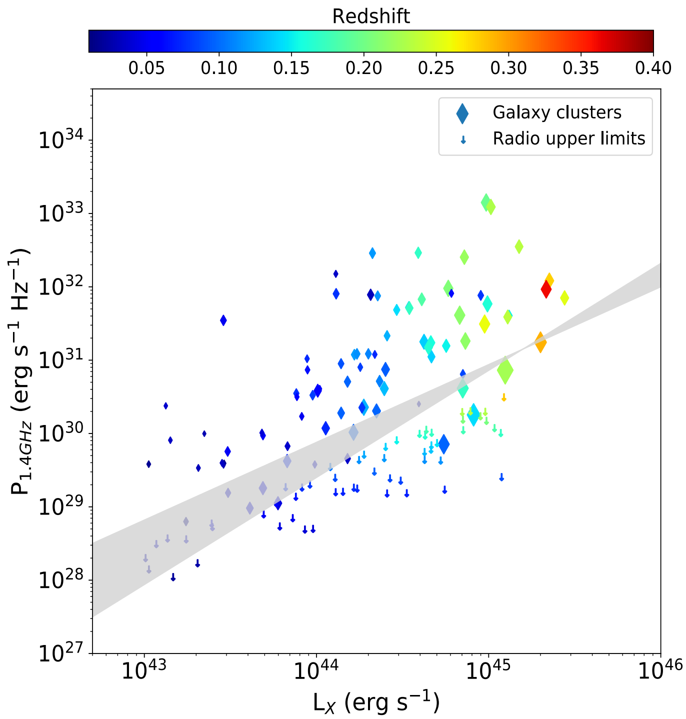

Figure 3.8: 1.4 GHz luminosity of the central radio galaxy vs. ICM X-ray luminosity in the 0.1-2.4 keV band for the cluster sample. The points are sized by the radio LLS and colorized for the redshift. Down arrows denote NVSS radio upper limits. The grey area represents the best fit: $\log L_R = (1.26 \pm 0.20) \cdot \log L_X$ - (25.80 $\pm$ 9.04).

test excluding groups hosting resolved radio sources. In fact, as discussed in more detail in Sec. 3.4, such objects could be characterized by a different balance between the X-ray and the radio emission, thus widening the correlation. We estimated, even for this subsample, $p < 0.0001$.

However, Bianchi et al. (2009) argued that the partial correlation Kendall's τ test may underestimate the redshift contribution to the relation, particularly when it comes to determining the functional correlation. On the other hand, they also showed that random scrambling of their radio luminosities is not able to produce the observed slope of the correlation with the X-ray luminosity, thus suggesting that a physical correlation may be present. We will return to this issue in Sec. 3.3.

Comparison with the cluster sample

In Fig. 3.8 we show the 0.1-2.4 keV ICM luminosity vs. the 1.4 GHz power of the central radio galaxy for the cluster sample. As in Fig. 3.6, the sizes of symbols are proportional to the LLS, and colour denotes redshift. It appears that a correlation also exists in galaxy clusters, albeit with more scatter compared to groups hosting unresolved radio sources. However, unlike for groups, the LLS seems to be less correlated with the central radio power, and there is only one radio source with LLS > 200 kpc. Since the cluster sample is

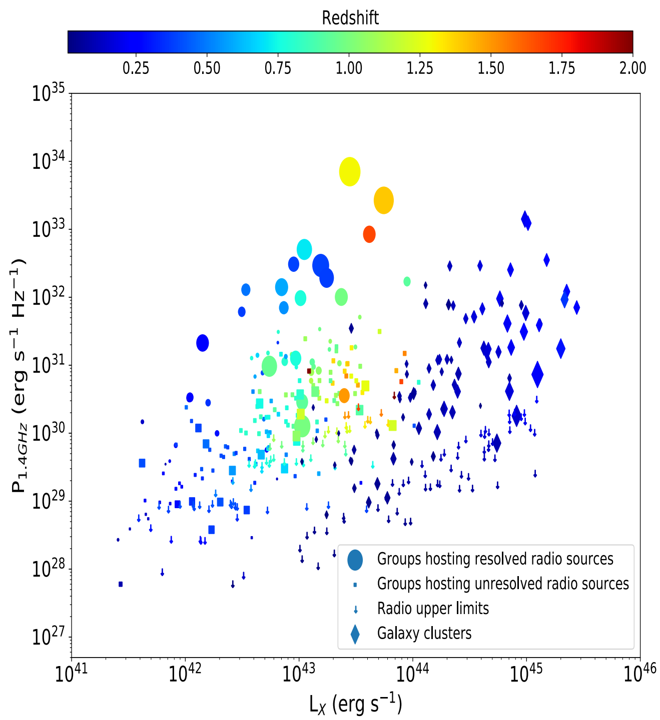

Figure 3.9: 1.4 GHz luminosity of the central radio galaxy vs. ICM X-ray luminosity in the 0.1-2.4 keV band for both the group sample (circles) and the cluster sample (diamonds). The points are sized by the radio LLS and colorized for the redshift.

restricted to lower redshifts, one could argue that large and powerful radio galaxies could be only found at $z \geq 0.3$. However, large radio sources in the group sample are already found at $z \leq 0.3$, where sources in the cluster sample are instead small (see Sec. 3.4 for a further discussion). Moreover, Gupta et al. (2020) have shown that there is little redshift evolution in the radio luminosity at fixed host stellar mass out to $z \sim 1$ for sources hosted in clusters. However, their results do show strong mass evolution in the number of radio-powerful AGN.

Again we applied the Kendall τ test in order to check whether the X-ray/radio correlation is significant, with the results listed in Table 3.3. We found a null-hypothesis probability of $p = 0.0028$. This suggests that clusters also show a correlation, even though it is weaker than for groups. Finally, combining the two samples (group sample and cluster sample), we obtain $p < 0.0001$.

The correlation for clusters and groups: comparison with simulated datasets

In Fig. 3.9 we show the X-ray luminosities vs the 1.4 GHz powers for both the group sample and the cluster sample. Obvious is the dearth of data at $L_X < 5 \cdot 10^{43}$ erg s^{-1} - $L_{1.4GHz} \sim 10^{32}$ erg s^{-1} Hz^{-1}, set by the flux cuts of our samples. Since we are dealing with left-censored data (i.e., upper limits), any correlation that depends on data where the lowest values are upper limits are hard to assess. This is a long-standing problem in astronomy (see e.g., Feigelson, 1992).

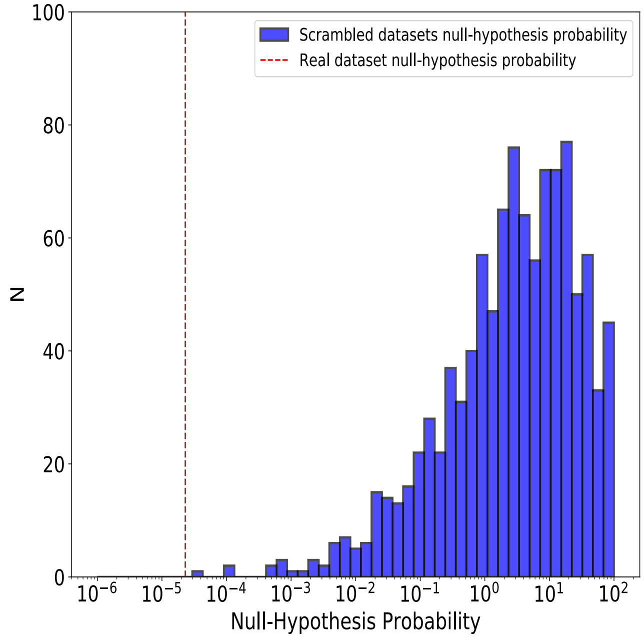

Figure 3.10: Null-hypothesis probability distribution of N=1000 scrambled datasets. The red dashed line represents the null-hypothesis probability of the real data.

In order to investigate the effects of this left-censoring we performed a "scrambling test", that was applied to similar problems by, e.g., Bregman (2005) and Merloni et al. (2006). In this test we keep each pair of X-ray luminosity and redshift of the group sample and 'shuffle' the associated radio fluxes, assigning each one to a random (L_X/z) pair. Applying the newly assigned redshift, we then calculate the radio luminosity from the flux. We produced 1000 scrambled datasets in this manner and calculated for each of them the null-hypothesis probability through the Kendall τ test. The distribution of such values is presented in Fig. 3.10.

Out of 1000 'shuffling', the null-hypothesis probability was never found to be lower than the real dataset. The distribution is similar to a lognormal, with the peak lying between $\sim 2\%$ and 20%. The mean sets around ~ 12.5 %, with a standard deviation of ~ 3.5 %. The null-hypothesis probability of the real dataset lies more than 3σ away from it, suggesting that the correlation holds.

Alternatively, we can also simulate our population of radio and X-ray sources by randomly drawing them from luminosity functions and redshift distributions, then applying the respective flux cuts in the X-ray and radio and measuring the correlation. This Monte-Carlo simulation can be performed with and without an underlying correlation between X-ray and radio powers.

The simulation was performed along the following steps:

- We first draw a random redshift within the ranges $z = 0.01 - 2$ for the group sample and $z = 0.01 - 0.4$ for the cluster sample, assuming a constant comoving source density, i.e.:

$$\frac{dN}{dz} = \frac{4\pi c D_L{}^2(z)}{(1+z)H_0 E(z)}, \tag{3.2}$$

with N being the number of objects, c the speed of light, E(z)= $\sqrt{\Omega_M(1+z)^3+\Omega_\Lambda}$ and D_L the luminosity distance at redshift z.

- We then sampled N X-ray luminosities, assuming two different luminosity functions as probability density functions (pdf). For clusters, we assumed the $0.1-2.4$ keV luminosity function (LF) of BCS (Ebeling et al., 1997a), since the cluster sample was built starting from this catalog. On the other hand, for groups we used the LF presented in Koens et al. (2013) that goes down to lower luminosities and out to $z \sim 1.1$. Multiple studies have shown hints of negative redshift evolution of the LF, with a reduction in the number density of massive, luminous clusters at high redshifts (e.g., Moretti et al., 2004; Koens et al., 2013). As usual, they use a Schechter function in the form:

$$\Phi(L) = \Phi^* \exp(-L/L^*) L^{-\alpha}, \tag{3.3}$$

where L is the X-ray luminosity in units of 10^{44} erg s^{-1}, Φ^* is the normalization, L^* is the luminosity at the function cutoff and α determines the steepness of the function at $\mathrm{L} < \mathrm{L}^*$. Following the same approach described in Koens et al. (2013) and Böhringer et al. (2014), the redshift evolution is taken into account by parametrizing density and luminosity evolution through a power-law:

$$\Phi^*(z) = \Phi_0^*(1+z)^A, \tag{3.4}$$

$$L^*(z) = L_0^*(1+z)^B, \tag{3.5}$$

where Φ_0^* and L_0^* are the values at the current epoch, A $\sim$ -1.2 and B $\sim$ -2 (Moretti et al., 2004). As we first draw a redshift, we can then sample the X-ray luminosity. The number of mock objects, N, was chosen to match the numbers in our samples.

- We estimated the flux and applied an X-ray flux cut of $2 \cdot 10^{-15}$ erg s^{-1} cm^{-2} for groups and $4.4 \cdot 10^{-12}$ erg s^{-1} cm^{-2} for clusters, as for our samples.

- We associated every X-ray luminosity-redshift pair with a radio luminosity assuming (i) no correlation between X-ray and radio power, (ii) $\log L_{\mathrm{R}}$ = $(1.07 \pm 0.12) \cdot \log L_{\mathrm{X}}$ - (15.90 ± 5.13) for both clusters and groups, and (iii) the above correlation for groups, and $\log L_{\mathrm{R}}$ = $(1.26 \pm 0.20) \cdot \log L_{\mathrm{X}}$ - (25.80 ± 9.04) for clusters. The correlations were estimated exploiting the parametric EM algorithm coded in the AStronomical SURVival statistics package (ASURV, Feigelson et al. 2014), that takes into account different contributions by detections and left-censored data.

The results for groups assuming no correlation between X-ray and radio power are presented in the top panel of Fig. 3.11. The empty bottom-right area of the plot is produced by the Malmquist bias. Apart from this, the distribution of simulated data looks significantly different from both the group sample and the cluster sample. In fact, Fig. 3.6 shows no groups with $L_X < 10^{43}$ erg s^{-1} hosting a radio galaxy with $L_R > 10^{33}$ erg s^{-1} Hz^{-1}. However, we can see such objects in the top panel of Fig. 3.11, despite the simulation having the same flux cuts of the real observation. This means that groups are prevented by physical limitations from being found at these luminosities: the lack of them in this region is not produced by biases.

The middle panel of Fig. 3.11 shows simulated data assuming the same correlation for clusters and groups. The plot still looks different from Fig. 3.9, in which low X-ray luminosity clusters are offset from groups, producing a tail that stands out from the distribution. In order to properly measure the differences between the simulated and the real distributions, we used the two sample Kolmogorov-Smirnov test. The test estimates the null-hypothesis probability that two samples belong to the same distribution. The X-ray luminosities of the simulated clusters are drawn from the BCS luminosity function, that is the same catalog used for building the cluster sample. Since the KS test is not accurate when performed on two samples if one of them is drawn from the other one, we chose to perform it only on radio luminosities. Comparing the simulated data of the middle panel of Fig. 3.11 with the real dataset, the KS test gives a null-hypothesis probability of $\sim 2.7\%$, confirming that the two distributions are intrinsically different. This suggests that X-ray and radio luminosities of clusters and groups could follow different correlations.

Finally, the bottom panel of Fig. 3.11 shows the results of the simulation assuming two different correlations for clusters and groups. The distribution of the simulated data is now similar to the real correlation, suggesting that this is the assumption that better fits our data. This is also confirmed by the KS test, that gives a null-hypothesis probability of $\sim 39.1\%$, indicating that the two samples likely belong to the same distribution. We also argue that, without providing any relation between radio and X-ray luminosity, the simulation is not able to reproduce the correlation, indicating that the redshift is not the only factor contributing the correlation. This supports the picture of a physical connection between ICM and AGN emission.

3.4 Discussion

Large radio galaxies in galaxy groups

Fig. 3.6 and 3.7 show that AGN in the centre of groups typically reach only tens of kpc in linear size and up to $\sim 10^{32}$ erg s^{-1} Hz^{-1} in power. However, a few of them (~ 10) are able to grow to hundreds of kpc, reaching radio powers comparable to massive clusters' BCGs (Fig. 3.8) and surpassing such sources in terms of size. We then argue that the biggest

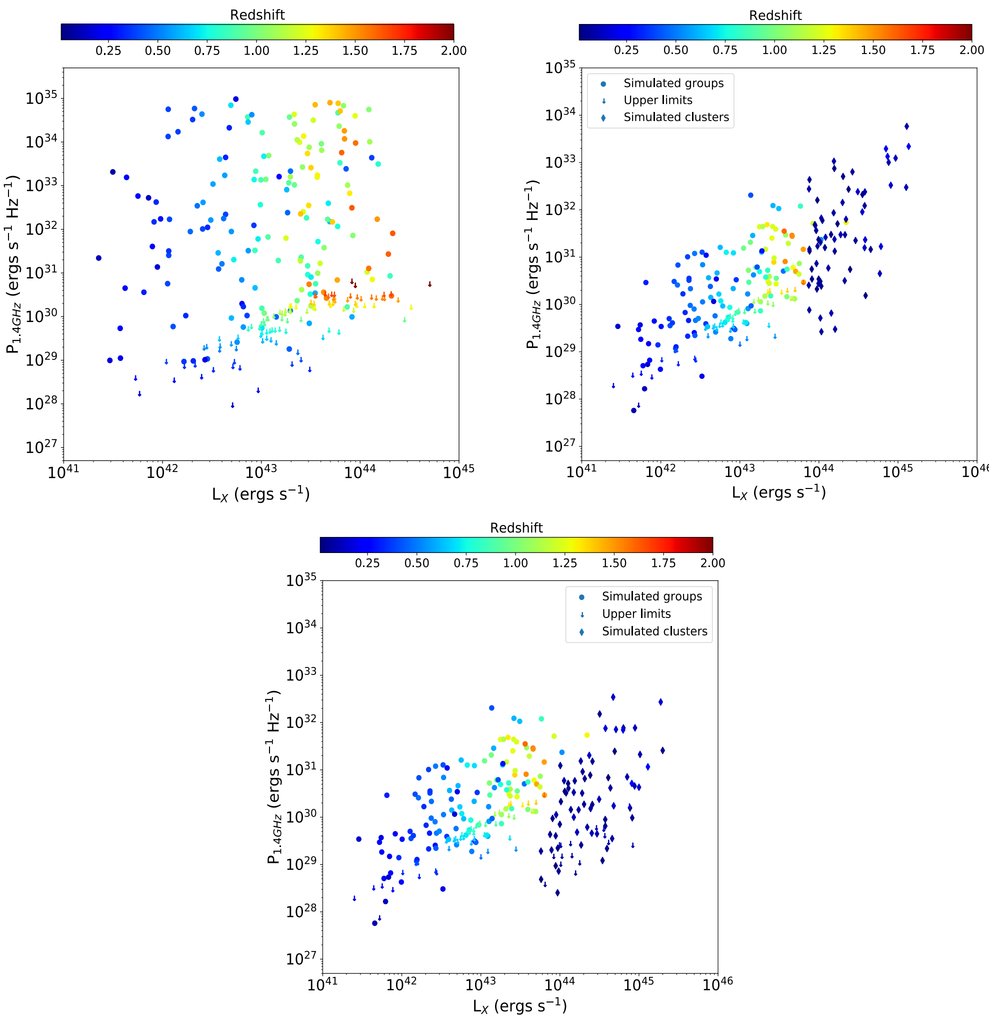

Figure 3.11: 1.4 GHz power of the central radio source vs. X-ray luminosity of the ICM in the 0.1-2.4 keV band for the simulated data. *Top-left panel*: No correlation. *Top-right panel*: Same correlation (see text) for both galaxy clusters (diamonds) and groups (circles). *Bottom panel*: Two different correlations for galaxy clusters (diamonds) and groups (circles).

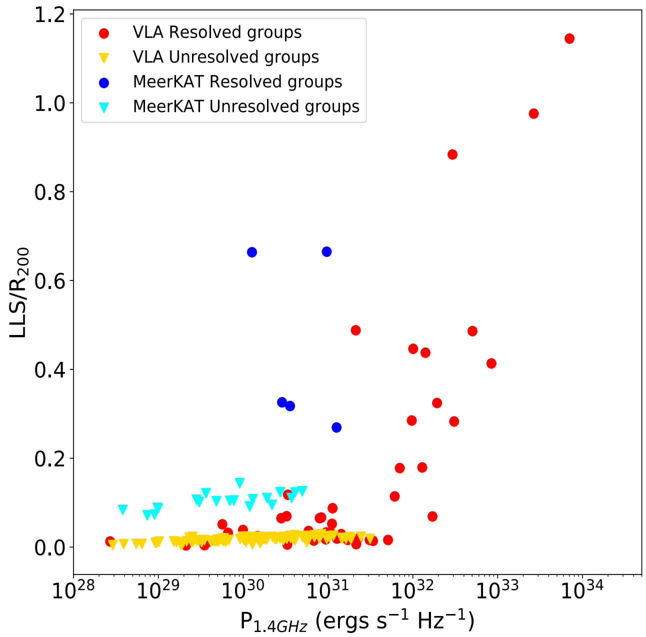

Figure 3.12: Ratio of LLS of the radio galaxy and R_{200} of corresponding group (in kpc) vs. radio power of the radio galaxy. Circles represent groups hosting resolved radio sources, while triangles denote unresolved ones.

radio galaxies are found in the centre of galaxy groups. This was already hinted by multiple works on giant radio galaxies (e.g., Mack et al. 1998; Machalski et al. 2004; Subrahmanyan et al. 2008; Chen et al. 2012; Grossová et al. 2019; Cantwell et al. 2020, and references therein). However, this is the first time that they are included as sources in a large sample of groups, and their link to the environment is studied with respect to "classical" radio sources. Large radio galaxies have been found in galaxy clusters, too. An example is the giant radio fossil recently observed in the Ophiucus clusters (Giacintucci et al., 2020) that reaches a size of ~ 1 Mpc. However, they look more like outliers produced by unusually energetic AGN outburst, rather than widespread cases. This is also supported by Fig. 3.9, which shows that the LLS of radio galaxies hosted in clusters is usually significantly smaller with respect to sources found in groups. The cluster sample only shows one cluster with a central radio source bigger than 200 kpc ($\sim 0.7\%$ of the sample), while the group sample has 10 of them ($\sim 4\%$ of the sample), ranging from 200 to 600 kpc.

We suggest that the lower gas density in groups when compared to clusters and a different, more efficient accretion mechanism could be responsible for this effect. This is supported by Ineson et al. (2013, 2015), who found a very similar relationship between intra-group medium and AGN luminosities and showed that large radio galaxies, lying in the top region of Fig. 3.6, are mostly HERGs, powered by a radiatively efficient accretion mode (e.g., Best and Heckman, 2012), while groups lying within the narrower radio power distribution mostly contain LERGs. Similarly, we tried to classify the radio galaxies of the group sample into HERGs and LERGs, by retrieving optical spectra from the zCOSMOS survey (Lilly and Zcosmos Team, 2005) and measuring the equivalent width (EW) of the [OIII] line. Objects showing $EW_{[OIII]} < 5$ Å were classified as LERGs, while radio galaxies with $EW_{[OIII]} > 5$ Å are HERGs. However, we were able to properly perform such analysis only on 9 radio galaxies, 4 of which were classified as HERGs, and 5 as LERGs. This was due to most objects not having a zCOSMOS detection, while for others the fit of the spectrum was inconclusive. Therefore, since this sample is too small to draw any conclusion from it, we will not discuss it and leave it for future follow-up works.

Fig. 3.12 shows the radio power of the radio galaxy on the x-axis, and the LLS and corresponding group's R_{200} ratio on the y-axis. The largest radio galaxies have dimensions comparable to the group's virial radius.

The power output supplied by such AGN could potentially have strong consequences for the intra-group medium. However, the energy is transferred to the diffuse gas at large distances from the centre ($\sim$ hundreds of kpc), due to the dimensions of the radio galaxy, while the cores of groups are typically only $\sim$ tens of kpc. This means that, when heating mainly occurs through radio mode feedback (i.e., by generating cold fronts and X-ray cavities), the centres of groups are less affected by such process, and thus cooling could be less suppressed than in galaxy clusters. On the other hand, when shocks are the dominant source of heating, it could still be enough to adequately quench radiative losses. This scenario looks very similar to some galaxy clusters, that are shown to host giant cavities, with lobes extending over the cooling region (e.g., Gitti et al., 2007). Some analyses of singular groups already suggested that jets extending well over the core could violate the standard AGN feeding-feedback model (e.g., O'Sullivan et al., 2011d; Grossová et al., 2019). However, this is the first work to prove that a significant fraction of the galaxy groups population effectively shows hints that support this scenario.

This hypothesis needs to be tested by performing a thorough study of the jets and structure of these large radio sources, and possibly by comparing the results with a accurate analysis of the diffuse gas within the cooling radius of the host group. Such a radius is usually defined as the radius within which the cooling time of the ICM falls under the lookback time at z=1, corresponding to 7.7 Gyr. While meticolous estimates of the cooling radius are usually feasible for galaxy clusters, there are only a few, closeby groups (e.g., O'Sullivan et al., 2017) that have been observed with the required depth and resolution to accurately measure it. Therefore, we are currently unable to perform this comparison for our sample.

Do clusters and groups show the same X-ray - radio correlation?

In the previous sections we showed how, according to our analysis, the relation between the X-ray luminosity and the power of the central radio source is not produced by biases or selection effects. Clusters and groups seem to follow two different correlations, albeit with a similar slope. Furthermore, central radio galaxies in some groups show enhanced emission up to $\sim$ 3 orders of magnitude. The hypothesis of two, distinct correlations is

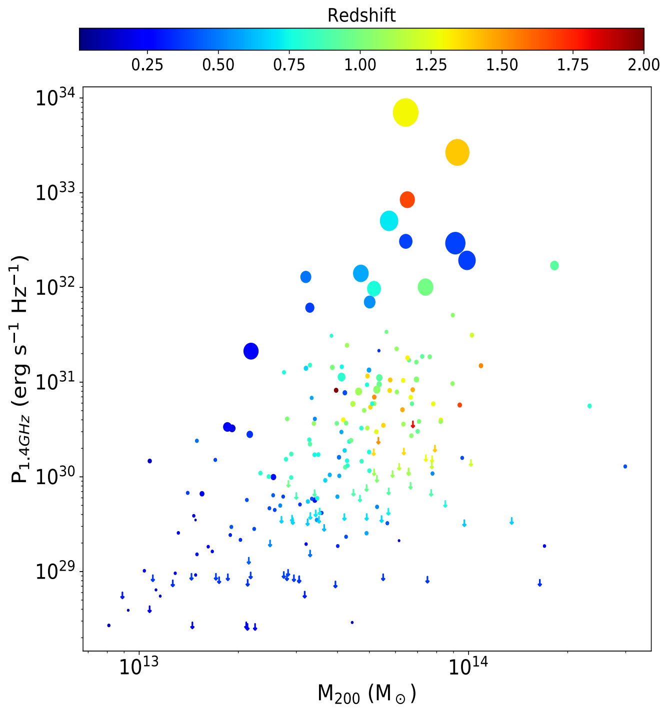

Figure 3.13: AGN power at 1.4 GHz for the group sample vs. mass (M_{200}). Colors denote redshift, and the points are sized for the LLS of the radio source. Down arrows represent radio upper limits.

supported by the analysis previously performed on our simulated datasets.

However, we suggest that clusters and groups could follow the same correlation, in which the latter populate the low X-ray and low radio luminosity regions, while the former are usually stronger. The correlation is mainly produced by groups and clusters that have not recently experienced a significant interaction with the surrounding environment, while those which have undergone recent mergers or accretion from other objects tend to broaden the distribution. Specifically, we would expect these clusters to show a lower AGN power at a given X-ray luminosity, since the lack of cooling ICM prevents the AGN from accreting gas. This could also explain the low-radio luminosity tail of clusters. The result of this scenario is a distribution that is narrower for galaxy groups, and then broadens because of the difference between cool cores and merging clusters.

Recent results by Gupta et al. (2020) (hereafter G20) already suggested the existence of a link between the large-scale properties of clusters and AGN feedback. Using SUMSS data (843 MHz) for two different cluster samples ($\sim$ 1000 X-ray selected, $\sim$ 12000 optically selected), they have shown that the probability of a cluster hosting radio-loud AGN scales with its mass. This could suggest a connection between AGN feedback and cluster mass. A similar link was already explored by Hogan et al. (2015). G20 also found *no* evidence that the AGN radio power scales with the cluster halo mass (see Fig. 10 of G20). However, their sample is built taking into account every radio AGN within clusters, even those not hosted in BCGs. Therefore, it is not straightforward to compare it to the properties of central radio

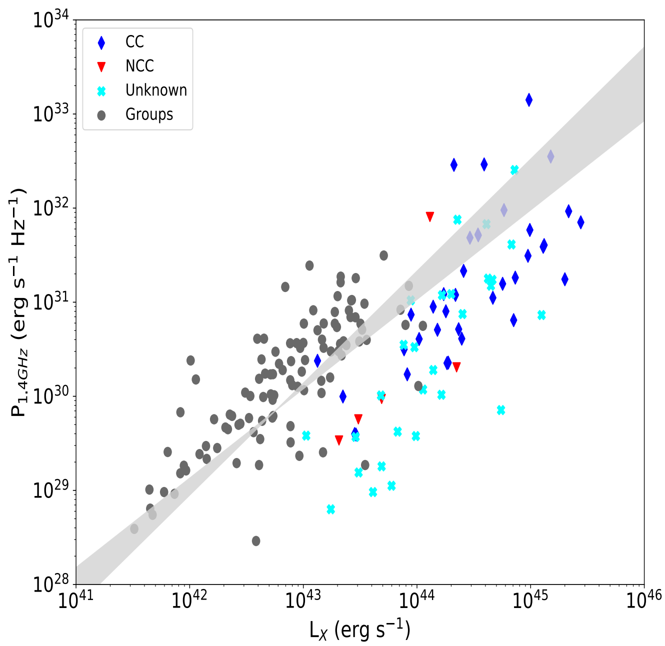

Figure 3.14: 1.4 GHz power of the central radio source vs. X-ray luminosity in the 0.1-2.4 keV band for 71 of the cluster sample objects, classified into cool cores (blue diamonds), non-cool cores (red triangles) and clusters with unknown dynamical state (cyan crosses). Grey circles represents groups hosting unresolved radio sources, for comparison. The grey area is the best-fit relation for galaxy groups: $\log L_R = (1.07 \pm 0.12) \cdot \log L_X$ - (15.90 ± 5.13).

sources.

In Fig. 3.13 we show the AGN radio power at 1.4 GHz vs. the mass of the group sample (M_{200}). We find no hints of groups under $M_{200} \sim 6 \cdot 10^{13}$ $M_\odot$ hosting radio sources with log P (erg s^{-1} Hz^{-1}) > 32. This suggest that, even in the group regime, low-mass objects usually host weaker radio sources, while radio-loud AGN are usually found at higher masses.

One could argue that our sample is simply missing low-mass groups that host powerful AGN. These objects could therefore be rare. Since we do not detect them with a ~ 250 objects sample, the probability of observing one has to be lower than 0.4%. This suggests that, even if they do exist, they can be considered outliers. In the group sample, the only process we found that could bring to these consequences is the combination of low density medium and the more efficient accretion mechanism that produces large radio galaxies. (see Sec. 3.4). However, all these sources are found at higher masses. Either low-mass groups hosting radio-loud AGN do not exist or, if they do, they are extremely rare ($p < 0.4\%$).

In order to support the hypothesis that clusters and groups follow the same correlation, we were able to classify 38 clusters of the cluster sample ($\sim 30\%$) into cool-core and non-cool core. The classification, based on the presence of optical line emission, is presented by

Hogan et al. (2015).

There are 33 clusters for which we have no information about their dynamical state. Not surprisingly, most cool cores populate the high-luminosity area of the plot. Furthermore, 4 out of 5 non-cool cores are found at low radio power. We thus argue that cool cores produce the high-power tail of the correlation shown in Fig. 3.9, while more dynamically disturbed clusters tend to broaden it.

One possible scenario is that the feedback cycle in galaxy groups is much tighter and the central AGN can affect the entropy of the gas more efficiently, as seen in our group sample. Over their lifetime, central radio galaxies can undergo phases of higher power, allowing them to grow to hundreds of kpc. Once central radio galaxies have grown to a certain size, the energy from the AGN is injected at greater radii with respect to the cooling radius (see Sec. 3.4), weakening the efficiency of feedback and broadening the correlation between X-ray luminosity and radio power. Via mergers and accretion, groups can grow to become clusters (White and Frenk, 1991b). Events occurring during their lifetime, such as mergers, accretion or any interaction with other objects, that significantly affect both the cooling of the ICM and the central radio galaxy, can widen the distribution.

3.5 Conclusions

We have studied the correlation between the X-ray emission of the intra-group medium and the radio power of the central AGN for a sample of 247 X-ray selected galaxy groups detected in the COSMOS field. We compared the properties of these groups with a control sample of galaxy clusters and with simulated datasets of X-ray and radio luminosities. Our conclusions can be summarized as follows:

- Groups show a correlation between the intra-group medium emission and the radio galaxy power, with more X-ray luminous objects hosting more powerful radio sources. Using Kendall's partial correlation τ test, combined with data 'scrambling' and Monte-Carlo simulations, we showed that this correlation is not produced by the flux cut. Groups hosting large radio sources ($\geq$ 150-200 kpc) stand out of the correlation.

- Galaxy clusters are usually more luminous but show a similar correlation to groups, albeit with more scatter.

- Despite the observational evidence of two, distinct correlations, we argue that clusters and groups could follow the same correlation once the dynamical state is taken into account. Groups populate the low-luminosity region, while cool-core clusters are found at high luminosities.

- Mergers between galaxy clusters and the resulting changes to central cooling times, as well as changes in the accretion mechanism, can increase the scatter in the observed correlation.

- Galaxy groups host a significantly higher fraction of large (LLS > 200 kpc) radio galaxies ($\sim 4\%$) than clusters ($\sim 0.7\%$), albeit the redshift range of our cluster sample is narrower. The growth of these radio sources, that in this work reach up to $\sim$ 600 kpc, is probably favored by the low ambient densities and aided by an efficient accretion mode (HERGs). Radiative cooling of the diffuse thermal gas could be less suppressed in these objects, since the AGN energy injection happens at larger radii compared to the cooling region of the corresponding group.

More detailed studies are needed to address these results. Volume-limited catalogs are essential in order to reduce biases that can be introduced by redshift-dependent luminosity functions and other effects. Deep, high angular resolution observations of single groups and optical spectra could also be helpful for a better understanding of the physical link between the intra-group medium and the central AGN.

Acknowledgements. *The authors thank the anonymous referee for useful comments and suggestions. T. Pasini is supported by the DLR Verbundforschung under grant number 50OR1906. We acknowledge discussions with J. Liske and J. Mohr. The spectral analysis on zCOSMOS data was performed by M. Owers. The MeerKAT telescope is operated by the South African Radio Astronomy Observatory, which is a facility of the National Research Foundation, an agency of the Department of Science and Innovation. We acknowledge use of the Inter-University Institute for Data Intensive Astronomy (IDIA) data intensive research cloud for data processing. IDIA is a South African university partnership involving the University of Cape Town, the University of Pretoria and the University of the Western Cape.*

Data Availability

The data underlying this article are available in the article and in its online supplementary material.

.1 Properties of the group sample

The properties of the group sample are listed in Table 4. The full table is available as online material, while a part of it is showed here; the listed properties include X-ray coordinates of the group, redshift, M_{200}, R_{200}, X-ray luminosity, radio coordinates, flux density at 1.4 GHz, radio luminosity at 1.4 GHz and LLS (when resolved). The last column reports 1 if the radio source was detected with both VLA and MeerKAT, and 2 if it was detected only by MeerKAT.

RAJ2000$_X^{(1)}$ [deg]	DECJ2000$_X^{(2}$ [deg]	z$^{(3)}$	M$_{200}^{(4)}$ [10^{13} M$_\odot$]	R$_{200}^{(5)}$ [kpc]	L$_X^{(6)}$ [10^{42} erg s^{-1}]	RAJ2000$_R^{(7)}$	DECJ2000$_R^{(8)}$	S$_{1.4}^{(9)}$ [mJy]	L$_{1.4}^{(10)}$ [10^{30} erg s^{-1} Hz^{-1}]	LLS$^{(11)}$ [kpc]	Detection$^{(12)}$
150.5111	2.02699	0.899	3.86 ± 1.10	513.45	8.624 ± 4.052	10:02:02.549	+02:01:45.36	0.441 ± 0.040	14.31 ± 1.56	15.06	1
150.62251	2.16039	1.5	6.52 ± 1.70	500.37	41.48 ± 18.12	10:02:30.117	+02:09:12.45	7.751 ± 0.010	844.3 ± 0.01	206.85	1
150.57957	2.47898	0.61	3.21 ± 0.72	539.28	4.306 ± 1.597	10:02:18.308	+02:28:04.29	1.081 ± 0.043	14.02 ± 0.64	12.79	1
150.17097	2.52363	0.697	2.75 ± 0.59	495.76	3.826 ± 1.359	10:00:41.418	+02:31:24.17	0.716 ± 0.028	12.71 ± 0.58	9.57	1
149.83842	2.67517	0.26	2.56 ± 0.54	569.03	1.901 ± 0.665	09:59:21.341	+02:40:30.45	0.546 ± 0.082	0.995 ± 0.16	21.96	1
...											

Table 4: The table lists all the properties of the group sample and of their central radio sources, when detected. The first 5 lines of it are shown here; the columns of the table are: X-ray RA (1) and DEC (2) of the group, redshift (3), M_{200} (4) with error in 10^{13} $M_\odot$, R_{200} (5) in kpc, X-ray luminosity (6) and error in 10^{42} erg s^{-1} in the 0.1-2.4 keV band, radio RA (7) and DEC (8), flux density at 1.4 GHz in mJy (9) with error, radio luminosity at 1.4 GHz (10) in 10^{30} erg s^{-1} Hz^{-1} with error, and LLS in kpc (when resolved) (11). The last column (12) reports 1 if the radio source was detected with both VLA and MeerKAT, and 2 if it was detected only by MeerKAT.

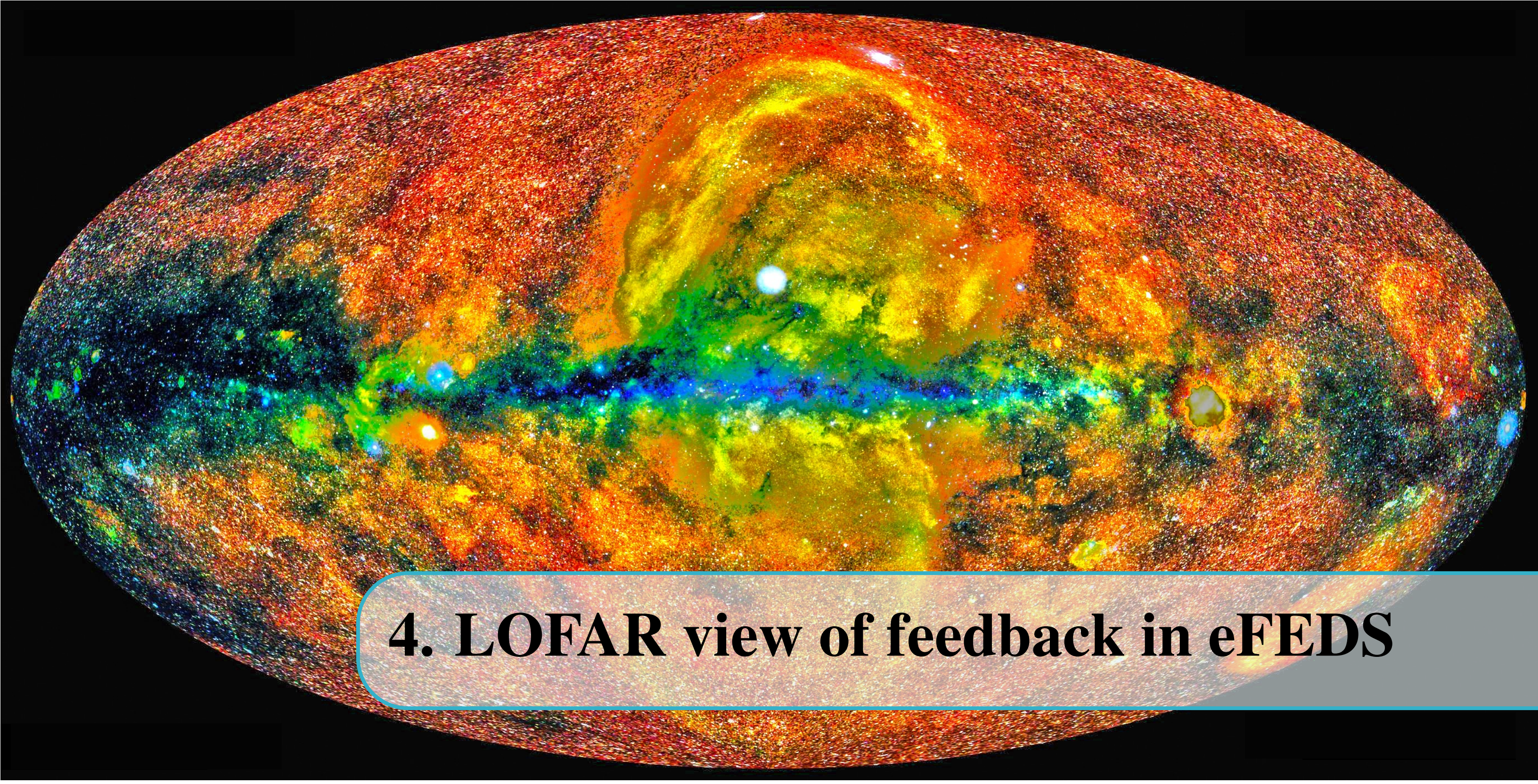

4. LOFAR view of feedback in eFEDS

The eROSITA Final Equatorial-Depth Survey (eFEDS): LOFAR view of brightest cluster galaxies and AGN feedback

T. Pasini, M. Brüggen., D. N. Hoang et al. A&A, 661A, 13P.

Abstract. *During the performance verification phase of the Spectrum-Roentgen-Gamma (SRG) eROSITA telescope, the eROSITA Final Equatorial-Depth Survey (eFEDS) was carried out. It covers a 140 deg^2 field located at 126° < R.A. < 146° and -3° < Dec. < +6° with a nominal unvignetted exposure over the field of 2.2 ks. Five hundred and fourty-two candidate clusters and groups were detected in this field, down to a flux limit $F_X \sim 10^{-14}$ erg s^{-1} cm^{-2} in the 0.5-2 keV band. In order to understand radio-mode feedback in galaxy clusters, we study the radio emission of brightest cluster galaxies (BCGs) of eFEDS clusters and groups, and we relate it to the X-ray properties of the host cluster. Using LOFAR, we identified 227 radio galaxies hosted in the BCGs of the 542 galaxy clusters and groups detected in eFEDS. We treated non-detections as radio upper limits. We analysed the properties of radio galaxies, such as redshift and luminosity distribution, offset from the cluster centre, largest linear size, and radio power. We studied their relation to the intracluster medium of the host cluster. We find that BCGs with radio-loud active galactic nucleus (AGN) are more likely to lie close to the cluster centre than radio-quiet BCGs. There is a clear relation between the cluster X-ray luminosity and the 144 MHz radio power of the BCG. Statistical tests indicate that this correlation is not produced by biases or selection effects in the radio band. We see no apparent link between largest linear size of the radio galaxy and the central density in the host cluster. Converting the radio luminosity into kinetic luminosity, we find that radiative losses of the intracluster medium are in an overall balance with the heating provided by the central AGN. Finally, we tentatively classify our objects into disturbed and relaxed based on different morphological parameters, and we*

show that the link between the AGN and the ICM apparently holds for both subsamples, regardless of the dynamical state of the cluster.

4.1 Introduction

Radio galaxies that sit at the centres of galaxy clusters and galaxy groups play an important role in regulating the temperature of the intra-cluster medium (ICM) and intra-group medium (IGrM). Radio-loud active galactic nuclei (AGN) are usually hosted by brightest cluster galaxies (BCG) and they quench the cooling of the hot ($\sim 10^7$ K) ICM through mechanical feedback (see e.g. reviews by McNamara and Nulsen 2012; Gitti et al. 2012). Effects of AGN feedback are manifested in the form of X-ray cavities and ripples in the cluster atmosphere (e.g. McNamara et al., 2000; Bîrzan et al., 2004; Fabian et al., 2006; Markevitch and Vikhlinin, 2007; Gastaldello et al., 2009). Consequences are also observed in the thermodynamical properties of the ICM, such as the gas entropy distribution (e.g. Cavagnolo et al., 2009) or in the transport of high-metallicity gas from the cluster centre to the outskirts (e.g. Liu et al., 2019a). This type of feedback is generally positive, in the sense that when the radiative losses of the ICM increase, the AGN counteracts this by heating the ICM. The more gas cools and fuels the super-massive black hole (SMBH) at the centre of the BCG, the higher the energy output that is able to quench the ICM radiative losses and establish what is commonly known as the AGN feedback loop (see the review from Gaspari et al. 2020). AGN feedback has been observed in systems ranging from isolated elliptical galaxies (Croton et al., 2006; Sijacki et al., 2015; O'Sullivan et al., 2011b) to massive clusters where it prevents the formation of cooling flows (McDonald et al., 2019; Ehlert et al., 2011; Pasini et al., 2021b). Most of the AGN associated with BCGs are in the so-called radio- or maintenance-mode (to distinguish it from the radiatively dominated quasar-mode feedback), where the accretion rate is modest and the feedback is mediated via mechanical work from powerful jets. A scaling relation between cavity power and radio luminosity, spanning over seven orders of magnitude in radio and jet power, has been observed in nearby systems (Bîrzan et al., 2004; Merloni and Heinz, 2007; Bîrzan et al., 2008; Cavagnolo et al., 2010; O'Sullivan et al., 2011c; Heckman and Best, 2014).

It has been pointed out that AGN feedback may operate differently in galaxy groups, where the gravitational potential is shallower (Sun, 2012). Here, less energetic AGN than in clusters can have a larger impact on the IGrM (Giodini et al., 2010) because outbursts are also capable of expelling cool gas from the central region (Alexander et al., 2010; Morganti et al., 2013). As a result, AGN feedback may break the self-similarity between galaxy clusters and groups, especially in terms of their baryonic properties (Jetha et al., 2007). Hence, galaxy groups may be particularly interesting to study AGN feedback because their different environment should be reflected in the properties of the central AGN (e.g. Giacintucci et al., 2011).

Von Der Linden et al. (2007) found that brightest group galaxies (BGGs) and BCGs lie on a different fundamental plane in terms of velocity dispersion, effective radius, and average surface brightness and have experienced star formation for a shorter time than non-BCGs [1]. In the companion paper by Best et al. (2007), they also argued that BCGs are more likely to host radio-loud AGN than satellites of the same mass (cluster-hosted and not), but are less likely to host an optical AGN. These differences are particularly pertinent for BGGs. Main et al. (2017) studied the relation between AGN feedback and central (at $0.004R_{500}$) cooling time in a sample of 45 galaxy clusters. They reported a clear correlation between AGN power, halo mass, and X-ray luminosity in clusters with a central cooling time of < 1 Gyr.

X-ray observations of galaxy groups are more difficult than for galaxy clusters because groups have lower surface brightnesses and emit at lower temperatures that are outside of the sweet spot of most X-ray observatories (see e.g. Willis et al. 2005). Some notable work on groups has been reported, however. Lovisari et al. (2015) presented scaling relations in the group regime, and Johnson et al. (2009) and O'Sullivan et al. (2017) classified their samples of groups into cool-core and non-cool-core. Kolokythas et al. (2018) focused on central radio galaxies in the so-called Complete Local Volume Group Sample (CLoGS) and found that $\sim 92\%$ of groups in their high-richness sample (26 objects) have dominant galaxies (BGGs) hosting radio sources. They also argued that radio galaxies showing jets are more common in bright groups, while radio non-detections are mostly found in X-ray faint systems. In the CLoGS low-richness sample (27 objects) studied in Kolokythas et al. (2019), the same authors report a radio detection rate of $\sim$82% in the luminosity range $10^{20} - 10^{25}$ W Hz^{-1} at 235 MHz. Malarecki et al. (2015) proposed that the lower densities in the IGrM compared to the ICM allow the lobes of group radio galaxies to expand to large distances. Werner et al. (2014) used far-infrared (FIR), optical, and X-ray data to study eight nearby giant elliptical galaxies, all central members of relatively low-mass groups. The authors found evidence that cold gas in these centrals galaxies is produced mostly by cooling from the hot phase and that this cool gas fuels outbursts of the AGN. Dunn et al. (2010) investigated a statistically complete sample of 18 nearby massive galaxies with X-ray and radio coverage and reported that 10 of them exhibit extended radio emission, with 9 also showing indications of interplay with the surrounding hot gas.

Mittal et al. (2009) determined that all cool-core clusters in a complete sample of ~ 60 clusters show a central radio galaxy, while only half of the non-cool core clusters have one. Interestingly, when this study was extended to galaxy groups, the trend became much weaker (Bharadwaj et al., 2014b, 2015a). A similar result was recently discussed in Pasini et al. (2020) (hereafter P20). In this paper, the authors studied a sample of 247 X-ray detected galaxy groups in the COSMOS field, matching them to radio galaxies detected in the VLA-COSMOS Deep Survey (Schinnerer et al., 2010) and in the COSMOS MeerKAT survey (MIGHTEE, Jarvis et al. 2016). They found that more than 70% of their radio galaxies are not hosted in BGGs, while in clusters, $\sim$85% of the central radio galaxies are associated with BCGs. They also discussed a correlation between the X-ray luminosity of groups and the radio power from the central radio galaxy because more massive groups seem to host more powerful sources. Pasini et al. (2021a) recently showed that in their sample of groups, BGGs showing powerful radio emission are always found within 0.2

[1] hereafter we refer to them as satellites for more clarity.

$R_{\rm vir} \sim 0.3R_{200}$ from the centre.

The extended ROentgen Survey with an Imaging Telescope Array (eROSITA) on board the Spectrum-Roentgen-Gamma (SRG) mission (Predehl et al., 2021) was launched on July 13, 2019. The large effective area (1365 cm^2 at 1 keV), large field of view (FoV, 1 deg diameter), good spatial resolution (half-energy width of 26 " averaged over the FoV at 1.49 keV, 16 " on-axis) and spectral resolution ($\sim$ 80 eV full width at half maximum at 1 keV) of eROSITA allow unique survey science capabilities by scanning large areas of the X-ray sky quickly and efficiently (Merloni et al., 2012). Thus, eROSITA is detecting a large number of previously undetected groups and clusters, most of them with low surface brightnesses and at low redshifts, even though the confirmation of these groups in the optical is challenging for $z < 0.1 - 0.2$.

In this work, we exploit the results of the eROSITA Final Equatorial-Depth Survey (eFEDS), a mini-survey designed to demonstrate the science capabilities of eROSITA. We study the radio galaxies observed in cluster centres at a frequency of 144 MHz by the LOw Frequency ARray (LOFAR, van Haarlem et al. 2013) in order to investigate their relation to their host clusters. This paper is structured as follows: in Sec. 4.2 we give a detailed description of how we built the sample. In Sec. 4.3 we show the results, compare them to previous work, and analyse the implications for AGN feedback. Finally, in Sec. 4.4 we summarise our results. Throughout this paper, we assume a standard ΛCDM cosmology with $\mathrm{H_0} = 70$ km s^{-1} Mpc^{-1}, $\Omega_\Lambda = 0.7$ and $\Omega_{\rm M} = 1 - \Omega_\Lambda = 0.3$.

4.2 Sample

eROSITA observation of eFEDS and the cluster catalogue

eFEDS covers a 140 deg^2 field located in an equatorial region, with R.A. from $\sim$126 to $\sim$146 deg, and declination from $\sim$-3 to $\sim$6 deg. This field was uniformly scanned by eROSITA during the Performance Verification phase, resulting in a nominal exposure of about 2.2 ks (unvignetted) over the field, which is similar in depth to the final exposure that will be reached in four years in equatorial fields in the eROSITA all-sky survey (Liu et al., 2021).

The eFEDS data were acquired by eROSITA over four days, between November 4 and 7, 2019. These data were processed by the eROSITA Standard Analysis Software System (eSASS, Brunner et al. 2021). We refer to Ghirardini et al. (2021, hereafter G21) for further details on the data processing. The source detection was performed using the tool `erbox` in eSASS on the merged 0.2 – 2.3 keV image of all seven eROSITA telescope modules (TMs). `erbox` is a modified sliding-box algorithm that searches for sources in the input image that are brighter than the expected background fluctuation at a given image position. For each candidate source, the detection likelihood and the extent likelihood are determined by fitting the image with the source model, which is a β-model convolved with the calibrated point spread function (PSF). Sources for which the extension is too broad to be fitted by the PSF have a higher extent likelihood. For further details on the source detection procedure, we refer to Brunner et al. (2021). We detect 542 candidate clusters over the full field (Liu et al., 2021). This corresponds to a source density of $\sim$ 4 clusters per square degree at the

Table 4.1: LOFAR HBA observations of the eFEDS field

Telescope	LOFAR
Project	LC13_029, LT5_007, LT10_010, LT14_004
Mode	HBA_DUAL_INNER
Pointing	eFEDS_128, eFEDS_131, eFEDS_134, eFEDS_136, eFEDS_139, eFEDS_142 P129+02, P132+02, P134+02, P137+02, P139+02, P126+02 G09_A, G09_B, G09_C, G09_D
Calibrator	3C 196, 3C 295
Frequency (usable, MHz)	120–168
Central frequency (MHz)	144
Number of subbands (SB)	241
Bandwidth per SB (kHz)	195.3
Channels per SB	16
On-source time (hr)	184[a]
Integration time (s)	1
Frequency resolution (kHz)	12.2
Correlations	XX, XY, YX, YY
Number of stations	73–75 (48 split core, 14 remote, 9–13 international[b])

Notes: [a]: calculated from the total duration on all pointings, including simultaneous observations with two LOFAR beams; [b]: international stations are not used in this study.

equatorial depth. Photometric redshifts are obtained through the multi-component matched filter (MCMF) cluster confirmation tool (Klein et al., 2018). Optical data from the Hyper Suprime-Cam Subaru Strategic Program (HSC-SSP, Aihara et al. 2018) and from the DESI Legacy Survey (LS, Dey et al. 2019) were exploited. We refer to Klein et al. (2021) and Liu et al. (2021) for further details. Spectroscopic redshifts derived from 2MRS (Huchra et al., 2012), SDSS (Blanton et al., 2017), or GAMA (Driver et al., 2009) were used when available (296 out of 542 clusters). For each cluster, a massive red-sequence galaxy near the X-ray emission peak was selected as the BCG, following Klein et al. (2021).

The sample of clusters can be expected to be contaminated by spurious sources or by misclassified AGN at a level of ∼19.7% (see Liu et al. 2021). Cluster contamination is therefore taken into account through the parameter $f_{\mathrm{cont},i}$ (Klein et al., 2019), which is defined as

$$f_{\mathrm{cont},i} = \frac{\int_{\lambda_i}^{\infty} f_{\mathrm{rand}}(\lambda, z_i) d\lambda}{\int_{\lambda_i}^{\infty} f_{\mathrm{obs}}(\lambda, z_i) d\lambda}, \tag{4.1}$$

where $f_{\mathrm{rand,z}}$ is the richness distribution of random positions at the cluster candidate redshift z_i, $f_{\mathrm{obs}}(\lambda, z_i)$ is the richness distribution of true candidates, and λ_i is the richness of the cluster candidate. The estimator $f_{\mathrm{cont},i}$ is correlated with the probability of a source being a chance superposition. Applying a given cut to this parameter allowed us to reduce the initial contamination of the cluster sample. When independence of contaminants in the X-ray sample is assumed, the fractional contamination of the sample is simply the product of the initial fractional contamination of the X-ray sample and the applied cut in $f_{\rm cont}$. For example, applying a cut in $f_{{\rm cont},i} < 0.3$ results in a sample of about 88% (477 out of 542) of the eFEDS extended sources that are confirmed as galaxy clusters. When an initial contamination of the X-ray sample of 20% is assumed (Klein et al., 2021), this $f_{\rm cont}$ selected sample is expected to contain $\sim$6% contamination. Subsequent tests described in Klein et al. (2021) confirmed the expected amount of contamination to be $6 \pm 3\%$. For more details about the X-ray catalog, we refer to Liu et al. (2021), while further details on the optical confirmation and contamination can be found in Klein et al. (2021).

LOFAR observations of eFEDS and the radio source catalogue

The eFEDS field was observed with the LOFAR high band antennae (HBA) for a total of 184 hours (including simultaneous observations by two LOFAR pointings) between February 24, 2016, and May 27, 2020, by projects LC13_029 (100 hours), LT5_007 (32 hours), LT10_010 (44 hours), and LT14_004 (8 hours). The eFEDS field is entirely covered by six pointings of LC13_029 that are separated by 2.7 degree in a row. The LT5_007 observations that are centred on the GAMA 09 field cover the central region of the eFEDS field with four pointings separated by 2.4 degree. LT10_010 and LT14_004, as part of the LOFAR Two-meter Sky Survey (LoTSS; Shimwell et al., 2017, 2019), are positioned on the LoTSS grid where pointings are typically 2.58 degree apart. We present a layout of the LOFAR observations of the eFEDS field in Fig. 4.1. The setup for all observations is described in detail in Shimwell et al. (2017, 2019). The observing frequency is from 120 MHz to 187 MHz, but we removed the data above 168 MHz where the signal is highly contaminated by RFI. Each pointing was performed by multiple chunks of 2 or 4 hours when the field was at high elevation (i.e. an average elevation of 35 degrees). Bright radio sources 3C 196 and/or 3C 295 were observed for 10 minutes each before and after the observations of the target fields and were used as primary calibrators. Details of the observations are given in Table 4.1.

We adopted the standard calibration procedure that has been developed for LoTSS (Shimwell et al., 2017, 2019). The calibration aims to correct for the direction-independent and direction-dependent effects (e.g. ionosphere and beam model errors), which need to be corrected for high-fidelty imaging with the LOFAR HBA. The data for each pointing were separately processed with `PREFACTOR`[2] (van Weeren et al., 2016; Williams et al., 2016a; de Gasperin et al., 2019a) and `DDF-pipeline`[3] (Tasse, 2014a,b; Smirnov and Tasse, 2015; Tasse et al., 2018; Tasse et al., 2021a). In detail, the processing was identical to that described by Tasse et al. (2021a), with one exception: in order to deal with the effect of sources that lie outside the target 8×8 degree field, but are still covered by the very N-S elongated LOFAR primary beam, the first step of the pipeline for each image was to make a

[2] https://github.com/lofar-astron/prefactor
[3] https://github.com/mhardcastle/ddf-pipeline

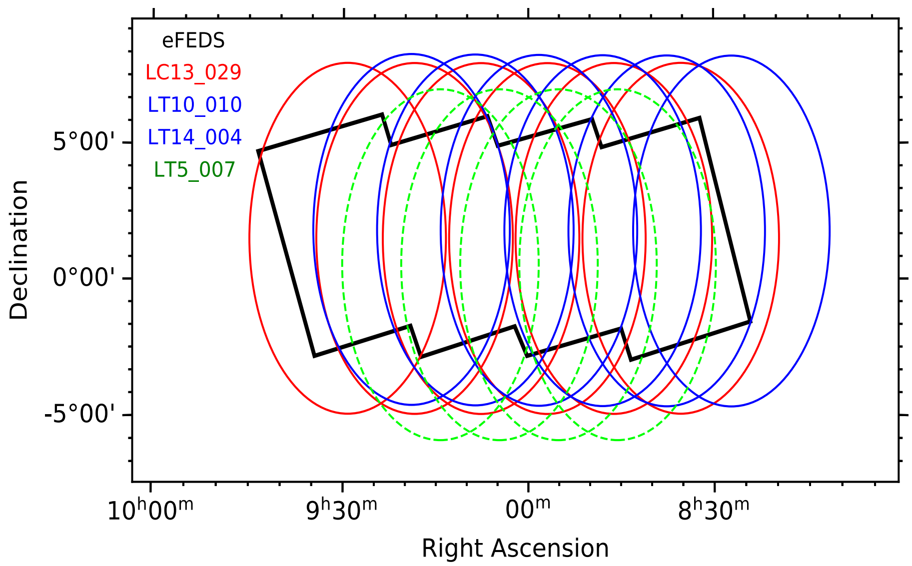

Figure 4.1: LOFAR observations of the eFEDS field, shown in the black region. The elliptical lines show the LOFAR pointing locations in the projects LC13_029 (red), LT5_007 (green), LT10_010 (blue), and LT14_004 (blue). The major and minor axes of the ellipse (i.e. 4.0 degrees and 6.7 degrees) are the FWHM of the LOFAR station beam along the RA and Dec axes, respectively.

very large (27×27 degree) image of the whole primary beam and subtract sources detected by `DDFacet` that appeared in this image, but lay outside the target field.

The pipeline produces high-resolution (< 9") images for each pointing with an rms noise of ≈170 μJy beam^{-1} in the pointing centre and ≈335 μJy beam^{-1} in the regions 2.5 degree from the pointing centres. Given the large LOFAR station beam (i.e. FWHM of 4 degrees in an E-W direction at the central frequency of 144 MHz), the separation of 2.4–2.7 degrees between the pointings leads to a significant overlap between the images. To increase the fidelity of the images, we convolved the images to a common resolution of $8" \times 9"$ and made a mosaic of the entire eFEDS field in the manner described by Shimwell et al. (2019) by reprojecting each image onto a $50,000 \times 27,000$ pixel image with 1.5 arcsec pixels centred on RA=9h, Dec=1 degree and then combining the reprojected images weighting by the local image noise at each pixel, taking the primary station beam into account. No astrometric blanking was carried out in the mosaicing, and each image was corrected before mosaicing to the flux scale of Roger et al. (1973) in the manner described by Hardcastle et al. (2021). The noise in the resulting mosaic is non-uniform, but reduces to ≈135 μJy beam^{-1} in the central parts of the image.

To produce a catalog of radio sources, we performed source detection on the high-resolution ($8" \times 9"$) mosaic of the eFEDS field with the Python Blob Detector and Source Finder (`PyBDSF`[4]; Mohan and Rafferty 2015b). Sources were detected with a peak detection threshold of 5σ (`thresh_pix=5`) and an island threshold of 4σ (`thresh_isl=4`) that limits the boundary for the source fitting. Here the local noise rms, σ, was calculated

[4] https://github.com/lofar-astron/PyBDSF

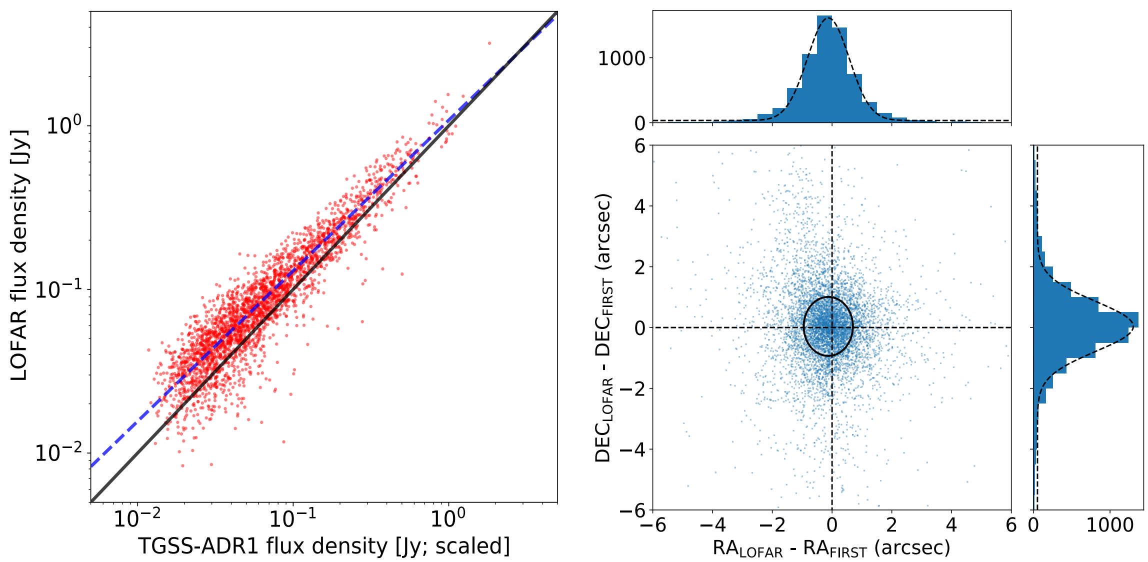

Figure 4.2: *Left*: Scatter plot between the TGSS-ADR1 (scaled) and LOFAR flux densities for single-Gaussian sources. The dashed blue line is the best fit of the LOFAR and TGSS-ADR1 (scaled) flux densities, $\log_{10}(S_{\rm LOFAR}) = 0.92 \times \log_{10}(S_{\rm TGSS-ADR1;scaled}) + 0.03$ [Jy]. The solid black line is a diagonal line with slope 1. *Right*: RA and Dec offsets for the LOFAR and FIRST detected single-Gaussian sources. The histograms of the offsets, including the best-fit Gaussian dashed lines, are plotted in the top and right panels. The ellipse shows the peak location (i.e. 0.13" to the left and 0.04" to the top of the centre point) and the FWHM (i.e. 0.70" and 0.82" in RA and Dec.) of the Gaussian functions that are obtained from the fitting of the RA and Dec offset histograms.

using a box of (150×150) pixels^2 that slides across the mosaic with a step of 15 pixels. Around bright sources, typically compact, where the pixel values are higher than 150σ (`adaptive_thresh` $= 150$), we used a smaller box of (60×60) pixels^2 and a sliding step of 15 pixels. The smaller box is more accurate for the estimate of the high noise rms around bright sources. The source detection produces a catalog of 45,207 sources, most of which (99.6 percent) have 144 MHz flux densities below 1 Jy.

The mosaic that is made with the standard procedure described above typically has a flux density uncertainty of 10%. However, to further check the flux scale in the eFEDS mosaic, we compared the integrated flux densities of the LOFAR detected sources with those in the TGSS-ADR1 (TIFR GMRT Sky Survey - Alternative Data Release 1, Intema et al. 2017) 150 MHz data, which have a similar central frequency. The LOFAR mosaic was smoothed to the resolution of the TGSS-ADR1 (i.e. 25") and regridded to match the spatial dimensions of the TGSS-ADR1 image. Radio sources in the LOFAR and TGSS-ADR1 25" images are detected with `PyBDSF` in an identical manner as for the LOFAR 8" $\times$ 9" mosaic above. There are 4,585 sources detected with both LOFAR and TGSS-ADR1 observations. Sixty percent of these sources (i.e. 2,695) were modeled with a single Gaussian and were used for the flux scale comparison. Because the observing frequencies for the LOFAR and TGSS-ADR1 data are different, we rescaled the flux densities of the TGSS-ADR1 sources to match those at the frequency of the LOFAR data (144 MHz) by assuming a common spectral index of 0.8 (see Sec. 4.2 for a definition). We performed a linear fit to the LOFAR and TGSS-ADR1 scaled flux densities, weighting by the LOFAR flux densities, and obtained a relation $\log_{10}(S_{\rm LOFAR}) = 0.92 \times \log_{10}(S_{\rm TGSS-ADR1;scaled}) + 0.03$ [Jy]. The integrated flux densities of the radio sources in the LOFAR catalog are $\sim$10% higher than those in the TGSS-ADR1 catalogue. We assumed an uncertainty of 20% for the integrated flux densities of the LOFAR detected sources. In Fig. 4.2 we present a scatter plot of the flux densities of the LOFAR and TGSS-ADR1 detected sources. The LOFAR detected sources, especially the faint ones, have higher flux densities than those found with the TGSS-ADR1 observations.

Following Shimwell et al. (2019), we checked the astrometry of the sources detected with `PyBDSF` in the LOFAR 8” $\times$ 9” mosaic by comparing their locations with those of their FIRST 1.4 GHz counterparts. We used the FIRST survey because of its high astrometric accuracy of 0.1” compared to the absolute radio reference frame (White et al., 1997) and the comparable spatial resolution of both surveys (i.e. 5” $\times$ 5” for FIRST and 8” $\times$ 9” for LOFAR). We cross-matched the sources within a radius of 9” in the LOFAR and FIRST catalogues and found 10,709 sources in common, of which 6,601 are single-Gaussian LOFAR sources. We calculated the offsets in RA and Dec for these single-Gaussian sources and present them in Fig. 4.2. The histograms of the RA and Dec offsets are fitted with a Gaussian whose location and standard deviation are defined as the systematic offsets and total astrometric uncertainty. There are systematic offsets of 0.13” and 0.04” in RA and Dec, respectively. The standard deviations of the offsets in RA and Dec are 0.70” and 0.82”, respectively. When this is compared to the offsets of FIRST and LoTSS sources (Shimwell et al., 2019), our results on the RA and Dec offsets are a factor of two to seven higher, and the standard deviations are a factor of two to three higher. These are likely due to the lower declination of the eFEDS field compared with the declination of $\approx 50^\circ$ of the LoTSS-DR1 field, which results in a larger elongated beam and slightly more disturbed ionospheric conditions. However, the uncertainties are well within the resolution of the LOFAR observations (i.e. 8” $\times$ 9”).

Sample construction and properties

The catalogue of radio sources was cross-matched with the BCG positions (see Sec. 4.2) by setting a sky threshold $\sim 3\theta$, with θ being the synthesised beam of the interferometric radio observation. The results were then manually inspected to check for the presence of false positives (i.e. radio sources incorrectly associated with an optical BCG) or false negatives (i.e. radio emission lying at more than 3θ from the BCG, but with an obvious association to it). We find no incorrect BCG-radio association, while two clusters were initially mistakenly classified as non-detections. To limit contamination, we applied the same cut $f_{{\rm cont},i} < 0.3$ as discussed in Sec. 4.2. According to Eq. 4.1, this implies that we statistically allowed for 6% contamination. This value, albeit conservative, produces a relatively small impact on our results.

The final catalog contains a total of 227 clusters, with only $\sim$1% (3 out of 230) of objects lost to contamination. This is consistent with our expectations because the cut we applied should result in a cluster catalogue that is $\sim$99% complete (see Klein et al. 2021 and Liu et al. 2021). Out of the parent sample of 542 X-ray clusters, 312 did not match any of LOFAR radio sources. After applying the same contamination criteria, we were left with 248 clusters without detected radio emission, which is a loss of ∼21% of the original sample. These were then treated as radio upper limits assuming a flux limit of 3σ, where σ is the local *rms* noise of the LOFAR mosaic at the position of the cluster. The increase in the number of clusters lost to contamination with respect to detections is easy to explain when we consider that excluded objects are not real clusters, but mostly contaminants (e.g. bright AGN). This makes finding a radio counterpart less likely. Again, we refer to Klein et al. (2021) and Liu et al. (2021) for further details.

Nevertheless, not every cluster or group hosts radio galaxies in reality. Some groups only contain a few (< 10) galaxies, and only ∼1% of all observed galaxies are active (Padovani et al., 2017). This fraction should also be significantly higher in overdense environments such as clusters. Sabater et al. (2019) found that 100% of their sample of AGN in massive galaxies ($> 10^{11}$ $M_\odot$) are always switched on above a 144 MHz luminosity of 10^{21} W Hz^{-1}. A strong link between radio AGN activity and the host galaxy mass is observed (Best et al., 2005a; Sabater et al., 2013). As already discussed in Sec. 4.1, Kolokythas et al. (2018, 2019) reported rates at 235 MHz of 92% and 82% for their sample of 26 and 27 galaxy groups, respectively. P20 reported a detection rate for COSMOS groups of ∼70%, with $rms \sim 12\mu$Jy beam^{-1}. Here, the same fraction is only 48% (given the cut we applied for contamination). This is likely due to the lower signal-to-noise ratio (S/N) of LOFAR eFEDS with respect to the single-target observations that were used to build CLoGS, while P20 exploited the VLA-COSMOS Deep Survey. Furthermore, CLoGS was built with low-redshift ($z < 0.02$) groups, while our sample reaches $z \sim 1.3$.

The luminosity of all the radio sources, including upper limits, was estimated as

$$L_{144\mathrm{MHz}} = S_{144} 4\pi D_{\mathrm{L}}^2 (1+z)^{\alpha-1}, \tag{4.2}$$

where S_{144} is the flux density at 144 MHz, D_L is the luminosity distance at redshift z , and α is the spectral index $S_\nu \propto \nu^{-\alpha}$, assumed to be ~ 0.8 for all radio galaxies because our study is conducted at low frequency and most sources show a relatively extended morphology, rather than being compact and point-like, as is usually observed at higher frequency.

The left panel of Fig. 4.3 presents the redshift distribution for the sample, classified into detections and radio upper limits. The detection and non-detection distributions look similar up to $z \sim 0.9$. The highest-z detection is at $z \sim 1.1$, while there is one radio upper limit at $z \sim 1.3$. The right panel shows $L_{X,500\mathrm{kpc}}$ versus redshift with the same classification, with $L_{X,500\mathrm{kpc}}$ being the 0.5-2.0 keV luminosity measured within a 500 kpc radius. The flux sensitivity is $F_X = 1.5 \times 10^{-14}$ erg s^{-1} cm^{-2}. Further details on the eROSITA selection function and completeness can be found in Liu et al. (2021).

4.3 Analysis and discussion

X-ray and radio luminosity distributions

In Fig. 4.4 we show the X-ray and radio luminosity distributions. The X-ray distribution, in the left panel, spans the range from $L_{X,500\mathrm{kpc}} \sim 10^{41}$ erg s^{-1} to 4×10^{44} erg s^{-1} for objects

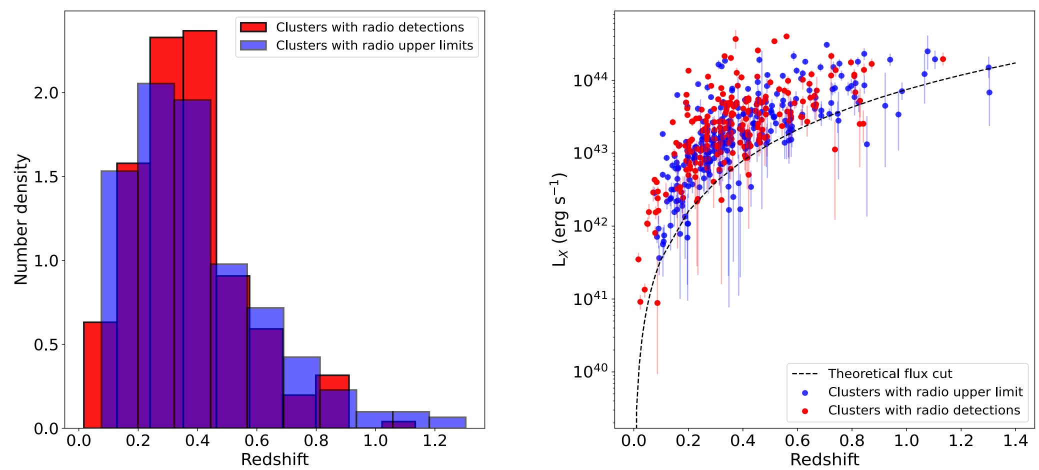

Figure 4.3: *Left*: Histogram showing the redshift distribution of the sample, classified into radio detections (red) and upper limits (blue). *Right*: $L_{X,500}$ vs. redshift for the sample. The dashed line denotes the theoretical flux cut of the eROSITA observation.

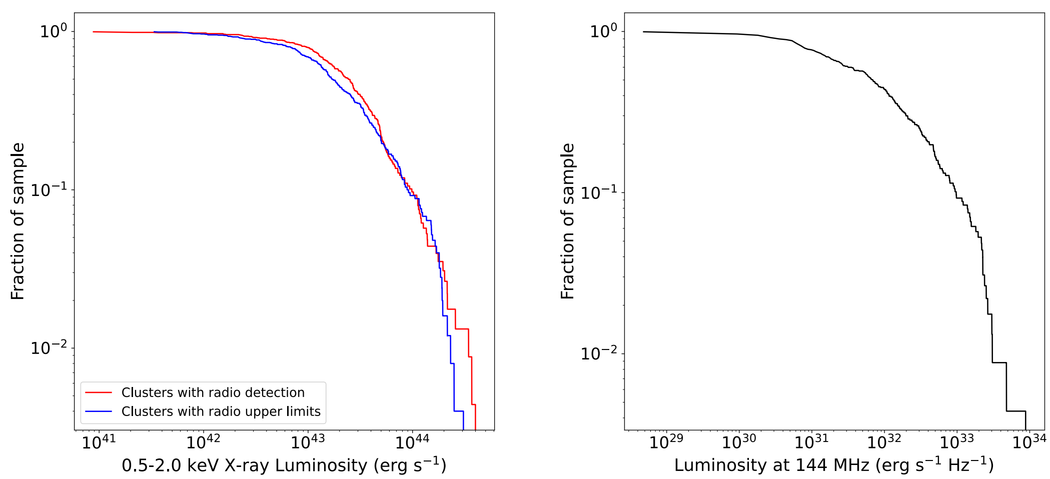

Figure 4.4: *Left*: X-ray luminosity distribution for the parent sample of clusters and groups divided into objects with (red) and without (blue) radio detection. *Right*: Radio luminosity distribution for clusters and groups with radio detection.

with radio detections, while the range for clusters with upper limits is slightly narrower, reaching 3×10^{44} erg s^{-1}. Due to the high sensitivity of eROSITA, we are able to reach lower luminosities than the existing X-ray samples of clusters and groups. The BCS sample, compiled with *ROSAT* (Ebeling et al., 1997b), reaches $L_X \sim 10^{42}$ erg s^{-1}, similarly to the REFLEX II catalogue (Böhringer et al., 2014). On the other hand, our upper range is lower than both the BCS and the REFLEX II, which extend well beyond $L_X \sim 10^{45}$ erg

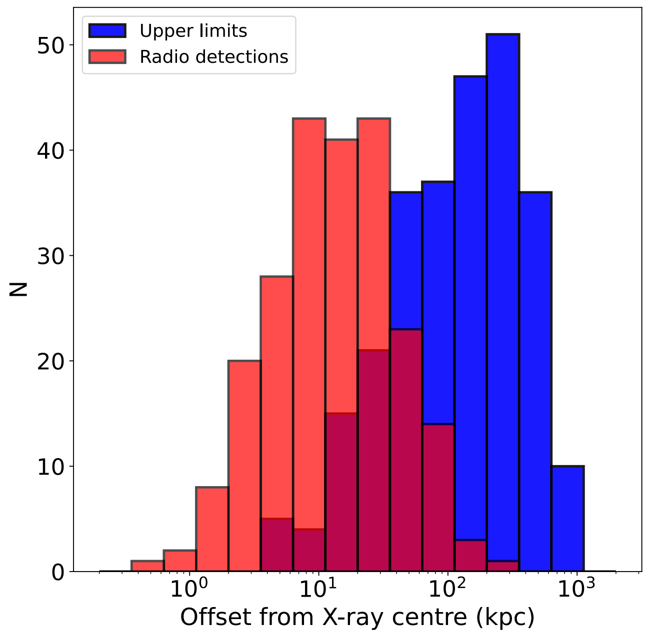

Figure 4.5: Histogram showing BCG offsets from the X-ray emission peak, assumed as the centre of the cluster or group, for galaxies with AGN radio emission (red) and for those with radio upper limits (blue).

s^{-1}, because our sample comes from a relatively small field in the sky. The forthcoming eROSITA all-sky survey (eRASS, Bulbul et al. in prep.) will observe a large number of clusters and groups, allowing us to extend our analysis to higher luminosities.

The radio luminosity distribution at 144 MHz, in the right panel, ranges from $L_{144\mathrm{MHz}} \sim 10^{29}$ erg s^{-1} Hz^{-1} to $\sim 10^{34}$ erg s^{-1} Hz^{-1}. Given the assumption on the spectral index made above, the upper range of luminosities at 144 MHz corresponds to $L_{1.4\mathrm{GHz}} \sim 1.6 \times 10^{33}$ erg s^{-1} Hz^{-1}. This is lower than other samples that have recently been studied at this frequency. The catalogue of 1.4 GHz radio sources in galaxy groups analysed in P20 reaches $L_{1.4\mathrm{GHz}} \sim 10^{34}$ erg s^{-1} Hz^{-1}, similarly to the sample of BCG radio galaxies by Hogan et al. (2015). Finally, we note that the sample studied at 235 MHz by Kolokythas et al. (2018, 2019) ranges from $L_{235\mathrm{MHz}} \sim 10^{27}$ to 10^{32} erg s^{-1} Hz^{-1}. Converting from 144 MHz luminosity, eFEDS radio galaxies span from $L_{235\mathrm{MHz}} \sim 6.8 \times 10^{28}$ to 6.7×10^{33} erg s^{-1} Hz^{-1}. Therefore our sample extends to higher radio powers, but does not reach as deeply as CLoGS. Nevertheless, it consists of 227 clusters and groups, compared to the 53 groups that belong to CLoGS.

BCG offsets

Fig. 4.5 shows the histogram of the BCG offset from the centre of the host cluster or group. The centre was estimated by fitting a two-dimensional β-model (Cavaliere and Fusco-Femiano, 1976b) to the X-ray emission. Most BCGs with detected AGN radio emission lie

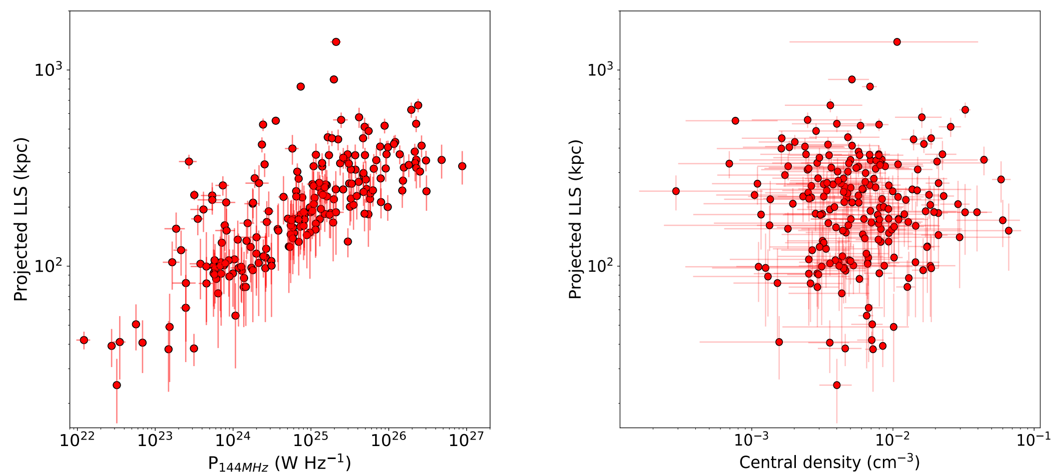

Figure 4.6: *Top*: Projected LLS vs. radio power of eFEDS radio galaxies. *Bottom*: Projected LLS of the radio galaxy vs. ICM central density.

within $\sim$50 kpc from the cluster centre ($\sim$84%). For these clusters, the median value of the offset distribution is $\sim$15 kpc, with dispersion $\sim$30 kpc. At larger offsets, it is easier to find BCGs that do not host a radio galaxy. For clusters with no radio detection, the median is $\sim$130 kpc with a dispersion of $\sim$190 kpc.

Small offsets (<50 kpc) are expected and found in most relaxed clusters because even a minor merger can induce sloshing and displace the X-ray emission peak from the BCG (e.g. Hamer et al., 2016; Pasini et al., 2019; Ubertosi et al., 2021; Pasini et al., 2021b). Large offsets (100-1000 kpc) are often an indication of a strongly disturbed cluster environment (Rossetti et al., 2016; De Propris et al., 2021, and references therein). The relation of BCGs, the triggering of the AGN, and the offset from the cluster centre has been widely discussed and was recently studied in Pasini et al. (2021a). In that paper, the authors found that it is more common for more central BCGs to show radio-loud AGN because in these galaxies the accretion onto the central BH is boosted by the strong cooling in the cluster core. Similar results have also been discussed in Burns (1990), Best et al. (2007), Cavagnolo et al. (2008) and Shen et al. (2017). On the other hand, off-centre galaxies have to rely on more episodic processes, such as cluster and group mergers and/or galaxy interactions. We find the same results in this sample because, as discussed above, radio-loud AGNs are mostly found at an offset <50 kpc.

Extent of BCG radio galaxies

Radio galaxies exhibit a plethora of different shapes and sizes. The reasons for the unusual size of some giant radio galaxies (e.g. Brüggen et al., 2021; Dabhade et al., 2020) and for the significantly smaller extent of some others (e.g. FR0, Baldi et al. 2015) have been investigated previously. Hardcastle et al. (2019) presented the currently largest sample of radio galaxies in which the relation between the radio power and the linear size was

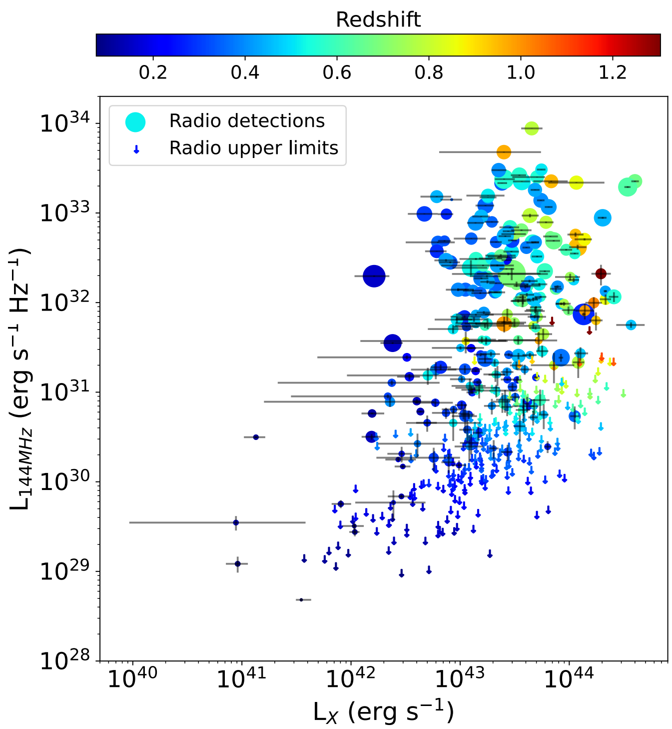

Figure 4.7: 144 MHz power of radio galaxies vs. X-ray luminosity of the host cluster. Symbol sizes are proportional to the LLS of the source, and their colour indicates the redshift. Downward-pointing arrows denote radio upper limits. Bars represent errors on both axes.

investigated. The location of a source in this diagram is indicative of its initial conditions and current evolutionary state (Hardcastle, 2018). Kolokythas et al. (2018) found a clear link between the 235 MHz power and the projected largest linear size (LLS) of their resolved radio galaxies. The same relation was already found for cluster and field radio galaxies by Ledlow et al. (2002) and is investigated for our sample of BCGs at 144 MHz (top panel of Fig. 4.6). The LLS of radio galaxies was manually measured from the LOFAR eFEDS mosaic, assuming an error equal to the synthesised beam. To exclude unresolved sources, only those with a largest angular size LAS $> 2\times$beam were taken into account.

Most sources show an LLS between 100 and 300 kpc, with the mean at LLS$\sim$235 kpc and standard deviation $\sim$ 160 kpc. Large sources mostly show a classical double-lobed morphology, while the smallest ones are point-like. As previously observed, there is a positive correlation between LLS and luminosity, with larger radio galaxies being more powerful. The relation holds even at relatively high luminosities[5]. Nevertheless, we note that we are likely missing large, low-power radio sources because of surface brightness limitations. This issue has been extensively addressed in Hardcastle et al. (2019) based on a significantly larger sample (23344 objects) of radio galaxies.

Multiple environmental factors are likely to contribute to the size of the radio source. The most important factor is the age, which necessarily introduces scatter into any relation

[5] CLoGS only reaches $L_R \sim 10^{25}$ W Hz^{-1} at 235 MHz.

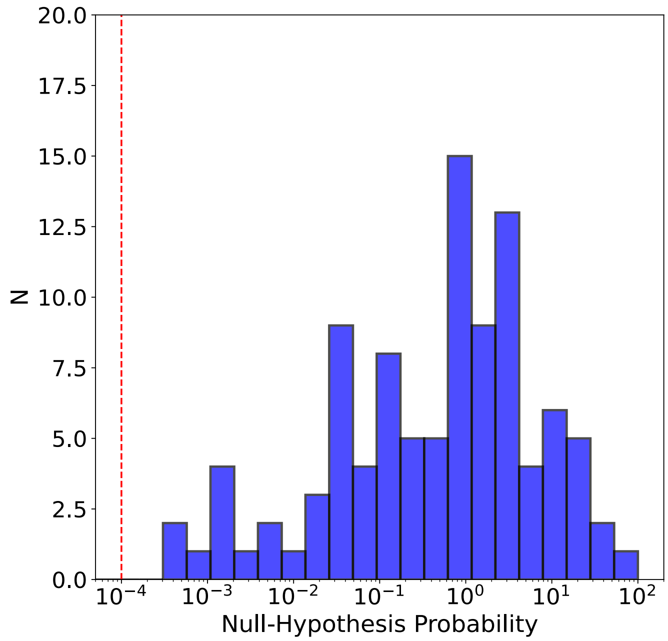

Figure 4.8: Null-hypothesis probability distribution that the correlation is not real for 100 mock datasets produced by the scrambling test. The dashed red line indicates the probability of the real sample.

with other physical quantities. Other factors include the location of the galaxy within the host cluster, the density of the ICM at the position of the galaxy, the efficiency of the accretion onto the AGN, and the radio power of the outburst (see e.g. Moravec et al., 2020, and references therein).

To this end, in the bottom panel of Fig. 4.6 we show the LLS of the radio galaxy plotted against the central density (at $R = 0.02R_{500}$) of the host cluster, obtained by fitting the cluster model by Vikhlinin et al. (2006) to density profiles (see G21 for further details). We see no correlation of the LLS with the central density, suggesting that radio power is more prominent than ambient density in determining the size of the radio galaxy and that the contribution of other factors could affect a possible link.

Correlation between X-ray and 144 MHz radio luminosity

In P20, we have studied the correlation between the 1.4 GHz power of radio galaxies and the X-ray luminosity of the host group for 247 galaxy groups in COSMOS. A similar correlation between the mass of galaxy clusters, known to correlate with the X-ray luminosity (e.g. Lovisari et al., 2020), and the radio power of BCGs has been found by Hogan et al. (2015). Here, we focus on the same relation, but at the lower radio frequency of 144 MHz.

Fig. 4.7 shows the 144 MHz power of the radio galaxy plotted against the X-ray luminosity of the host group or cluster. The size of the symbols is proportional to the LLS of the radio sources, and the colour corresponds to the redshift. Upper limits are represented by downward-pointing arrows. There is a clear trend for stronger radio galaxies to be hosted in more X-ray luminous clusters, as found by P20. However, the significant number of radio upper limits makes it harder to determine whether the observed correlation is real or produced by selection effects set by the sensitivity of the observation.

To ascertain if the correlation is genuinely detected, we performed the partial correlation Kendall's τ (Akritas and Siebert, 1996) test. This tool has already been used in a number of papers (e.g. Ineson et al., 2015; Pasini et al., 2020) to test correlations in the presence of upper limits and redshift dependence. The algorithm estimates the null-hypothesis probability that selection effects produce the correlation. If the probability is low, then it is likely that the correlation is real. The test performed on our sample gives a null-hypothesis probability $p < 0.0001\%$ ($\tau = 0.1178$, $\sigma = 0.0227$), indicating that the correlation is real and not generated by selection effects. This result is consistent with P20, who also found that such a correlation, but at higher frequency, was not produced by biases.

Bianchi et al. (2009) argued that the Kendall τ test may underestimate the redshift contribution, particularly when the significance and the functional relation are to be determined. For this reason, they performed a 'scrambling' test that has also been used in other works (e.g. Merloni et al., 2006). The principle of this algorithm is to keep each L_X/z pair because their association comes from the source selection. Then they shuffled the corresponding radio fluxes, assigning them to a new L_X/z pair. The new radio luminosity is then computed at the new redshift (see Eq. 4.2). If the correlation is real, it is expected to disappear when the luminosity pairs are shuffled. We applied this test 100 times and estimated for each cycle the null-hypothesis probability through the Kendall τ test. The results are shown in Fig. 4.8. In 100 cycles, the null-hypothesis probability is never found to be lower than the real sample. The mean probability value lies at $\sim$4%, with a standard deviation of $\sim$9%, while the peak lies between 0.7% and 5%. This result supports the hypothesis that the observed correlation is real.

X-ray/radio correlation at 1.4 GHz

We compared our 144 MHz sample in eFEDS with a subsample of 137 systems from the 247 COSMOS galaxy groups studied at 1.4 GHz in P20. A further cross-match of our sample with all-sky surveys at this frequency (e.g. NVSS, Condon et al. 1998) is not trivial because of the significant differences in surface brightness sensitivity and resolution. For this reason, the 144 MHz luminosities were converted into luminosities at a frequency of 1.4 GHz assuming $\alpha = 0.8 \pm 0.2$. The assumed uncertainty on the spectral index dominates the previous 144 MHz flux error. Combining the two catalogues, we obtain 364 galaxy clusters and groups that allow us to assess the radio/X-ray correlation using a larger sample. The corresponding $\log L_R$ - $\log L_X$ plot is shown in Fig. 4.9.

The distributions of COSMOS and eFEDS clusters and groups agree well. This is confirmed by the two-dimensional Kolmogorov-Smirnov test, which gives $p = 0.41$ under the null-hypothesis that the two samples are drawn from the same parent distribution. This implies that our assumption of a uniform spectral index of $\alpha = 0.8$ for every radio galaxy is valid, although it introduces more scatter in the correlation. Still, a clear trend for more massive groups and clusters hosting more powerful radio sources is seen. This is also

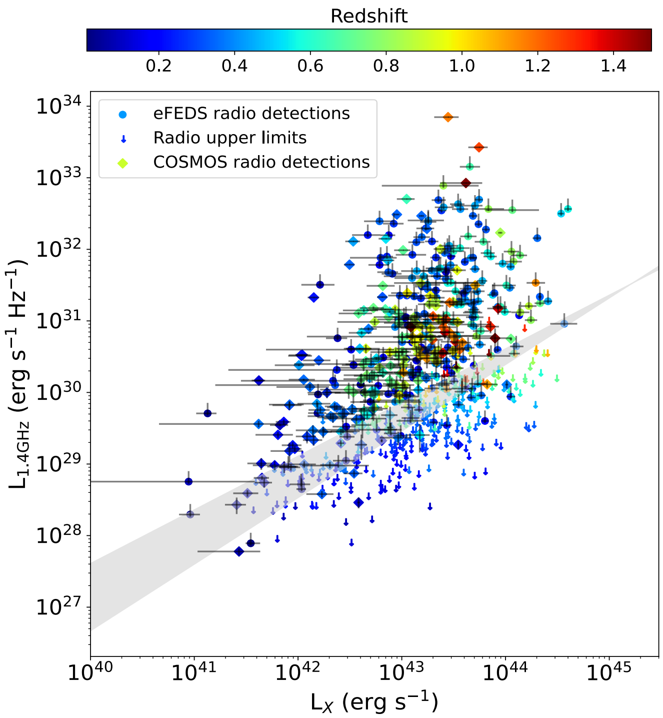

Figure 4.9: 1.4 GHz power of radio galaxies vs. X-ray luminosity of the host cluster for the eFEDS and P20 samples. The colours correspond to the redshift. eFEDS data are represented by circles, while diamonds are COSMOS systems. Downward-pointing arrows denote radio upper limits. Bars represent errors on both axes. Errors on the y-axis are dominated by the assumed uncertainty on the spectral index. The best-fit relation is shown in grey: $\log L_R = (0.84 \pm 0.09)\, \log L_X - (6.46 \pm 4.07)$.

supported by the Kendall τ test, which results in $p < 0.0001$ ($\tau = 0.1331$, $\sigma = 0.0138$) for eFEDS+COSMOS. The best-fit relation was estimated by exploiting the parametric EM algorithm coded in the AStronomical SURVival statistics package (ASURV, Feigelson et al. 2014), which takes into account different contributions by detections and upper limits. We find $\log L_R = (0.84 \pm 0.09)\, \log L_X - (6.46 \pm 4.07)$. This estimate is marginally consistent with the best-fit relations of P20 ($\log L_R = (1.07 \pm 0.12) \times \log L_X - (15.90 \pm 5.13)$ and Pasini et al. (2021a) ($\log L_R = (0.94 \pm 0.43) \times \log L_X - (9.53 \pm 18.19)$), obtained through the same method and applying Bayesian inference, respectively.

The correlation may imply a link between radiative cooling from the ICM and the more variable and episodic activity of the AGN. Because the X-ray luminosity is predominantly driven by the cluster or group mass, this correlation may be produced by massive clusters hosting more massive BCGs and in turn more massive BHs. In relaxed clusters, the cooling of the ICM is able to efficiently feed the central AGN, leading to higher radio powers (Soker and Pizzolato, 2005; Gaspari et al., 2011). This is reflected in the well-studied link between the cavity power of systems hosting X-ray bubbles and the luminosity of the cluster cooling region (e.g. Bîrzan et al., 2004; Rafferty et al., 2006; Bîrzan et al., 2017). Sun (2009) also argued that small coronae of X-ray emitting gas in BCGs are able to trigger strong radio

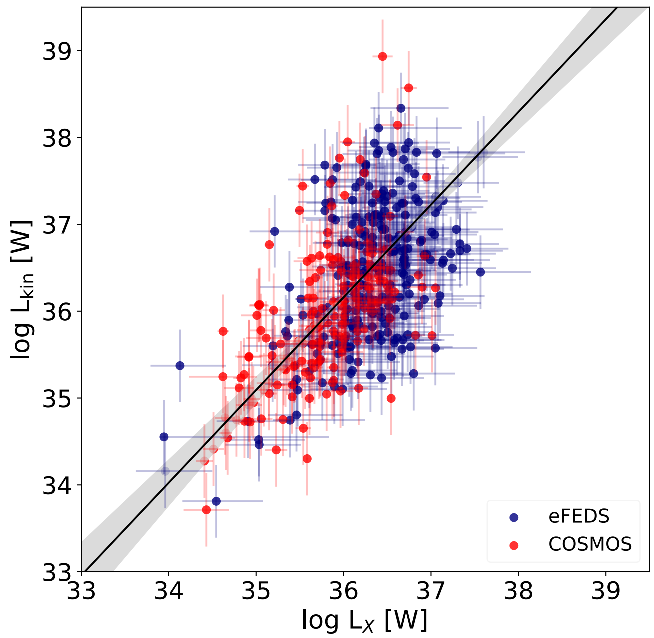

Figure 4.10: Kinetic luminosity of BCG radio galaxies estimated at 1.4 GHz vs. X-ray luminosity of the host cluster or group for the eFEDS (blue) and P20 (red) samples. The black line represents the best-fit estimated from Bayesian inference: $\log L_{\rm kin} = (1.07 \pm 0.11)\,\log L_X - (2.19 \pm 4.05)$. The grey area indicates 1σ errors.

outbursts long before cool cores are formed in the host cluster, leading to heating in their surroundings and even preventing their formation, especially in low-mass systems. The correlation presented here shows a large scatter, especially at high luminosities. This might for instance be caused by differences in the dynamical states, which we explore in the next section.

Kinetic luminosity and AGN feedback

The radio luminosity is a measure of the instantaneous radiative loss rate of the radio lobes, and as such is only indirectly related to the energy produced by the AGN through accretion onto the SMBH. For an active source, only a small fraction of the total power supplied to the lobes has been radiated away at any given time, while a much larger fraction is stored in the lobes and a similar amount has been dissipated into the surrounding ICM during the expansion of the jets through the ICM (Willott et al., 1999; Smolčić et al., 2017). The latter, which we refer to as kinetic luminosity, is directly linked to the heating of the ICM and contributes to quenching the radiative losses of the hot plasma (see Sec. 4.1 for references).

The relation of the kinetic and radio luminosity has been the subject of many works (e.g. Willott et al., 1999; Bîrzan et al., 2004; Bîrzan et al., 2008; Cavagnolo et al., 2010; O'Sullivan et al., 2011c; Smolčić et al., 2017). As thoroughly discussed in Hardcastle et al. (2019), there are currently two methods to infer the kinetic luminosity. The first relies on the

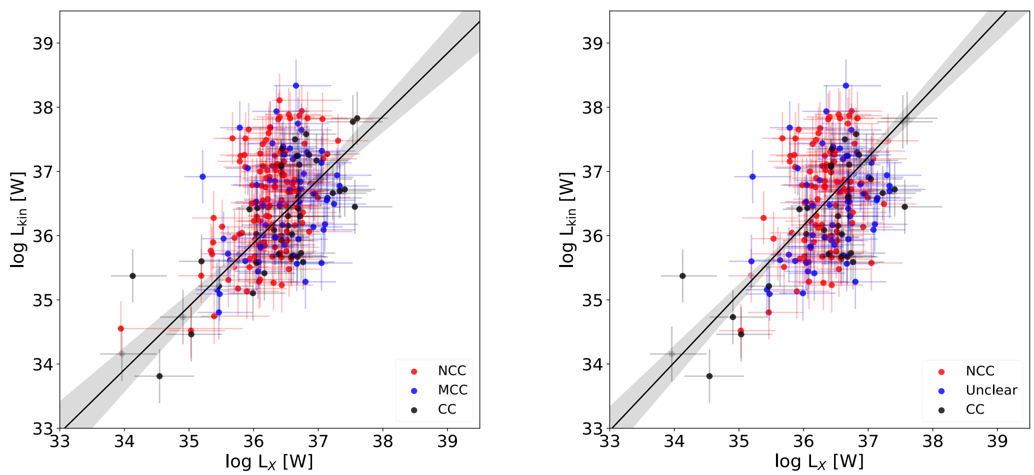

Figure 4.11: *Left*: Kinetic luminosity of BCG radio galaxies estimated at 1.4 GHz vs. X-ray luminosity of the host cluster or group for the eFEDS sample. Data are classified into non-cool cores (red), moderately cool cores (blue), and cool cores (black) based on the concentration parameter. *Right*: Same as in the left panel, with data classified based on the $R_{\rm score}$ (see discussion).

identification of X-ray cavities and is affected by assumptions on the cavity age and biased towards small sources in cluster-rich environments (Bîrzan et al., 2012). The second method relies on a conversion based on a theoretical model and, as such, can lead to unrealistic results if the contribution of source age, environment, and redshift to the radio luminosity are not taken into account properly. We refer to Hardcastle et al. (2019) and Appendix A of Smolčić et al. (2017) for a detailed discussion of this scaling relation. Here, we assume the relation adopted by Willott et al. (1999) to convert into the 1.4 GHz rest-frame luminosity (Heckman and Best, 2014),

$$\log L_{\rm kin,1.4GHz} = 0.86 \log L_{\rm 1.4GHz} + 14.08 + 1.5 \log f_W, \tag{4.3}$$

where $L_{\rm kin,1.4GHz}$ is the kinetic luminosity, $L_{\rm 1.4GHz}$ is the luminosity as measured at 1.4 GHz, and f_W is an uncertainty parameter that we assumed, $f_W = 15$, as estimated by X-ray observations of ICM bubbles in galaxy clusters (e.g. Merloni and Heinz, 2007; Bîrzan et al., 2008). We determined the kinetic luminosity for the radio galaxies of the eFEDS and the P20 sample, and we compared it to the X-ray luminosity within 500 kpc of the host cluster. The result is shown in Fig. 4.10.

In order to infer the relation of the X-ray and the kinetic luminosity, we applied Bayesian inference on the two samples using the `linmix`[6] package (Kelly, 2007). With this tool, we performed a linear fit in the log-log scale of the form

$$Y = \alpha + \beta X + \varepsilon, \tag{4.4}$$

[6] https://github.com/jmeyers314/linmix

with α and β representing the intercept and the slope, respectively, while ε is the intrinsic scatter of the relation. We find $\alpha = -2.19 \pm 4.05$, $\beta = 1.07 \pm 0.11$ and $\varepsilon = 0.25 \pm 0.05$. We note that the conversion from radio into kinetic luminosity, which also depends on external factors such as the morphology and age of the radio source, the extrapolation of 1.4 GHz fluxes, or the surrounding environment, and which relies on theoretical models, may have introduced artificial scatter into the correlation.

Nevertheless, the plot suggests that in most clusters and groups, the heating from the central AGN efficiently counterbalances the ICM radiative losses, as has been found in a large number of publications (see the references above and McNamara and Nulsen 2007, 2012 for reviews). However, most of these papers take the luminosity from within the cooling region into account, which is usually defined as the cluster region within which the cooling time of the ICM is shorter than 7.7 Gyr. These usually range between $\sim$50 and $\sim$150 kpc (Bîrzan et al., 2017), and their extent can only be estimated through a deprojected analysis of the thermodynamical profiles (i.e. temperature, density, and cooling time) derived from X-ray observations. The detection of cavities as an indication for AGN heating (McNamara et al., 2000; Bîrzan et al., 2004) usually requires deep, high-resolution X-ray observations as well.

The kinetic luminosity–X-ray luminosity relation, estimated through survey data but with the unprecedented sensitivity of eROSITA is able to provide a first insight into the processes of AGN feedback of a large number of clusters and groups. Kinetic and X-ray luminosity act as proxy for mechanical feedback and cooling luminosity, respectively, which together constitute the 'parent' correlation usually found in cool core clusters. Nevertheless, we performed the analysis on all our objects and did not distinguish between cool cores and merging clusters. Main et al. (2017) found that in their sample of clusters, this correlation only holds for cool cores. Their classification was based on the central cooling time, determined through *Chandra* observations at $0.004R_{500}$ by Hudson et al. (2010). The eROSITA observations do not yield cooling times at such small cluster-centric radii, and we are not able to reproduce the same classification for our objects. Instead, we quantified the dynamical state of clusters through the concentration parameter as defined in Lovisari et al. (2017) and estimated for eFEDS clusters in G21 as

$$c_{\mathrm{SB}} = \frac{S_B(< 0.1R_{500})}{S_B(< R_{500})}, \tag{4.5}$$

where S_B is the surface brightness estimated inside $0.1R_{500}$ for the numerator and inside R_{500} for the denominator. This parameter is an indicator of a centrally peaked X-ray surface brightness profile, which correlates with the dynamical state of the cluster. Lovisari et al. (2017) discussed the use of different thresholds to classify clusters into cool cores and disturbed systems, showing how completeness (i.e. being able to select all clusters belonging to a given class) and purity (i.e. being able to securely assign clusters to a given class) change depending on the chosen threshold. Here, following the work cited above, we chose to define as non-cool cores (NCC) clusters with $c_{\mathrm{SB}} < 0.15$, while cool cores (CC) have $c_{\mathrm{SB}} > 0.27$. This classification allows for 100% purity for both subsamples, but the completeness decreases to $\sim$53% for CC and $\sim$75% for NCC (see Lovisari et al.

2017 for more details). Clusters with $0.15 < c_{\rm SB} < 0.27$ cannot be securely categorised and are arbitrarily referred to as moderately cool cores (MCC). In the left panel of Fig. 4.11 we show the $L_{\rm kin}$–L_X plot for the eFEDS cluster sample, in which clusters were classified through the concentration parameter. We find that $\sim$53% of clusters are NCC, $\sim$28% are MCC, and $\sim$19% are CC. We see no obvious difference in the distribution between the three subsamples. Therefore the dynamical state of the cluster does not seem to have a large effect on the scatter in the X-ray/radio relation.

As discussed in more detail in G21, the concentration acts as an indicator of a cool core. However, while a relaxed cluster will generally present a cool core, a cool core is not always an indication of relaxation: a merger in its initial stage predominantly affects the cluster outskirts and does not disrupt the cool core (see e.g. theoretical work by Rasia et al. 2015 and Biffi et al. 2016). This means that classifying the dynamical state of clusters based on concentration alone is useful to distinguish disturbed objects with low concentration, but does not provide a clear identification of relaxed clusters (see Fig. 9 of G21 and related discussion). For this reason, we performed an alternative classification based on a new morphological parameter first introduced in the same paper, the so-called relaxation score ($R_{\rm score}$). Because a complete, physical definition of this parameter requires detailed discussion of a number of parameters (see below), we refer to G21 for more insights, and provide a brief description here. The $R_{\rm score}$ combines a number of morphological parameters that are usually determined for galaxy clusters, such as concentration, central density, ellipticity (ratio of the minor and major axes of the cluster), and cuspiness (slope of the density profile at a given radius). The resulting $R_{\rm score}$ provides a clearer indication than concentration alone of the dynamical state of a cluster. In particular, the $R_{\rm score}$ should be higher for relaxed objects, which show a high concentration, central density, ellipticity, and cuspiness. On the other hand, the same parameter should decrease in disturbed clusters.

Following the discussion in G21, we defined as relaxed objects with $R_{\rm score} > 0.0137$. The results of this alternative classification are shown in the right panel of Fig. 4.11. We only plot clusters for which a proper estimate of the $R_{\rm score}$ was feasible in G21. Objects classified as relaxed through the $R_{\rm score}$ and as CC through the concentration are generally referred to as CC, those with low $R_{\rm score}$ and concentration are NCC, and clusters with a high concentration (same threshold as used for left panel) but $R_{\rm score} < 0.0137$ are labelled unclear. We refer to G21 for a discussion and comparisons of the different classifications and focus on the correlation here.

Even when a more accurate parameter such as the $R_{\rm score}$ is introduced, the distinction in the distribution between cool cores and merging objects is still unclear, as was instead found in Main et al. (2017), for instance. Furthermore, it is not clear how this relation can be present in disturbed systems. In these objects, the cooling of the ICM is slow and BCGs are often hard to identify. Morphological parameters have been widely used to determine the dynamical state of clusters, but a more secure classification based on the central cooling time may be more useful for understanding in which clusters a connection of AGN and cooling ICM can ensue. A possibility is that the link between AGN and their environment could be produced, even in disturbed objects, by rapidly cooling coronae permeating the host galaxy (Sun et al., 2007; Gastaldello et al., 2008; Sun, 2009). This idea has been suggested for NCC hosting radio AGN, such as A2028 (Gastaldello et al., 2010). It is also plausible that small, low-entropy regions of the cluster core such as cool core remnants (Rossetti and Molendi, 2010) could affect the AGN, leading to the observed relation. Another possibility is that NCC do not in fact belong to the correlation. To test this, we studied the scatter of the correlation after applying Bayesian inference only on CC. If NCC are not part of the correlation, the scatter of the data should decrease when CC are fitted alone. We find $\varepsilon = 0.17 \pm 0.10$, consistent within errors with the previous estimate. Nevertheless, the uncertainty increases because of the relatively small number of CC, and further analyses exploiting larger samples are needed to investigate this further.

4.4 Conclusions

We usedf eROSITA (X-ray) and LOFAR (radio) observations of the eFEDS field in order to investigate radio galaxies hosted in BCGs. Our results are summarised below.

- Our sample yields 227 detections and 248 upper limits in the redshift range $0.01 < z < 1.3$ and luminosity range 10^{22} – 10^{27} W Hz^{-1} at 144 MHz. The remaining 67 clusters were excluded from the analysis to avoid contamination by misclassified AGN (see Sec. 4.2). The radio detection rate is $\sim$48%, which is lower than in other samples of well-studied groups and clusters.
- BCGs hosting radio-loud AGN mostly ($\sim$84%) lie within 50 kpc from the cluster centre. BCGs that are more offset tend to have lower levels of radio emission or lie below our detection threshold.
- As was argued in previous works, larger radio galaxies are usually more powerful. However, we note that a relevant selection effect is present in our sample because we lack large, low-power radio sources because the surface brightness is limited. We see no correlation of the central cluster density ($R = 0.02R_{500}$) with the LLS, suggesting that the luminosity is a better predictor for the size of the radio galaxy.
- We studied the relation of the 144 MHz radio galaxy power and the host cluster X-ray luminosity measured within 500 kpc from the cluster centre and found a positive correlation. Because of the large number of upper limits, we relied on statistical tests, such as the partial correlation Kendall's τ test and the scrambling test, to show that the correlation is not produced by selection effects in the radio band.
- Converting the 144 MHz power of radio galaxies into 1.4 GHz, we compared our results with the correlation between the X-ray luminosity and the 1.4 GHz power of a COSMOS galaxy groups sample first investigated by Pasini et al. (2020). We found that the two samples agree well based on a Kolmogorov-Smirnov test, which under the null-hypothesis that the samples are drawn from the same parent distribution, gives $p = 0.41$. We estimated a best-fit relation $\log L_R = (0.84 \pm 0.09)\log L_X - (6.46 \pm 4.07)$.
- We converted the radio powers of radio galaxies into kinetic luminosities, making use of widely used scaling relations. Comparing the kinetic luminosity to the X-ray luminosity within 500 kpc from the cluster centre, we found that in most objects the

ICM radiative losses are efficiently counterbalanced by heating supplied from the central AGN. We derived the best-fit relation applying Bayesian inference, obtaining $\log L_{\rm kin} = (-2.19 \pm 4.05) + (1.07 \pm 0.11) \log L_X + (0.25 \pm 0.05)$.

- We classified eFEDS clusters into disturbed and relaxed objects based on two different parameters: concentration, and the relaxation score (see Sec. 4.3 for a definition). No significant differences in the $L_{\rm kin} - L_X$ relation of the subsamples were visible.

Future prescriptions of radio-mode AGN feedback in simulations need to be able to recover the properties described in this paper. In addition to massive halo gas fractions, entropy slopes, and galaxy properties, they need to recover radio luminosities as a function of the host cluster properties. With the new all-sky X-ray surveys, a correlation between the cluster X-ray luminosity and the BCG radio power can be used to probe AGN feedback across a wider range of host masses and to control for the effect of other observables. Particularly, the synergy between eRASS (Bulbul et al. in prep.) and the LOFAR Two-Metre Sky Survey (LoTSS, Shimwell et al. 2017), as well as the forthcoming LOFAR LBA Sky Survey (LoLSS, de Gasperin et al. 2021), will provide samples of thousands of clusters and groups for which the interplay between the AGN and the ICM can be investigated.

Acknowledgements. *The authors thank the anonymous referee for useful suggestions that have improved the presentation of the results. TP thanks Philip Best for useful comments. TP is supported by the BMBF Verbundforschung under grant number 50OR1906. MB acknowledges support from the Deutsche Forschungsgemeinschaft under Germany's Excellence Strategy - EXC 2121 "Quantum Universe" - 390833306. DNH acknowledges support from the ERC through the grant ERC-Stg DRANOEL n. 714245. AB acknowledges support from the VIDI research programme with project number 639.042.729, which is financed by the Netherlands Organisation for Scientific Research (NWO). FG acknowledges support from INAF mainstream project 'Galaxy Clusters Science with LOFAR' 1.05.01.86.05. RJvW acknowledges support from the ERC Starting Grant ClusterWeb 804208. WLW acknowledges support from the CAS-NWO programme for radio astronomy with project number 629.001.024, which is financed by the Netherlands Organisation for Scientific Research (NWO). This work is based on data from eROSITA, the soft X-rays instrument aboard SRG, a joint Russian-German science mission supported by the Russian Space Agency (Roskosmos), in the interests of the Russian Academy of Sciences represented by its Space Research Institute (IKI), and the Deutsches Zentrum für Luft- und Raumfahrt (DLR). The SRG spacecraft was built by Lavochkin Association (NPOL) and its subcontractors, and is operated by NPOL with support from the Max Planck Institute for Extraterrestrial Physics (MPE). The development and construction of the eROSITA X-ray instrument was led by MPE, with contributions from the Dr. Karl Remeis Observatory Bamberg & ECAP (FAU Erlangen-Nuernberg), the University of Hamburg Observatory, the Leibniz Institute for Astrophysics Potsdam (AIP), and the Institute for Astronomy and Astrophysics of the University of Tübingen, with the support of DLR and the Max Planck Society. The Argelander Institute for Astronomy of the University of Bonn and the Ludwig Maximilians Universität Munich also participated in the science preparation for eROSITA. The eROSITA data shown here were processed using the eSASS/NRTA software system developed by the German eROSITA consortium. LOFAR data products were provided by the LOFAR Surveys Key Science project (LSKSP; https://lofar-surveys.org/) and were derived from observations with the International LOFAR Telescope (ILT). LOFAR (van Haarlem et al. 2013) is the Low Frequency Array designed and constructed by ASTRON. It has observing, data processing, and data storage facilities in several countries, that are owned by various parties (each with their own funding sources), and that are collectively operated by the ILT foundation under a joint scientific policy. The efforts of* *the LSKSP have benefited from funding from the European Research Council, NOVA, NWO, CNRS-INSU, the SURF Co-operative, the UK Science and Technology Funding Council and the Jülich supercomputing centre.*

.1 Examples of interesting systems

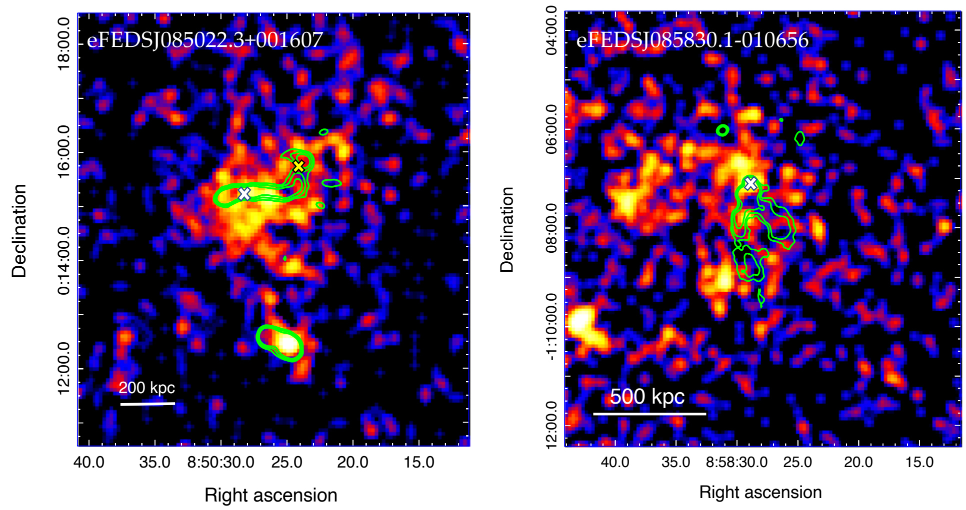

Figure 12: eROSITA 0.2-2.3 keV images of eFEDSJ085022.3+001607 (left panel) and eFEDSJ085830.1-010656 (right panel), smoothed with a 3σ Gaussian filter. LOFAR 144 MHz contours at 3,6,12,24 $\cdot$ *rms* (local) are plotted in green. The white cross represents the cluster X-ray peak, and the yellow cross is the BCG position. For eFEDSJ085830.1-010656, the BCG is coincident with the X-ray peak.

The high flux sensitivity and spatial coverage of eROSITA and LOFAR at their respective frequencies allows for interesting comparisons. In the past, the combination of X-ray and radio observations of galaxy clusters and of their BCGs have led to a significant improvement in the understanding of the thermal and non-thermal processes in these environments (e.g. Gitti et al. 2010; Kolokythas et al. 2018; Botteon et al. 2020b; see Sec. 4.1 for more references and reviews).

We used the eROSITA and LOFAR observations to search for systems showing interesting morphologies and signs of possible interaction between the ICM and the central AGN. In this section, we present four of the most interesting examples of these clusters. We focus on AGN emission, and diffuse emission more directly associated with the ICM and clusters dynamical state will be presented in a forthcoming paper (Hoang et al. in prep.). Table 2 summarises the main properties of these systems.

eFEDSJ085022.3+001607

eFEDSJ085022.3+001607 (left panel of Fig. 12) is located at a redshift of $z = 0.196$ (spectroscopic). The strongly elliptical and irregular morphology of the X-ray emission and low concentration ($c_{\rm SB} = 0.02$) suggest that this cluster is disturbed. The BCG hosts an elongated, head-tail shaped radio galaxy (major axis $\sim$ 500 kpc), with a 144 MHz luminosity of $L_R = (4.1 \pm 0.2) \times 10^{24}$ W Hz^{-1}. The AGN lies at $\sim$ 150 kpc from the X-ray

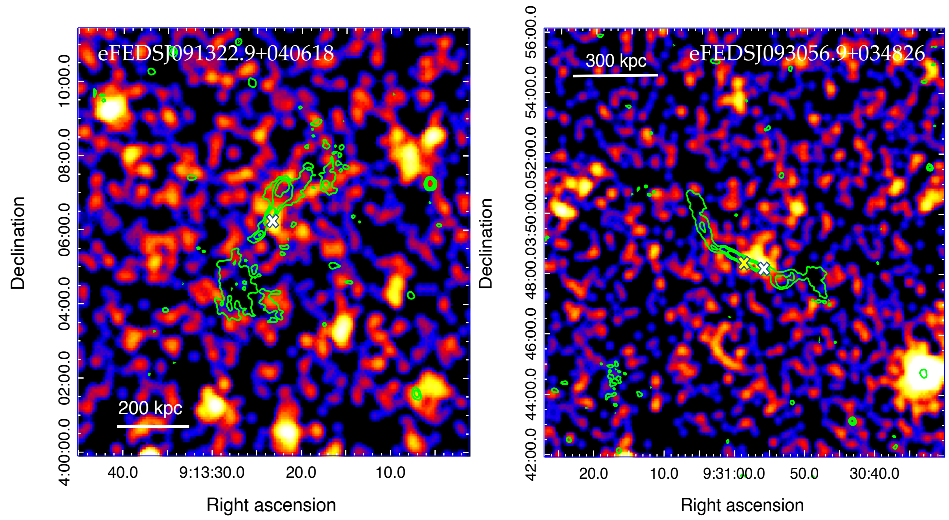

Figure 13: eROSITA 0.2-2.3 keV images of eFEDSJ091322.9+040618 (left panel) and eFEDSJ093056.f9+034826 (right panel), smoothed with a 3σ Gaussian filter. LOFAR 144 MHz contours at 3,6,12,24 $\cdot$ *rms* (local) are plotted in green. The white cross represents the cluster X-ray peak. For eFEDSJ091322.9+040618, the BCG is coincident with the X-ray peak.

peak. Surface brightness discontinuities that coincide with the lobes of the radio galaxy are detected in the X-ray image. However, the relatively low resolution does not reveal any ICM cavities, which have never been detected around head-tails, however. The shape of the non-thermal emission follows that of the hot plasma, with the jet extending towards the east through the X-ray ripple. Meanwhile, the expansion in the opposite direction appears to be halted.

eFEDSJ085830.1-010656

The irregular morphology and low concentration ($c_{\rm SB} = 0.13$) of eFEDSJ085830.1-010656 (right panel of Fig. 12) leads us to classify it as a non-cool core. The BCG hosts a wide-angle tail radio galaxy with two tails departing in the S and SW directions for ~ 250 kpc each. The tails are expanding into a lower-density region within the group. Deeper X-ray observations are needed to study the ICM emission of this group because of its low surface brightness and relatively high redshift.

eFEDSJ091322.9+040618

eFEDSJ091322.9+040618 (left panel of Fig. 13) is a low-redshift ($z = 0.088$, spectroscopic) galaxy group classified as a disturbed cluster due to its irregular shape and low concentration ($c_{\rm SB} = 0.04$). The radio galaxy extends for more than 200 kpc along the NW-SE axis. The lobes are expanding into the SE and NW directions following the hot plasma. Diffuse emission with unclear origin is detected in the SE direction, correspondingly to a low surface brightness region, extending for ~ 150 kpc.

Table 2: X-ray observables and BCG radio power for four relevant eFEDS clusters

Name	z	kT^a [keV]	$L^a_{\rm bol}$ [10^{43} erg s^{-1}]	$c_{\rm SB}$	L^b_R [10^{24} W Hz^{-1}]
eFEDSJ085022.3+001607	0.196	$3.1\pm^{1.1}_{0.7}$	$2.7\pm^{1.3}_{0.9}$	0.02	4.1 ± 0.2
eFEDSJ085830.1-010656	0.224	$2.1\pm^{1.7}_{0.8}$	$2.1\pm^{0.5}_{0.4}$	0.13	25.0 ± 1.0
eFEDSJ091322.9+040618	0.088	$0.45\pm^{0.29}_{0.17}$	$4.1\pm^{1.2}_{0.9}$	0.04	0.74 ± 0.05
eFEDSJ093056.9+034826	0.09	$0.61\pm^{0.75}_{0.27}$	$2.7\pm^{1.2}_{0.9}$	0.21	0.77 ± 0.02

Notes: ^{a}: estimated within 500 kpc. ^{b}: 144 MHz luminosity of the BCG.

eFEDSJ093056.9+034826

eFEDSJ093056.9+034826 (right panel of Fig. 13) is a galaxy group located at $z = 0.09$ (photometric). The elliptical shape and relatively high concentration ($c_{\rm SB} = 0.21$) classify it as a moderately cool core. The BCG hosts a double-lobe elongated radio galaxy with a major axis of $\sim$ 600 kpc and $L_R = (7.7\pm0.2)\times10^{23}$ W Hz^{-1}. The long lobes ($\sim$ 300 kpc) of the central radio galaxy extend far beyond the X-ray bright core of the group. The low X-ray flux of this group makes it difficult to identify depressions in the surface brightness.

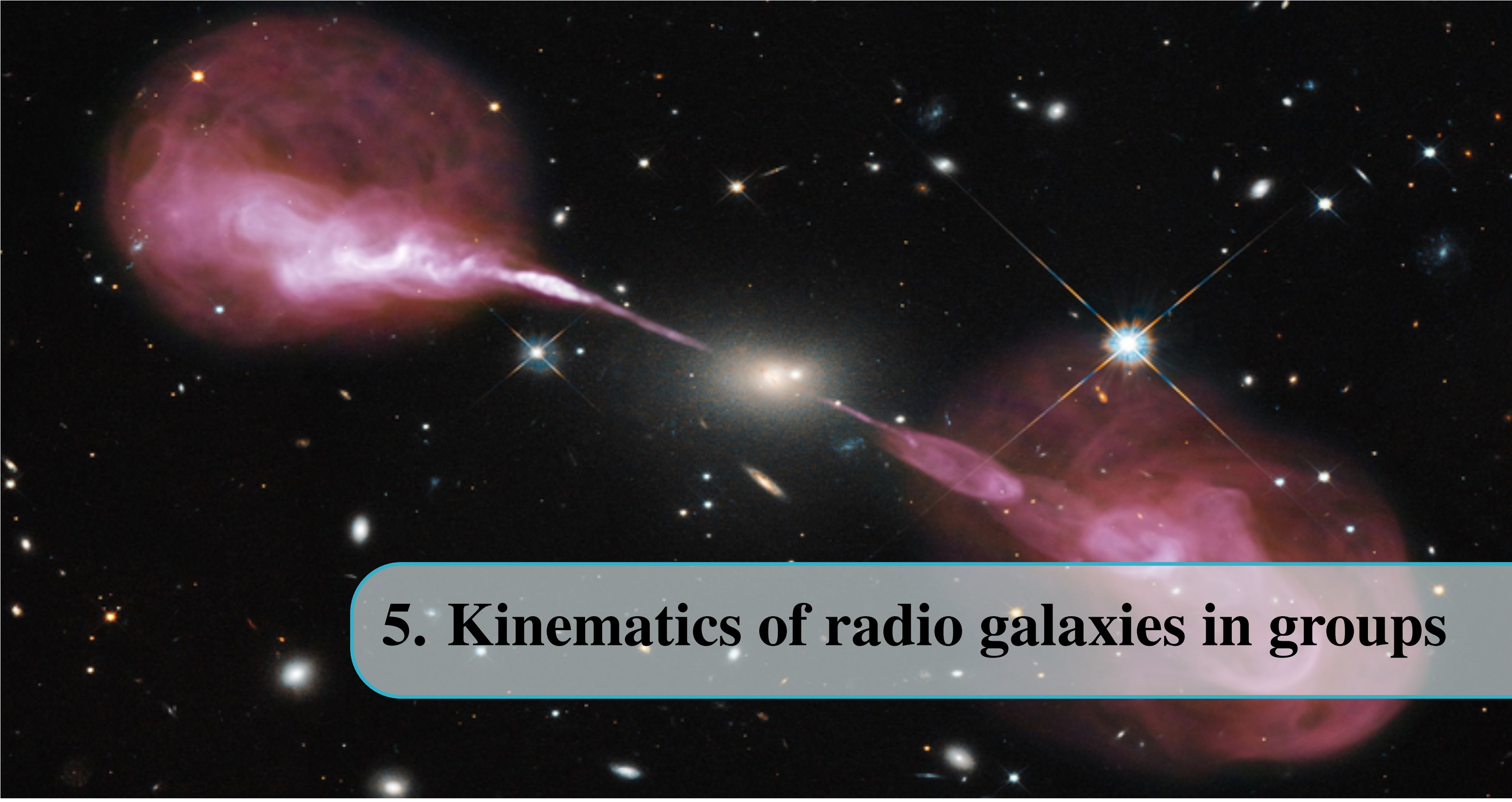

5. Kinematics of radio galaxies in groups

Radio galaxies in galaxy groups: kinematics, scaling relations and AGN feedback

T. Pasini, A. Finoguenov, M. Brüggen et al. MNRAS, 505, 2628 (2021)

Abstract. *We investigate the kinematic properties of a large (N=998) sample of COSMOS spectroscopic galaxy members distributed among 79 groups. We identify the Brightest Group Galaxies (BGGs) and cross-match our data with the VLA-COSMOS Deep survey at 1.4 GHz, classifying our parent sample into radio/non-radio BGGs and radio/non-radio satellites. The radio luminosity distribution spans from* $L_R \sim 2 \times 10^{21}$ *W Hz*$^{-1}$ *to* $L_R \sim 3 \times 10^{25}$ *W Hz*$^{-1}$. *A phase-space analysis, performed by comparing the velocity ratio (line-of-sight velocity divided by the group velocity dispersion) with the galaxy-group centre offset, reveals that BGGs (radio and non-radio) are mostly (∼80%) ancient infallers. Furthermore, the strongest (*$L_R > 10^{23}$ *W Hz*$^{-1}$*) radio galaxies are always found within 0.2*$R_{\rm vir}$ *from the group centre. Comparing our samples with HORIZON-AGN, we find that the velocities and offsets of simulated galaxies are more similar to radio BGGs than to non-radio BGGs, albeit statistical tests still highlight significant differences between simulated and real objects. We find that radio BGGs are more likely to be hosted in high-mass groups. Finally, we observe correlations between the powers of BGG radio galaxies and the X-ray temperatures,* $T_{\rm x}$*, and X-ray luminosities,* $L_{\rm x}$*, of the host groups. This supports the existence of a link between the intragroup medium and the central radio source. The occurrence of powerful radio galaxies at group centres can be explained by Chaotic Cold Accretion, as the AGN can feed from both the galactic and intragroup condensation, leading to the observed positive* $L_{\rm R} - T_{\rm x}$ *correlation.*

5.1 Introduction

The hot plasma inside of galaxy clusters and groups is governed by processes that can be observed at multiple wavelengths: from thermal cooling of the hot ($\sim 10^7$ K) intracluster medium (ICM) (e.g., Fabian, 1994; Peterson and Fabian, 2006), to line emission produced by warm gas (e.g., Hamer et al., 2016; Pulido et al., 2018), to feedback from central Active Galactic Nuclei (AGN). The latter can heat their surroundings and can prevent the catastrophic cooling of the cool core (see reviews by, e.g., McNamara and Nulsen, 2007; Gitti et al., 2012), establishing what is known as *AGN feedback cycle*.

Brightest Cluster Galaxies (BCGs) and Brightest Group Galaxies (BGGs) are the most optically luminous and massive galaxies in a cluster and group, respectively. Usually they lie at the centres of their host structures. Owing to their special location, the evolution and assembly history of massive galaxies and of their hosts has been studied widely (Bernstein and Bhavsar, 2001; Bernardi, 2007; Liu et al., 2009; Stott et al., 2010). Notably, BGGs look dissimilar from other massive galaxies, showing different surface brightness profiles and obeying different scaling relations, which suggests that their formation process may be different, too (see e.g., Von Der Linden et al., 2007; Liu et al., 2008; Stott et al., 2008; Shen et al., 2014).

In galaxy clusters, the evolution of BCGs is tightly linked to that of the host cluster (e.g. Lin and Mohr, 2007). Several observational studies (e.g., Giodini et al., 2010; Giacintucci et al., 2011; Ineson et al., 2013, 2015; Kolokythas et al., 2018; Pasini et al., 2020) and numerical simulations (Gaspari et al. 2020 for a review) have demonstrated the importance of AGN feedback in galaxy groups, that are known to be the hosts of more than half of all galaxies (Eke et al., 2006). However, there is no consensus on where to draw the boundary between galaxy clusters and galaxy groups. It is sometimes assumed that the boundary lies close to the virial temperature of 1 keV since this is the temperature where the slope of the relation between X-ray luminosity and virial temperature changes. However, this change of slope could be caused by observational systematics (see e.g., Voit et al., 2018).

The trigger mechanism for radio-loud AGN activity is still unclear (e.g., Shakura and Sunyaev, 1973; Merloni and Heinz, 2007; Best and Heckman, 2012), but gas that cools out of the hot X-ray halo seems to play a key role (e.g., Best et al. 2005b). Shen et al. (2017) found that, in a sample of 89 radio galaxies located in clusters and groups, AGN are preferentially located in dense environments such as the cores, suggesting that their activity is strongly linked to that of the host cluster. In the *Chaotic Cold Accretion* (CCA) scenario (Gaspari et al., 2013; Gaspari, 2016) the AGN is frequently switched on and off through self-regulated feeding and feedback cycles. CCA can occur in every galaxy with a hot halo, regardless of the position. However, central galaxies - BGGs or not - lie in dense regions, where the condensation is significantly stronger (Gaspari et al., 2019). Non-linear thermal instabilities produced by the cooling plasma lead to precipitation, which is able to feed the SMBH through inelastic collisions between the condensed cold clouds and filaments (e.g., Gaspari and Sądowski 2017; McDonald et al. 2018; Tremblay et al. 2018; Temi et al. 2018; Juráňová et al. 2019; Rose et al. 2019; Schellenberger et al. 2020).

Pasini et al. (2020) presented a study of the relation between the ICM X-ray luminosity of a sample of 247 X-ray selected galaxy groups in COSMOS (Gozaliasl et al., 2019) and the radio luminosity produced by the corresponding central radio galaxy, defined as the radio source at 1.4 GHz found closest to the X-ray emission peak. Cross-matching this sample with optical catalogs, they found that only in 30 per cent of the groups central radio galaxies were hosted in BGGs. This is consistent with Gozaliasl et al. (2019), who showed that 70 per cent of COSMOS BGGs are found more than $0.1\,R_{200}$ away from the X-ray peak. This suggests that BGGs do not always lie at the bottom of the potential well. This does not seem to be the case for galaxy clusters, where ~ 85 per cent of central radio galaxies were found in BCGs (Pasini et al., 2020). Nevertheless, there are some cases in which an apparently brightest galaxy near a cluster centre has a significantly large velocity offset with respect to the mean redshift of cluster members ($> 300\,\mathrm{km\,s^{-1}}$; Coziol et al. 2009; Lauer et al. 2014), suggesting that these objects may not reside at the bottom of the cluster potential well.

Recent work (e.g., Rhee et al., 2017; Gozaliasl et al., 2020) combines the cluster-centric velocities and cluster-centric radii in a single diagram. This phase-space diagram can be used to extract information about the assembly history of clusters (Mahajan et al., 2011; Hernández-Fernández et al., 2014, e.g.). For example, one expects recently accreted galaxies to show higher relative velocities and offsets from the centre than objects accreted at an earlier time. Objects accreted early are usually found within the core of the virialised region and show a small velocity spread (Noble et al., 2016; Gozaliasl et al., 2020).

In this paper, we investigate the kinematics of the hosts of radio galaxies in groups (BGGs and 'satellites[1]'), comparing them to the kinematics of galaxies with no detected radio emission. To this end, we rely on a recently published sample of X-ray galaxy groups (Gozaliasl et al., 2019), combining it with optical, kinematic and spectroscopic data. All host groups were identified in the 2 square degree COSMOS field, with a mass range of $M_{200} = 8 \times 10^{12} - 3 \times 10^{14} M_{\odot}$, where the upper limit of this range corresponds to a virial temperature of ~ 4 keV.

This paper is structured as follows: In Sec. 2 we describe our sample and how we compiled it. In Sec. 3.1 we perform a phase-space analysis and in Sec. 3.2, we compare it to cosmological simulations. In Sec. 3.3 we explore the properties of our sample and derive scaling relations in Sec. 3.4. In Sec. 3.5 we discuss implications for AGN feedback before we conclude in Sec. 4.

Throughout the paper, we assume a standard ΛCDM cosmology with $H_0 = 70$ km s^{-1} Mpc^{-1}, $\Omega_{\Lambda} = 0.73$ and $\Omega_{M} = 1 - \Omega_{\Lambda} = 0.27$.

5.2 The sample

Gozaliasl et al. (2019) presented a sample of 247 X-ray selected galaxy groups in the 2 square degree COSMOS field at a redshift range of $0.08 \leq z < 1.53$. The same sample was also studied in Pasini et al. (2020) making use of radio data from the VLA-COSMOS survey (Schinnerer et al., 2010) and of new MeerKAT observations that are part of the MIGHTEE

[1] Throughout this work, we will refer to non-BGGs as satellites for easier reading

	BGGs	Satellites
Radio detection	28	51
No radio detection	42[a]	877[b]
Total	70	928

Table 5.1: Properties of the samples studied in this work.
[a]: 19 from the 50 groups with at least one radio galaxy detected and 23 from the remaining 29 groups.
[b]: 664 from the 50 groups with at least one radio galaxy detected and 213 from the remaining 29 groups.

survey (Jarvis et al., 2016). In this paper, they found evidence for a correlation between the X-ray luminosity of galaxy groups and the radio luminosity of the central AGN (see Pasini et al. 2020 for further details).

Before we can perform a dynamical analysis, we need to determine cluster membership through spectroscopic redshifts. To this end, we have vetted the group membership catalog of Gozaliasl et al. (2019) by applying the CLEAN algorithm of Mamon et al. (2013), which removes the galaxies exceeding the escape velocity of the group as a function of cluster-centric radius from the group. We kept groups with more than four member galaxies and removed all of those galaxies that have no spectroscopic data. This resulted in a total of 79 groups, with 998 member galaxies, which limits our study to redshifts of $z \leq 1.0$. Among these members, we identified 70 BGGs, that were found to be the most massive in each group by Gozaliasl et al. (2014, 2019). We have computed the gapper velocity dispersion estimates $\sigma_{\rm v}$ following Beers et al. (1990).

If the most massive galaxy only has photometric redshifts, it gets excluded from our sample. As a result, not every group has its BGG included in this work, and for some groups the BGG identification could even be wrong if another galaxy was mistakenly identified as BGG. Therefore, we performed a further check and found this to be the case only in one group, where the galaxy previously classified as BGG was actually a satellite.

The spectroscopic member galaxies thus obtained were then matched to the VLA-COSMOS Deep survey at 1.4 GHz (rms $\sim$ 12 μJy beam^{-1}, beam = 2.5"x 2.5", Schinnerer et al. 2010). The cross-match was performed by assuming an association between radio emission and optical galaxy when their angular distance is less than the width of the beam in the VLA-COSMOS survey. We found that 50 groups host at least 1 radio source according to our criteria, with a total of 79 detected radio galaxies (28 in BGGs and 51 in satellites). 19 of these groups host more than one radio galaxy, while for 31 we only detect one source. Groups with no detected radio emission are therefore 29, with 236 member galaxies in total (23 BGGs and 213 satellites). The remaining 683 galaxies (19 BGGs and 664 satellites) with no radio emission belong to the 50 groups with at least one radio galaxy. The characteristics of the samples are briefly summarized in Table 5.1.

The temperature of the groups was determined through the T_X - L_X scaling relation (Giles et al., 2016; Kettula et al., 2015). A small subsample also had a direct measurement of the temperature available (Kettula et al., 2013). We find that these measurements are consistent with the scaling relation above.

The final catalog presents a set of multi-wavelength observables for each group (X-

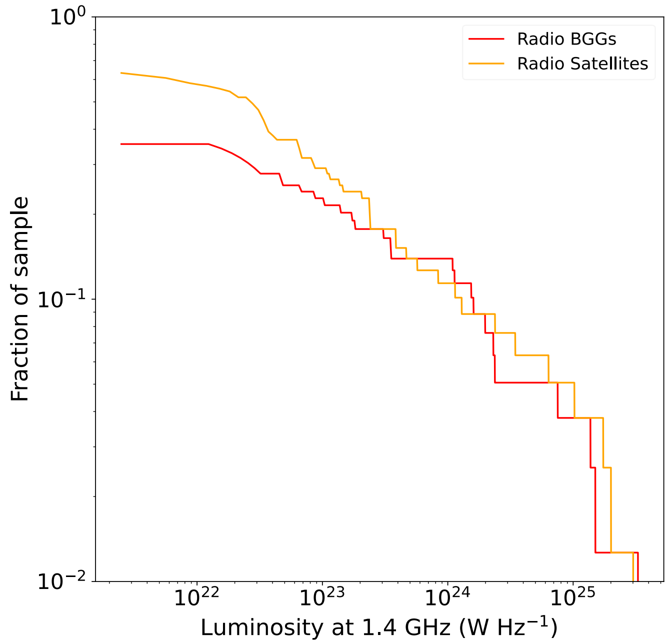

Figure 5.1: Cumulative 1.4 GHz luminosity distribution for all 79 galaxies with radio emission, divided into BGGs (red) and satellites (orange). The *y-axis* reflects the relative fractions of BGGs (28 out of 79 galaxies) and satellites (51 out of 79 galaxies) that compose the radio galaxy sample.

ray luminosity, temperature), for the member galaxies (spectroscopic redshift, velocity dispersion, proper velocity, stellar mass) and for the corresponding radio source, when present (1.4 GHz power, Largest Linear Size). A selection bias could be introduced by those galaxies - and therefore the host groups - that do not show radio emission according to our criteria. The reason for this could be the lack of an AGN, or limitations set by the sensitivity of VLA-COSMOS. Among all observable galaxies, Padovani et al. (2017) claim that around $\sim 1\%$ host an AGN. Nevertheless, this value should increase in overdense environments such as galaxy groups. Sabater et al. (2019) report a 100% detection rate for galaxies with M$>10^{11}$ M$_\odot$, but this fraction has been observed to strongly vary depending on the host galaxy stellar mass (Kauffmann et al., 2003). Among our sample, $\sim 8\%$ host an AGN. The radio luminosity distribution for all galaxies with detected radio emission is shown in Fig. 5.1.

The luminosity distributions span the range $L_R \sim 2 \times 10^{21}$ W Hz^{-1} - $L_R \sim 3 \times 10^{25}$ W Hz^{-1}. The end of the range is lower than the BCG luminosity distribution of Hogan et al. (2015) that reaches $L_R \sim 10^{27}$ W Hz^{-1}. The reason for this is that we are only considering galaxy groups, where the radio power of the central galaxy is generally lower than for clusters. This was also found in Pasini et al. (2020) by investigating the same parent sample used for this work, composed by 247 COSMOS galaxy groups. In Pasini et al. (2020), the luminosity reaches $\sim 10^{27}$ W Hz^{-1} in a small (<5 out of 247 groups) number of outliers

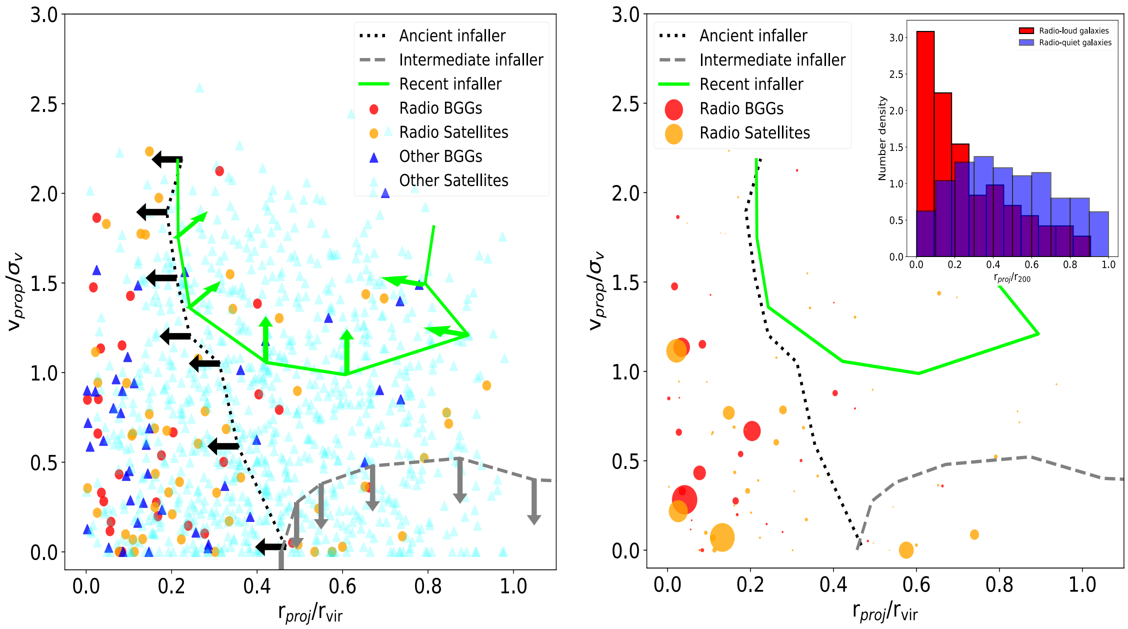

Figure 5.2: *Left*: Phase-space diagram for radio BGGs (red), non-radio BGGs (blue), radio satellites (orange) and non-radio satellites (cyan). The x-axis represents the ratio between the distance from the group centre and $R_{\rm vir}$, while the y-axis is the ratio between the line-of-sight velocity and the (one-dimensional) velocity dispersion. The different regions in the diagram indicate ancient infallers (left of black dotted line), intermediate infallers (below the grey dashed line) and recent infallers (above the green line). *Right*: Phase-space diagram restricted to radio BGGs and radio satellites only, with the points sized for the power of the corresponding radio galaxy. The top-right histogram shows the offset distribution for galaxies with (red) and without (blue) radio emission.

that show very extended AGN emission. The reason why these sources are excluded from the present work is that no spectroscopic data is available for the optical host. Our analysis will therefore be limited to $L_R < 10^{26}$ W Hz^{-1}.

At the highest redshift of the sample ($z \sim 0.98$), the VLA-COSMOS sensitivity at 3σ corresponds to $L_{1.4\,\rm GHz} \sim 2 \times 10^{23}$ W Hz^{-1}. With the mean redshift setting around $z \sim 0.4$, we should be able to pick most of the radio sources brighter than 10^{22} W Hz^{-1} at 1.4 GHz. This yields a sample that is representative of the radio luminosity function usually observed for radio galaxies (e.g. Hogan et al., 2015). Therefore, undetected radio emission should not affect our analysis, which focuses on the comparison between BGGs with detected radio emission (hereafter radio BGGs), satellites with detected radio emission (hereafter radio satellites), BGGs with no radio emission and satellites with no radio emission.

5.3 Results and discussion

Phase-space analysis

We performed a phase-space analysis by comparing the cluster/group-centric velocity with the cluster/group-centric offset of the hosted galaxies. This diagram conveys information about the assembly and accretion history of these objects. In the left panel of Fig. 5.2 we show the phase-space diagram for radio BGGs, radio satellites, non-radio BGGs and non-radio satellites. Following Rhee et al. (2017) and Gozaliasl et al. (2020), the position of each object in this diagram is an indicator of the infall time ($t_{\rm inf}$) of the galaxy, with ancient infallers (6.45 Gyr $< t_{\rm inf} <$ 13.7 Gyr) found to the left of the black dotted line in Fig. 5.2, while intermediate infallers (3.63 Gyr $< t_{\rm inf} <$ 6.45 Gyr) cover the whole offset range below the grey dashed curve. Galaxies above the green line are classified as recent infallers, while the remaining ones cannot be attributed to any of these classes. This does not affect the following analysis since our purpose is to distinguish ancient infallers from all the other objects. Out of 28 radio BGGs, only 5 ($\sim$ 18%) are not classified as ancient infallers, which constitute $\sim$82% of the sample. On the other hand, the sample of 42 non-radio BGGs is composed of 33 ancient infallers ($\sim$78%), consistently with Gozaliasl et al. (2019), who also found that BGGs are mostly ancient infallers. The sample of radio satellites show $\sim$65% ancient infallers. Finally, only $\sim$41% of non-radio satellites present this classification.

The right panel of Fig. 5.2 shows objects with radio emission only (BGGs and satellites), with the size of the symbols proportional to the power of the radio source. The top-right histogram shows the offset distribution for galaxies with and without radio emission. The comparison between the radio and non-radio samples in the histogram clearly indicates that most of the galaxies with radio emission are ancient infallers (56 out of 79, $\sim$ 71%), strongly peaking at low offsets, while the distribution of the distances from the group centre for galaxies with no radio emission is more uniform across $R_{\rm vir}$. The phase-space analysis applied to radio objects-only also suggests that powerful radio galaxies ($L_R > 10^{23}$ W Hz^{-1}) are always located close to the group centre ($< 0.2\,R_{\rm vir}$). This is expected since central galaxies switch the SMBH on much easily. The gas cooled out of the Intra-Group Medium (IGrM) can feed the AGN if the galaxy lies close to the group density peak, where the cooling is more efficient. Nevertheless, galaxies located in the outskirts or outside the cooling radius of the group can still show radio emission. However, they might have to rely on more episodic triggers, such as mergers or interactions with other objects. Only in a few cases, their radio power is able to become comparable to those of central galaxies. This happens especially because the low density in the outskirts of galaxy groups sometimes allow them to grow rapidly in size (see also Pasini et al. 2020).

A further consequence of this is that radio BGGs have a higher chance than non-radio BGGs to lie close to the group centre. This is particularly true for the most powerful ones ($L_R > 10^{23}$ W Hz^{-1}), that in our samples always lie within $0.2\,R_{\rm vir}$. Therefore, the detection of a powerful radio source in a group can help identify the group centre. Finally, it is worth noting that no difference is visible in terms of velocity ratio between powerful BGGs and those with $L_R < 10^{23}$ W Hz^{-1}.

Comparison with cosmological simulations

Here, we compare our samples with the theoretical predictions from the HORIZON-AGN (HZ) simulation[2] (Dubois et al., 2014). The HORIZON-AGN simulation is a cosmological

[2]https://www.horizon-simulation.org

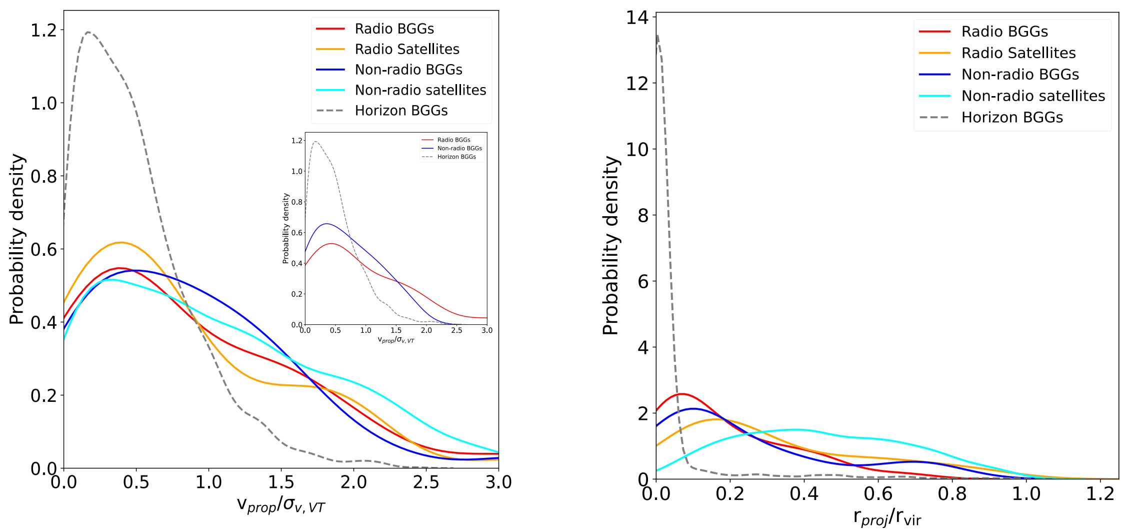

Figure 5.3: *Left*: Probability density (obtained through a gaussian kernel density estimate) vs. velocity ratio for radio and non-radio BGGs (red and blue), for radio and non-radio satellites (orange and cyan) and for HZ-simulated BGGs (dashed gray).The subplot shows the same distribution restricted to only BGGs with offset $< 0.3R_{\rm vir}$. *Right*: Probability density vs. offset from the group centre for radio and non-radio BGGs (red and blue), for radio and non-radio satellites (orange and cyan) and for HZ-simulated BGGs (dashed gray).

hydrodynamical simulation of 100 Mpc/h comoving box containing 1024^3 Dark Matter particles. The simulation is performed with the adaptive-mesh refinement code RAMSES (Teyssier, 2002) including gas dynamics, gas cooling and heating, and sub-grid models for star formation, stellar and AGN feedback. The AdaptaHOP halo finder (Aubert et al., 2004) was run on both the stellar and DM particle distributions to identify galaxies and halos (see Laigle et al. 2019 and Gozaliasl et al. 2019 for further details). Each galaxy is then associated with its closest main halo. To match the observational definition, the BGG is identified as the most massive galaxy within the virial radius of the main halo.

The left panel of Fig. 5.3 shows the probability density distribution of the velocity ratio for radio and non-radio BGGs and for radio and non-radio satellites. Here, instead of the gapper velocity dispersion $\sigma_{\rm v}$ exploited in Fig. 5.2, we use the velocity dispersion estimated from X-ray emission $\sigma_{{\rm v},VT}$ (see below). The gray dashed curve represents the distribution for simulated BGGs obtained by HZ-AGN, whose mass and redshift evolution were already studied and compared to COSMOS BGGs and satellites in Gozaliasl et al. (2020). Here, our purpose is to understand whether the dynamical properties of our four samples differ significantly from each other, and how they compare to simulated galaxies.

The distributions of radio and non-radio BGGs peak at $v_{\rm prop}/\sigma_{\rm v,VT} \sim 0.4$ and 0.5, respectively. For radio BGGs, the mean velocity ratio is ~ 0.84 and the median velocity ratio is ~ 0.63. For non-radio BGGs the mean velocity ratio is ~ 0.85 and the median is $\sim$ 0.78. Radio satellites have the peak velocity ratio around ~ 0.45, with a mean of ~ 0.78 and a median of ~ 0.59. The distribution for non-radio satellites is broader, setting the peak at ~ 0.3 but becoming the dominant sources at $v_{\rm prop}/\sigma_{\rm v,VT} \geq 1.6$, with a mean of ~ 1.04 and a median of ~ 0.89. Finally, BGGs in the HZ-AGN simulation are strongly peaked around $v_{\rm prop}/\sigma_{\rm v,VT} \sim 0.2$, with a mean of ~ 0.49 and a median of ~ 0.41.

Given that the simulation represents the dynamics of the central galaxy, in the subplot of Fig. 5.3 we select only BGGs within $0.3R_{\rm vir}$ from the X-ray center, to see if this changes the observed displacement of the curve with respect to HZ BGGs. We see no difference in the distribution for radio BGGs, while the curve for non-radio BGGs becomes tighter. Nevertheless, the distribution for HZ BGGs remains much more strongly peaked at low velocity with respect to real BGGs, with a steeper decrease after the peak.

The probability distribution of offsets from the group centre, shown in the right panel of Fig. 5.3, confirms that BGGs (radio, non-radio and simulated) are highly concentrated within 0.2 $R_{\rm vir}$. At higher radii the curves of radio and non-radio BGGs decrease in a similar fashion, while the probability density of simulated BGGs already steepens at ~ 0.1 $R_{\rm vir}$. Nevertheless, in simulations BGGs tend to be more massive than their observational counterparts (e.g., Bahé et al., 2017; Henden et al., 2019; Bassini et al., 2020). For this reason, they are closer to the centre and exhibit less spread in velocity. On the other hand, satellites exhibit a broader distribution, with radio satellites prevailing at offsets ≤ 0.3, while at outer radii non-radio satellites become dominant.

All BGGs were observed as a part of zCOSMOS survey (Lilly et al., 2007), with a redshift error of ~55 km/s. Missing objects were covered by FORS2 program (George et al., 2011), with a similar redshift precision, and at $z > 0.7$ by GEEC2 (Balogh et al., 2011), with a redshift precision of 80 km/s. Based on the work of Saro et al. (2013), the uncertainty of velocity dispersion measurement is high with typical number of spectroscopic members of COSMOS X-ray galaxy groups. Better constraints on the velocity dispersion are obtained using scaling relations of $L_X - M_{200}$ (Leauthaud et al., 2010) and $M_{200} - \sigma_{\rm v,VT}$ (Carlberg et al., 1997). The log-normal scatter $L_X - \sigma_{\rm v,VT}$ relation is measured to be 0.13 by Kirkpatrick et al. (2021). Using the velocity dispersion from scaling relations, the disagreement with simulations consists in a wider tail above 0.7σ extending to 2.5σ. The spread due to uncertainty in the mean redshift is typically $0.3\sigma_{\rm v,VT}$ and always better than $0.45\sigma_{\rm v,VT}$ and cannot explain the large tail.

Positional displacement of BGGs from the center of the halo is constrained to be within 0.1 $R_{\rm vir}$ in simulations, while our data shows much broader range of offsets between BGG and X-ray peak. George et al. (2012) found that BGGs in the vicinity of X-ray centers (within 0.25 $R_{\rm vir}$) are good tracers of projected mass centers, with an offset less than 0.1 $R_{\rm vir}$, but BGGs with strong offsets from X-ray center do not trace the center of mass and the corresponding mass profiles suggest merging. Thus, the broad distribution of offsets within 0.3 $R_{\rm vir}$ is due to displacements of X-ray peak, while larger offsets are merger driven. For the offset peak of HZ galaxies to match that of our data, it would require a systematic shift of ~0.1 $R_{\rm vir}$ (10" - 6′).

To quantify our results, we performed a Kolmogorov-Smirnov (KS) test to compare the radio and non-radio BGG distributions with simulated BGGs. Our null-hypothesis is that the samples are drawn from the same parent distribution. The KS-test on the phase-space distributions of radio BGGs and simulated BGGs gives a null-hypothesis probability of

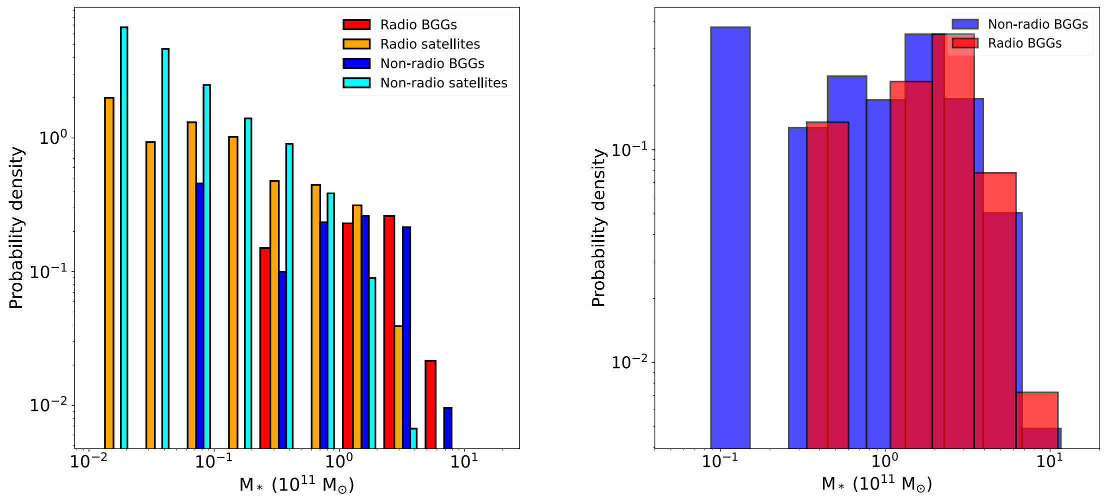

Figure 5.4: *Left*: Stellar mass distribution for radio (red) and non-radio (blue) BGGs, and for radio (orange) and non-radio (cyan) satellites. *Right*: Stellar mass distribution restricted to radio (red) and non-radio (blue) BGGs.

$p = 1.6 \times 10^{-13}$, while the comparison between non-radio BGGs and simulated BGGs results in $p = 3.1 \times 10^{-17}$. This suggests that the simulation is not able to reproduce our samples, indicating that it may need additional physics to reproduce the true population of BGGs.

Properties of the samples

The left panel of Fig. 5.4 shows the stellar mass distribution for the four samples: radio BGGs, radio satellites, non-radio BGGs and non-radio satellites. Non-radio satellites dominate the low-mass regime, from 10^9 $M_\odot$ to 5×10^{10} $M_\odot$. Low-mass radio BGGs start to appear around 3×10^{10} $M_\odot$, while non-radio BGGs go down to 10^{10} $M_\odot$. Radio BGGs become dominant for stellar masses $\geq 3 \times 10^{11}$ $M_\odot$. In order to compare the mass distributions of the BGG samples, we show the histograms of radio and non-radio BGGs in the right panel of Fig. 5.4. Out of 28 radio BGGs, 27 have $M_* > 10^{11}$ $M_\odot$ ($\sim$96%), while the same fraction for non-radio BGGs is $\sim$83% (35 out of 42). The small size of the samples does not lead to statistically significant results, but radio BGGs trend towards higher masses, while it is less likely for a BGG with $M_* < 10^{11}$ $M_\odot$ to host a radio galaxy.

This is even more significant when considering that massive BGGs are found in more massive groups and vice versa, as discussed in several papers (e.g., Stott et al., 2010; Gozaliasl et al., 2016) and shown in Fig. 5.5. This is in agreement with Gaspari et al. (2019) who observed that more massive SMBHs correlate with larger and hotter X-ray halos. The same is also found in cosmological simulations by, e.g., Bassini et al. (2019); Truong et al. (2021). In combination with the result shown above that radio BGGs are usually more massive than those with no radio emission, this suggests that radio BGGs are more likely to

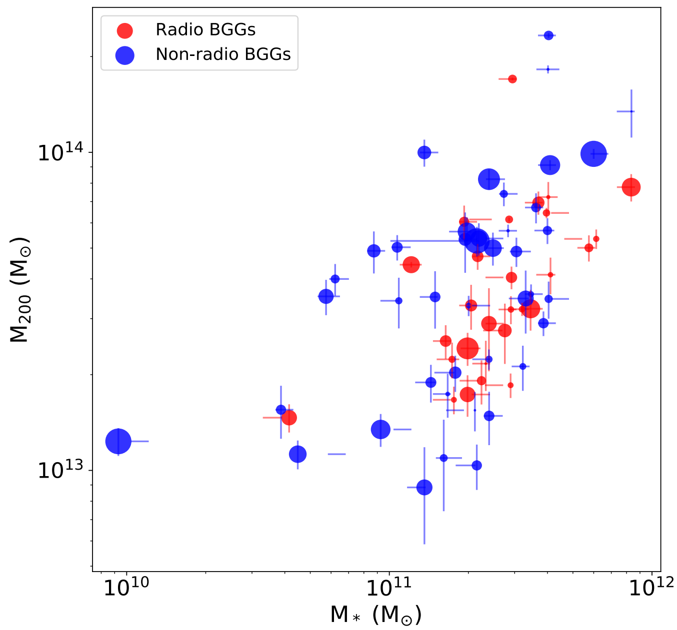

Figure 5.5: Galaxy groups M_{200} vs. stellar mass for the radio-BGG (red) and non-radio BGG (blue) samples. The size denotes the distance of the BGG from the group centre, with bigger points indicating larger offsets.

be hosted in high-mass groups. Since radio-BGGs statistically exhibit smaller offsets from the centre than non-radio BGGs (see Sec. 5.3), we can argue that this could affect the trigger of the AGN. Indeed, Fig. 5.2 shows that a number of non-radio BGGs have large offsets. This is not surprising considering that the group centre as we defined it, i.e., the bottom of the potential well, is where the hot gas density is higher and cooling is faster, especially in more relaxed systems. Stronger cooling implies more condensing mass (Gaspari et al. 2019) which feeds the supermassive black hole (SMBH) (e.g., see the GR-rMHD simulations by Sądowski and Gaspari 2017). Nevertheless, there are also high-mass non-radio BGGs which do not host a radio source, at least with our sensitivity limit. This could likely be explained by the flickering duty cycle involved in the AGN feeding and feedback self-regulation (Sec. 5.3) .

In order to determine whether one of our samples shows any divergence from standard scaling relations, we investigated the correlation between X-ray luminosity and observed velocity dispersion (σ_v) for groups hosting radio and non-radio BGGs, plotted in Fig. 5.6 (e.g., Wu et al., 1999; Mahdavi and Geller, 2001; Zhang et al., 2011; Gozaliasl et al., 2020). None of the samples seem to show any deviation and both follow the same correlation. This is confirmed by the KS test ($p = 0.06$), which suggests that the two distributions are similar and that no discernible difference exists in the σ_v-L_X correlation between the groups hosting radio and non-radio BGGs.

We also looked for evidence of recent interactions with other galaxy groups by inspecting

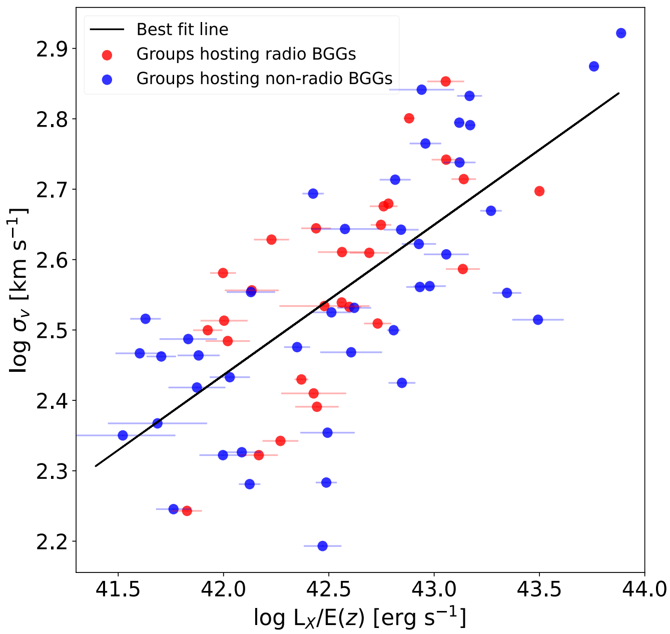

Figure 5.6: Observed velocity dispersion of the host group vs. X-ray luminosity for radio (red) and non-radio (blue) BGGs. The black line represents the scaling relation obtained by computing the L_X - M and the M - $\sigma_{v,VT}$ correlations presented in Leauthaud et al. (2010) and Mamon et al. (2013), respectively.

the *Chandra* and XMM-Newton observations used to build the original galaxy groups catalog (Gozaliasl et al., 2019). We find that only for one group it is possible to detect hints of mergers (LSS 17, see Smolčić et al. 2007). The images are too shallow to reveal anything for the other objects. We will return to this issue in Sec. 5.3, but deeper X-ray observations will be needed for this purpose.

It is well-known that the magnitude difference between the first- and second-rank galaxies in a group/cluster is helpful to trace their merger history and evolution (Ponman et al., 1994; Gozaliasl et al., 2014, 2019). Simulations have shown that mergers in galaxy groups lead to runaway growth of the BGG (e.g., Cavaliere et al., 1986; Mamon, 1992), at the expense of the second brightest galaxy. Therefore, the magnitude gap between the BGG and the second-rank galaxy should increase in time, finally leading to a situation in which the central, elliptical BGG, lying in an X-ray luminous halo, is surrounded by faint satellites. These groups are known as *fossil groups* (Jones et al., 2003). Therefore, one expects larger gaps in more relaxed groups, where the offset between the BGG and the halo centre is lower. The magnitude gap - offset relation for our parent sample of galaxy groups has already been studied in Gozaliasl et al. (2019). Here, we wish to understand how this gap relates to BGGs with and without radio emission.

In Fig. 5.7, we show the R-band magnitude gap distribution for our brightest groups galaxies, classified into radio and non-radio BGGs. The gap was measured within 0.5

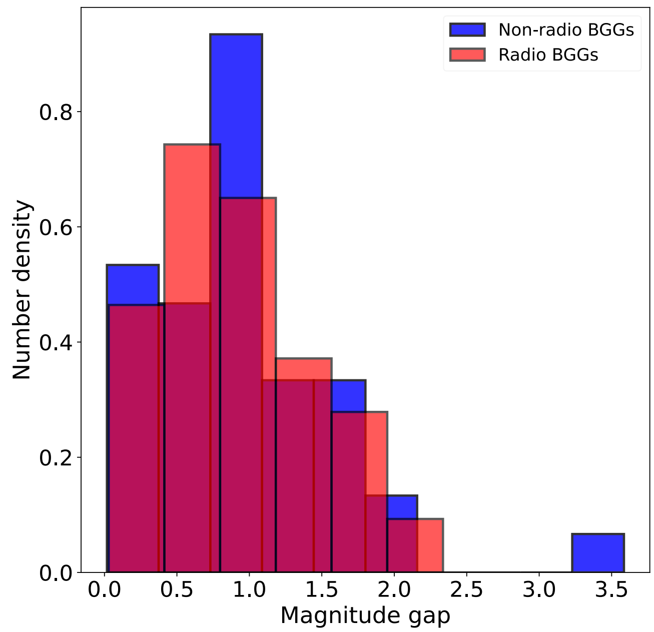

Figure 5.7: Magnitude gaps (R-band) of radio (red) and non-radio (blue) BGGs from the corresponding second-rank galaxy.

R_{200}, following (Jones et al., 2003). The second-rank galaxy of each group was picked, regardless of it having spectroscopic or photometric identification, using the full membership catalog studied in Gozaliasl et al. (2020). Both distributions peak around ~ 1, with a clear concentration of objects before $\sim$1.5. No clear difference in the trend is detected between radio and non-radio BGGs, as also confirmed by the KS test ($p = 0.13$). Nevertheless, our catalogs only have a few tens of objects, and analyses on larger samples could help to address how the magnitude gap relates to radio and non-radio BGGs.

Scaling relations

Pasini et al. (2020) explored a correlation between the 1.4 GHz radio power of the central AGN and the X-ray luminosity of the host galaxy group. Since the sample of radio BGGs studied in this work is derived from the same parent catalog of X-ray groups (Gozaliasl et al., 2019), we expect to find a similar correlation, which is shown in the left panel of Fig. 5.8.

The sample was divided into relaxed objects (offset $< 0.2\,R_{\rm vir}$ and $v < 0.5\,v_{\rm disp}$), high-velocity objects (offset $< 0.2\,R_{\rm vir}$ and $v > 0.5\,v_{\rm disp}$) and offset objects (offset $> 0.2\,R_{\rm vir}$). We find no significant differences between the three subsamples. We then applied Bayesian inference to extract the best-fit relation, by using `linmix`[3] (cf. Sec. 2.2 in Gaspari et al.

[3]https://github.com/jmeyers314/linmix.

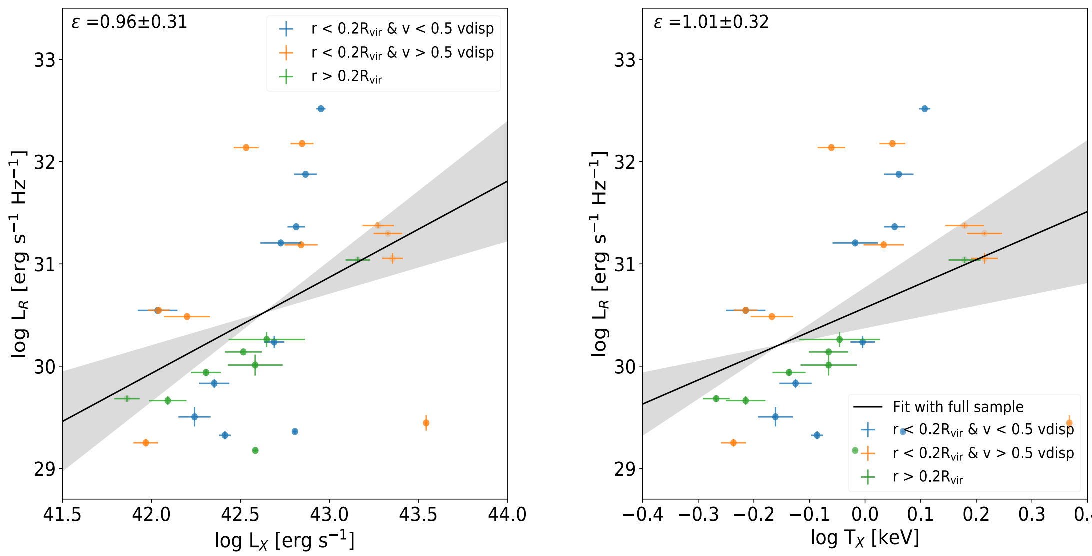

Figure 5.8: *Left:* 1.4 GHz AGN radio power vs. X-ray luminosity of the host group for the radio BGG sample. The sample was divided into relaxed objects (cyan, offset $< 0.2R_{\rm vir}$ and $v < 0.5v_{\rm disp}$), high-velocity objects (yellow, offset $< 0.2R_{\rm vir}$ and $v > 0.5v_{\rm disp}$) and offset objects (green, offset $> 0.2R_{\rm vir}$). The black line represents the best-fit relation obtained through a Bayesian statistical analysis (the intrinsic scatter is labeled in the top-left corner). *Right:* 1.4 GHz AGN radio power vs. temperature of the host group. The classification is the same as in the left panel. The grey line shows 1σ errors on the best fit.

2019 for a discussion of its features). A linear fit in log-log scale was performed in the form:

$$Y = \alpha + \beta X + \varepsilon, \tag{5.1}$$

with α and β representing the intercept and the slope, respectively, while ε is the intrinsic scatter of the relation. For the AGN power versus X-ray luminosity correlation, we find $\alpha = -9.53 \pm 18.19$, $\beta = 0.94 \pm 0.43$ and $\varepsilon = 0.96 \pm 0.31$. As expected, this estimate is consistent with the slope of $L_R \propto (1.07 \pm 0.12) L_X$ presented in Pasini et al. (2020), obtained through least-squares linear regression. However, we note that the errors are large due to the small sample size. It is generally understood that the X-ray emission by clusters and groups is tightly linked to the temperature of the ICM (Lovisari et al., 2020). Therefore, if a correlation of the hot plasma with the AGN exists, we expect a similar link with the gas temperature, too. The right panel of Fig. 5.8 shows the correlation between the 1.4 GHz AGN power and the X-ray temperature of the intragroup medium of the host. Again, no difference is apparent among the subsamples. We find $\alpha = 30.57 \pm 0.19$ and $\beta = 2.35 \pm 1.25$, with intrinsic scatter $\varepsilon = 1.01 \pm 0.32$.

The significant positive and steep correlation with X-ray halo properties can be compared with those by Gaspari et al. (2019), who found also key positive X-ray halo correlations between the (direct/dynamical) SMBH masses and the observed $T_{\rm x}$ and $L_{\rm x}$. Specifically, their group-dominated sample show a slope $M_{\rm BH} \propto T_{\rm x}^{2.14 \pm 0.25}$, which is well consistent with the above mean relation. This suggests that, despite the AGN power being an instantaneous measure ($L_R \sim P_{BH} \propto \dot{M}_{BH}$), the mean $L_R - T_x$ is not drastically altered by the details of the feedback duty cycle, except by introducing a larger intrinsic scatter ($4\times$) due to the chaotic intermittency. Such a variable duty cycle is a feature corroborated by a wide range of numerical and observational studies (e.g., McNamara and Nulsen 2007; Gaspari et al. 2011; Fabian 2012; Prasad et al. 2015; Yang and Reynolds 2016). The $L_R - L_x$ relation appears to be slightly steeper than the $M_{BH} - L_x$, although still comparable within the 1-σ uncertainty. Overall, as we will discuss in Sec. 5.3, a hotter halo implies a larger gas mass, stronger CCA feeding and stronger AGN feedback power, thus establishing major positive correlations. In this regard, the $L_R - T_x$ relation can be used as a proxy to describe AGN feedback and feeding rates.

In passing, it is worth noting that all BGGs found at distances of more than $0.2\,R_{vir}$ from the X-ray centre (green) lie underneath the mean best-fit line suggesting that, at a given X-ray luminosity (or temperature), their radio luminosity is lower than in the more central BGGs. Again, the centeredness of the system appears to be key to initiate stronger feedback (and related feeding; see next Sec. 5.3).

AGN feeding and feedback cycle

In the previous sections, we showed that AGN activity is usually detected at the centres of galaxy groups, regardless of the properties of the optical galaxy. The triggering of the (mechanical) AGN activity thus appears to depend on the position of the host halo. In CCA, the central position in the group promotes the condensation and inflow of low-momentum gas from both the internal galactic gas and external intragroup medium. As a consequence, in CCA the AGN radio power correlates with the X-ray halo temperature (and luminosity), consistent with the results in Sec. 5.3. During CCA, inelastic collisions between the condensed clouds and filaments drive a rapid inflow toward the micro scale (a few tens of the Schwarzschild radius; Gaspari and Sądowski 2017). The ultrafast outflows and jets then entrain gas at the meso-scale (~ 1 kpc), with their kinetic energy dissipated and released at the macro-scale (tens kpc) via X-ray bubbles, shocks, and turbulence (e.g., Gaspari et al. 2011; Barai et al. 2016; Yang et al. 2019; Liu et al. 2019b; Wittor and Gaspari 2020). Thus, the ensuing cooling flow of the central intragroup medium can be quenched rapidly by AGN heating, leading to a new feedback cycle (Gaspari et al. 2020 for a review and unification diagram of such processes). On the other hand, the AGN in non-centrals/'satellites' can only feed from the diffuse gas inside its host galaxy ('internal weather'), and cannot easily tap into the reservoir of the intragroup medium due to their large infall/relative velocity. This is supported by our results, as powerful radio galaxies mostly lie at the group centre.

An alternative accretion mode for the SMBH is hot accretion. This mode can take various forms, from pure Bondi accretion – usually based on idealized assumptions such as the presence of a spherically symmetric, steady, adiabatic and gaseous atmosphere (Bondi, 1952) – to Advection-Dominated Accretion Flow (ADAF, Narayan and Yi 1995). Unlike in CCA, in hot-mode accretion, the gravitational pull of the SMBH is strongly counterbalanced by the thermal pressure of the hot X-ray halo, which needs to be overcome to allow the inner SMBH feeding. As a result, hot-mode accretion is often feeble and ~ 2 orders of magnitude less intense compared with cold modes (e.g., Gaspari et al. 2013). Moreover, the hot accretion modes would develop a negative trend between the SMBH mass and plasma entropy/temperature ($\dot{M}_{\rm B} \propto K_{\rm x}^{-3/2} \propto T_{\rm x}^{-3/2}$), with hotter halos accreting relatively less gas mass, which is ruled out by the observed SMBH mass versus X-ray halo scaling relations (Gaspari et al. 2019) and by our retrieved positive correlation $L_{\rm R} - T_{\rm x}$, a proxy for $P_{\rm BH} - T_{\rm x}$ (Sec. 5.3). Finally, no major duty cycle is expected from this mode. This is in conflict with a large intrinsic ε and with what is usually found in groups and clusters. There AGN feedback needs to rapidly suppress cooling of the hot halo via the AGN kinetic/radio power, i.e. establish frequent and efficient self-regulation (McNamara and Nulsen, 2007; Gaspari et al., 2011; Fabian, 2012; Gitti et al., 2012; Prasad et al., 2015; Yang and Reynolds, 2016).

Finally, we note that major mergers are unlikely to represent efficient triggers of the AGN and produce the scaling relations discussed here. The typical timescale of $\sim$ 5-6 Gyr between two major mergers (e.g., Rodriguez-Gomez et al., 2015) is too long to provide steady support for the feeding of AGN. This is also consistent with Sharma et al. (2021), who recently showed that AGN activity is not enhanced by mergers. Moreover, we do not find substantive evidence for violent mergers in our sample. Nevertheless, mergers can still play a role over time in terms of supplying and preserving a significant amount of gas on the outskirts of the group halo.

5.4 Conclusions

We have carried out a comparison of the kinematic and optical properties of four different samples of COSMOS spectroscopic galaxy members: BGGs with and without radio emission, and satellites with and without radio emission. Scaling relations for the BGG samples were also investigated. Our results can be summarised as follows:

- Out of 70 BGGs, 56 ($\sim$80%) are classified as ancient infallers, while the same fraction for satellites is only $\sim$42%. We find that the fraction of ancient infaller among radio BGGs is $\sim$82%, while the fraction of non-radio BGGs falling into this category is $\sim$78%. This suggests that most BGGs, and in particular those hosting radio emission, have been accreted by the group at an early time.
- We find that radio galaxies with $L_R > 10^{23}$ W Hz^{-1} always lie within 0.2 $R_{\rm vir}$ from the group centre, which has been defined as the X-ray emission peak. This is consistent with the current view of AGN feedback since the gas cooling out of the hot IGrM can feed the central SMBH, while outer galaxies need to rely on more episodic triggers.
- Our samples were compared to simulated BGGs from the HORIZON-AGN simulation. The ratio between the galaxy line-of-sight velocity and the group velocity dispersion for real BGGs (both radio and non-radio) shows a broader distribution than simulated galaxies, but still narrower than satellites. Statistical tests suggest that significant differences exist between simulated and real galaxies, indicating that additional physics may be needed to reproduce the true population of BGGs.
- We find that the stellar mass for radio BGGs is statistically higher than for non-radio BGGs. This, in combination with the correlation between BGG mass and group mass,

suggests that it is easier to find radio BGGs in higher-mass groups.

- We find positive correlations between the 1.4 GHz power of radio BGGs and the main properties of the diffuse X-ray halo/intragroup medium, namely, $L_{\rm R} - T_{\rm x}$ and $L_{\rm R} - L_{\rm x}$, suggesting a link between AGN heating and cooling processes in the gaseous halo.
- We tested and discussed the two major AGN feeding/feedback scenarios. Our finding that galaxies at group centres are often radio galaxies better supports the CCA scenario since the AGN can feed from both the galactic and intragroup halo condensations via a flickering duty cycle. This is more difficult to explain in hot accretion modes (e.g., Bondi or ADAF), which can only tap into the nuclear ($r < 100$ pc) pressure-supported plasma region via continuous accretion. Unlike in hot modes, CCA becomes more vigorous in hotter and more luminous/massive halos. Thus, CCA naturally induces positive $L_{\rm R} - T_{\rm x}$ and $L_{\rm R} - L_{\rm x}$ correlations, as found in our samples.

Acknowledgements. *We thank the referee for thoughtful comments that have improved the presentation of our results. AF thanks Gary Mamon and Stefano Borgani for insightful discussions. TP is supported by the BMBF Verbundforschung under grant number 50OR1906. MB acknowledges support from the Deutsche Forschungsgemeinschaft under Germany's Excellence Strategy - EXC 2121 "Quantum Universe" - 390833306. MG acknowledges partial support by NASA Chandra GO8-19104X/GO9-20114X and HST GO-15890.020-A grants.*

Data Availability

The data underlying this article are available upon reasonable request.

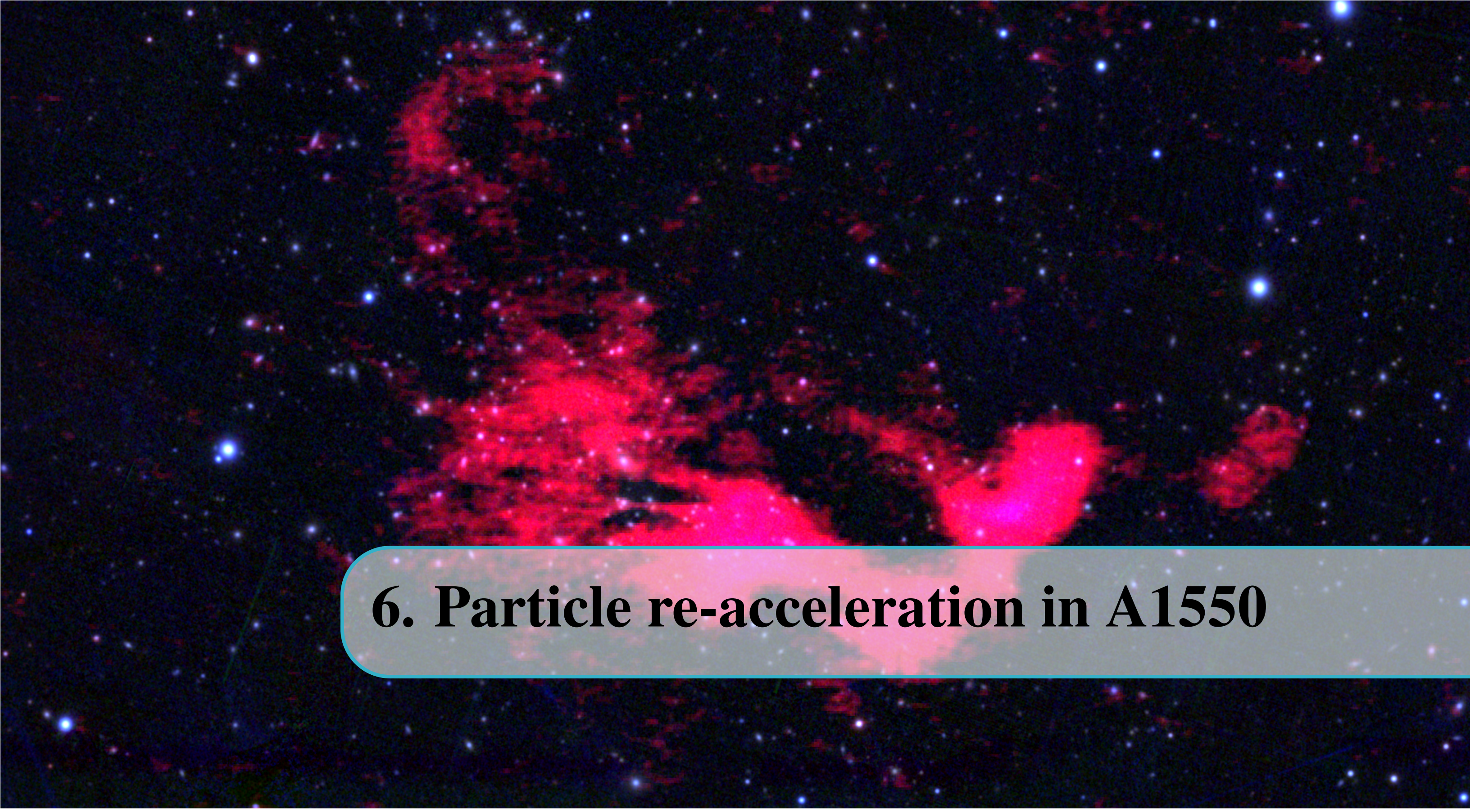

6. Particle re-acceleration in A1550

Particle re-acceleration and diffuse radio sources in the galaxy cluster Abell 1550

T. Pasini, H. W. Edler, M. Brüggen et al. Accepted by A&A (2022)

Abstract. *Radio observations of galaxy clusters reveal a plethora of diffuse, steep-spectrum sources related to the re-acceleration of cosmic-ray electrons, such as halos, relics, and phoenices. In this context, the LOw Frequency ARray Low-Band Antenna (LOFAR-LBA) Sky Survey (LoLSS) provides the most sensitive images of the sky at 54 MHz to date, allowing us to investigate re-acceleration processes in a poorly explored frequency regime. We study diffuse radio emission in the galaxy cluster Abell 1550, with the aim of constraining particle re-acceleration in the intra-cluster medium. We exploited observations at four different radio frequencies: 54, 144, 400, and 1400 MHz. To complement our analysis, we made use of archival Chandra X-ray data. At all frequencies we detect an ultra-steep spectrum radio halo ($S_\nu \propto \nu^{-1.6}$) with an extent of $\sim$ 1.2 Mpc at 54 MHz. Its morphology follows the distribution of the thermal intra-cluster medium inferred from the Chandra observation. West of the centrally located head-tail radio galaxy, we detect a radio relic with a projected extent of $\sim$ 500 kpc. From the relic, a $\sim$600 kpc long bridge departs and connects with the halo. Between the relic and the radio galaxy, we observe what is most likely a radio phoenix, given its curved spectrum. The phoenix is connected to the tail of the radio galaxy through two arms, which show a nearly constant spectral index for $\sim$ 300 kpc. The halo could be produced by turbulence induced by a major merger, with the merger axis lying in the NE-SW direction. This is supported by the position of the relic, whose origin could be attributed to a shock propagating along the merger axis. It is possible that the same shock has also produced the phoenix through adiabatic compression, while we propose that the bridge could be generated by electrons which were pre-accelerated by the shock, and then*

re-accelerated by turbulence. Finally, we detect hints of gentle re-energisation in the two arms that depart from the tail of the radio galaxy.

6.1 Introduction

Radio observations reveal the presence of diffuse synchrotron emission in galaxy clusters which is not directly associated with galaxies. This kind of emission is thought to be produced by the (re-)acceleration of cosmic-ray (CR) electrons due to shocks and turbulence in the intra-cluster medium (ICM) (Brüggen et al., 2012; Brunetti and Jones, 2014). The synchrotron spectra of these electrons typically show a power-law distribution, $S(\nu) \propto \nu^{\alpha}$, with $S(\nu)$ being the flux density at frequency ν, and α being the spectral index.

Giant radio halos (RHs) are megaparsec-scale sources centred in the central regions of merging clusters (Cassano et al., 2010). They usually exhibit a spherically symmetric morphology, even though filamentary structures are sometimes detected (van Weeren et al., 2017; Botteon et al., 2020a). The radio emission is spatially correlated to the distribution of the ICM revealed by X-ray observations (Govoni et al., 2001; Giacintucci et al., 2005; Rajpurohit et al., 2018), suggesting a link between thermal and non-thermal plasma. The integrated spectral index of RHs typically ranges between $-1.1 \leq \alpha \leq -1.4$ (Giovannini et al., 2009; Feretti et al., 2012). Nevertheless, an increasing number of RHs with ultra-steep spectra (USSRH) were discovered, with indices in the range $-1.5 \leq \alpha \leq -2$ (e.g. Brunetti et al., 2008; Macario et al., 2010; Dallacasa et al., 2009; Bonafede et al., 2012; Wilber et al., 2018; Bruno et al., 2021; Duchesne et al., 2022). The luminosity of RHs correlates with the host cluster's X-ray luminosity, making their detection easier in high-mass objects (e.g. Cassano et al., 2013; Cuciti et al., 2015). Radio halos are mainly observed in merging clusters (Cassano et al., 2013; Cuciti et al., 2015) and their origin is traced back to mechanisms driven by large-scale turbulence (e.g. Brunetti et al., 2009; Cassano et al., 2010; Eckert et al., 2017). Cuciti et al. (2021) found that, in their sample of 75 galaxy clusters, 90% of halos are hosted in disturbed objects, while only 10% are in relaxed systems.

Cluster radio relics are usually found in the outskirts of merging galaxy clusters. They exhibit elongated morphologies and high degrees of polarisation above 1 GHz (up to 70%, Ensslin et al. 1998; Bonafede et al. 2014; Loi et al. 2019; de Gasperin et al. 2022). The resolved spectral index in radio relics shows a gradient: it steepens towards the cluster centre and flattens towards the outskirts. Their size can reach up to $\sim$2 Mpc, and high-resolution observations have revealed filamentary structures within relics themselves (Di Gennaro et al., 2018; Rajpurohit et al., 2020; de Gasperin et al., 2022; Rajpurohit et al., 2022a,b). The Largest Linear Sizes (LLS) and radio powers of relics are correlated, as well as the integrated spectral index and the radio power (van Weeren et al., 2009b; Bonafede et al., 2012; de Gasperin et al., 2014). Relics trace ICM shock waves with relatively low (M<3) Mach numbers (Finoguenov et al., 2010; Akamatsu et al., 2013; Shimwell et al., 2015; Botteon et al., 2016). The acceleration of electrons is believed to proceed via diffusive shock acceleration (DSA) in the ICM (Ensslin et al., 1998; Roettiger et al., 1999), in which particles scatter back and forth across the shock front gaining energy at every crossing. Nevertheless, this mechanism has been shown to be rather inefficient in accelerating electrons from the thermal pool (Vazza and Brüggen 2014; Vazza et al. 2016; Botteon et al. 2020b; Brüggen and Vazza 2020b; see Brunetti and Jones 2014 for a review). Recently, it has been suggested that seed electrons could originate from the tails and lobes (driven by AGN outflows) of cluster radio galaxies (Bonafede et al., 2014; van Weeren et al., 2017; Stuardi et al., 2019), which alleviates the requirements of high acceleration efficiencies at cluster shocks (e.g. Markevitch et al., 2005; Kang et al., 2012; Botteon et al., 2016; Eckert et al., 2016; Kang et al., 2017). In some cases, double relics have been detected on opposite sides of the cluster centre (e.g. Rottgering et al., 1997; van Weeren et al., 2010, 2012a; Bonafede et al., 2012; de Gasperin et al., 2015a). In these clusters it is possible to constrain the merger history, providing important information about the formation processes of relics.

Relativistic electrons with higher energies lose energy faster via synchrotron and Inverse Compton (IC) radiation. Therefore, the emission at high frequencies fades first. An old population of relativistic electrons, sometimes referred to as fossil plasma, can in some cases be 'revived', for instance by adiabatic compression (Enßlin and Gopal-Krishna, 2001), leading to radio phoenices. These sources are characterised by steep and curved spectra ($\alpha <$ -1.5, van Weeren et al. 2009a; Clarke et al. 2013; de Gasperin et al. 2015b; Mandal et al. 2019). They can exhibit different morphologies, even though in most cases they look elongated and filamentary (e.g. Slee et al., 2001). Compared to relics, phoenices are found at smaller distances from the cluster centre (Feretti et al., 2012) and they are smaller (<500 kpc). They can also be found in relaxed objects (e.g. van Weeren et al., 2011), suggesting that major mergers are not strictly necessary for their formation. An alternative mechanism to re-accelerate old plasma was recently proposed by de Gasperin et al. (2017). This was based on radio observations of Abell 1033 (A1033), in which long tails of radio bright plasma, generated by a radio galaxy moving within the cluster environment, are seen to brighten, in coincidence with a spectral index flattening. A possible explanation is that instabilities, generated by the interaction of the magnetically confined plasma in the tails and the turbulence in the surrounding medium, can lead to turbulent waves. These, in turn, are able to accelerate seed electrons through second-order Fermi mechanisms. This source was labelled Gently Re-Energised Tail (GReET) since the re-acceleration mechanism is barely efficient enough to balance the radiative losses of the electrons. Low-frequency observations of galaxy clusters are detecting an increasing number of tailed radio galaxies undergoing similar re-acceleration processes (e.g. Cuciti et al., 2018; Wilber et al., 2018; Botteon et al., 2021; Ignesti et al., 2022; Brienza et al., 2022; Pandge et al., 2022).

The contribution of the LOw-Frequency ARray (LOFAR, van Haarlem et al. 2013) is essential to achieve a better understanding of re-acceleration processes because of its unprecedented combination of sensitivity at low frequencies and resolution. Two surveys are currently being carried out with LOFAR. The LOFAR Two-Metre Sky Survey (LoTSS, Shimwell et al. 2017, $< rms >\sim 100\mu$Jy beam^{-1}) will observe the Northern Sky at a nominal frequency of 144 MHz (High Band Antennas, HBA) with a resolution of ∼6". This survey is currently undergoing the second Data Release (DR2, Shimwell et al. 2022), covering $\sim$6000 deg^2, while DR1 covered the HETDEX spring field[1] (Shimwell et al., 2019). Similarly to LoTSS, the Lofar LBA Sky Survey (LoLSS, de Gasperin et al. 2021) will observe the Northern Sky at a nominal frequency of 54 MHz (Low Band Antennas, LBA) with a resolution of $\sim$15", with the first Data Release covering HETDEX (de Gasperin et al., 2021). The data reduction and calibration of HETDEX is now completed. The analysis of all known galaxy clusters in this field at 54 MHz, similarly to what was done at 144 MHz by van Weeren et al. 2021 (hereafter VW21), will be carried out in a forthcoming publication (Pasini et al. in prep.).

In this paper, we present LOFAR, Upgraded Giant Metrewave Radio Telescope (uGMRT) and Very Large Array (VLA) observations of one of the most interesting HETDEX clusters, Abell 1550 (alternatively PSZ2G133.60+69.04, hereafter A1550). This is a dynamically disturbed cluster located at $z \sim 0.254$, with M_{500}[2] $\sim 5.88 \times 10^{14} M_{\odot}$ (Planck Collaboration et al., 2016). According to Wen and Han (2013), the cluster hosts about a hundred confirmed member galaxies within $R_{200} \sim 2$ Mpc. Extended emission was already claimed by Govoni et al. (2012) through 1.4 GHz Very Large Array (VLA) data in D and C configuration. LOFAR observations at 144 MHz confirm the presence of diffuse emission (VW21, Botteon et al. 2022), albeit on a greater scale of 1.8 Mpc. The difference in size is due to the high sensitivity and low frequency coverage of LOFAR. A *Chandra* 7 ks archival observation is also available, while the ROSAT All-Sky Survey (RASS) measures an X-ray luminosity of $L_X \sim 3.5 \times 10^{44}$ erg s^{-1} in the 0.1-2.4 keV band (Böhringer et al., 2000). In Sec. 6.2 we discuss the data reduction and calibration, while in Sec. 6.3 we present our results which are then discussed in Sec. 6.4. Finally, in Sec. 6.5 we summarise our main conclusions. We assume a standard ΛCDM cosmology with $H_0 = 70$ km s^{-1} Mpc^{-1}, $\Omega_\Lambda = 0.7$ and $\Omega_M = 1 - \Omega_\Lambda = 0.3$, and errors are at 68% confidence level (1σ).

6.2 Data analysis

LBA observations

The galaxy cluster A1550 was observed by LOFAR in the 42 – 66 MHz band as part of the HETDEX field, which is the first region of the sky targeted by LoLSS (de Gasperin et al., 2021). The cluster is covered by four different pointings (see Table 6.1 for details), for a total of 27 hours after data reduction and calibration.

Data were calibrated using the automated Pipeline for LOFAR LBA (PiLL[3]). The pipeline was independently run for each of the pointings and it is described in detail in de Gasperin et al. (2021). Here, we summarise the main steps. First, phase and bandpass solutions of the calibrator are determined and transferred to the target field. Then, direction-independent calibration of the target field is performed to correct for the direction-averaged ionospheric delays, Faraday rotation and second-order beam errors. At this step, wide-field images are produced and direction-dependent (DD) errors, mainly due to ionospheric

[1] RA: 11h to 16h and Dec: 45° to 62° (Hill et al., 2008).

[2] Mass within R_{500}, defined as the radius at which the medium density is 500 times the critical density of the Universe.

[3] Publicly available at https: //github.com/revoltek/LiLF

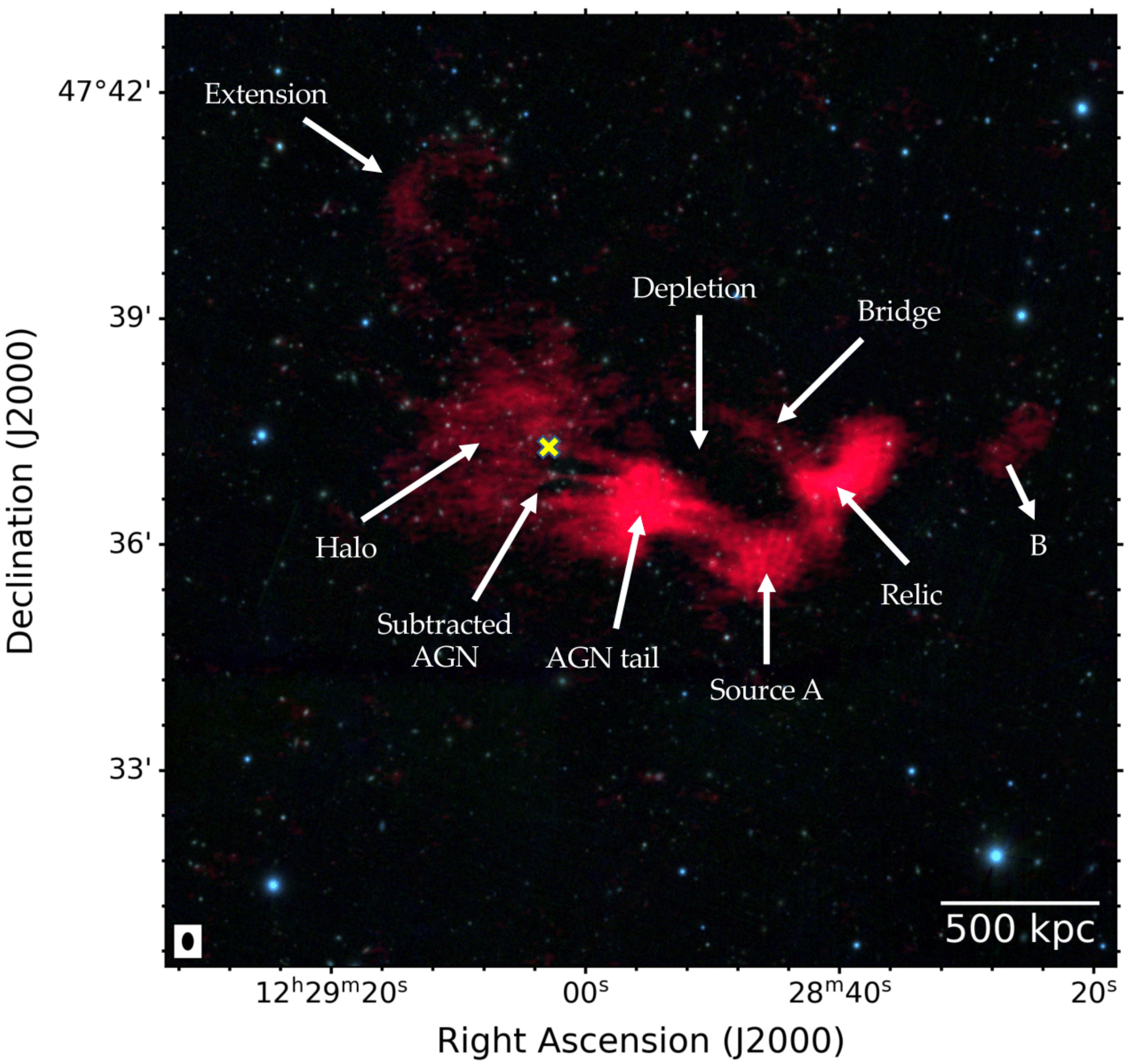

Figure 6.1: A1550 seen in 144 MHz emission (red) as detected by LOFAR overlaid on the PanSTARSS optical (RGB filters) image. The radio image has a resolution of 13"×8", and the beam is shown on the bottom right. The most prominent structures that are discussed in the text are labelled. Compact sources are subtracted to enhance diffuse emission as described in Sec. 6.2. The yellow cross marks the cluster X-ray centre, defined as the peak of the emission and estimated from the *Chandra* image presented in Sec. 6.2.

inhomogeneities, still affect the data. To correct these errors, we adopt the following strategy for direction-dependent calibration: we subtract all sources from the visibilities using the model obtained during direction-independent calibration. Then, we re-add the brightest source to the data and derive calibration solutions for the direction corresponding to this source using self-calibration. Using these solutions and the improved source model, we subtract the source again, this time more accurately. This cycle is repeated for all sufficiently bright sources (DD sources) in the field of view (FoV). We then divide the FoV into facets whose position and shape depend on the position of DD sources. Each facet is calibrated for DD effects during imaging using the correction of the respective calibrator. This is done

Observation	Central frequency	RA [*hh:mm:ss*]	DEC [*deg:mm:ss*]	Total exposure	Target distance [deg]	Antenna configuration
P183+47	54 MHz	12:13:09.65	+47:15:17.30	6hr	2.75	LOFAR LBA_OUTER
P186+50	54 MHz	12:27:40.70	+49.46.59.83	7hr	2.09	LOFAR LBA_OUTER
P187+47	54 MHz	12:28:25.34	+47.16.29.19	7hr	0.45	LOFAR LBA_OUTER
P190+47	54 MHz	12:43:41.37	+47.17.41.33	7hr	2.48	LOFAR LBA_OUTER
P23Hetdex	144 MHz	12:21:08.60	+47:29:24.00	8hr	1.30	LOFAR HBA_DUAL_INNER
P26Hetdex	144 MHz	12:29:37.60	+49:44:24.00	8hr	2.13	LOFAR HBA_DUAL_INNER
P27Hetdex	144 MHz	12:38:06.70	+47:29:24.00	8hr	1.55	LOFAR HBA_DUAL_INNER
12435	400 MHz	12:28:54.00	+47:36:44.00	3hr	0.03	uGMRT BAND 3
18A-172*	1.4 GHz	12:29:12.7	+47:42:25.38	1hr	0.09	JVLA C array
18A-172*	1.4 GHz	12:29:12.7	+47:42:25.38	1hr	0.09	JVLA D array

Table 6.1: The table shows the details of the LBA, HBA, uGMRT and JVLA observations used for the analysis of A1550. From left to right: pointing or observation name, nominal frequency of the observation, coordinates of the phase centre, distance of A1550 from the phase centre and configuration of the antennae of the related observation. *: *Project name*.

using `DDFacet` (Tasse et al., 2018), and produces a DD-calibrated wide-field image. To further improve image quality, we repeat the steps of the direction-dependent calibration, starting from the DD-calibrated image.

It is still possible to optimise the calibration for a specific target of interest (not included among DD sources), as in our case for A1550. Here, we adapted the extraction process described in VW21 to LBA data. The procedure has already been tested in Biava et al. (2021). During DD calibration, it is assumed that DD effects are uniform across the facet. By selecting a smaller region (typically $15' - 20'$) around the target, it is possible to relax this assumption and improve calibration (see also VW21 for more details). The extraction region should contain enough flux density to allow a good calibration of the target.

The procedure consists of the following steps: first, we subtract all sources outside the extraction region. We then shift the phase centre of the observation to the centre of the region, and we average the data in frequency and time. We apply a correction to account for the LOFAR primary beam response at the new phase centre through IDG (Image-Domain Gridder, van der Tol et al. 2018). Pointings for which the beam response drops below 30% are excluded, while all the others are combined and weighted so that pointings with higher beam sensitivity contribute more to the extracted dataset. Then we perform self-calibration cycles as in VW21 to further reduce the noise and improve the quality of the images. Final imaging is carried out using `WSClean` (Offringa et al., 2014) applying suitable weighting and tapering of the visibilities in order to obtain images at different resolutions. Also we use multi-scale deconvolution (Offringa, 2016), and we assume that flux errors are $\sim$10%, as for LoLSS (de Gasperin et al., 2021).

In some cases we needed to highlight the emission from diffuse sources. When specified, we subtracted compact sources as follows: first, we produced a high-resolution image by applying `Briggs -0.6` and cutting visibilities below 100λ, which correspond to angular scales above $35'$. We chose the resolution such that only compact sources with a Largest Linear Size (LLS) below a given threshold are imaged. Through the `predict` option of WSClean, the clean components of the previous image are stored as model. Finally, we subtract this model out of the *uv*-data. This leaves us with only the visibilities of the diffuse emission.

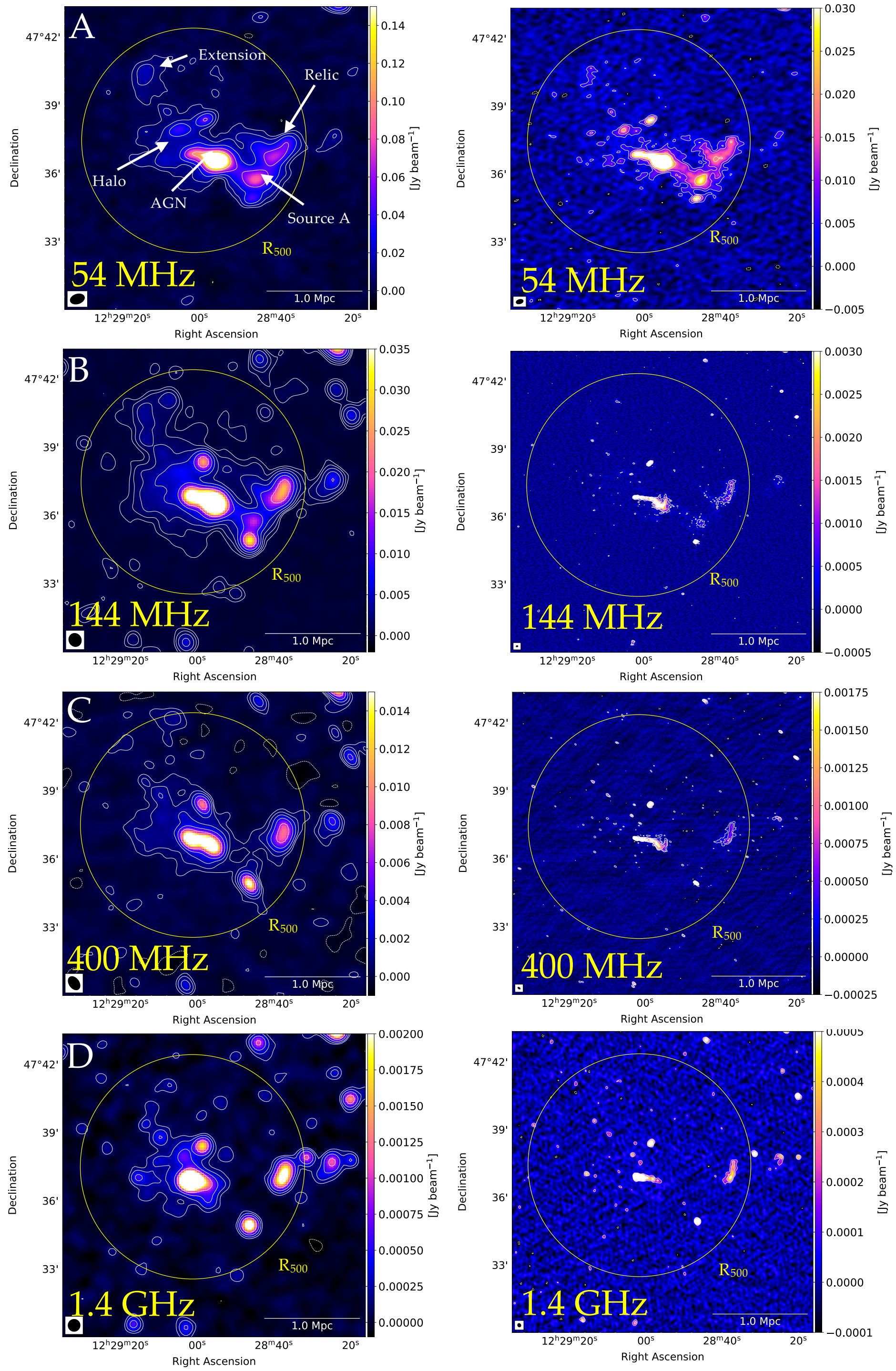

Figure 6.2: First to last row: 54, 144, 400 MHz and 1.4 GHz, low- (left column) and high-resolution (right column) images of A1550, produced by tapering visibilities at 30"and applying `Briggs -0.6`, respectively. The yellow circle denotes $R_{500} = 1173$ kpc (Botteon et al., 2022). *Row A, left panel*: 54 MHz low-resolution image. The beam is 38"×25", with *rms* noise $\sigma \sim$1.6 mJy beam^{-1}. Contours are at [-3, 3, 6, 12, 24] $\times\sigma$. *Row A, right panel*: 54 MHz high-resolution image. The beam is 18"×11", with *rms* noise $\sigma \sim$1.5 mJy beam^{-1}. *Row B, left panel*: 144 MHz low-resolution image. The beam is 35"×32", with *rms* noise $\sigma \sim$0.14 mJy beam^{-1}. *Row B, right panel*: 144 MHz high-resolution image. The beam is 8"×4", with *rms* noise $\sigma \sim$69 μJy beam^{-1}. *Row C, left panel*: 400 MHz low-resolution image. The beam is 38"×26", with *rms* noise $\sigma \sim$0.28 mJy beam^{-1}. *Row C, right panel*: 400 MHz high-resolution image. The beam is 6"×3", with *rms* noise $\sigma \sim 60$ μJy beam^{-1}. *Row D, left panel*: 1.4 GHz low-resolution image. The beam is 32"×32", with *rms* noise $\sigma \sim 26$ μJy beam^{-1}. *Row D, right panel*: 1.4 GHz high-resolution image. The beam is 13"×12", with *rms* noise $\sigma \sim 18$ μJy beam^{-1}.

HBA observations

A1550 was observed by LOFAR in the frequency range 120-166 MHz as part of the second Data Release (DR2) of LoTSS (Shimwell et al., 2022). The cluster is covered by three pointings (see Table 6.1 for details), for a total of ∼24 hours. The data were processed with a set of fully automated pipelines developed by the LOFAR Surveys Key Science Project team: `prefactor` (van Weeren et al., 2016; Williams et al., 2016b; de Gasperin et al., 2019b) and `ddf-pipeline` (Tasse et al., 2021b). These pipelines are able to correct for both direction-independent and direction-dependent effects. The pipelines also include flagging of the radio frequency interference (RFI). Then the *uv*-data is averaged in time and frequency, and complex gains, clock offsets and phase delays are obtained and applied to each station. The calibration of direction-dependent effects (DDE) is then performed using the same facet method discussed for LBA.

In this work, we exploit the same datasets which were recently presented in Botteon et al. (2022). New images were produced through `WSClean` with different sets of parameters, depending on our purposes, applying multiple weighting schemes and visibility tapering. The flux density scale was aligned with the LoTSS-DR2 data release (Botteon et al., 2022), where the flux calibration uncertainty is estimated to be ∼10% (Hardcastle et al., 2021). Where explicited, compact-source subtraction was performed exploiting the same method described in Sec. 6.2.

GMRT observation

A1550 was observed by uGMRT on September 17th, 2020, for a total integration time of 3 hours (ObsID = 12435, PI V. Cuciti). Observations were carried out in band 3 (330-500 MHz), with nominal frequency 400 MHz. 3C286 was used as absolute flux density calibrators. Data reduction and calibration were carried out using the Source Peeling and Atmospheric Modeling (`SPAM`) pipeline (Intema et al., 2009, 2017), which corrects for ionospheric effects and removes direction-dependent gain errors. Direction-dependent gains were derived through bright sources in the field of view. Finally, data were corrected for the system temperature variations between calibrators and target. Imaging is carried out through `WSClean` applying different weightings and visibility tapering. The flux uncertainty is assumed to be 6% (Chandra et al., 2004). When specified, we applied the same compact-source subtraction procedure described in Sec. 6.2.

JVLA observations

We obtained JVLA observations of A1550 in the 1-2 GHz JVLA L-band, in C and D antenna configuration (Project ID = 18A-172, PI R. J. van Weeren). The former was performed on January 19, 2019 for a total of 1 hour, pointed at RA=12h29m12.75s DEC=47°42′25.4", while the latter is a 1 hour observation performed on 20 September, 2018 and pointed at the same coordinates. Data reduction was carried out with the National Radio Astronomy Observatory (NRAO) Common Astronomy Software Applications package (CASA, version 6.1.2.7), exploiting 3C286 as primary calibrator for both observations, while J1219+4829 was used as phase calibrator. First, RFI and bad visibilities for calibrators and target were flagged. Amplitude and phase solutions were derived from the calibrators, and applied to the target. For the purpose of self-calibration, phase-solutions are then calculated from the model of the target, produced by a first, shallow imaging, and computed on a given timescale for which the phase is assumed to be constant. After applying these solutions, the cycle is repeated in order to increase the signal-to-noise ratio (S/N) and improve the quality of the image, decreasing the interval at each cycle. After this step, datasets were accurately combined to achieve longer integration time and increase the sampling of the *uv*-plane. Final imaging is carried out with `WSClean`, and the flux uncertainty is assumed to be 5%. When specified, we applied the same compact-source subtraction procedure described in Sec. 6.2. Finally, for polarisation calibration, the leakage response was determined using the unpolarised calibrator 3C147. The absolute position angle (the R-L phase difference) was corrected using the polarised calibrator 3C286. The polarisation intensity (P) and polarisation angle (Ψ) maps were derived from Stokes Q and U maps:

$$\begin{aligned} P &= \sqrt{Q^2+U^2}, \\ \Psi &= \frac{1}{2}\tan^{-1}\frac{U}{Q}. \end{aligned} \tag{6.1}$$

Finally, the fractional polarisation map was obtained as:

$$p = \frac{P}{I}, \tag{6.2}$$

where I and P are the total intensity and polarisation intensity, respectively, of the source.

Chandra observation

The *Chandra* data of A1550 (obsID 11766) were taken with the Advanced CCD Imaging Spectrometer (ACIS) in S configuration, operating in VFAINT mode, with a short exposure time of $\sim$7 ks. The ACIS-S configuration consists of an array of 6 chips. We use the ACIS-S3 chip, where the aimpoint of the telescope lies. Unfortunately, the cluster emission covers a projected region larger than the CCD area ($8.3' \times 8.3'$). For this reason, part of the cluster emission is out of the FoV and cannot be studied. The maximal area that can be reached lies within a radius of 4 arcmin from the cluster centre, which corresponds to $\sim 0.8 R_{500}$.

The data were reprocessed with CIAO 4.11[4] using CALDB 4.8.4.1. The `Chandra_repro` script was executed to perform the standard calibration process. Background flares were removed and the `Blanksky` template files, filtered and normalised to the count rate of the source in the hard X-ray band (9-12 keV), were exploited to model the background contribution to the emission. Finally, point sources were identified and removed using the CIAO task `WAVDETECT` with a default significance threshold of 10^{-6}. The final exposure time is 6948 s. Exposure-corrected images were produced in the 0.5-7 keV band.

[4] https://cxc.harvard.edu/ciao/

6.3 Results

HBA and LBA comparison

In Fig. 6.1 we show the radio emission as detected at 144 MHz by HBA, overlaid on the Panoramic Survey Telescope and Rapid Response System (PanSTARRS, Chambers et al. 2016) image of A1550. Projected at the cluster centre, an head-tail (HT) radio galaxy (labelled as AGN+tail in the figure) dominates the emission. The galaxy is embedded within the giant radio halo originally detected by Govoni et al. (2012). In the SW, a roundish patch of emission (A) is observed, without a clear optical counterpart. NW of source A, we clearly detect a source which resembles a radio relic, as already hinted at in VW21 and Botteon et al. (2022). From this image, it is not clear whether the putative relic and source A are part of the same structure. From here, two filaments extend to the E and W directions. The eastern filament (bridge) looks connected to the halo, as already found at 144 MHz by VW21 from low-resolution images. The western filament, labelled B, has no clear counterpart as well, even though its morphology suggests that it could be a radio galaxy, possibly unrelated to the diffuse emission. An elliptical depletion of radio emission is observed between the bridge, the head-tail and source A. Finally, in the NE region of the cluster, we observe an arc-shaped extension of emission. As already discussed in VW21, it lies in front (at least in projection) of a group of galaxies with the same redshift of A1550. Low-resolution images at 144 MHz showed that it is likely connected to the halo (VW21 and Botteon et al. 2022). We return on this throughout this paper.

With the purpose of unveiling the nature and morphology of each of these structures, we produced images at different frequencies and resolution. In the left panels of the first two rows in Fig. 6.2, we show the cluster as detected at 54 MHz and 144 MHz by tapering visibilities at 30". The head-tail dominates the radio emission, with integrated flux density inside 3σ contours[5] of $S_{144\mathrm{MHz}} = 264 \pm 26$ mJy and $S_{54\mathrm{MHz}} = 707 \pm 71$ mJy, respectively. The putative relic and halo are clearly visible at both frequencies, and the morphology and orientation of the NE extension suggest that it is connected to the halo. The bridge connecting the candidate relic to the halo, while resolved in HBA, is hardly distinguishable in the LBA image due to lower resolution.

In order to resolve all the detected structures, we produced high-resolution images by setting `Briggs -0.6` and excluding baselines shorter than 100λ. The halo almost disappears at both frequencies (see right panels of Fig. 6.2), while we are still able to see the candidate relic and source A. At 144 MHz, the emission that connects source A to the AGN/halo is split into two arms, which will be better defined and analysed in Sec. 6.4. The lack of optical counterparts, together with the shape and orientation of the head-tail radio galaxy and relic, might suggest that source A could be constituted by re-accelerated electrons (see Sec. 6.4).

We then subtracted compact sources as described in Sec. 6.2 on the HBA and LBA observations and tapered visibilities at 30", with the purpose of imaging more accurately the diffuse emission. The resulting images are shown in Fig. 6.3. Without the AGN, it is much easier to assess the different structures observed in A1550, and we can therefore estimate

[5] If not specified otherwise, all flux densities are calculated within 3σ contours.

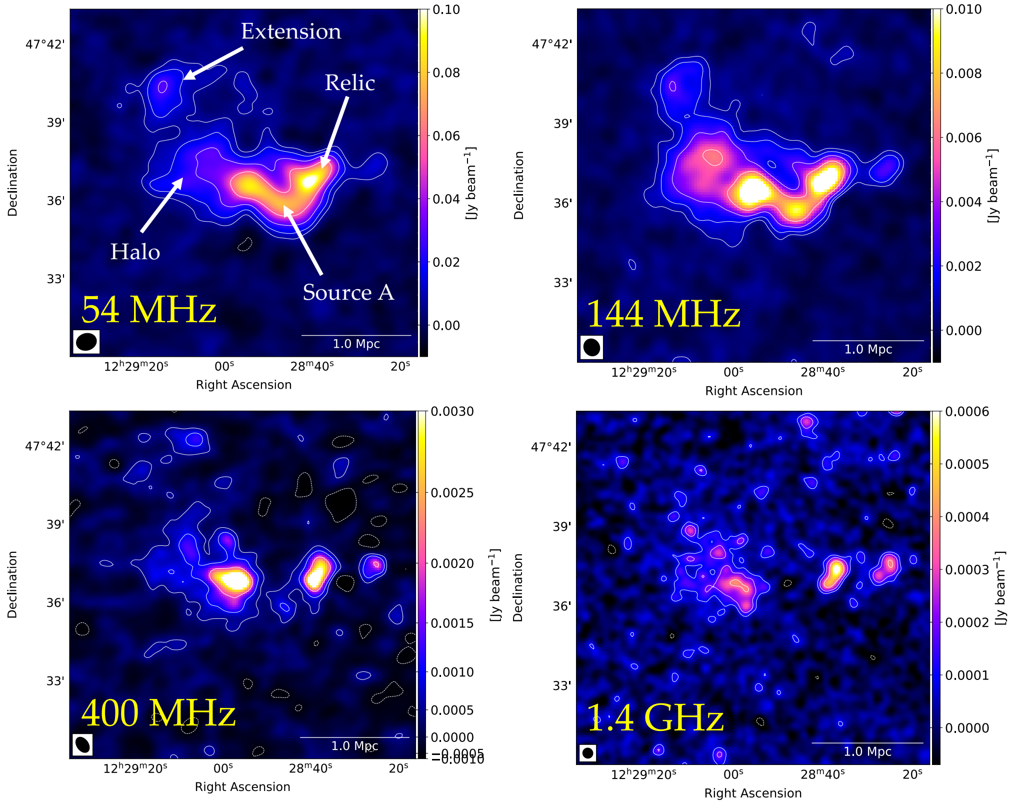

Figure 6.3: Source-subtracted images of A1550 at different frequencies. *Top left*: 54 MHz source-subtracted image of A1550 obtained applying `Briggs -0.3` and tapering the visibilities to 30". The beam, shown on the bottom left, is 46"×36", with *rms* noise $\sigma \sim$ 1.9 mJy beam^{-1}. Contours are at -3, 3, 6, 12, 24 $\times\sigma$. *Top right*: 144 MHz source-subtracted image of A1550 obtained applying `Briggs -0.3` and tapering the visibilities to 30". The beam is 36"×35", with *rms* noise $\sigma \sim$ 0.14 mJy beam^{-1}. Contours are the same as above. *Bottom left*: 400 MHz source-subtracted image of A1550 obtained applying `Briggs -0.3` and tapering the visibilities to to 30". The beam is 36"×26", with *rms* noise $\sigma \sim$ 0.23 mJy beam^{-1}. *Bottom right*: 1.4 GHz source-subtracted image of A1550 obtained applying `Briggs -0.3` and tapering the visibilities to to 30". The beam is 32"×32", with *rms* noise $\sigma \sim$ 23 μJy beam^{-1}.

their physical properties, such as flux density and extent, more accurately.

To estimate the flux density of the halo, we used the Halo Flux Density CAlculator (Halo-FDCA, Boxelaar et al. 2021) on the subtracted maps. This code fits the surface brightness of radio halos to 2D exponential models using Bayesian inference, and calculates the flux density analytically. The plots of the halo models and masks used for the fit are shown in Appendix .1. After accounting for the contribution of the radio galaxy tail and masking both source A and NE extension, we measure a flux density for the halo of $S_{144\mathrm{MHz}} = 108 \pm 11$ mJy, which is in agreement with what we measure from 2σ contours, and a maximum extent of $\sim$1 Mpc. The fit also provides an estimate of the e-folding radius of $r_e = 183 \pm 4$ kpc. We note that VW21 reported a flux density of $S_{144\mathrm{MHz}} = 129 \pm 26$ mJy, while Botteon et al. (2022) provides an estimate of $S_{144\mathrm{MHz}} = 145 \pm 18$ mJy. The difference with the previous results is likely related to the fact that although VW21 and Botteon et al.

Source	$S_{54\mathrm{MHz}}$ [mJy]	$S_{144\mathrm{MHz}}$ [mJy]	$S_{400\mathrm{MHz}}$ [mJy]	$S_{1.4\mathrm{GHz}}$ [mJy]	$\alpha_{54\mathrm{MHz}}^{144\mathrm{MHz}}$	$\alpha_{144\mathrm{MHz}}^{400\mathrm{MHz}}$	$\alpha_{400\mathrm{MHz}}^{1.4\mathrm{GHz}}$
Halo	498 ± 57	108 ± 11	25 ± 3	2.6 ± 0.2	-1.6 ± 0.2	-1.4 ± 0.1	-1.8 ± 0.1
Relic	265 ± 26	94 ± 9	25 ± 2	5.2 ± 0.3	-1.1 ± 0.2	-1.3 ± 0.2	-1.2 ± 0.2
Source A	165 ± 17	27 ± 3	3.1 ± 0.2	$< 0.13^*$	-1.9 ± 0.2	-2.1 ± 0.1	/

Table 6.2: Flux densities and integrated spectral indices of halo, relic and source A at different radio frequencies.*: 3σ upper limit, with σ being the *rms* noise of the 1.4 GHz image.

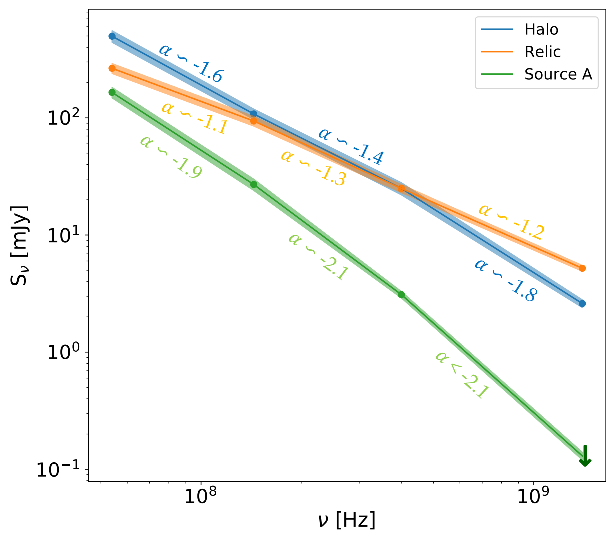

Figure 6.4: Flux density as a function of frequency for the halo, the relic and source A at the four frequencies covered in our analysis. Coloured areas denote flux density errors. We note that the flux density at 1.4 GHz for source A is a 3σ upper limit, with σ being the *rms* noise of the 1.4 GHz image.

(2022) also used FDCA, they performed the fit with an elliptical model, while we used a circle model. In Botteon et al. (2022), this resulted in radii of 377 ± 5 and 201 ± 4 kpc, for the major and minor axes respectively. Given the wealth of radio data studied in this work, the circle model appears to better suit the morphology of the halo emission. From the LBA image, we find $S_{54\mathrm{MHz}} = 498 \pm 57$ mJy and projected LLS$\sim$1.2 Mpc. This implies a relatively steep spectral index of $\alpha_{54\mathrm{MHz}}^{144\mathrm{MHz}} = -1.6 \pm 0.2$. The *e*-folding radius is estimated to be $r_e = 177 \pm 6$ kpc, consistent within errors with HBA.

The putative relic shows $S_{144\mathrm{MHz}} = 94 \pm 9$ mJy, with a projected length of $\sim$500 kpc. With LBA, we measure $S_{54\mathrm{MHz}} = 265 \pm 26$ mJy. This implies $\alpha_{54\mathrm{MHz}}^{144\mathrm{MHz}} = -1.1 \pm 0.2$, which is typical of relics (VW21). Finally, for source A we find $S_{144\mathrm{MHz}} = 27 \pm 3$ mJy and $S_{54\mathrm{MHz}} = 165 \pm 17$ mJy, resulting in a steep spectrum with $\alpha_{54\mathrm{MHz}}^{144\mathrm{MHz}} = -1.9 \pm 0.2$. A more detailed investigation of spectral indices in this cluster is presented in Sec. 6.3. In Table 6.2, we summarise the flux densities at different frequencies of the halo, candidate relic and source A. Their spectra are plotted in Fig. 6.4.

The cluster at 400 MHz

In the third row of Fig. 6.2 we show the 400 MHz low- and high-resolution images of A1550. The head-tail radio galaxy dominates the emission. To the West of the head-tail, the putative relic is clearly visible, with a flux density $S_{400\mathrm{MHz}} = 25 \pm 2$ mJy. Hence, its integrated spectral index between 144 and 400 MHz is $\alpha_{144\mathrm{MHz}}^{400\mathrm{MHz}} = -1.3 \pm 0.2$, consistent with what estimated at LOFAR frequencies. At 400 MHz we do not see the bridge, suggesting that it has a steep spectrum. Furthermore, it is not trivial to understand whether the emission between the head-tail and the candidate relic belongs to source A or comes from these two sources. Instead, around the radio galaxy we clearly observe the radio halo.

As before, we then subtracted compact sources and tapered visibilities to a resolution of 30", with the result shown in the bottom-left panel of Fig. 6.3. We observe what is probably a hint of emission of source A, even though it is detected barely at 3σ significance. At this frequency, we measure a maximal extent of the halo of $\sim$950 kpc and a flux density (with Halo-FDCA) of $S_{400\mathrm{MHz}} = 25 \pm 3$ mJy. This translates into a spectral index between 144 MHz and 400 MHz of $\alpha_{144\mathrm{MHz}}^{400\mathrm{MHz}} = -1.4 \pm 0.2$, consistent within errors with the one estimated between 54 and 144 MHz. The e-folding radius is $r_e = 171 \pm 10$ kpc, which is comparable to those estimated at lower frequencies.

Finally, the flux density of source A at this frequency is $S_{400\mathrm{MHz}} = 3.1 \pm 0.2$ mJy. The integrated spectral index between 144 and 400 MHz is as steep as $\alpha_{144\mathrm{MHz}}^{400\mathrm{MHz}} = -2.1 \pm 0.2$. We therefore observe a steepening at higher frequencies, hinting that the spectrum of source A might be significantly curved.

The cluster at 1.4 GHz

In the bottom panels of Fig. 6.2 we show A1550 at 1.4 GHz as observed by JVLA, at low and high resolution. At this frequency the halo appears less extended, as expected, but still clearly visible. We also detect the candidate relic, while we observe no emission from source A and the bridge which are detected with LOFAR. NE to the halo, there is a hint of what probably is the high-frequency counterpart of the extension. As above, we performed the subtraction of compact sources, with the caveat that JVLA array D provides, by definition, low-resolution, making the subtraction trickier. The result is shown in the bottom right panel of Fig. 6.3.

The total extent of the halo is $\sim$900 kpc. Similarly to what observed at 144 MHz, the inconsistency with the previous measurement ($\sim$1.4 Mpc) by Govoni et al. (2012), performed exploiting older VLA datasets, might be due to the exclusion of the NE extension (allowed by the higher resolution), other than to a better uv-coverage of the most recent observations. We estimate a total flux density for the halo (with Halo-FDCA[6]) of $S_{1.4\mathrm{GHz}} = 2.6 \pm 0.2$ mJy, implying $\alpha_{400\mathrm{MHz}}^{1.4\mathrm{GHz}} = -1.8 \pm 0.1$, consistent within errors with the spectral index determined at LOFAR frequencies. Govoni et al. (2012) provided an estimate of ~ 7.7 mJy at the same frequency. However, their calculation included, both, the NE extension and source A. Even after source subtraction we do not detect the latter, confirming that it might

[6]We note that, due to a less trivial source subtraction for JVLA, we had to use a larger number of masks for the flux density estimate. See also Appendix .1.

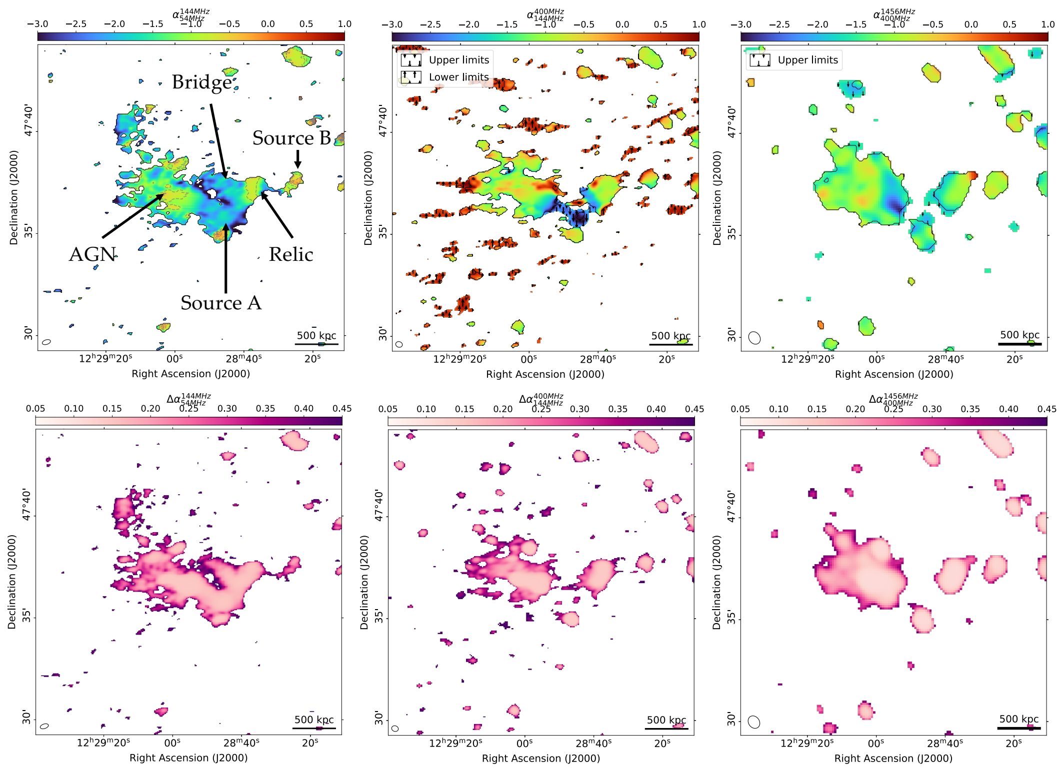

Figure 6.5: Spectral index and spectral index maps of A1550 between different frequencies. *Top Left*: Spectral index map between 54 MHz and 144 MHz, generated by combining total intensity maps produced with matching uv-cut 80λ-14kλ. Contours are at 3σ from the LBA map. The beam is 25"$\times$13". *Top Middle*: Spectral index map between 144 MHz and 400 MHz, generated by combining total intensity maps produced with matching uv-cut 80λ-14kλ. The beam is 20"$\times$17". *Top Right*: Spectral index map between 400 MHz and 1.4 GHz, generated by combining total intensity maps produced with matching uv-cut 140λ-14kλ. The beam is 38"$\times$32". *Bottom Left*: Spectral index error map between 54 MHz and 144 GHz. *Bottom Middle*: Spectral index error map between 144 MHz and 300 MHz. *Bottom Right*: Spectral index error map between 400 MHz and 1.4 GHz.

have a steep spectrum. The e-folding radius is $r_e = 174 \pm 18$ kpc, consistent with the value at lower frequencies within errors. For the candidate relic, we measure $S_{1.4\mathrm{GHz}} = 5.2 \pm 0.3$ mJy, leading to $\alpha_{144\mathrm{MHz}}^{1.4\mathrm{GHz}} = -1.2 \pm 0.2$.

Spectral analysis

To investigate the nature of the diffuse emission, we have produced spectral index maps making use the frequency coverage available for A1550. First, HBA, LBA and uGMRT maps were produced by applying the same visibility cut of 80 λ-14 kλ and `Briggs -0.3`, in order to compensate for the different uv-coverage of the instruments and match spatial scales. To avoid possible artefacts produced by the source subtraction, this procedure was applied to the non-subtracted data. The spectral index map was generated by estimating α and $\Delta\alpha$ in each pixel as:

$$\alpha_{\nu 1}^{\nu 2} = \frac{\ln S_1 - \ln S_2}{\ln \nu_2 - \ln \nu_1} \pm \frac{1}{\ln \nu_2 - \ln \nu_1} \sqrt{\left(\frac{\sigma_1}{S_1}\right)^2 + \left(\frac{\sigma_2}{S_2}\right)^2}, \tag{6.3}$$

where S_1 and S_2 are the flux densities at frequencies ν_1 and ν_2, respectively, while σ is the corresponding error. Similarly, spectral index maps between 1.4 GHz (VLA) and 400 MHz were produced by applying a baseline cut at 140λ-14kλ and `Briggs -0.3`. Visibilities were tapered at 30" to highlight the diffuse emission.

The spectral index map between 54 and 144 MHz is shown in the top-left panel of Fig. 6.5. The spectral index looks flatter (-1< α <-0.5) in the position of the AGN and of the point source S to A, as expected from compact objects where self-absorption is relevant. A similar behaviour is observed in the patch labelled B, West to the candidate relic, with the spectrum being flatter ($\alpha \sim$ -0.4) in the centre and becoming steeper ($\alpha \sim$ -0.8) moving to the periphery. This suggests that source B is likely a double-lobed radio galaxy, even though we cannot find any obvious optical counterpart. The region of the halo E to the head-tail shows a steep index ranging between -1.2 and -2.2, which becomes even steeper at the periphery and, more interestingly, West to the tail of the AGN, where source A is located. In this region we observe a mean index of $\alpha \simeq -1.7$, but it reaches $\alpha \simeq -2.3$ around A. The bridge E to the candidate relic also shows a similar spectrum. At the position of the relic, we observe a spectral index which steepens from $\alpha \simeq -0.5$ to $\alpha \simeq -1.8$ in the westernmost region, even though the relatively low resolution makes it hard to observe the typical gradients observed in relics. Finally, the NE extension shows $\alpha \simeq -1.8$ in the direction of the cluster centre, while moving to the outskirts we observe a steepening to $\alpha \simeq -2.2$.

In the top-middle panel of Fig. 6.5 we show the spectral index map between 144 and 400 MHz. We placed upper and lower limits on the spectral index where the emission was not detected at the higher or lower frequency, respectively. This might be due to the different frequency range of the instruments, and to the spectral curvature of the sources. We observe a number of lower limits around the main emission, which are likely uGMRT calibration artefacts which could not be improved. The region of the halo looks consistent with what observed between 54 and 144 MHz, with α ranging between -1.2 and -1.9. Due to the lower resolution set to detect the halo, it is hard to assess the spectral index gradient in the relic. However, we observe a steep ($\alpha < -2$) spectrum for source A, for which we are only able to place upper limits because of the low emission detected by uGMRT. This indicates a relatively high curvature at high frequencies, suggesting a cutoff in the electron energy spectrum.

Finally, in the top-right panel of Fig. 6.5 we show the spectral index map between 400 MHz and 1.4 GHz. Upper limits are placed where no emission is observed with VLA. Due to the lower resolution, it is hard to resolve all the structures which are observed by LOFAR (especially HBA) and uGMRT. The spectral index across the halo is consistent with what we found at lower frequencies, and steepens towards the candidate relic and source A, which is not detected at 1.4 GHz. Hints of upper limits $\alpha < -2$ can be observed around the position of source A, even though they are not as clear as in the LOFAR-uGMRT map. In

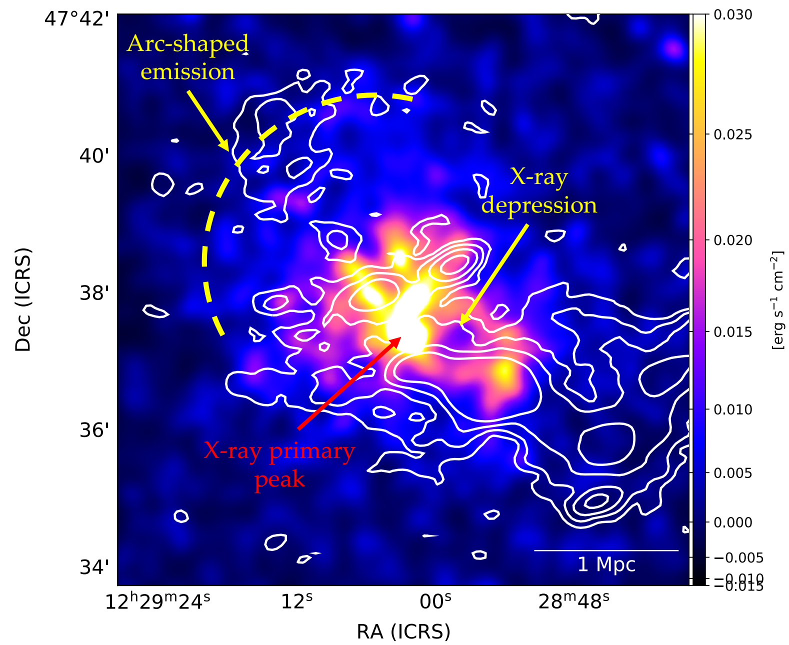

Figure 6.6: *Chandra* exposure-corrected, background-subtracted 0.5-7 keV image of A1550, smoothed to a resolution of 30 kpc at the cluster redshift. LOFAR LBA contours are overlaid in white. The image is cut at the edge of the CCD FoV.

the putative relic we seemingly observe a flattening of the spectrum moving towards the cluster outskirts, even though the low resolution makes this result uncertain.

Diffuse radio emission and thermal plasma

The short exposure time of the *Chandra* observation does not allow us to perform a thorough analysis of the ICM in A1550. Still, we can study the morphology of the X-ray emission and compare it to the structures observed in the radio band.

In Fig. 6.6 we show the *Chandra* image of A1550 in the 0.5-7 keV band, where the emission of the ICM is best visible. The morphology of the ICM looks roughly elliptical (ellipticity[7] = $\varepsilon \sim 0.75$) from the current X-ray image. The morphological parameters presented in Table A.2 of Botteon et al. 2022, such as concentration ($c = (8.67 \pm 0.89) \times 10^{-2}$) and centroid shift ($w = (3.80 \pm 0.35) \times 10^{-2}$), confirm that the cluster is disturbed, accordingly to the thresholds defined in Cassano et al. (2010). This is consistent with the presence of radio diffuse emission. The X-ray peak is found at ~150 kpc (~38") from the AGN, and the morphology of the emission seems to roughly correlate with that of the radio halo. The archival observation does not show hints of either X-ray cavities or cold fronts, apart from a ~ 50 kpc depression between the AGN and its tail. However, due to the significant smoothing that was applied, it is currently hard to confirm whether this structure is real, or just an artefact. This putative detection needs to be supported by a surface brightness analysis to quantify the possible depression, which is not feasible with

[7] Estimated as the ratio between the minor and major axes.

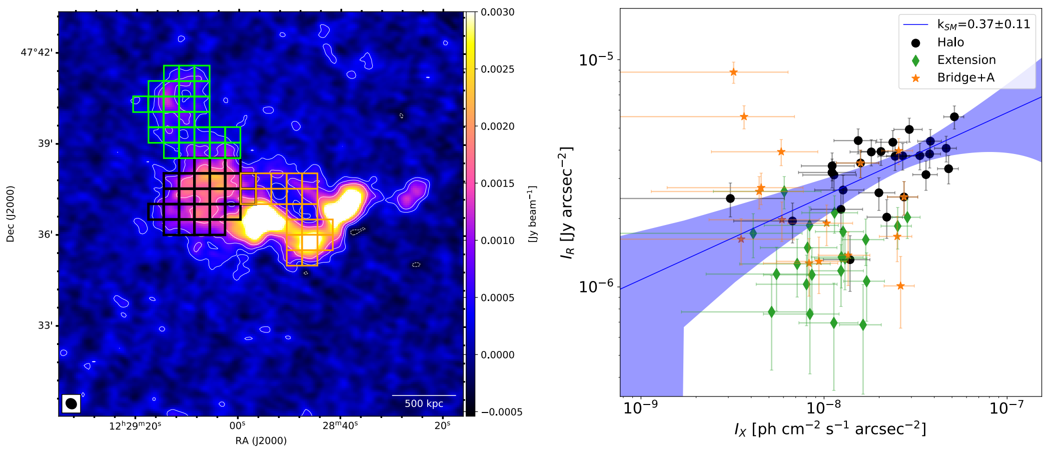

Figure 6.7: Results of the ptp analysis. *Left*: Grids used to sample the halo (black), the NE extension (red) and the bridge+source A region (orange). The dimension of the squares is 1.5 times the radio beam, with the beam being 22"×19". *Right*: Point-to-point correlation between radio (144 MHz) and X-ray surface brightness. Black data represents the halo, red represents the NE extension, while orange refers to the SW region including the bridge and source A.

the current *Chandra* observation. We do not detect X-ray emission in the region of the candidate relic and source A, even though the small area of the CCD does not allow us to cover the whole extent of the radio structure. A faint, arc-shaped patch of X-ray plasma stretches in the NE direction. Interestingly, the NE radio extension seems to follow the same morphology, and may be confined by the X-ray emission. This suggests that it could be part of the radio halo, as also supported by our HBA and LBA observations which clearly show that the extension is not detached from the halo emission. Nevertheless, this could also be due to projection effects. The correlation between the X-ray and radio surface brightness can be of help here to investigate which structures are part of the halo, and which constitute a separate kind of diffuse emission (Bruno et al., 2021; Rajpurohit et al., 2021; Duchesne et al., 2021). To this end we performed a point-to-point (ptp) analysis, in which the surface brightness at the two bands was sampled through a grid. One of the first applications of this analysis in galaxy clusters can be found in Govoni et al. (2001), and a dedicated algorithm was recently published by Ignesti (2022). First, we drew three grids: one on the halo, one on the NE extension and one on the bridge and source A (see Fig. 6.7). The size of the squares was chosen to be 1.5 times the radio beam. This is large enough to allow for relatively small error bars, especially for the X-ray image where the exposure time is short, but small enough to provide enough statistics. Nevertheless, the available X-ray observation prevents us from using smaller areas, which would increase our statistics.

The surface brightness was then extracted from each square through the procedure extensively described in Ignesti et al. (2022). The analysis was carried out on the HBA image, since the structures are better resolved, on the emission above 3σ. The result is shown for all three grids in Fig. 6.7. A sub-linear correlation is found for the halo, with slope

$k = 0.37 \pm 0.11$. The Pearson and Spearman coefficients are 0.53 and 0.56, respectively, suggesting that a correlation may exist, albeit weak. Given that such link is always observed in radio halos (see references above), it is likely that the short exposure time of the X-ray image, which led to the fit having low statistics, could be the reason for the relatively low coefficients. Furthermore, the slope is flatter than the values usually found in halos, which range between ∼0.5 and ∼0.7 (e.g. Rajpurohit et al., 2021). Similar sub-linear slopes were also found in the Bullet cluster (Shimwell et al., 2014) and in A520 (Hoang et al., 2019), and were interpreted as the halo being in a different evolutionary state with respect to typical halos. Longer X-ray observations in the future may provide smaller error bars and a larger number of bins, leading to a more reliable fit. On the other hand, we see no clear correlation for NE extension and for the SW region. The Pearson and Spearman coefficients are 0.18 and 0.13 for the NE extension, and -0.3 and -0.4 for the bridge and source A. The distribution of their X-ray and radio surface brightness values across the plot looks random, suggesting that they might not be part of the halo, but may constitute another kind of diffuse emission. This is relevant especially for the NE extension, given that both LBA and HBA detected patches of emission connecting it to the halo.

Finally, it would be interesting to perform the same kind of analysis at all four different frequencies, to assess if and how the slope eventually changes. However, as discussed above, the short X-ray exposure would significantly affect the results. Possibly, an accurate comparison of the X-ray and radio morphology in A1550 will be performed in the next future thanks to deeper observations.

6.4 Discussion

There are a number of interesting sources in A1550. As often observed in disturbed galaxy clusters, the optical BCG which hosts the head-tail radio galaxy is found relatively far from the X-ray peak (∼ 150 kpc), suggesting that the hot gas is disturbed. This is also supported by the lack of a central peak in the ICM, as well as from morphological parameters estimated in Botteon et al. (2022) and already discussed above. The radio diffuse emission spans a length of ∼2 Mpc, suggesting that a major merger might have occurred. Optical images are sometimes useful to assess the merger dynamics, but in the case of A1550 we do not see obvious hints from SDSS and PanSTARSS observations, since we do not detect any evidence for a companion cluster. As also briefly discussed in VW21, SDSS detects a subgroup of ∼ 20 galaxies N of the extension, which shows the same redshift of A1550. However, it lies far (∼1 Mpc) from the cluster centre and from the diffuse emission. Therefore, given also its relatively small extent, it is unlikely to be the cause of the extended emission detected in A1550. The orientation of the candidate radio relic might suggest that the merger axis lies in the NE-SW direction. This is also supported by the X-ray surface brightness distribution that is elongated in the same direction. Nevertheless, it is possible that diffuse emission is elongated along the line of sight, and that we are therefore underestimating its size. A method to infer the orientation of a cluster through observations of relics was recently suggested in Wittor et al. (2021). It exploits the ratio of the total projected X-ray luminosity of the cluster to the projected X-ray luminosity emitted within the candidate relic region. If the ratio approaches ~ 1, it is likely that we are observing the cluster merger face-on. On the other hand, lower ratios indicate that the cluster is elongated in the plane of the sky. Unfortunately, the *Chandra* observation does not fully cover the relic, preventing us from performing this test.

The ultra-steep radio halo and the NE extension

Regardless of the cluster orientation, the spectral index observed for the halo at all available frequencies suggests that it is a USSRH. Despite the number of detected USSRH is still low, radio halos with steep indices are being discovered more and more frequently in the last years thanks to the improved observational capabilities of low-frequency instruments such as GMRT, MWA (Murchison Widefield Array) and LOFAR (Shimwell et al., 2016; Wilber et al., 2018; Bruno et al., 2021; Di Gennaro et al., 2021; Duchesne et al., 2022). An in-depth analysis of all radio halos hosted in Planck clusters and observed in LoTSS, including A1550, has recently been presented in Botteon et al. (2022). USSRH are a prediction of turbulent re-acceleration models (Cassano et al., 2006; Brunetti et al., 2008), in which particles are re-accelerated by turbulence (Brunetti et al., 2001; Petrosian, 2001; Brunetti and Lazarian, 2011; Brunetti et al., 2017). On the other hand, the detection of such steep indices is not expected from hadronic (or secondary) models, in which the emission of halos comes from the production of secondary electrons from hadronic collisions between thermal and CR protons (Blasi and Colafrancesco, 1999; Dolag and Enßlin, 2000; Pfrommer et al., 2008). Given that the integrated spectral index observed for the USSRH with LOFAR is $\alpha_{54\mathrm{MHz}}^{144\mathrm{MHz}} \sim -1.6$, we expect an index for the spectral energy distribution[8] $\delta = 2\alpha - 1 = -4.2$. If there is no break in the spectrum, the energy budget for these particles would be untenable (Brunetti et al., 2008). Therefore, a break at low energies ($\sim$ GeV) should exist, suggesting a possible interplay between radiative losses and turbulent re-acceleration during the lifetime of emitting electrons (Brunetti and Jones, 2014). Moreover, re-acceleration models predict that a large fraction of halos associated with clusters of masses between 4-7 $\times 10^{14}$ $M_\odot$ should exhibit steep spectra (Cassano et al., 2010, 2012; Brunetti and Jones, 2014; Cuciti et al., 2021). The mass of A1550 of $\sim 6 \times 10^{14}$ $M_\odot$ estimated from Planck Collaboration et al. (2016) falls in this range.[9]

Assuming a NE-SW merger axis, the morphology and orientation of the NE extension suggest that this might also be a candidate relic. It is symmetric to the SW candidate relic with respect to the X-ray peak, and both relics lie along the merger axis. It is possible that the extension was generated by the re-acceleration of electrons caused by the counter-shock of the front that produced the SW relic. However, the X-ray observation is too shallow and the *Chandra* FoV too limited to detect any shock, in both directions. Furthermore, the spectral index distribution looks rather uniform across the source, albeit it steepens in the easternmost part. In fact, the same spectral index distribution seems more consistent with the halo, and even slightly steeper in some regions. Low-resolution images at both LOFAR

[8] Defined as $N(E) \propto E^{-\delta}$, with E being the energy.

[9] Since the correlation between the halo luminosity and the cluster mass has recently been studied for the whole LOFAR Planck-DR2 sample in Botteon et al. (2022), including A1550, we do not report it again in this work.

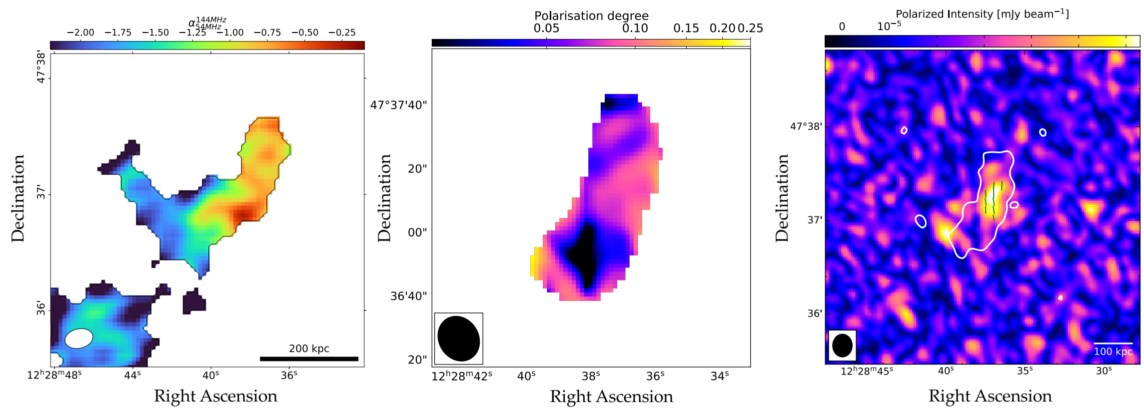

Figure 6.8: *Left*: High-resolution spectral index map of the candidate relic between 54 and 144 MHz. The beam (15"×10") is shown on the bottom-left as a white circle. Only pixels with flux density above 4σ are shown. *Middle*: Polarisation degree map for the relic in A1550. *Right*: Polarised intensity map of A1550. Magnetic field vectors are overlaid in green, while 3σ total power contours of the relic are shown in white. The vectors are corrected for Faraday rotation effect.

frequencies (see e.g. Fig. 6.3) show a patch of emission connecting the extension to the halo. The *Chandra* observation also detects X-ray plasma in the same region which seems to confine the radio emission. This supports the idea that the extension is part of the central radio halo. If this were true, one would expect the point-to-point analysis for the halo and the extension to have a similar brightness distribution. This is apparently not the case (see Fig. 6.7 and Sec. 6.3), even though the X-ray exposure time is too short to allow for good statistics. As for the bridge, deeper X-ray observations could shed light on the nature of the detected NE emission. Similar structures have also been detected in other radio halos (Markevitch, 2010; Bonafede et al., 2022; Hoang et al., 2019), and are presumably due to advection of plasma by motions and shocks. In this case, the compression of magnetic fields in such structure and the abrupt drop of the brightness upstream of the edge may also affect the ptp correlation, which could explain why we do not see the same trend observed for the halo.

The relic and the bridge

The source that we have classified as a relic shows an elongated shape and lies at ∼1 Mpc from the X-ray primary peak. However, due to the relatively low resolution of the LOFAR spectral index map (left panel of Fig. 6.5) it is hard to assess whether there is a real spectral index gradient towards the cluster centre. We have produced a high-resolution (15"×10") spectral index map between 54 and 144 MHz (shown in Fig. 6.8) since these frequencies provide the best combination of resolution, sensitivity and *uv*-coverage.

In the easternmost part, close to the bridge, the spectral index is as steep as $\alpha \sim -2$. Then, moving towards the outskirts, we observe a flattening from ~ -1.5 to ~ -0.75, reaching a lower limit of ~ -0.2 at the edge. The flatter spectrum is aligned with the presumed orientation of the merger, suggesting that the shock front has first accelerated electrons closer to the cluster centre, and is now travelling in the NE-SW direction. Unfortunately, we cannot independently confirm the presence of a shock at this location via X-ray observations.

We have produced polarisation maps for the candidate relic, as described in Sec. 6.2. As shown in Fig. 6.8 middle panel, a large portion of the relic shows a degree of polarisation which varies from $\sim 10\%$ to $\sim 25\%$. Interestingly, the highest polarisation is found in the SE region, close to the bridge and source A. The magnetic field vectors are aligned with the source orientation (see right panel of Fig. 6.8). The combination of elongated shape, spectral index gradient, location and degree of polarisation confirm the classification as a relic.

As already discussed in Sec. 6.3, we measure a total extent of $\sim$500 kpc at LOFAR frequencies and $\sim$460 kpc at 1.4 GHz. It is well-known that the radio power of relics correlates with the relic LLS (Bonafede et al., 2012), as well as with the host cluster mass (de Gasperin et al., 2014). To investigate whether the dynamic environment of A1550 has affected such relations, we can compare the radio power, LLS and cluster mass with systems studied in Bonafede et al. (2012), for the radio power-LLS correlation, and de Gasperin et al. (2014) for the radio power-cluster mass correlation. We find that the properties of the relic in A1550 are consistent with both relations.

We see that the relic is connected to the halo via a bridge. Similar cases of connected diffuse emission were also detected in Markevitch et al. (2005), Markevitch (2010), in the Toothbrush cluster (van Weeren et al., 2012b; Rajpurohit et al., 2018; de Gasperin et al., 2020), in A3667 (Carretti et al., 2013; de Gasperin et al., 2022) and others (e.g. Bonafede et al., 2018). In most of these clusters the halo is directly connected to the relic, at least seen in projection. One of the most spectacular examples of bridges is found in the Coma cluster where turbulence is believed to produce the radio emission in the bridge (Bonafede et al., 2021). In A1550 the nature of sources is different from Coma, since the bridge is apparently not related to the radio galaxy. If the merger proceeded along the NE-SW axis, as suggested by the (projected) orientation of the relic and by the morphology of the X-ray emission, then the bridge could consist of electrons that were pre-accelerated by the shock (e.g. Fujita et al. 2016), and then re-accelerated by the substantial merger-driven turbulence (e.g. Gaspari et al. 2014). However, the source of seed electrons is unclear. Furthermore, an elliptical region void of radio emission, labelled as 'depletion' in Fig. 6.1 and with a major axis of $\sim$ 400 kpc, is observed N of the radio galaxy. It is confined by the halo in the E and the relic and the phoenix in the West. It is possible that this region is related to a low-density region in the ICM since a spherical depression is also observed in the *Chandra* image (see Fig. 6.6). It is currently not clear if and how this depletion can be physically connected to the bridge.

Source A and gentle re-acceleration

In the HBA high-resolution map (see Fig. 6.2) we observe two faint arms[10] that depart from the bright tail of the central AGN, connecting the centre of the diffuse emission to source A, and that might be related to previous outbursts of the AGN. Although the tail of the radio galaxy looks well-confined, the high-resolution image seems to suggest that the electrons

[10] Also visible in Fig. 6.9.

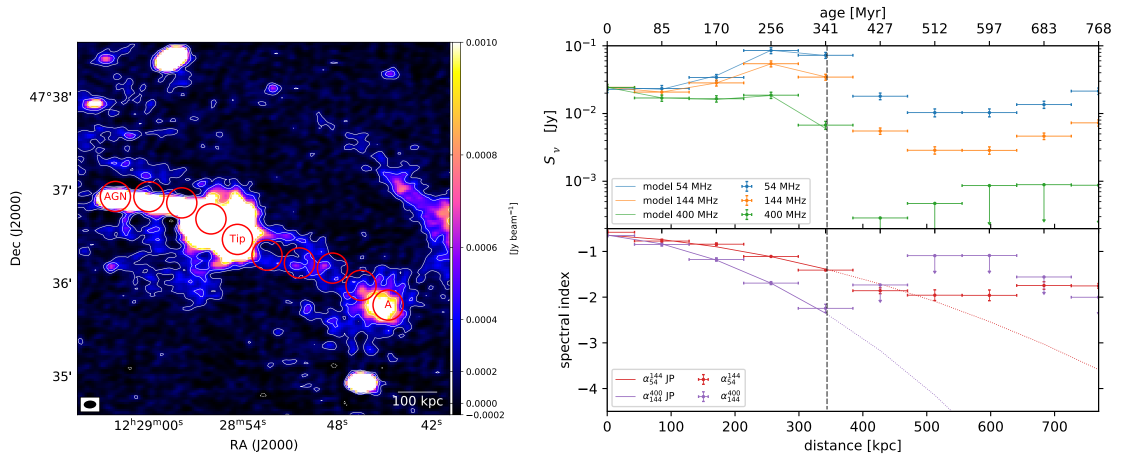

Figure 6.9: *Left*: Regions from which the spectral index between 54 and 144 MHz was extracted, overlaid on the high-resolution HBA map. Each region is as large as the smallest common circular beam (9.7"× 9.7"). The AGN, the tip of the AGN tail and source A are labelled. *Right*: Results of the fit of the spectral index. Top panel: flux density at 54 (blue) and 144 (orange) MHz for each region, starting from the AGN position. Bottom panel: spectral index, fitted with a JP ageing model. The curve becomes dashed from the point where the model was extrapolated, indicated by the grey vertical line.

which constitute the arms are originally injected from the head-tail. Corresponding to source A, the surface brightness increases again, producing a roundish structure with no visible counterparts in optical (SDSS) catalogues and spectral index $\alpha^{144\mathrm{MHz}}_{54\mathrm{MHz}} = -1.9 \pm 0.2$. When moving to 400 MHz, from the spectral index map in the middle panel of Fig. 6.5 we find an upper limit for the index of $\alpha^{400\mathrm{MHz}}_{144\mathrm{MHz}} \leq -2$. This hints at a curved spectrum, as also shown in Fig. 6.4[11]. The increase in terms of surface brightness compared to the region closer to the AGN, combined with the spectrum break-off, suggests that source A could be AGN plasma (e.g. phoenix) which was revived through re-acceleration. To trace the behaviour of the electron energy spectrum from the tail to source A, we have sampled the spectral index in regions as large as the smallest common beam (9.7"× 9.7") from high-resolution HBA, LBA and uGMRT images, which allow us to resolve both the arms and source A, and to get a reasonable statistics. This is done with the assumption that the arms are related to the head-tail radio galaxy, even though it is possible that they might just constitute some form of bridge/filaments, as observed E of the relic. We fitted the distribution by applying a non-linear least squares regression, with a Jaffe-Perola (JP) electron ageing model (Jaffe and Perola, 1973), which is assumed to be the same (i.e. same break frequency at same distance) at all frequencies. According to that model, the ageing only depends on the magnetic field and the projected velocity of the radio galaxy through the ICM. We have assumed a minimum energy magnetic field of $B_{\mathrm{min}} = \frac{3.25}{\sqrt{3}} \times 10^{-10}(1+z)^2$ T = 2.95 μG, similar to **?**. We fitted the model directly to the spectral index, with the only free parameter being the radio galaxy velocity, to remove any dependence on the normalisation (see **?**). The sampling regions were drawn from the high-resolution HBA image, and are shown in

[11]The flux density for source A at 1.4 GHz is an upper limit.

Fig. 6.9 together with the results of this analysis.

The spectral index between 54 and 144 MHz from the AGN to the tip of the tail, at a distance of ∼350 kpc, is in the range $-0.58 < \alpha_{54\mathrm{MHz}}^{144\mathrm{MHz}} < -1.41$. From the AGN position to the tip, the index keeps getting steeper as we are moving further from where electrons are injected. From the tip to source A, the distribution reaches a plateau around $\alpha_{54\mathrm{MHz}}^{144\mathrm{MHz}} \sim -1.9$, and then finally flattens at $\alpha_{54\mathrm{MHz}}^{144\mathrm{MHz}} \sim -1.7$ in the region of source A. The fit with a JP ageing model is accurate ($\chi^2/DoF \sim 0.8$) along the tail. However, when we move towards the arms and source A, it seems that the spectral index remains fairly uniform and does not follow a pure ageing model. This hints at some kind of re-acceleration process which re-energised the electrons in the region of source A. An alternative explanation is that the flatter regions are produced by an increase in the magnetic field strength. Nevertheless, this would require a precise fine-tuning of the magnetic field, making this solution less likely.

A possibility is that old radio plasma from past AGN outbursts was compressed by the same shock that produced the relic. The shock passing through fossil plasma could have produced the steep, curved spectrum (see Enßlin and Gopal-Krishna 2001 and Sec. 6.1 for more references). The curvature observed at 400 MHz for source A from Fig. 6.5 and the (likely) location of the shock front support this hypothesis. The small size (∼130 kpc radius) of this source is also consistent with expectations from revived plasma (VW21), as well as the apparently irregular distribution of the spectral index observed around source A (Kale and Dwarakanath, 2012).

Finally, the plateau shown by the spectral index distribution in the region of the two arms might point to some kind of gentle re-acceleration, which is barely able to compensate for the radiative losses of the electrons. A similar case has been studied in de Gasperin et al. (2017) in the galaxy cluster A1033, where the spectral index distribution across a long (∼500 kpc) radio galaxy tail remains level with increasing distance from the injection point (i.e. the AGN). The re-acceleration that we see in A1550 might be similar, even though the plateau in A1033 is reached at much steeper spectral indices ($\alpha \sim -4$), at least between 144 and 323 MHz. In A1033, compression by shocks is unlikely to explain the plateau as this would require precise geometrical tuning: the tail is so long that it would be hard for a shock to re-accelerate all electrons at once. Furthermore, simulations have shown that even mild (Mach number $\mathscr{M} < 2$) shocks are able to disrupt radio galaxy tails (e.g. O'Neill et al., 2019; Nolting et al., 2019). In A1550 the two arms are shorter than the tail in A1033, but it remains unlikely for a shock to compress and re-accelerate all particles at the same time across 300 kpc in order to produce a uniform spectral index (Fig. 6.9). Therefore, it is possible that the same gentle re-energisation which was invoked for A1033 can explain the two arms of A1550.

6.5 Conclusions

We have studied a plethora of diffuse emission sources in the galaxy cluster A1550 through multi-frequency radio observations, ranging from 54 MHz to 1.4 GHz. Our results can be summarised as follows:

- We observe an ultra-steep spectrum radio halo with a mean spectral index $\alpha \sim -1.6$, and an extent of $\sim$ 1.2 Mpc at 54 MHz. The halo encompasses the head-tail radio galaxy at the centre of the cluster, and extends towards the E. The detection of a USSRH favours primary models for the origin of the relativistic electrons.

- We found a relic West of the head-tail radio galaxy, with a projected extent of $\sim$ 500 kpc. From the relic, a bridge departs towards E and connects it to the halo, similarly to other clusters (see Sec. 6.4 for further details). The X-ray emission morphology and the orientation of the diffuse emission, and especially of the relic, point to a merger which occurred in the NE-SW direction. Then, the bridge could consist of electrons that were pre-accelerated by shocks, and then re-accelerated by the turbulence which also produced the halo.
- E of the halo, we detect an extension at low-frequencies that appears to depart from the halo. Even though its shape and orientation resembles a relic, the spectral index distribution indicates that it is an extension of the halo, as also suggested by the physical connection observed between the two. The point-to-point analysis performed on radio and (short exposure) X-ray images does not provide conclusive results.
- Between the radio galaxy and the relic, we observe a roundish source that we classify as a radio phoenix. This is supported by the steep and curved spectrum, which shows $\alpha \sim -1.9$ at LOFAR wavelengths, but steepens at values $\alpha < -2.1$ moving to higher frequencies. These electrons may have been re-accelerated through adiabatic compression by the same shock that has produced the relic.
- Two arms connect the tail of the radio galaxy to the phoenix. Our analysis shows that the spectral index in the arms does not steepen with increasing distance from the electron injection point. Instead, it reaches a plateau around $\alpha \sim -2$, which is maintained for more than 300 kpc. This is similar to the mild/gentle re-acceleration observed in GReET sources. It is also possible that the same shock which produced the relic and the phoenix was able to re-accelerate electrons along the arms, leading to the observed plateau in the spectral index distribution. However, it remains difficult for a shock that travels in the direction along the arms,to re-accelerate all electrons across 300 kpc at once.

Determining the origin of the different sources in the cluster A1550 remains complex. Deeper X-ray observations are needed to identify shocks in the ICM in order to determine the orientation of the merger and study the turbulence that produced the USSRH. A1550 is among the first of the LoLSS-HETDEX clusters which we have studied in detail at very low frequencies. In the future, it will be possible to perform a similar analysis on a much larger sample of objects. The synergy with other radio telescopes, such as GMRT and VLA, and complementary X-ray data will be key to shed more light on re-acceleration processes in galaxy clusters.

Acknowledgements. *We thank the referee for useful comments. TP is supported by the DLR Verbundforschung under grant number 50OR1906. MB acknowledges support from the Deutsche Forschungsgemeinschaft under Germany's Excellence Strategy - EXC 2121 "Quantum Universe" - 390833306. AB acknowledges support from the VIDI research programme with project number 639.042.729, which is financed by the Netherlands Organisation for Scientific Research (NWO). KR acknowledges financial support from the ERC Starting Grant "MAGCOW" no. 714196RJ. vW acknowledges support from the ERC Starting Grant Clus-*

terWeb 804208. FG, GB and MR acknowledge support from INAF main- stream project 'Galaxy Clusters Science with LOFAR' 1.05.01.86.05. MG acknowledges partial support by NASA Chandra GO9-20114X and HST GO-15890.020/023-A, and the BlackHoleWeather program. GDG acknowledges support from the Alexander von Humboldt Foundation. DNH and CJR acknowledges support from the ERC through the grant ERC-Stg DRANOEL n. 714245. LOFAR (van Haarlem et al., 2013) is the LOw Frequency ARray designed and constructed by ASTRON. It has observing, data processing, and data storage facilities in several countries, which are owned by various parties (each with their own funding sources), and are collectively operated by the ILT foundation under a joint scientific policy. The ILT resources have benefitted from the following recent major funding sources: CNRS-INSU, Observatoire de Paris and Université d'Orléans, France; BMBF, MIWF-NRW, MPG, Germany; Science Foundation Ireland (SFI), Department of Business, Enterprise and Innovation (DBEI), Ireland; NWO, The Netherlands; The Science and Technology Facilities Council, UK; Ministry of Science and Higher Education, Poland; Istituto Nazionale di Astrofisica (INAF), Italy. This research made use of the Dutch national e-infrastructure with support of the SURF Cooperative (e-infra 180169) and the LOFAR e-infra group, and of the LOFAR-IT computing infrastructure supported and operated by INAF, and by the Physics Dept. of Turin University (under the agreement with Consorzio Interuniversitario per la Fisica Spaziale) at the C3S Supercomputing Centre, Italy. The Jülich LOFAR Long Term Archive and the German LOFAR network are both coordinated and operated by the Jülich Supercomputing Centre (JSC), and computing resources on the supercomputer JUWELS at JSC were provided by the Gauss Centre for Supercomputing e.V. (grant CHTB00) through the John von Neumann Institute for Computing (NIC). This research made use of the University of Hertfordshire high-performance computing facility and the LOFAR-UK computing facility located at the University of Hertfordshire and supported by STFC [ST/P000096/1].

.1 Results of the Halo-FDCA pipeline

In Fig. 10 we show the output of the Halo-FDCA pipeline for the estimate of the halo flux density at the different frequencies. We fit a circle model and masked all the emission which we do not classify as being part of the halo. We applied the same masks at all frequencies except for 1.4 GHz, where we had to add more due to a trickier source subtraction (see Sec. 6.3).

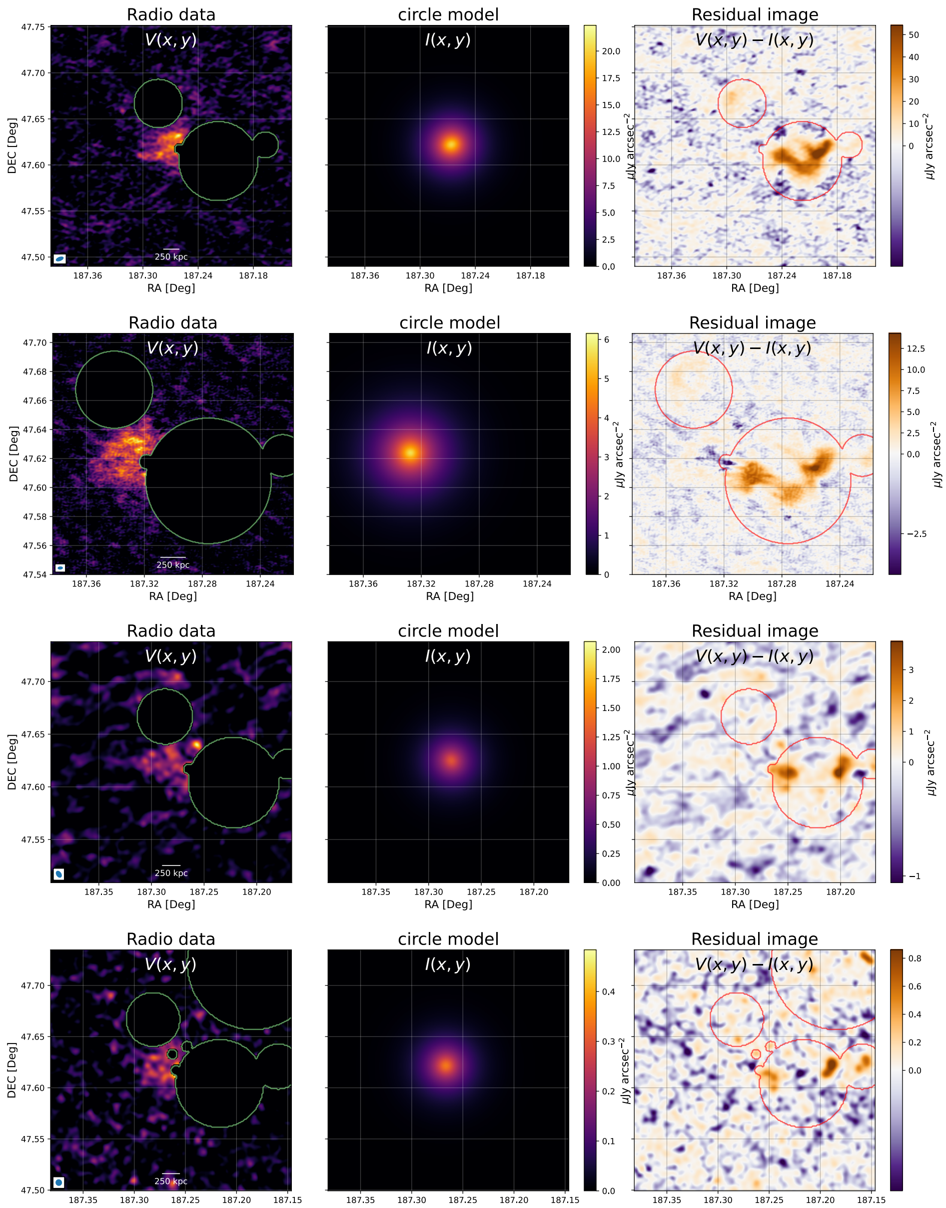

Figure 10: From top to bottom, from left to right: 54, 144, 400 and 1400 MHz modelling of the radio halo, halo centre as detected from a circle model, and residual images with masks applied to exclude sources from the flux density calculation.

7. Conclusions

Today, the comprehension of galaxies and galaxy clusters evolution, which are tightly linked to cosmology and to our understanding of the Universe, cannot disregard the role of AGN feedback. The more we observe the cosmos, the more we realize that AGN feedback is ubiquitous at all scales. It can limit star formation by sweeping cold clouds from galaxies, or vice versa compress cold gas boosting star formation. It can limit the radiative losses of the gas in clusters, preventing catastrophic cooling and establishing a duty cycle which can last for several Gyr. Furthermore, it can solve the long-lasting problem of the excessive cooling of baryons that is predicted from simulations not including feedback prescriptions, which results in more luminous galaxies with respect to observations. It can explain the observed scaling relations between SMBH and host galaxy, and it may also play a role in the injection of primordial magnetic field seeds in the Universe (Vazza et al., 2021).

This thesis has therefore explored multiple aspects of AGN feedback which were formerly poorly studied, with the purpose of addressing - or begin to address - previously unanswered questions (see Chapter 1). In this section, we elaborate upon these questions:

- **How does feedback act in galaxy clusters in which the AGN has been offset from the center of the cooling region?** We studied this scientific case in the galaxy cluster A1668 (Chapter 2), and I had previously begun to study such offsets in A2495 (Pasini et al., 2019). In both systems, we have shown that offsets of the order of $\sim$10 kpc are not able to break the feedback cycle: the link between the AGN and the ICM is clearly mantained. This is easily derived by the analysis of cavity systems, which demonstrates that mechanical heating is able to quench radiative losses even when the AGN is offset from the cooling region. It is, however, still unclear if larger offsets can lead to break the connection. This would be more likely to happen if the BCG hosting the AGN moves out of the cooling region; nevertheless, it is possible that such large offsets ($>$ 50 kpc) could only be caused by major merger, which would disrupt the cool core anyway. In the future, multi-wavelength analyses performed on similar systems could help to shed more light on this by investigating how smaller/larger offsets affect the duty cycle.

- **How do AGN feedback mechanisms act in the lower-mass regime of galaxy groups? What happens when we extend the analysis on large samples of clusters and groups?** Even though the same radio-X analysis which is usually performed on clusters is hard to apply in galaxy groups, due to surface brightness sensitivity and resolution issues, in Chapters 3 and 4 we tried to address this question by means of new-generation surveys at both spectrum bands. Our findings demonstrate that clusters and groups follow the same correlation between X-ray emission of the ICM and radio emission of the central radio galaxy. This suggests that the AGN duty cycle in clusters and groups might be similar, even though it might have different consequences. For instance, a possibility is that the central AGN could affect the gas entropy more efficiently in groups. If the radio galaxy grows to large sizes, the energy injection might happen at radii which are larger than the cooling region, weakening the feedback efficiency and broadening the correlation. Scatter in the relation can also be introduced by mergers, at both scales, and changes in the accretion mechanism of the AGN. We demonstrated that it is possible to exploit survey data to investigate AGN feedback, which opens a new window for future studies of large samples of clusters and groups.

- **Does the link between central AGN and ICM hold even in disturbed galaxy clusters? If yes, what keeps this link alive?** In chapter 4, thanks to the wealth of data provided by eROSITA, we were able to classify our systems into disturbed and relaxed, based on their dynamical state. Interestingly, we observe that the link between the AGN and the ICM is apparently maintained even in merging clusters, albeit cooling should be too slow to allow the trigger of any connection with the AGN in these systems. In the same chapter we propose a number of possible explanations, including hot, rapidly cooling coronae around galaxies and cool-core remnants, which are small, low-entropy regions in merging clusters which are still cooling. In the future, it is essential to pursue the analysis of large samples to better assess the nature of this link, which is not predicted by current prescriptions of AGN feedback. This will be pursued by means of new-generation surveys with unprecedented sensitivity, such as eRASS in the X-ray band and LoTSS and LoLSS in the radio band.

- **What are the differences, in terms of kinematic properties, between galaxies with and without radio emission in galaxy groups? Does AGN feedback play a role in this picture?** In chapter 5, we show that powerful ($L_R > 10^{23}$ W Hz^{-1}) radio galaxies, in our sample of 998 systems, always lie within 0.2 $R_{\rm vir}$ from the center of the host group, while radio-quiet galaxies are more widespread in the group environment. This likely happens because it is easier, for central galaxies, to tap into the gas reservoir of the host, and trigger the AGN. Such view is consistent with the state-of-the-art model of accretion onto the SMBH, CCA, which predicts the observed links between the radio power, the cooling and the gas temperature. On the other hand, we showed that simulations cannot fully reproduce the kinematic properties of central galaxies in groups, suggesting that additional physics, likely related to AGN feedback prescriptions, is needed to reproduce the true galaxy population.

- **What can we learn from 54 MHz observations of galaxy clusters? Can we better constrain re-acceleration mechanisms by combining them with other multi-frequency data?** Extreme low-frequency observations of the galaxy cluster A1550, discussed in Chapter 6, reveal a plethora of diffuse emission sources, including an ultra-steep radio halo, a relic, a phoenix, and hints of gentle re-acceleration in two tails extending from the head-tail radio galaxy hosted in the cluster center. This demonstrates the capabilities of LOFAR in helping to constrain the current models of particle acceleration, as well as to observe poorly-known processes such as those undergoing in GReETs. In the next future, I will lead the data reduction and analysis of 54 MHz observations of all galaxy clusters in the HETDEX field which, combined with 144 MHz and higher-frequency data, will provide even more evidence of diffuse emission in galaxy clusters.

7.1 Other works and future prospects

In this thesis, I have presented the work I have personally conducted during my PhD. Nevertheless, I have also taken part in other publications, mainly centered on the same topics, that I shortly summarise here.

- In Bulbul et al. (2022), we have extended the X-ray eFEDS cluster sample, previously studied in Pasini et al. (2022a) - see also Chapter 4 - by finding galaxy clusters that were previously classified as point sources, mainly because of their high redshift or because of a bright AGN at the center, which is dominating over extended emission. I have led the radio analysis of this new sample, performed using LOFAR observations. This publication is part of the eFEDS A&A Special Issue, similarly to Pasini et al. (2022a).
- In Brienza et al. (2022), we have analysed the galaxy group NGC 507 through LOFAR and GMRT observations. We found a clear example of interaction between old plasma, which was injected by outbursts of the AGN, and group medium. The same plasma was likely displaced by sloshing motions of the hot gas. Our observations demonstrate, in accordance with simulations, that disturbances in the group medium can disrupt the AGN lobes, mixing their material with the surrounding gas.
- In Shimwell et al. (2022), the LOFAR SKSP, which I am part of, published the second data release of the LOFAR Two-metre Sky Survey (LoTSS). These 144 MHz observations reach unprecedented sensitivity and resolution at this frequency, and provide data of millions of radio sources which will be used for years to come.

Even though we are moving forward towards a more complete understanding of the complex environments of galaxy clusters and groups, there is still much to do. As a follow-up to A1550, I am already leading the analysis of 54 MHz observations of galaxy clusters in HETDEX. Radio emission in these systems will be thoroughly investigated at different frequencies, using LOFAR and, possibly, GMRT and VLA, to better assess particle acceleration processes, as well as signatures of AGN feedback. Follow-up X-ray observations of A1668 (studied in Chapter 2) and A1550 (studied in Chapter 6) have already been proposed with the X-ray telescope *Chandra*. If obtained, these data will help us to analyse thermal emission in these clusters, to better assess feedback processes in A1668 and particle acceleration in A1550, respectively.

Ultimately, this thesis demonstrates the importance of combining radio and X-ray observations when studying galaxy clusters and groups. The interplay between thermal and non-thermal emission cannot be neglected, if one wishes to accurately assess their evolution. It is therefore essential to pursue this kind of analysis by exploiting the unprecedented wealth of data provided by new observatories, both ground- and space-based.

Acknowledgements

When I first started my PhD in September 2019, I had no idea of what I could expect by moving to a different country, with people I had never met before. It is never easy to tell your family and girlfriend that you will be living 1500 km away for at least 3 years. COVID obviously did not make things easier; nevertheless, 3 years later I feel extremely proud of what I have achieved, but I would not have been able to reach anything without the huge support that I got along the road.

As my heart is currently divided between Italy and Germany, I will start from the fantastic people I have met in Hamburg. First of all, thanks to Marcus for showing me, every single day, how exciting and fulfilling doing research can be. He has been a unique source of inspiration, and I could not hope to receive more support than the one he is giving me. To Francesco, for teaching me the right mindset to apply during this career, for always being available whenever I needed, and for showing me that it is possible to coordinate research and family, and still to be a great scientist. To Marco and Giulia, who have been nothing less but a second family to me. These years would have not been the same without our laughs, dinners and stupid office discussions. I could not imagine life in Hamburg without you, and I will cherish these memories forever. Thanks to Henrik, one of the first friends I have met in Hamburg and an incredibly talented young scientist, for being the best office mate I could hope for, for our discussions and mutual support, and for helping me with the german translation for this thesis. Thanks also to Gabriella, Sascha, Benedetta, and all the friends and colleagues I have met along the way in this fantastic city I have fell in love with.

Sometimes there is no better feeling that being at home. In my life I have been lucky enough to have a family which has always supported me; to my mum and dad, that helped me from the very first day I was moving to Hamburg, and could not wait to see me every time I went back home. To my sisters, Alice and Giulia; I could not be happier to see where life has brought you with Filippo and Marco. To the newborn Anna, who gives me chills every time I pick her up; I will try my best to be a good (and cool, hopefully) uncle. To my grandparents, those who are still here and those who will always live in my heart, for always making sure that I was fine despite not fully understanding what I was doing. And to the rest of my (big) family, for always being a place where I can return whenever I need to.

It is really rare to find good friends, and especially to keep the friendship going for many years as you grow up. Nevertheless, here we are, more than 20 years later: to the friends of a lifetime, who are too many to be listed here. Many things have changed in our lives, but us still sticking together is the best gift I could hope for. Special thanks to Mike for helping me with the cover of this thesis. To the friends and collaborators I still have in Bologna (and around Italy): Luca, Virginia, Gaia, Max, and my former master thesis supervisor, Myriam Gitti, who is always available for me.

And finally, to my girlfriend, soulmate and best friend Giulia. For accepting to stay apart for 3 years and still make things as easy as they could possibly be, for always being my first fan, and for all the support she is giving me to pursue this difficult career: thank you from the bottom of my heart.

Thomas

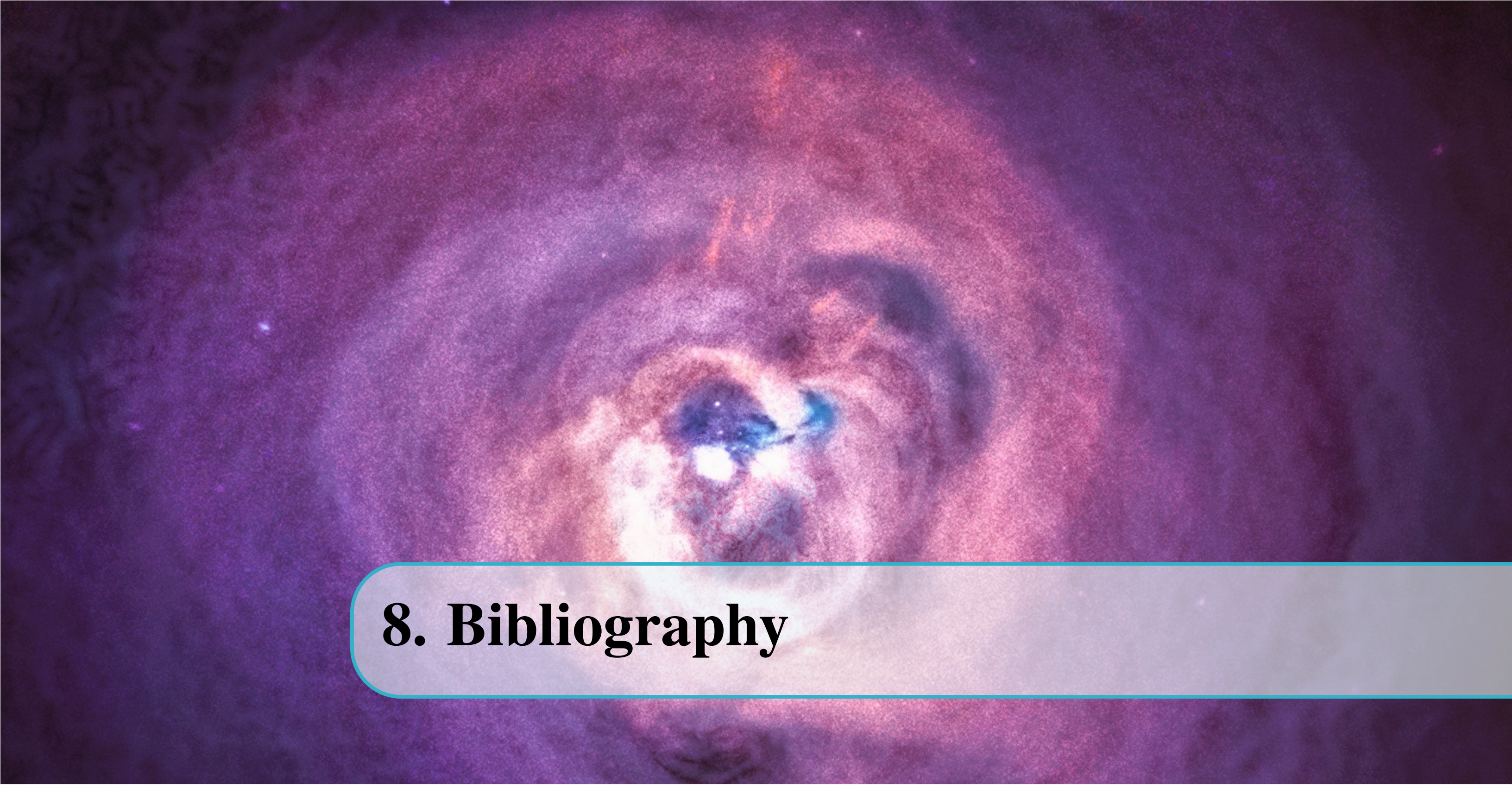

8. Bibliography

Aihara, H., Arimoto, N., Armstrong, R., Arnouts, S., Bahcall, N. A., Bickerton, S., Bosch, J., Bundy, K., Capak, P. L., Chan, J. H. H., Chiba, M., Coupon, J., Egami, E., Enoki, M., Finet, F., Fujimori, H., Fujimoto, S., Furusawa, H., Furusawa, J., Goto, T., Goulding, A., Greco, J. P., Greene, J. E., Gunn, J. E., Hamana, T., Harikane, Y., Hashimoto, Y., Hattori, T., Hayashi, M., Hayashi, Y., Hełminiak, K. G., Higuchi, R., Hikage, C., Ho, P. T. P., Hsieh, B.-C., Huang, K., Huang, S., Ikeda, H., Imanishi, M., Inoue, A. K., Iwasawa, K., Iwata, I., Jaelani, A. T., Jian, H.-Y., Kamata, Y., Karoji, H., Kashikawa, N., Katayama, N., Kawanomoto, S., Kayo, I., Koda, J., Koike, M., Kojima, T., Komiyama, Y., Konno, A., Koshida, S., Koyama, Y., Kusakabe, H., Leauthaud, A., Lee, C.-H., Lin, L., Lin, Y.-T., Lupton, R. H., Mandelbaum, R., Matsuoka, Y., Medezinski, E., Mineo, S., Miyama, S., Miyatake, H., Miyazaki, S., Momose, R., More, A., More, S., Moritani, Y., Moriya, T. J., Morokuma, T., Mukae, S., Murata, R., Murayama, H., Nagao, T., Nakata, F., Niida, M., Niikura, H., Nishizawa, A. J., Obuchi, Y., Oguri, M., Oishi, Y., Okabe, N., Okamoto, S., Okura, Y., Ono, Y., Onodera, M., Onoue, M., Osato, K., Ouchi, M., Price, P. A., Pyo, T.-S., Sako, M., Sawicki, M., Shibuya, T., Shimasaku, K., Shimono, A., Shirasaki, M., Silverman, J. D., Simet, M., Speagle, J., Spergel, D. N., Strauss, M. A., Sugahara, Y., Sugiyama, N., Suto, Y., Suyu, S. H., Suzuki, N., Tait, P. J., Takada, M., Takata, T., Tamura, N., Tanaka, M. M., Tanaka, M., Tanaka, M., Tanaka, Y., Terai, T., Terashima, Y., Toba, Y., Tominaga, N., Toshikawa, J., Turner, E. L., Uchida, T., Uchiyama, H., Umetsu, K., Uraguchi, F., Urata, Y., Usuda, T., Utsumi, Y., Wang, S.-Y., Wang, W.-H., Wong, K. C., Yabe, K., Yamada, Y., Yamanoi, H., Yasuda, N., Yeh, S., Yonehara, A., and Yuma, S. (2018). The Hyper Suprime-Cam SSP Survey: Overview and survey design. *PASJ*, 70:S4.

Akamatsu, H., Inoue, S., Sato, T., Matsusita, K., Ishisaki, Y., and Sarazin, C. L. (2013). Suzaku X-Ray Observations of the Accreting NGC 4839 Group of Galaxies and a Radio Relic in the Coma Cluster. *PASJ*, 65:89.

Akritas, M. G. and Siebert, J. (1996). A test for partial correlation with censored astronomical data. *MNRAS*, 278(4):919–924.

Alexander, D. M., Swinbank, A. M., Smail, I., McDermid, R., and Nesvadba, N. P. H. (2010). Searching for evidence of energetic feedback in distant galaxies: a galaxy wide outflow in a z ∼2 ultraluminous infrared galaxy. *MNRAS*, 402(4):2211–2220.

Allen, S. W., Evrard, A. E., and Mantz, A. B. (2011). Cosmological Parameters from Observations of Galaxy Clusters. *ARAA*, 49(1):409–470.

Anders, E. and Grevesse, N. (1989). Abundances of the elements - Meteoritic and solar. *Geochim. Cosmochim. Acta*, 53:197–214.

Andreon, S. (2016). Richness-based masses of rich and famous galaxy clusters. *A&A*, 587:A158.

Arnaud, K. A. (1996). XSPEC: The First Ten Years. In Jacoby, G. H. and Barnes, J., editors, *Astronomical Data Analysis Software and Systems V*, volume 101 of *Astronomical Society of the Pacific Conference Series*, page 17.

Arnaud, M. (2009). The β-model of the intracluster medium. Commentary on: Cavaliere A. and Fusco-Femiano R., 1976, A&A, 49, 137. *A&A*, 500(1):103–104.

Arnaud, M., Rothenflug, R., Boulade, O., Vigroux, L., and Vangioni-Flam, E. (1992). Some constraints on the origin of the iron enriched intra-cluster medium. *A&A*, 254:49–64.

Aubert, D., Pichon, C., and Colombi, S. (2004). The origin and implications of dark matter anisotropic cosmic infall on $\sim L_*$ haloes. *MNRAS*, 352(2):376–398.

Bahé, Y. M., Barnes, D. J., Dalla Vecchia, C., Kay, S. T., White, S. D. M., McCarthy, I. G., Schaye, J., Bower, R. G., Crain, R. A., Theuns, T., Jenkins, A., McGee, S. L., Schaller, M., Thomas, P. A., and Trayford, J. W. (2017). The Hydrangea simulations: galaxy formation in and around massive clusters. *MNRAS*, 470(4):4186–4208.

Baldi, R. D., Capetti, A., and Giovannini, G. (2015). Pilot study of the radio-emitting AGN population: the emerging new class of FR 0 radio-galaxies. *A&A*, 576:A38.

Balogh, M. L., McGee, S. L., Wilman, D. J., Finoguenov, A., Parker, L. C., Connelly, J. L., Mulchaey, J. S., Bower, R. G., Tanaka, M., and Giodini, S. (2011). Direct observational evidence for a large transient galaxy population in groups at $0.85 < z < 1$. *MNRAS*, 412(4):2303–2317.

Balogh, M. L., Pearce, F. R., Bower, R. G., and Kay, S. T. (2001). Revisiting the cosmic cooling crisis. *MNRAS*, 326(4):1228–1234.

Barai, P., Murante, G., Borgani, S., Gaspari, M., Granato, G. L., Monaco, P., and Ragone-Figueroa, C. (2016). Kinetic AGN feedback effects on cluster cool cores simulated using SPH. *MNRAS*, 461(2):1548–1567.

Barbosa, C. E., Arnaboldi, M., Coccato, L., Gerhard, O., Mendes de Oliveira, C., Hilker, M., and Richtler, T. (2018). Sloshing in its cD halo: MUSE kinematics of the central galaxy <ASTROBJ>NGC 3311</ASTROBJ> in the <ASTROBJ>Hydra I</ASTROBJ> cluster. *A&A*, 609:A78.

Bassini, L., Rasia, E., Borgani, S., Granato, G. L., Ragone-Figueroa, C., Biffi, V., Ragagnin, A., Dolag, K., Lin, W., Murante, G., Napolitano, N. R., Taffoni, G., Tornatore, L., and Wang, Y. (2020). The DIANOGA simulations of galaxy clusters: characterising star formation in protoclusters. *A&A*, 642:A37.

Bassini, L., Rasia, E., Borgani, S., Ragone-Figueroa, C., Biffi, V., Dolag, K., Gaspari, M., Granato, G. L., Murante, G., Taffoni, G., and Tornatore, L. (2019). Black hole mass of central galaxies and cluster mass correlation in cosmological hydro-dynamical simulations. *A&A*, 630:A144.

Bayer-Kim, C. M., Crawford, C. S., Allen, S. W., Edge, A. C., and Fabian, A. C. (2002). The peculiar cooling flow cluster RX J0820.9+0752. *MNRAS*, 337(3):938–952.

Beers, T. C., Flynn, K., and Gebhardt, K. (1990). Measures of Location and Scale for Velocities in Clusters of Galaxies—A Robust Approach. *AJ*, 100:32.

Bernardi, M. (2007). The σ-L Correlation in Nearby Early-Type Galaxies. *AJ*, 133(5):1954–1961.

Bernstein, J. P. and Bhavsar, S. P. (2001). Models for the magnitude-distribution of brightest cluster galaxies. *MNRAS*, 322(3):625–630.

Best, P. N. and Heckman, T. M. (2012). On the fundamental dichotomy in the local radio-AGN population: accretion, evolution and host galaxy properties. *MNRAS*, 421(2):1569–1582.

Best, P. N., Kauffmann, G., Heckman, T. M., Brinchmann, J., Charlot, S., Ivezić, Ž., and White, S. D. M. (2005a). The host galaxies of radio-loud active galactic nuclei: mass dependences, gas cooling and active galactic nuclei feedback. *MNRAS*, 362(1):25–40.

Best, P. N., Kauffmann, G., Heckman, T. M., and Ivezić, Ž. (2005b). A sample of radio-loud active galactic nuclei in the Sloan Digital Sky Survey. *MNRAS*, 362(1):9–24.

Best, P. N., von der Linden, A., Kauffmann, G., Heckman, T. M., and Kaiser, C. R. (2007). On the prevalence of radio-loud active galactic nuclei in brightest cluster galaxies: implications for AGN heating of cooling flows. *MNRAS*, 379:894–908.

Bharadwaj, V., Reiprich, T. H., Lovisari, L., and Eckmiller, H. J. (2015a). Extending the L_X–T relation from clusters to groups. Impact of cool core nature, AGN feedback, and selection effects. 573:A75.

Bharadwaj, V., Reiprich, T. H., Lovisari, L., and Eckmiller, H. J. (2015b). Extending the L_X - T relation from clusters to groups. Impact of cool core nature, AGN feedback, and selection effects. *A&A*, 573:A75.

Bharadwaj, V., Reiprich, T. H., Schellenberger, G., Eckmiller, H. J., Mittal, R., and Israel, H. (2014a). Intracluster medium cooling, AGN feedback, and brightest cluster galaxy properties of galaxy groups. Five properties where groups differ from clusters. *A&A*, 572:A46.

Bharadwaj, V., Reiprich, T. H., Schellenberger, G., Eckmiller, H. J., Mittal, R., and Israel, H. (2014b). Intracluster medium cooling, AGN feedback, and brightest cluster galaxy properties of galaxy groups. Five properties where groups differ from clusters. 572:A46.

Bianchi, S., Bonilla, N. F., Guainazzi, M., Matt, G., and Ponti, G. (2009). CAIXA: a catalogue of AGN in the XMM-Newton archive. II. Multiwavelength correlations. *A&A*, 501(3):915–924.

Biava, N., de Gasperin, F., Bonafede, A., Edler, H., Giacintucci, S., Mazzotta, P., Brunetti, G., Botteon, A., Brüggen, M., Cassano, R., Drabent, A., Edge, A., Enßlin, T., Gastaldello, F., Riseley, C., Rossetti, M., Rottgering, H., Shimwell, T., Tasse, C., and van Weeren, R. (2021). The ultra-steep diffuse radio emission observed in the cool-core cluster RX J1720.1+2638 with LOFAR at 54 MHz. *MNRAS*, 508(3):3995–4007.

Biffi, V., Borgani, S., Murante, G., Rasia, E., Planelles, S., Granato, G. L., Ragone-Figueroa, C., Beck, A. M., Gaspari, M., and Dolag, K. (2016). On the Nature of Hydrostatic Equilibrium in Galaxy Clusters. *ApJ*, 827(2):112.

Bîrzan, L., McNamara, B. R., Nulsen, P. E. J., Carilli, C. L., and Wise, M. W. (2008). Radiative Efficiency and Content of Extragalactic Radio Sources: Toward a Universal Scaling Relation between Jet Power and Radio Power. *ApJ*, 686:859–880.

Bîrzan, L., Rafferty, D., McNamara, B., Wise, M., and Nulsen, P. (2004). A Systematic Study of Radio-induced X-Ray Cavities in Clusters, Groups, and Galaxies. *ApJ*, 607:800–809.

Bîrzan, L., Rafferty, D. A., Brüggen, M., Botteon, A., Brunetti, G., Cuciti, V., Edge, A. C., Morganti, R., Röttgering, H. J. A., and Shimwell, T. W. (2020). LOFAR Observations of X-ray Cavity Systems. *MNRAS*.

Bîrzan, L., Rafferty, D. A., Brüggen, M., and Intema, H. T. (2017). A study of high-redshift AGN feedback in SZ cluster samples. *MNRAS*, 471:1766–1787.

Bîrzan, L., Rafferty, D. A., Nulsen, P. E. J., McNamara, B. R., Röttgering, H. J. A., Wise, M. W., and Mittal, R. (2012). The duty cycle of radio-mode feedback in complete samples of clusters. *MNRAS*, 427(4):3468–3488.

Blanton, E. L., Sarazin, C. L., and McNamara, B. R. (2003). Chandra Observation of the Cooling Flow Cluster Abell 2052. *ApJ*, 585:227–243.

Blanton, E. L., Sarazin, C. L., McNamara, B. R., and Wise, M. W. (2001). Chandra Observation of the Radio Source/X-Ray Gas Interaction in the Cooling Flow Cluster Abell 2052. *ApJ*, 558:L15–L18.

Blanton, M. R., Bershady, M. A., Abolfathi, B., Albareti, F. D., Allende Prieto, C., Almeida, A., Alonso-García, J., Anders, F., Anderson, S. F., Andrews, B., Aquino-Ortíz, E., Aragón-Salamanca, A., Argudo-Fernández, M., Armengaud, E., Aubourg, E., Avila-Reese, V., Badenes, C., Bailey, S., Barger, K. A., Barrera-Ballesteros, J., Bartosz, C., Bates, D., Baumgarten, F., Bautista, J., Beaton, R., Beers, T. C., Belfiore, F., Bender, C. F., Berlind, A. A., Bernardi, M., Beutler, F., Bird, J. C., Bizyaev, D., Blanc, G. A., Blomqvist, M., Bolton, A. S., Boquien, M., Borissova, J., van den Bosch, R., Bovy, J., Brandt, W. N., Brinkmann, J., Brownstein, J. R., Bundy, K., Burgasser, A. J., Burtin, E., Busca, N. G., Cappellari, M., Delgado Carigi, M. L., Carlberg, J. K., Carnero Rosell, A., Carrera, R., Chanover, N. J., Cherinka, B., Cheung, E., Gómez Maqueo Chew, Y., Chiappini, C., Choi, P. D., Chojnowski, D., Chuang, C.-H., Chung, H., Cirolini, R. F., Clerc, N., Cohen, R. E., Comparat, J., da Costa, L., Cousinou, M.-C., Covey, K., Crane, J. D., Croft, R. A. C., Cruz-Gonzalez, I., Garrido Cuadra, D., Cunha, K., Damke, G. J., Darling, J., Davies, R., Dawson, K., de la Macorra, A., Dell'Agli, F., De Lee, N., Delubac, T., Di Mille, F., Diamond-Stanic, A., Cano-Díaz, M., Donor, J., Downes, J. J., Drory, N., du Mas des Bourboux, H., Duckworth, C. J., Dwelly, T., Dyer, J., Ebelke, G., Eigenbrot, A. D., Eisenstein, D. J., Emsellem, E., Eracleous, M., Escoffier, S., Evans, M. L., Fan, X., Fernández-Alvar, E., Fernandez-Trincado, J. G., Feuillet, D. K., Finoguenov, A., Fleming, S. W., Font-Ribera, A., Fredrickson, A., Freischlad, G., Frinchaboy, P. M., Fuentes, C. E., Galbany, L., Garcia-Dias, R., García-Hernández, D. A., Gaulme, P., Geisler, D., Gelfand, J. D., Gil-Marín, H., Gillespie, B. A., Goddard, D., Gonzalez-Perez, V., Grabowski, K., Green, P. J., Grier, C. J., Gunn, J. E., Guo, H., Guy, J., Hagen, A., Hahn, C., Hall, M., Harding, P., Hasselquist, S., Hawley, S. L., Hearty, F., Gonzalez Hernández, J. I., Ho, S., Hogg, D. W., Holley-Bockelmann, K., Holtzman, J. A., Holzer, P. H., Huehnerhoff, J., Hutchinson, T. A., Hwang, H. S., Ibarra-Medel, H. J., da Silva Ilha, G., Ivans, I. I., Ivory, K., Jackson, K., Jensen, T. W., Johnson, J. A., Jones, A., Jönsson, H., Jullo, E., Kamble, V., Kinemuchi, K., Kirkby, D., Kitaura, F.-S., Klaene, M., Knapp, G. R., Kneib, J.-P., Kollmeier, J. A., Lacerna, I., Lane, R. R., Lang, D., Law, D. R., Lazarz, D., Lee, Y., Le Goff, J.-M., Liang, F.-H., Li, C., Li, H., Lian, J., Lima, M., Lin, L., Lin, Y.-T., Bertran de Lis, S., Liu, C., de Icaza Lizaola, M. A. C., Long, D., Lucatello, S., Lundgren, B., MacDonald, N. K., Deconto Machado, A., MacLeod, C. L., Mahadevan, S., Geimba Maia, M. A., Maiolino, R., Majewski, S. R., Malanushenko, E., Malanushenko, V., Manchado, A., Mao, S., Maraston, C., Marques-Chaves, R., Masseron, T., Masters, K. L., McBride, C. K., McDermid, R. M., McGrath, B., McGreer, I. D., Medina Peña, N., Melendez, M., Merloni, A., Merrifield, M. R., Meszaros, S., Meza, A., Minchev, I., Minniti, D., Miyaji, T., More, S., Mulchaey, J., Müller-Sánchez, F., Muna, D., Munoz, R. R., Myers, A. D., Nair, P., Nandra, K., Correa do Nascimento, J., Negrete, A., Ness, M., Newman, J. A., Nichol, R. C., Nidever, D. L., Nitschelm, C., Ntelis, P., O'Connell, J. E., Oelkers, R. J., Oravetz, A., Oravetz, D., Pace, Z., Padilla, N., Palanque-Delabrouille, N., Alonso Palicio, P., Pan, K., Parejko, J. K., Parikh, T., Pâris, I., Park, C., Patten, A. Y., Peirani, S., Pellejero-Ibanez, M., Penny, S., Percival, W. J., Perez-Fournon, I., Petitjean, P., Pieri, M. M., Pinsonneault, M., Pisani, A., Poleski, R., Prada, F., Prakash, A., Queiroz, A. B. d. A., Raddick, M. J., Raichoor, A., Barboza Rembold, S., Richstein, H., Riffel, R. A., Riffel, R., Rix, H.-W., Robin, A. C., Rockosi, C. M., Rodríguez-Torres, S., Roman-Lopes, A., Román-Zúñiga, C., Rosado, M., Ross, A. J., Rossi, G., Ruan, J., Ruggeri, R., Rykoff, E. S., Salazar-Albornoz, S., Salvato, M., Sánchez, A. G., Aguado, D. S., Sánchez-Gallego, J. R., Santana, F. A., Santiago, B. X., Sayres, C., Schiavon, R. P., da Silva Schimoia, J., Schlafly, E. F., Schlegel, D. J., Schneider, D. P., Schultheis, M., Schuster, W. J., Schwope, A., Seo, H.-J., Shao, Z., Shen, S., Shetrone, M., Shull, M., Simon, J. D., Skinner, D., Skrutskie, M. F., Slosar, A., Smith, V. V., Sobeck, J. S., Sobreira, F., Somers, G., Souto, D., Stark, D. V., Stassun, K., Stauffer, F., Steinmetz, M., Storchi-Bergmann, T., Streblyanska, A., Stringfellow, G. S., Suárez, G., Sun, J., Suzuki, N., Szigeti, L., Taghizadeh-Popp, M., Tang, B., Tao, C., Tayar, J., Tembe, M., Teske, J., Thakar, A. R., Thomas, D., Thompson, B. A., Tinker, J. L., Tissera, P., Tojeiro, R., Hernandez Toledo, H., de la Torre, S., Tremonti, C., Troup, N. W., Valenzuela, O., Martinez Valpuesta, I., Vargas-González, J., Vargas-Magaña, M., Vazquez, J. A., Villanova, S., Vivek, M., Vogt, N., Wake, D., Walterbos, R., Wang, Y., Weaver, B. A., Weijmans, A.-M., Weinberg, D. H., Westfall, K. B., Whelan, D. G., Wild, V., Wilson, J., Wood-Vasey, W. M., Wylezalek, D., Xiao, T., Yan, R., Yang, M., Ybarra, J. E., Yèche, C., Zakamska, N., Zamora, O., Zarrouk, P., Zasowski, G., Zhang, K., Zhao, G.-B., Zheng, Z., Zheng, Z., Zhou, X., Zhou, Z.-M., Zhu, G. B., Zoccali, M., and Zou, H. (2017). Sloan Digital Sky Survey IV: Mapping the Milky Way, Nearby Galaxies, and the Distant Universe. *AJ*, 154(1):28.

Blasi, P. and Colafrancesco, S. (1999). Cosmic rays, radio halos and nonthermal X-ray emission in clusters of galaxies. *Astroparticle Physics*, 12(3):169–183.

Böhringer, H., Chon, G., and Collins, C. A. (2014). The extended ROSAT-ESO Flux Limited X-ray Galaxy Cluster Survey (REFLEX II) IV. X-ray Luminosity Function and First Constraints on Cosmological Parameters. *ArXiv e-prints*.

Böhringer, H., Voges, W., Huchra, J. P., McLean, B., Giacconi, R., Rosati, P., Burg, R., Mader, J., Schuecker, P., Simiç, D., Komossa, S., Reiprich, T. H., Retzlaff, J., and Trümper, J. (2000). The Northern ROSAT All-Sky (NORAS) Galaxy Cluster Survey. I. X-Ray Properties of Clusters Detected as Extended X-Ray Sources. *ApJS*, 129(2):435–474.

Bonafede, A., Brüggen, M., Rafferty, D., Zhuravleva, I., Riseley, C. J., van Weeren, R. J., Farnes, J. S., Vazza, F., Savini, F., Wilber, A., Botteon, A., Brunetti, G., Cassano, R., Ferrari, C., de Gasperin, F., Orrú, E., Pizzo, R. F., Röttgering, H. J. A., and Shimwell, T. W. (2018). LOFAR discoveryof radio emission in MACS J0717.5+3745. *MNRAS*, 478(3):2927–2938.

Bonafede, A., Brüggen, M., van Weeren, R., Vazza, F., Giovannini, G., Ebeling, H., Edge, A. C., Hoeft, M., and Klein, U. (2012). Discovery of radio haloes and double relics in distant MACS galaxy clusters: clues to the efficiency of particle acceleration. *MNRAS*, 426(1):40–56.

Bonafede, A., Brunetti, G., Rudnick, L., Vazza, F., Bourdin, H., Giovannini, G., Shimwell, T. W., Zhang, X., Mazzotta, P., Simionescu, A., Biava, N., Bonnassieux, E., Brienza, M., Brüggen, M., Rajpurohit, K., Riseley, C. J., Stuardi, C., Feretti, L., Tasse, C., Botteon, A., Carretti, E., Cassano, R., Cuciti, V., de Gasperin, F., Gastaldello, F., Rossetti, M., Rottgering, H. J. A., Venturi, T., and van Weeren, R. J. (2022). The Coma cluster at LOFAR frequencies II: the halo, relic, and a new accretion relic. *arXiv e-prints*, page arXiv:2203.01958.

Bonafede, A., Brunetti, G., Vazza, F., Simionescu, A., Giovannini, G., Bonnassieux, E., Shimwell, T. W., Brüggen, M., van Weeren, R. J., Botteon, A., Brienza, M., Cassano, R., Drabent, A., Feretti, L., de Gasperin, F., Gastaldello, F., di Gennaro, G., Rossetti, M., Rottgering, H. J. A., Stuardi, C., and Venturi, T. (2021). The Coma Cluster at LOw Frequency ARray Frequencies. I. Insights into Particle Acceleration Mechanisms in the Radio Bridge. *ApJ*, 907(1):32.

Bonafede, A., Feretti, L., Murgia, M., Govoni, F., Giovannini, G., Dallacasa, D., Dolag, K., and Taylor, G. B. (2010). The Coma cluster magnetic field from Faraday rotation measures. *A&A*, 513:A30.

Bonafede, A., Intema, H. T., Brüggen, M., Girardi, M., Nonino, M., Kantharia, N., van Weeren, R. J., and Röttgering, H. J. A. (2014). Evidence for Particle Re-acceleration in the Radio Relic in the Galaxy Cluster PLCKG287.0+32.9. *ApJ*, 785(1):1.

Bonafede, A., Intema, H. T., Brüggen, M., Russel, H. R., Ogrean, G., Basu, K., Sommer, M., Van Weeren, R. J., Cassano, R., Fabian, A. C., and Röttgering, H. J. (2014). A giant radio halo in the cool core cluster CL1821+643. *Monthly Notices of the Royal Astronomical Society: Letters*, 444(1):L44–L48.

Bondi, H. (1952). On spherically symmetrical accretion. *MNRAS*, 112:195.

Botteon, A., Brunetti, G., Ryu, D., and Roh, S. (2020a). Shock acceleration efficiency in radio relics. *A&A*, 634:A64.

Botteon, A., Brunetti, G., van Weeren, R. J., Shimwell, T. W., Pizzo, R. F., Cassano, R., Iacobelli, M., Gastaldello, F., Bîrzan, L., Bonafede, A., Brüggen, M., Cuciti, V., Dallacasa, D., de Gasperin, F., Di Gennaro, G., Drabent, A., Hardcastle, M. J., Hoeft, M., Mandal, S., Röttgering, H. J. A., and Simionescu, A. (2020b). The Beautiful Mess in Abell 2255. *ApJ*, 897(1):93.

Botteon, A., Cassano, R., van Weeren, R. J., Shimwell, T. W., Bonafede, A., Brggen, M., Brunetti, G., Cuciti, V., Dallacasa, D., de Gasperin, F., Di Gennaro, G., Gastaldello, F., Hoang, D. N., Rossetti, M., and Röttgering, H. J. A. (2021). Discovery of a Radio Halo (and Relic) in a $M_{500}<2\times10^{14}$ $M_\odot$ Cluster. *ApJ*, 914(2):L29.

Botteon, A., Gastaldello, F., Brunetti, G., and Kale, R. (2016). A $M \gtrsim 3$ shock in 'El Gordo' cluster and the origin of the radio relic. *MNRAS*, 463(2):1534–1542.

Botteon, A., Shimwell, T. W., Cassano, R., Cuciti, V., Zhang, X., Bruno, L., Camillini, L., Natale, R., Jones, A., Gastaldello, F., Simionescu, A., Rossetti, M., Akamatsu, H., van Weeren, R. J., Brunetti, G., Brüggen, M., Groenveld, C., Hoang, D. N., Hardcastle, M. J., Ignesti, A., Di Gennaro, G., Bonafede, A., Drabent, A., Röttgering, H. J. A., Hoeft, M., and de Gasperin, F. (2022). The Planck clusters in the LOFAR sky. I. LoTSS-DR2: new detections and sample overview. *arXiv e-prints*, page arXiv:2202.11720.

Boxelaar, J. M., van Weeren, R. J., and Botteon, A. (2021). A robust model for flux density calculations of radio halos in galaxy clusters: Halo-FDCA. *Astronomy and Computing*, 35:100464.

Bregman, J. N. (2005). The Absence of the Fundamental Plane of Black Hole Activity. *arXiv e-prints*, pages astro–ph/0511368.

Bregman, J. N. (2007). The Search for the Missing Baryons at Low Redshift. *ARAA*, 45(1):221–259.

Brienza, M., Lovisari, L., Rajpurohit, K., Bonafede, A., Gastaldello, F., Murgia, M., Vazza, F., Bonnassieux, E., Botteon, A., Brunetti, G., Drabent, A., Hardcastle, M. J., Pasini, T., Riseley, C. J., Röttgering, H. J. A., Shimwell, T., Simionescu, A., and van Weeren, R. J. (2022). The galaxy group NGC 507: newly detected AGN remnant plasma transported by sloshing. *arXiv e-prints*, page arXiv:2201.04591.

Brighenti, F., Mathews, W. G., and Temi, P. (2015). Hot Gaseous Atmospheres in Galaxy Groups and Clusters Are Both Heated and Cooled by X-Ray Cavities. *ApJ*, 802:118.

Brüggen, M. (2003). Simulations of Buoyant Bubbles in Galaxy Clusters. *ApJ*, 592(2):839–845.

Brüggen, M. (2013). Magnetic field amplification by cosmic ray-driven turbulence - I. Isotropic CR diffusion. *MNRAS*, 436(1):294–303.

Brüggen, M., Bykov, A., Ryu, D., and Röttgering, H. (2012). Magnetic fields, relativistic particles, and shock waves in cluster outskirts. *Space Science Reviews*, 166(1-4):187–213.

Brüggen, M. and Kaiser, C. R. (2002). Hot bubbles from active galactic nuclei as a heat source in cooling-flow clusters. *Nature*, 418(6895):301–303.

Brüggen, M., Reiprich, T. H., Bulbul, E., Koribalski, B. S., Andernach, H., Rudnick, L., Hoang, D. N., Wilber, A. G., Duchesne, S. W., Veronica, A., Pacaud, F., Hopkins, A. M., Norris, R. P., Johnston-Hollitt, M., Brown, M. J. I., Bonafede, A., Brunetti, G., Collier, J. D., Sanders, J. S., Vardoulaki, E., Venturi, T., Kapinska, A. D., and Marvil, J. (2021). Radio observations of the merging galaxy cluster system Abell 3391-Abell 3395. *A&A*, 647:A3.

Brüggen, M. and Vazza, F. (2020a). Analytical model for cluster radio relics. *MNRAS*, 493(2):2306–2317.

Brüggen, M. and Vazza, F. (2020b). Analytical model for cluster radio relics. *MNRAS*, 493(2):2306–2317.

Brunetti, G., Cassano, R., Dolag, K., and Setti, G. (2009). On the evolution of giant radio halos and their connection with cluster mergers. *A&A*, 507:661–669.

Brunetti, G., Giacintucci, S., Cassano, R., Lane, W., Dallacasa, D., Venturi, T., Kassim, N. E., Setti, G., Cotton, W. D., and Markevitch, M. (2008). A low-frequency radio halo associated with a cluster of galaxies. *Nature*, 455(7215):944–947.

Brunetti, G. and Jones, T. W. (2014). Cosmic Rays in Galaxy Clusters and Their Nonthermal Emission. *International Journal of Modern Physics D*, 23(4):1430007–98.

Brunetti, G. and Jones, T. W. (2014). Cosmic rays in galaxy clusters and their nonthermal emission. *International Journal of Modern Physics D*, 23(4):30007.

Brunetti, G. and Lazarian, A. (2011). Acceleration of primary and secondary particles in galaxy clusters by compressible MHD turbulence: from radio haloes to gamma-rays. *MNRAS*, 410:127–142.

Brunetti, G., Setti, G., Feretti, L., and Giovannini, G. (2001). Particle reacceleration in the Coma cluster: radio properties and hard X-ray emission. *MNRAS*, 320:365–378.

Brunetti, G., Zimmer, S., and Zandanel, F. (2017). Relativistic protons in the Coma galaxy cluster: first gamma-ray constraints ever on turbulent reacceleration. *MNRAS*, 472(2):1506–1525.

Brunner, H., Liu, T., Lamer, G., Georgakakis, A., Merloni, A., Brusa, M., Bulbul, E., and Dennerl, K. (2021). The eROSITA Final Equatorial Depth Survey (eFEDS): The X-ray catalog. *A&A*, page (submitted).

Bruno, L., Rajpurohit, K., Brunetti, G., Gastaldello, F., Botteon, A., Ignesti, A., Bonafede, A., Dallacasa, D., Cassano, R., van Weeren, R. J., Cuciti, V., Di Gennaro, G., Shimwell, T., and Brüggen, M. (2021). The LOFAR and JVLA view of the distant steep spectrum radio halo in MACS J1149.5+2223. *A&A*, 650:A44.

Bulbul, E., Liu, A., Pasini, T., Comparat, J., Hoang, D. N., Klein, M., Ghirardini, V., Salvato, M., Merloni, A., Seppi, R., Wolf, J., Anderson, S. F., Bahar, Y. E., Brusa, M., Brüggen, M., Buchner, J., Dwelly, T., Ibarra-Medel, H., Ider Chitham, J., Liu, T., Nandra, K., Ramos-Ceja, M. E., Sanders, J. S., and Shen, Y. (2022). The eROSITA Final Equatorial-Depth Survey (eFEDS). Galaxy clusters and groups in disguise. *A&A*, 661:A10.

Burns, J. O. (1990). The Radio Properties of cD Galaxies in Abell Clusters. I. an X-ray Selected Sample. *AJ*, 99:14.

Cantwell, T. M., Bray, J. D., Croston, J. H., Scaife, A. M. M., Mulcahy, D. D., Best, P. N., Brüggen, M., Brunetti, G., Callingham, J. R., Clarke, A. O., Hardcastle, M. J., Harwood, J. J., Heald, G., Heesen, V., Iacobelli, M., Jamrozy, M., Morganti, R., Orrú, E., O'Sullivan, S. P., Riseley, C. J., Röttgering, H. J. A., Shulevski, A., Sridhar, S. S., Tasse, C., and Van Eck, C. L. (2020). Low-frequency observations of the giant radio galaxy NGC 6251. *MNRAS*, 495(1):143–159.

Carilli, C. L. and Taylor, G. B. (2002). Cluster Magnetic Fields. *ARA&A*, 40:319–348.

Carlberg, R. G., Yee, H. K. C., Ellingson, E., Morris, S. L., Abraham, R., Gravel, P., Pritchet, C. J., Smecker-Hane, T., Hartwick, F. D. A., Hesser, J. E., Hutchings, J. B., and Oke, J. B. (1997). The Average Mass Profile of Galaxy Clusters. *ApJ*, 485(1):L13–L16.

Carretti, E., Brown, S., Staveley-Smith, L., Malarecki, J. M., Bernardi, G., Gaensler, B. M., Haverkorn, M., Kesteven, M. J., and Poppi, S. (2013). Detection of a radio bridge in Abell 3667. *MNRAS*, 430(2):1414–1422.

Cassano, R., Brunetti, G., Norris, R. P., Röttgering, H. J. A., Johnston-Hollitt, M., and Trasatti, M. (2012). Radio halos in future surveys in the radio continuum. *A&A*, 548:A100.

Cassano, R., Brunetti, G., and Setti, G. (2006). Statistics of giant radio haloes from electron reacceleration models. *MNRAS*, 369(4):1577–1595.

Cassano, R., Ettori, S., Brunetti, G., Giacintucci, S., Pratt, G. W., Venturi, T., Kale, R., Dolag, K., and Markevitch, M. (2013). Revisiting Scaling Relations for Giant Radio Halos in Galaxy Clusters. *ApJ*, 777(2):141.

Cassano, R., Ettori, S., Giacintucci, S., Brunetti, G., Markevitch, M., Venturi, T., and Gitti, M. (2010). On the Connection Between Giant Radio Halos and Cluster Mergers. *ApJ*, 721(2):L82–L85.

Cavagnolo, K. W., Donahue, M., Voit, G. M., and Sun, M. (2008). An Entropy Threshold for Strong Hα and Radio Emission in the Cores of Galaxy Clusters. *ApJ*, 683:L107.

Cavagnolo, K. W., Donahue, M., Voit, G. M., and Sun, M. (2009). Intracluster Medium Entropy Profiles for a Chandra Archival Sample of Galaxy Clusters. *ApJS*, 182:12–32.

Cavagnolo, K. W., McNamara, B. R., Nulsen, P. E. J., Carilli, C. L., Jones, C., and Bîrzan, L. (2010). A Relationship Between AGN Jet Power and Radio Power. *ApJ*, 720(2):1066–1072.

Cavaliere, A. and Fusco-Femiano, R. (1976a). Reprint of 1976A&A....49..137C. X-rays from hot plasma in clusters of galaxies. *A&A*, 500:95–102.

Cavaliere, A. and Fusco-Femiano, R. (1976b). X-rays from hot plasma in clusters of galaxies. *A&A*, 49:137–144.

Cavaliere, A., Santangelo, P., Tarquini, G., and Vittorio, N. (1986). The Dynamical Evolution of Clusters of Galaxies. *ApJ*, 305:651.

Chadayammuri, U., ZuHone, J., Nulsen, P., Nagai, D., and Russell, H. (2022). Turbulent magnetic fields in merging clusters: a case study of Abell 2146. *MNRAS*, 512(2):2157–2170.

Chambers, K. C., Magnier, E. A., Metcalfe, N., Flewelling, H. A., Huber, M. E., Waters, C. Z., Denneau, L., Draper, P. W., Farrow, D., Finkbeiner, D. P., Holmberg, C., Koppenhoefer, J., Price, P. A., Rest, A., Saglia, R. P., Schlafly, E. F., Smartt, S. J., Sweeney, W., Wainscoat, R. J., Burgett, W. S., Chastel, S., Grav, T., Heasley, J. N., Hodapp, K. W., Jedicke, R., Kaiser, N., Kudritzki, R. P., Luppino, G. A., Lupton, R. H., Monet, D. G., Morgan, J. S., Onaka, P. M., Shiao, B., Stubbs, C. W., Tonry, J. L., White, R., Bañados, E., Bell, E. F., Bender, R., Bernard, E. J., Boegner, M., Boffi, F., Botticella, M. T., Calamida, A., Casertano, S., Chen, W. P., Chen, X., Cole, S., Deacon, N., Frenk, C., Fitzsimmons, A., Gezari, S., Gibbs, V., Goessl, C., Goggia, T., Gourgue, R., Goldman, B., Grant, P., Grebel, E. K., Hambly, N. C., Hasinger, G., Heavens, A. F., Heckman, T. M., Henderson, R., Henning, T., Holman, M., Hopp, U., Ip, W. H., Isani, S., Jackson, M., Keyes, C. D., Koekemoer, A. M., Kotak, R., Le, D., Liska, D., Long, K. S., Lucey, J. R., Liu, M., Martin, N. F., Masci, G., McLean, B., Mindel, E., Misra, P., Morganson, E., Murphy, D. N. A., Obaika, A., Narayan, G., Nieto-Santisteban, M. A., Norberg, P., Peacock, J. A., Pier, E. A., Postman, M., Primak, N., Rae, C., Rai, A., Riess, A., Riffeser, A., Rix, H. W., Röser, S., Russel, R., Rutz, L., Schilbach, E., Schultz, A. S. B., Scolnic, D., Strolger, L., Szalay, A., Seitz, S., Small, E., Smith, K. W., Soderblom, D. R., Taylor, P., Thomson, R., Taylor, A. N., Thakar, A. R., Thiel, J., Thilker, D., Unger, D., Urata, Y., Valenti, J., Wagner, J., Walder, T., Walter, F., Watters, S. P., Werner, S., Wood-Vasey, W. M., and Wyse, R. (2016). The Pan-STARRS1 Surveys. *arXiv e-prints*, page arXiv:1612.05560.

Chandra, P., Ray, A., and Bhatnagar, S. (2004). The Late-Time Radio Emission from SN 1993J at Meter Wavelengths. *ApJ*, 612(2):974–987.

Chen, R., Peng, B., Strom, R. G., and Wei, J. (2012). Galaxy group around giant radio galaxy NGC 315. *MNRAS*, 420(3):2715–2726.

Clarke, T. E., Blanton, E. L., and Sarazin, C. L. (2004). The Complex Cooling Core of A2029: Radio and X-Ray Interactions. *ApJ*, 616(1):178–191.

Clarke, T. E., Randall, S. W., Sarazin, C. L., Blanton, E. L., and Giacintucci, S. (2013). Chandra View of the Ultra-steep Spectrum Radio Source in A2443: Merger Shock-induced Compression of Fossil Radio Plasma? *ApJ*, 772(2):84.

Cole, S. (1991). Modeling Galaxy Formation in Evolving Dark Matter Halos. *ApJ*, 367:45.

Condon, J. J., Cotton, W. D., Greisen, E. W., Yin, Q. F., Perley, R. A., Taylor, G. B., and Broderick, J. J. (1998). The NRAO VLA Sky Survey. *AJ*, 115(5):1693–1716.

Condon, J. J., Cotton, W. D., White, S. V., Legodi, S., Goedhart, S., McAlpine, K., Ratcliffe, S. M., and Camilo, F. (2021). Threads, Ribbons, and Rings in the Radio Galaxy IC 4296. *ApJ*, 917(1):18.

Coziol, R., Andernach, H., Caretta, C. A., Alamo-Martínez, K. A., and Tago, E. (2009). The Dynamical State of Brightest Cluster Galaxies and The Formation of Clusters. *AJ*, 137(6):4795–4809.

Crawford, C. S., Allen, S. W., Ebeling, H., Edge, A. C., and Fabian, A. C. (1999). The ROSAT Brightest Cluster Sample - III. Optical spectra of the central cluster galaxies. *MNRAS*, 306:857–896.

Crawford, C. S., Sanders, J. S., and Fabian, A. C. (2005). The giant Hα/X-ray filament in the cluster of galaxies A1795. *MNRAS*, 361(1):17–33.

Croton, D. J., Springel, V., White, S. D. M., De Lucia, G., Frenk, C. S., Gao, L., Jenkins, A., Kauffmann, G., Navarro, J. F., and Yoshida, N. (2006). The many lives of active galactic nuclei: cooling flows, black holes and the luminosities and colours of galaxies. *MNRAS*, 365:11–28.

Cuciti, V., Brunetti, G., van Weeren, R., Bonafede, A., Dallacasa, D., Cassano, R., Venturi, T., and Kale, R. (2018). New giant radio sources and underluminous radio halos in two galaxy clusters. *A&A*, 609:A61.

Cuciti, V., Cassano, R., Brunetti, G., Dallacasa, D., de Gasperin, F., Ettori, S., Giacintucci, S., Kale, R., Pratt, G. W., van Weeren, R. J., and Venturi, T. (2021). Radio halos in a mass-selected sample of 75 galaxy clusters. II. Statistical analysis. *A&A*, 647:A51.

Cuciti, V., Cassano, R., Brunetti, G., Dallacasa, D., Kale, R., Ettori, S., and Venturi, T. (2015). Occurrence of radio halos in galaxy clusters. Insight from a mass-selected sample. *A&A*, 580:A97.

Dabhade, P., Röttgering, H. J. A., Bagchi, J., Shimwell, T. W., Hardcastle, M. J., Sankhyayan, S., Morganti, R., Jamrozy, M., Shulevski, A., and Duncan, K. J. (2020). Giant radio galaxies in the LOFAR Two-metre Sky Survey. I. Radio and environmental properties. *A&A*, 635:A5.

Dallacasa, D., Brunetti, G., Giacintucci, S., Cassano, R., Venturi, T., Macario, G., Kassim, N., Lane, W., and Setti, G. (2009). Deep 1.4 GHz Follow-up of the Steep Spectrum Radio Halo in A521. *ApJ*, 699(2):1288–1292.

de Gasperin, F., Brunetti, G., Brüggen, M., van Weeren, R., Williams, W. L., Botteon, A., Cuciti, V., Dijkema, T. J., Edler, H., Iacobelli, M., Kang, H., Offringa, A., Orrú, E., Pizzo, R., Rafferty, D., Röttgering, H., and Shimwell, T. (2020). Reaching thermal noise at ultra-low radio frequencies. Toothbrush radio relic downstream of the shock front. *A&A*, 642:A85.

de Gasperin, F., Dijkema, T. J., Drabent, A., Mevius, M., Rafferty, D., van Weeren, R., Brüggen, M., Callingham, J. R., Emig, K. L., Heald, G., Intema, H. T., Morabito, L. K., Offringa, A. R., Oonk, R., Orrù, E., Röttgering, H., Sabater, J., Shimwell, T., Shulevski, A., and Williams, W. (2019a). Systematic effects in LOFAR data: A unified calibration strategy. *A&A*, 622:A5.

de Gasperin, F., Dijkema, T. J., Drabent, A., Mevius, M., Rafferty, D., van Weeren, R., Brüggen, M., Callingham, J. R., Emig, K. L., Heald, G., Intema, H. T., Morabito, L. K., Offringa, A. R., Oonk, R., Orrù, E., Röttgering, H., Sabater, J., Shimwell, T., Shulevski, A., and Williams, W. (2019b). Systematic effects in LOFAR data: A unified calibration strategy. *A&A*, 622:A5.

de Gasperin, F., Intema, H. T., Shimwell, T. W., Brunetti, G., Brüggen, M., Enßlin, T. A., van Weeren, R. J., Bonafede, A., and Röttgering, H. J. A. (2017). Gentle reenergization of electrons in merging galaxy clusters. *Science Advances*, 3(10):e1701634.

de Gasperin, F., Ogrean, G. A., van Weeren, R. J., Dawson, W. A., Brüggen, M., Bonafede, A., and Simionescu, A. (2015a). Abell 1033: birth of a radio phoenix. *MNRAS*, 448(3):2197–2209.

de Gasperin, F., Ogrean, G. A., van Weeren, R. J., Dawson, W. A., Brüggen, M., Bonafede, A., and Simionescu, A. (2015b). Abell 1033: birth of a radio phoenix. *MNRAS*, 448(3):2197–2209.

de Gasperin, F., Orrú, E., Murgia, M., Merloni, A., Falcke, H., Beck, R., Beswick, R., Bîrzan, L., Bonafede, A., Brüggen, M., Brunetti, G., Chyży, K., Conway, J., Croston, J. H., Enßlin, T., Ferrari, C., Heald, G., Heidenreich, S., Jackson, N., Macario, G., McKean, J., Miley, G., Morganti, R., Offringa, A., Pizzo, R., Rafferty, D., Röttgering, H., Shulevski, A., Steinmetz, M., Tasse, C., van der Tol, S., van Driel, W., van Weeren, R. J., van Zwieten, J. E., Alexov, A., Anderson, J., Asgekar, A., Avruch, M., Bell, M., Bell, M. R., Bentum, M., Bernardi, G., Best, P., Breitling, F., Broderick, J. W., Butcher, A., Ciardi, B., Dettmar, R. J., Eisloeffel, J., Frieswijk, W., Gankema, H., Garrett, M., Gerbers, M., Griessmeier, J. M., Gunst, A. W., Hassall, T. E., Hessels, J., Hoeft, M., Horneffer, A., Karastergiou, A., Köhler, J., Koopman, Y., Kuniyoshi, M., Kuper, G., Maat, P., Mann, G., Mevius, M., Mulcahy, D. D., Munk, H., Nijboer, R., Noordam, J., Paas, H., Pandey, M., Pandey, V. N., Polatidis, A., Reich, W., Schoenmakers, A. P., Sluman, J., Smirnov, O., Sobey, C., Stappers, B., Swinbank, J., Tagger, M., Tang, Y., van Bemmel, I., van Cappellen, W., van Duin, A. P., van Haarlem, M., van Leeuwen, J., Vermeulen, R., Vocks, C., White, S., Wise, M., Wucknitz, O., and Zarka, P. (2012). M 87 at metre wavelengths: the LOFAR picture. *A&A*, 547:A56.

de Gasperin, F., Rudnick, L., Finoguenov, A., Wittor, D., Akamatsu, H., Brüggen, M., Chibueze, J. O., Clarke, T. E., Cotton, W., Cuciti, V., Domínguez-Fernández, P., Knowles, K., O'Sullivan, S. P., and Sebokolodi, L. (2022). MeerKAT view of the diffuse radio sources in Abell 3667 and their interactions with the thermal plasma. *A&A*, 659:A146.

de Gasperin, F., van Weeren, R. J., Brüggen, M., Vazza, F., Bonafede, A., and Intema, H. T. (2014). A new double radio relic in PSZ1 G096.89+24.17 and a radio relic mass-luminosity relation. *MNRAS*, 444(4):3130–3138.

de Gasperin, F., Williams, W. L., Best, P., Brüggen, M., Brunetti, G., Cuciti, V., Dijkema, T. J., Hardcastle, M. J., Norden, M. J., Offringa, A., Shimwell, T., van Weeren, R., Bomans, D., Bonafede, A., Botteon, A., Callingham, J. R., Cassano, R., Chyży, K. T., Emig, K. L., Edler, H., Haverkorn, M., Heald, G., Heesen, V., Iacobelli, M., Intema, H. T., Kadler, M., Małek, K., Mevius, M., Miley, G., Mingo, B., Morabito, L. K., Sabater, J., Morganti, R., Orrú, E., Pizzo, R., Prandoni, I., Shulevski, A., Tasse, C., Vaccari, M., Zarka, P., and Röttgering, H. (2021). The LOFAR LBA Sky Survey. I. Survey description and preliminary data release. *A&A*, 648:A104.

De Propris, R., West, M. J., Andrade-Santos, F., Ragone-Figueroa, C., Rasia, E., Forman, W., Jones, C., Kipper, R., Borgani, S., Lambas, D. G., Romashkova, E. A., and Patra, K. C. (2021). Brightest cluster galaxies: the centre can(not?) hold. *MNRAS*, 500(1):310–318.

Dey, A., Schlegel, D. J., Lang, D., Blum, R., Burleigh, K., Fan, X., Findlay, J. R., Finkbeiner, D., Herrera, D., Juneau, S., Landriau, M., Levi, M., McGreer, I., Meisner, A., Myers, A. D., Moustakas, J., Nugent, P., Patej, A., Schlafly, E. F., Walker, A. R., Valdes, F., Weaver, B. A., Yèche, C., Zou, H., Zhou, X., Abareshi, B., Abbott, T. M. C., Abolfathi, B., Aguilera, C., Alam, S., Allen, L., Alvarez, A., Annis, J., Ansarinejad, B., Aubert, M., Beechert, J., Bell, E. F., BenZvi, S. Y., Beutler, F., Bielby, R. M., Bolton, A. S., Briceño, C., Buckley-Geer, E. J., Butler, K., Calamida, A., Carlberg, R. G., Carter, P., Casas, R., Castander, F. J., Choi, Y., Comparat, J., Cukanovaite, E., Delubac, T., DeVries, K., Dey, S., Dhungana, G., Dickinson, M., Ding, Z., Donaldson, J. B., Duan, Y., Duckworth, C. J., Eftekharzadeh, S., Eisenstein, D. J., Etourneau, T., Fagrelius, P. A., Farihi, J., Fitzpatrick, M., Font-Ribera, A., Fulmer, L., Gänsicke, B. T., Gaztanaga, E., George, K., Gerdes, D. W., Gontcho, S. G. A., Gorgoni, C., Green, G., Guy, J., Harmer, D., Hernandez, M., Honscheid, K., Huang, L. W., James, D. J., Jannuzi, B. T., Jiang, L., Joyce, R., Karcher, A., Karkar, S., Kehoe, R., Kneib, J.-P., Kueter-Young, A., Lan, T.-W., Lauer, T. R., Le Guillou, L., Le Van Suu, A., Lee, J. H., Lesser, M., Perreault Levasseur, L., Li, T. S., Mann, J. L., Marshall, R., Martínez-Vázquez, C. E., Martini, P., du Mas des Bourboux, H., McManus, S., Meier, T. G., Ménard, B., Metcalfe, N., Muñoz-Gutiérrez, A., Najita, J., Napier, K., Narayan, G., Newman, J. A., Nie, J., Nord, B., Norman, D. J., Olsen, K. A. G., Paat, A., Palanque-Delabrouille, N., Peng, X., Poppett, C. L., Poremba, M. R., Prakash, A., Rabinowitz, D., Raichoor, A., Rezaie, M., Robertson, A. N., Roe, N. A., Ross, A. J., Ross, N. P., Rudnick, G., Safonova, S., Saha, A., Sánchez, F. J., Savary, E., Schweiker, H., Scott, A., Seo, H.-J., Shan, H., Silva, D. R., Slepian, Z., Soto, C., Sprayberry, D., Staten, R., Stillman, C. M., Stupak, R. J., Summers, D. L., Sien Tie, S., Tirado, H., Vargas-Magaña, M., Vivas, A. K., Wechsler, R. H., Williams, D., Yang, J., Yang, Q., Yapici, T., Zaritsky, D., Zenteno, A., Zhang, K., Zhang, T., Zhou, R., and Zhou, Z. (2019). Overview of the DESI Legacy Imaging Surveys. *AJ*, 157(5):168.

Di Gennaro, G., van Weeren, R. J., Cassano, R., Brunetti, G., Brüggen, M., Hoeft, M., Osinga, E., Botteon, A., Cuciti, V., de Gasperin, F., Röttgering, H. J. A., and Tasse, C. (2021). A LOFAR-uGMRT spectral index study of distant radio halos. *A&A*, 654:A166.

Di Gennaro, G., van Weeren, R. J., Hoeft, M., Kang, H., Ryu, D., Rudnick, L., Forman, W., Röttgering, H. J. A., Brüggen, M., Dawson, W. A., Golovich, N., Hoang, D. N., Intema, H. T., Jones, C., Kraft, R. P., Shimwell, T. W., and Stroe, A. (2018). Deep Very Large Array Observations of the Merging Cluster CIZA J2242.8+5301: Continuum and Spectral Imaging. *ApJ*, 865(1):24.

Dolag, K. and Enßlin, T. A. (2000). Radio halos of galaxy clusters from hadronic secondary electron injection in realistic magnetic field configurations. *A&A*, 362:151–157.

Donahue, M. and Voit, G. M. (2022). Baryon Cycles in the Biggest Galaxies. *arXiv e-prints*, page arXiv:2204.08099.

Driver, S. P., Norberg, P., Baldry, I. K., Bamford, S. P., Hopkins, A. M., Liske, J., Loveday, J., Peacock, J. A., Hill, D. T., Kelvin, L. S., Robotham, A. S. G., Cross, N. J. G., Parkinson, H. R., Prescott, M., Conselice, C. J., Dunne, L., Brough, S., Jones, H., Sharp, R. G., van Kampen, E., Oliver, S., Roseboom, I. G., Bland-Hawthorn, J., Croom, S. M., Ellis, S., Cameron, E., Cole, S., Frenk, C. S., Couch, W. J., Graham, A. W., Proctor, R., De Propris, R., Doyle, I. F., Edmondson, E. M., Nichol, R. C., Thomas, D., Eales, S. A., Jarvis, M. J., Kuijken, K., Lahav, O., Madore, B. F., Seibert, M., Meyer, M. J., Staveley-Smith, L., Phillipps, S., Popescu, C. C., Sansom, A. E., Sutherland, W. J., Tuffs, R. J., and Warren, S. J. (2009). GAMA: towards a physical understanding of galaxy formation. *Astronomy and Geophysics*, 50(5):5.12–5.19.

Dubois, Y., Pichon, C., Welker, C., Le Borgne, D., Devriendt, J., Laigle, C., Codis, S., Pogosyan, D., Arnouts, S., Benabed, K., Bertin, E., Blaizot, J., Bouchet, F., Cardoso, J. F., Colombi, S., de Lapparent, V., Desjacques, V., Gavazzi, R., Kassin, S., Kimm, T., McCracken, H., Milliard, B., Peirani, S., Prunet, S., Rouberol, S., Silk, J., Slyz, A., Sousbie, T., Teyssier, R., Tresse, L., Treyer, M., Vibert, D., and Volonteri, M. (2014). Dancing in the dark: galactic properties trace spin swings along the cosmic web. *MNRAS*, 444(2):1453–1468.

Duchesne, S. W., Johnston-Hollitt, M., Riseley, C. J., Bartalucci, I., and Keel, S. R. (2022). The merging galaxy cluster Abell 3266 at low radio frequencies. *MNRAS*, 511(3):3525–3535.

Duchesne, S. W., Johnston-Hollitt, M., and Wilber, A. G. (2021). MWA and ASKAP observations of atypical radio-halo-hosting galaxy clusters: Abell 141 and Abell 3404. *PASA*, 38:e031.

Dunn, R. J. H., Allen, S. W., Taylor, G. B., Shurkin, K. F., Gentile, G., Fabian, A. C., and Reynolds, C. S. (2010). The radio properties of a complete, X-ray selected sample of nearby, massive elliptical galaxies. *MNRAS*, 404:180–197.

Ebeling, H., Edge, A. C., Bohringer, H., Allen, S. W., Crawford, C. S., Fabian, A. C., Voges, W., and Huchra, J. P. (1998). The ROSAT Brightest Cluster Sample - I. The compilation of the sample and the cluster log N-log S distribution. *MNRAS*, 301:881–914.

Ebeling, H., Edge, A. C., Fabian, A. C., Allen, S. W., Crawford, C. S., and Böhringer, H. (1997a). The ROSAT Brightest Cluster Sample (BCS): The Cluster X-Ray Luminosity Function within Z = 0.3. *ApJ*, 479(2):L101–L104.

Ebeling, H., Edge, A. C., Fabian, A. C., Allen, S. W., Crawford, C. S., and Böhringer, H. (1997b). The ROSAT Brightest Cluster Sample (BCS): The Cluster X-Ray Luminosity Function within Z = 0.3. *ApJ*, 479(2):L101–L104.

Eckert, D., Gaspari, M., Gastaldello, F., Le Brun, A. M. C., and O'Sullivan, E. (2021). Feedback from Active Galactic Nuclei in Galaxy Groups. *Universe*, 7(5):142.

Eckert, D., Gaspari, M., Vazza, F., Gastaldello, F., Tramacere, A., Zimmer, S., Ettori, S., and Paltani, S. (2017). On the Connection between Turbulent Motions and Particle Acceleration in Galaxy Clusters. *ApJ*, 843(2):L29.

Eckert, D., Jauzac, M., Vazza, F., Owers, M. S., Kneib, J. P., Tchernin, C., Intema, H., and Knowles, K. (2016). A shock front at the radio relic of Abell 2744. *MNRAS*, 461(2):1302–1307.

Edge, A. C. (2001). The detection of molecular gas in the central galaxies of cooling flow clusters. *MNRAS*, 328:762–782.

Edwards, L. O. V., Robert, C., Mollá, M., and McGee, S. L. (2009). The diverse nature of optical emission lines in brightest cluster galaxies: IFU observations of the central kiloparsec. *MNRAS*, 396(4):1953–1971.

Ehlert, S., Allen, S. W., von der Linden, A., Simionescu, A., Werner, N., Taylor, G. B., Gentile, G., Ebeling, H., Allen, M. T., Applegate, D., Dunn, R. J. H., Fabian, A. C., Kelly, P., Million, E. T., Morris, R. G., Sanders, J. S., and Schmidt, R. W. (2011). Extreme active galactic nucleus feedback and cool-core destruction in the X-ray luminous galaxy cluster MACS J1931.8-2634. *MNRAS*, 411(3):1641–1658.

Eke, V., Baugh, C. M., Cole, S., Frenk, C. S., and Navarro, J. F. (2006). Galaxy groups in the 2dF Galaxy Redshift Survey: the number density of groups. *MNRAS*, 370(3):1147–1158.

Ensslin, T. A., Biermann, P. L., Klein, U., and Kohle, S. (1998). Cluster radio relics as a tracer of shock waves of the large-scale structure formation. *A&A*, 332:395–409.

Enßlin, T. A. and Gopal-Krishna (2001). Reviving fossil radio plasma in clusters of galaxies by adiabatic compression in environmental shock waves. *A&A*, 366:26–34.

Ettori, S., Gastaldello, F., Gitti, M., O'Sullivan, E., Gaspari, M., Brighenti, F., David, L., and Edge, A. C. (2013). Cold fronts and metal anisotropies in the X-ray cool core of the galaxy cluster Zw 1742+3306. *A&A*, 555:A93.

Fabian, A. C. (1994). Cooling Flows in Clusters of Galaxies. *ARAA*, 32:277–318.

Fabian, A. C. (1999). The obscured growth of massive black holes. *MNRAS*, 308(4):L39–L43.

Fabian, A. C. (2012). Observational Evidence of Active Galactic Nuclei Feedback. *ARA&A*, 50:455–489.

Fabian, A. C., Nulsen, P. E. J., and Canizares, C. R. (1991). Cooling flows in clusters of galaxies. *A&A Rev.*, 2(3-4):191–226.

Fabian, A. C., Sanders, J. S., Taylor, G. B., Allen, S. W., Crawford, C. S., Johnstone, R. M., and Iwasawa, K. (2006). A very deep Chandra observation of the Perseus cluster: shocks, ripples and conduction. *MNRAS*, 366(2):417–428.

Fanaroff, B. L. and Riley, J. M. (1974). The morphology of extragalactic radio sources of high and low luminosity. *MNRAS*, 167:31P–36P.

Feigelson, E. D. (1992). Censoring in astronomical data due to nondetections. In *Statistical Challenges in Modern Astronomy*, pages 221–245.

Feigelson, E. D., Nelson, P. I., Isobe, T., and LaValley, M. (2014). ASURV: Astronomical SURVival Statistics.

Feretti, L. and Giovannini, G. (2008). *Clusters of Galaxies in the Radio: Relativistic Plasma and ICM/Radio Galaxy Interaction Processes*, volume 740, page 24.

Feretti, L., Giovannini, G., Govoni, F., and Murgia, M. (2012). Clusters of galaxies: observational properties of the diffuse radio emission. *A&A Rev.*, 20:54.

Finoguenov, A., Böhringer, H., and Zhang, Y. Y. (2005). XMM-Newton study of the two-dimensional structure of the REFLEX-DXL galaxy clusters. *A&A*, 442(3):827–839.

Finoguenov, A., Rykoff, E., Clerc, N., Costanzi, M., Hagstotz, S., Ider Chitham, J., Kiiveri, K., Kirkpatrick, C. C., Capasso, R., Comparat, J., Damsted, S., Dupke, R., Erfanianfar, G., Henry, J. P., Kaefer, F., Kneib, J.-P., Lindholm, V., Rozo, E., van Waerbeke, L., and Weller, J. (2019). CODEX clusters. The Survey, the Catalog, and Cosmology of the X-ray Luminosity Function. *arXiv e-prints*, page arXiv:1912.03262.

Finoguenov, A., Sarazin, C. L., Nakazawa, K., Wik, D. R., and Clarke, T. E. (2010). XMM-Newton Observation of the Northwest Radio Relic Region in A3667. *ApJ*, 715(2):1143–1151.

Forman, W., Churazov, E., Jones, C., Heinz, S., Kraft, R., and Vikhlinin, A. (2017). Partitioning the Outburst Energy of a Low Eddington Accretion Rate AGN at the Center of an Elliptical Galaxy: The Recent 12 Myr History of the Supermassive Black Hole in M87. *ApJ*, 844(2):122.

Forman, W., Nulsen, P., Heinz, S., Owen, F., Eilek, J., Vikhlinin, A., Markevitch, M., Kraft, R., Churazov, E., and Jones, C. (2005). Reflections of Active Galactic Nucleus Outbursts in the Gaseous Atmosphere of M87. *ApJ*, 635(2):894–906.

Freeman, P., Doe, S., and Siemiginowska, A. (2001). Sherpa: a mission-independent data analysis application. In Starck, J.-L. and Murtagh, F. D., editors, *Proc. SPIE*, volume 4477 of *Society of Photo-Optical Instrumentation Engineers (SPIE) Conference Series*, pages 76–87.

Fruscione, A., McDowell, J. C., Allen, G. E., Brickhouse, N. S., Burke, D. J., Davis, J. E., Durham, N., Elvis, M., Galle, E. C., Harris, D. E., Huenemoerder, D. P., Houck, J. C., Ishibashi, B., Karovska, M., Nicastro, F., Noble, M. S., Nowak, M. A., Primini, F. A., Siemiginowska, A., Smith, R. K., and Wise, M. (2006). CIAO: Chandra's data analysis system. In *Proc. SPIE*, volume 6270 of *Society of Photo-Optical Instrumentation Engineers (SPIE) Conference Series*, page 62701V.

Fujita, Y., Akamatsu, H., and Kimura, S. S. (2016). Turbulent cosmic ray reacceleration and the curved radio spectrum of the radio relic in the Sausage Cluster. *PASJ*, 68(3):34.

Gaspari, M. (2016). The self-regulated AGN feedback loop: the role of chaotic cold accretion. In Kaviraj, S., editor, *Galaxies at High Redshift and Their Evolution Over Cosmic Time*, volume 319, pages 17–20.

Gaspari, M., Brighenti, F., D'Ercole, A., and Melioli, C. (2011). AGN feedback in galaxy groups: the delicate touch of self-regulated outflows. *MNRAS*, pages 1003–+.

Gaspari, M., Churazov, E., Nagai, D., Lau, E. T., and Zhuravleva, I. (2014). The relation between gas density and velocity power spectra in galaxy clusters: High-resolution hydrodynamic simulations and the role of conduction. *A&A*, 569:A67.

Gaspari, M., Eckert, D., Ettori, S., Tozzi, P., Bassini, L., Rasia, E., Brighenti, F., Sun, M., Borgani, S., Johnson, S. D., Tremblay, G. R., Stone, J. M., Temi, P., Yang, H. Y. K., Tombesi, F., and Cappi, M. (2019). The X-Ray Halo Scaling Relations of Supermassive Black Holes. *ApJ*, 884(2):169.

Gaspari, M., Melioli, C., Brighenti, F., and D'Ercole, A. (2011). The dance of heating and cooling in galaxy clusters: Three-dimensional simulations of self-regulated active galactic nuclei outflows. *MNRAS*, 411(1):349–372.

Gaspari, M., Melioli, C., Brighenti, F., and D'Ercole, A. (2011). The dance of heating and cooling in galaxy clusters: three-dimensional simulations of self-regulated active galactic nuclei outflows. *MNRAS*, 411:349–372.

Gaspari, M., Ruszkowski, M., and Oh, S. P. (2013). Chaotic cold accretion on to black holes. *MNRAS*, 432(4):3401–3422.

Gaspari, M., Ruszkowski, M., and Sharma, P. (2012). Cause and Effect of Feedback: Multiphase Gas in Cluster Cores Heated by AGN Jets. *ApJ*, 746:94.

Gaspari, M. and Sądowski, A. (2017). Unifying the Micro and Macro Properties of AGN Feeding and Feedback. *ApJ*, 837(2):149.

Gaspari, M., Tombesi, F., and Cappi, M. (2020). Linking macro-, meso- and microscales in multiphase AGN feeding and feedback. *Nature Astronomy*, 4:10–13.

Gastaldello, F., Buote, D. A., Brighenti, F., and Mathews, W. G. (2008). Trouble for AGN Feedback? The Puzzle of the Core of the Galaxy Cluster AWM 4. *ApJ*, 673(1):L17.

Gastaldello, F., Buote, D. A., Temi, P., Brighenti, F., Mathews, W. G., and Ettori, S. (2009). X-ray cavities, filaments, and cold fronts in the core of the galaxy group NGC 5044. *ApJ*, 693(1):43–55.

Gastaldello, F., Ettori, S., Balestra, I., Brighenti, F., Buote, D. A., de Grandi, S., Ghizzardi, S., Gitti, M., and Tozzi, P. (2010). Apparent high metallicity in 3-4 keV galaxy clusters: the inverse iron-bias in action in the case of the merging cluster Abell 2028. *A&A*, 522:A34+.

Gentile, G., Rodríguez, C., Taylor, G. B., Giovannini, G., Allen, S. W., Lane, W. M., and Kassim, N. E. (2007). Monitoring the Bidirectional Relativistic Jets of the Radio Galaxy 3C 338. *ApJ*, 659(1):225–234.

George, M. R., Leauthaud, A., Bundy, K., Finoguenov, A., Ma, C.-P., Rykoff, E. S., Tinker, J. L., Wechsler, R. H., Massey, R., and Mei, S. (2012). Galaxies in X-Ray Groups. II. A Weak Lensing Study of Halo Centering. *ApJ*, 757(1):2.

George, M. R., Leauthaud, A., Bundy, K., Finoguenov, A., Tinker, J., Lin, Y.-T., Mei, S., Kneib, J.-P., Aussel, H., Behroozi, P. S., Busha, M. T., Capak, P., Coccato, L., Covone, G., Faure, C., Fiorenza, S. L., Ilbert, O., Le Floc'h, E., Koekemoer, A. M., Tanaka, M., Wechsler, R. H., and Wolk, M. (2011). Galaxies in X-Ray Groups. I. Robust Membership Assignment and the Impact of Group Environments on Quenching. *ApJ*, 742(2):125.

Ghirardini, V., Bahar, Y. E., Bulbul, E., Liu, A., Clerc, N., Pacaud, F., Comparat, J., and Liu, T. (2021). The eROSITA Final Equatorial-Depth Survey (eFEDS): Characterization of Morphological Properties of Galaxy Groups and Clusters. *A&A*, page (submitted).

Ghizzardi, S., Rossetti, M., and Molendi, S. (2010). Cold fronts in galaxy clusters. *A&A*, 516:A32.

Giacintucci, S., Markevitch, M., Brunetti, G., ZuHone, J. A., Venturi, T., Mazzotta, P., and Bourdin, H. (2014). Mapping the Particle Acceleration in the Cool Core of the Galaxy Cluster RX J1720.1+2638. *ApJ*, 795:73.

Giacintucci, S., Markevitch, M., Cassano, R., Venturi, T., Clarke, T. E., and Brunetti, G. (2017). Occurrence of Radio Minihalos in a Mass-limited Sample of Galaxy Clusters. *ApJ*, 841:71.

Giacintucci, S., Markevitch, M., Johnston-Hollitt, M., Wik, D. R., Wang, Q. H. S., and Clarke, T. E. (2020). Discovery of a Giant Radio Fossil in the Ophiuchus Galaxy Cluster. *ApJ*, 891(1):1.

Giacintucci, S., O'Sullivan, E., Vrtilek, J., David, L. P., Raychaudhury, S., Venturi, T., Athreya, R. M., Clarke, T. E., Murgia, M., Mazzotta, P., Gitti, M., Ponman, T., Ishwara-Chandra, C. H., Jones, C., and Forman, W. R. (2011). A Combined Low-radio Frequency/X-ray Study of Galaxy Groups. I. Giant Metrewave Radio Telescope Observations at 235 MHz AND 610 MHz. *ApJ*, 732:95–+.

Giacintucci, S., Venturi, T., Brunetti, G., Bardelli, S., Dallacasa, D., Ettori, S., Finoguenov, A., Rao, A., and Zucca, E. (2005). Spectral properties and origin of the radio halo in A3562. *A&A*, 440(3):867–879.

Giles, P. A., Maughan, B. J., Pacaud, F., Lieu, M., Clerc, N., Pierre, M., Adami, C., Chiappetti, L., Démoclés, J., Ettori, S., Le Févre, J. P., Ponman, T., Sadibekova, T., Smith, G. P., Willis, J. P., and Ziparo, F. (2016). The XXL Survey. III. Luminosity-temperature relation of the bright cluster sample. *A&A*, 592:A3.

Giodini, S., Smolić, V., Finoguenov, A., Boehringer, H., Birzan, L., Zamorani, G., Oklopić, A., Pierini, D., Pratt, G. W., Schinnerer, E., Massey, R., Koekemoer, A. M., Salvato, M., Sanders, D. B., Kartaltepe, J. S., and Thompson, D. (2010). Radio galaxy feedback in x-ray-selected groups from cosmos: The effect on the intracluster medium. *ApJ*, 714(1):218–228.

Giovannini, G., Bonafede, A., Feretti, L., Govoni, F., Murgia, M., Ferrari, F., and Monti, G. (2009). Radio halos in nearby ($z < 0.4$) clusters of galaxies. *A&A*, 507(3):1257–1270.

Gitti, M., Brighenti, F., and McNamara, B. R. (2012). Evidence for AGN Feedback in Galaxy Clusters and Groups. *Advances in Astronomy*, 2012.

Gitti, M., Brunetti, G., Feretti, L., and Setti, G. (2004). Particle acceleration in cooling flow clusters of galaxies: The case of Abell 2626. *A&A*, 417:1–11.

Gitti, M., McNamara, B. R., Nulsen, P. E. J., and Wise, M. W. (2007). Cosmological Effects of Powerful AGN Outbursts in Galaxy Clusters: Insights from an XMM-Newton Observation of MS 0735+7421. *ApJ*, 660:1118–1136.

Gitti, M., O'Sullivan, E., Giacintucci, S., David, L. P., Vrtilek, J., Raychaudhury, S., and Nulsen, P. E. J. (2010). Cavities and Shocks in the Galaxy Group HCG 62 as Revealed by Chandra, XMM-Newton, and Giant Metrewave Radio Telescope Data. *ApJ*, 714:758–771.

Govoni, F., Feretti, L., Giovannini, G., Böhringer, H., Reiprich, T. H., and Murgia, M. (2001). Radio and X-ray diffuse emission in six clusters of galaxies. *A&A*, 376:803–819.

Govoni, F., Ferrari, C., Feretti, L., Vacca, V., Murgia, M., Giovannini, G., Perley, R., and Benoist, C. (2012). Detection of diffuse radio emission in the galaxy clusters A800, A910, A1550, and CL 1446+26. *A&A*, 545:A74.

Govoni, F., Murgia, M., Markevitch, M., Feretti, L., Giovannini, G., Taylor, G. B., and Carretti, E. (2009). A search for diffuse radio emission in the relaxed, cool-core galaxy clusters A1068, A1413, A1650, A1835, A2029, and Ophiuchus. *A&A*, 499:371–383.

Gozaliasl, G., Finoguenov, A., Khosroshahi, H. G., Laigle, C., Kirkpatrick, C. C., Kiiveri, K., Devriendt, J., Dubois, Y., and Ahoranta, J. (2020). Kinematic unrest of low mass galaxy groups. *A&A*, 635:A36.

Gozaliasl, G., Finoguenov, A., Khosroshahi, H. G., Mirkazemi, M., Erfanianfar, G., and Tanaka, M. (2016). Brightest group galaxies: stellar mass and star formation rate (paper I). *MNRAS*, 458(3):2762–2775.

Gozaliasl, G., Finoguenov, A., Khosroshahi, H. G., Mirkazemi, M., Salvato, M., Jassur, D. M. Z., Erfanianfar, G., Popesso, P., Tanaka, M., Lerchster, M., Kneib, J. P., McCracken, H. J., Mellier, Y., Egami, E., Pereira, M. J., Brimioulle, F., Erben, T., and Seitz, S. (2014). Mining the gap: evolution of the magnitude gap in X-ray galaxy groups from the 3-square-degree XMM coverage of CFHTLS. *A&A*, 566:A140.

Gozaliasl, G., Finoguenov, A., Tanaka, M., Dolag, K., Montanari, F., Kirkpatrick, C. C., Vardoulaki, E., Khosroshahi, H. G., Salvato, M., Laigle, C., McCracken, H. J., Ilbert, O., Cappelluti, N., Daddi, E., Hasinger, G., Capak, P., Scoville, N. Z., Toft, S., Civano, F., Griffiths, R. E., Balogh, M., Li, Y., Ahoranta, J., Mei, S., Iovino, A., Henriques, B. M. B., and Erfanianfar, G. (2019). Chandra centres for COSMOS X-ray galaxy groups: differences in stellar properties between central dominant and offset brightest group galaxies. *MNRAS*, 483(3):3545–3565.

Grossová, R., Werner, N., Rajpurohit, K., Mernier, F., Lakhchaura, K., Gabányi, K., Canning, R. E. A., Nulsen, P., Massaro, F., Sun, M., Connor, T., King, A., Allen, S. W., Frisbie, R. L. S., Donahue, M., and Fabian, A. C. (2019). Powerful AGN jets and unbalanced cooling in the hot atmosphere of IC 4296. *MNRAS*, 488(2):1917–1925.

Gupta, N., Pannella, M., Mohr, J. J., Klein, M., Rykoff, E. S., Annis, J., Avila, S., Bianchini, F., Brooks, D., Buckley-Geer, E., Bulbul, E., Carnero Rosell, A., Carrasco Kind, M., Carretero, J., Chiu, I., Costanzi, M., da Costa, L. N., De Vicente, J., Desai, S., Dietrich, J. P., Doel, P., Everett, S., Evrard, A. E., García-Bellido, J., Gaztanaga, E., Gruen, D., Gruendl, R. A., Gschwend, J., Gutierrez, G., Hollowood, D. L., Honscheid, K., James, D. J., Jeltema, T., Kuehn, K., Lidman, C., Lima, M., Maia, M. A. G., Marshall, J. L., McDonald, M., Menanteau, F., Miquel, R., Ogand o, R. L. C., Palmese, A., Paz-Chinchón, F., Plazas, A. A., Reichardt,

C. L., Sanchez, E., Santiago, B., Saro, A., Scarpine, V., Schindler, R., Schubnell, M., Serrano, S., Sevilla-Noarbe, I., Shao, X., Smith, M., Stott, J. P., Strazzullo, V., Suchyta, E., Swanson, M. E. C., Vikram, V., and Zenteno, A. (2020). Constraining radio mode feedback in galaxy clusters with the cluster radio AGN properties to z$\sim$1. *MNRAS*.

Haarsma, D. B., Leisman, L., Donahue, M., Bruch, S., Böhringer, H., Croston, J. H., Pratt, G. W., Voit, G. M., Arnaud, M., and Pierini, D. (2010). Brightest Cluster Galaxies and Core Gas Density in REXCESS Clusters. *ApJ*, 713(2):1037–1047.

Hamer, S. L., Edge, A. C., Swinbank, A. M., Wilman, R. J., Combes, F., Salomé, P., Fabian, A. C., Crawford, C. S., Russell, H. R., Hlavacek- Larrondo, J., McNamara, B. R., and Bremer, M. N. (2016). Optical emission line nebulae in galaxy cluster cores 1: the morphological, kinematic and spectral properties of the sample. *MNRAS*, 460:1758–1789.

Hamer, S. L., Edge, A. C., Swinbank, A. M., Wilman, R. J., Russell, H. R., Fabian, A. C., Sand ers, J. S., and Salomé, P. (2012). The relation between line emission and brightest cluster galaxies in three exceptional clusters: evidence for gas cooling from the intracluster medium. *MNRAS*, 421(4):3409–3417.

Hamer, S. L., Fabian, A. C., Russell, H. R., Salomé, P., Combes, F., Olivares, V., Polles, F. L., Edge, A. C., and Beckmann, R. S. (2019). Discovery of a diffuse optical line emitting halo in the core of the Centaurus cluster of galaxies: line emission outside the protection of the filaments. *MNRAS*, 483(4):4984–4998.

Hardcastle, M., Shimwell, T., Tasse, C., Best, P., Drabent, A., Jarvis, M., Prandoni, I., Röttgering, H., Sabater, J., and Schwarz, D. (2021). The contribution of discrete sources to the sky temperature at 144 MHz. *A&A*, 648:A10.

Hardcastle, M. J. (2018). A simulation-based analytic model of radio galaxies. *ArXiv e-prints*.

Hardcastle, M. J. and Croston, J. H. (2020). Radio galaxies and feedback from AGN jets. *New A Rev.*, 88:101539.

Hardcastle, M. J., Shimwell, T. W., Tasse, C., Best, P. N., Drabent, A., Jarvis, M. J., Prandoni, I., Röttgering, H. J. A., Sabater, J., and Schwarz, D. J. (2021). The contribution of discrete sources to the sky temperature at 144 MHz. *A&A*, 648:A10.

Hardcastle, M. J., Williams, W. L., Best, P. N., Croston, J. H., Duncan, K. J., Röttgering, H. J. A., Sabater, J., Shimwell, T. W., Tasse, C., Callingham, J. R., Cochrane, R. K., de Gasperin, F., Gürkan, G., Jarvis, M. J., Mahatma, V., Miley, G. K., Mingo, B., Mooney, S., Morabito, L. K., O'Sullivan, S. P., Prandoni, I., Shulevski, A., and Smith, D. J. B. (2019). Radio-loud AGN in the first LoTSS data release. The lifetimes and environmental impact of jet-driven sources. *A&A*, 622:A12.

Heckman, T. M. and Best, P. N. (2014). The Coevolution of Galaxies and Supermassive Black Holes: Insights from Surveys of the Contemporary Universe. *ARA&A*, 52:589–660.

Heesen, V., Staffehl, M., Basu, A., Beck, R., Stein, M., Tabatabaei, F. S., Hardcastle, M. J., Chyży, K. T., Shimwell, T. W., Adebahr, B., Beswick, R., Bomans, D. J., Botteon, A., Brinks, E., Brüggen, M., Dettmar, R. J., Drabent, A., de Gasperin, F., Gürkan, G., Heald, G. H., Horellou, C., Nikiel-Wroczynski, B., Paladino, R., Piotrowska, J., Röttgering, H. J. A., Smith, D. J. B., and Tasse, C. (2022). Nearby galaxies in LoTSS-DR2: insights into the non-linearity of the radio-SFR relation. *arXiv e-prints*, page arXiv:2204.00635.

Henden, N. A., Puchwein, E., and Sijacki, D. (2019). The redshift evolution of X-ray and Sunyaev-Zel'dovich scaling relations in the FABLE simulations. *MNRAS*, 489(2):2439–2470.

Hernández-Fernández, J. D., Haines, C. P., Diaferio, A., Iglesias-Páramo, J., Mendes de Oliveira, C., and Vilchez, J. M. (2014). Star formation activity and gas stripping in the Cluster Projected Phase-Space (CPPS). *MNRAS*, 438(3):2186–2200.

Hill, G., Gebhardt, K., Komatsu, E., Drory, N., MacQueen, P., Adams, J., Blanc, G., Koehler, R., Rafal, M., Roth, M., Kelz, A., Gronwall, C., Ciardullo, R., and Schneider, D. (2008). The Hobby-Eberly Telescope Dark Energy Experiment (HETDEX): Description and Early Pilot Survey Results. In Kodama, T., Yamada, T., and Aoki, K., editors, *Panoramic Views of Galaxy Formation and Evolution*, volume 399 of *Astronomical Society of the Pacific Conference Series*, page 115.

Hoang, D. N., Shimwell, T. W., van Weeren, R. J., Brunetti, G., Röttgering, H. J. A., Andrade-Santos, F., Botteon, A., Brüggen, M., Cassano, R., Drabent, A., de Gasperin, F., Hoeft, M., Intema, H. T., Rafferty, D. A., Shweta, A., and Stroe, A. (2019). Radio observations of the merging galaxy cluster Abell 520. *A&A*, 622:A20.

Hogan, M. T., Edge, A. C., Hlavacek-Larrondo, J., Grainge, K. J. B., Hamer, S. L., Mahony, E. K., Russell, H. R., Fabian, A. C., McNamara, B. R., and Wilman, R. J. (2015). A comprehensive study of the radio properties of brightest cluster galaxies. *MNRAS*, 453(2):1201–1222.

Hogan, M. T., McNamara, B. R., Pulido, F., Nulsen, P. E. J., Russell, H. R., Vantyghem, A. N., Edge, A. C., and Main, R. A. (2017a). Mass Distribution in Galaxy Cluster Cores. *ApJ*, 837(1):51.

Hogan, M. T., McNamara, B. R., Pulido, F. A., Nulsen, P. E. J., Vantyghem, A. N., Russell, H. R., Edge, A. C., Babyk, I., Main, R. A., and McDonald, M. (2017b). The Onset of Thermally Unstable Cooling from the Hot Atmospheres of Giant Galaxies in Clusters: Constraints on Feedback Models. *ApJ*, 851(1):66.

Huchra, J. P., Macri, L. M., Masters, K. L., Jarrett, T. H., Berlind, P., Calkins, M., Crook, A. C., Cutri, R., Erdoğdu, P., Falco, E., George, T., Hutcheson, C. M., Lahav, O., Mader, J., Mink, J. D., Martimbeau, N., Schneider, S., Skrutskie, M., Tokarz, S., and Westover, M. (2012). The 2MASS Redshift Survey—Description and Data Release. *ApJS*, 199(2):26.

Hudson, D. S., Mittal, R., Reiprich, T. H., Nulsen, P. E. J., Andernach, H., and Sarazin, C. L. (2010). What is a cool-core cluster? a detailed analysis of the cores of the X-ray flux-limited HIFLUGCS cluster sample. *A&A*, 513:A37.

Ignesti, A. (2022). Introducing PT-REX, the point-to-point TRend EXtractor. *New A*, 92:101732.

Ignesti, A., Brunetti, G., Shimwell, T., Gitti, M., Birzan, L., Botteon, A., Brüggen, M., de Gasperin, F., Di Gennaro, G., Edge, A. C., Riseley, C. J., Röttgering, H. J. A., and van Weeren, R. J. (2022). A LOFAR view into the stormy environment of the galaxy cluster 2A0335+096. *A&A*, 659:A20.

Ineson, J., Croston, J. H., Hardcastle, M. J., Kraft, R. P., Evans, D. A., and Jarvis, M. (2013). Radio-loud Active Galactic Nucleus: Is There a Link between Luminosity and Cluster Environment? *ApJ*, 770(2):136.

Ineson, J., Croston, J. H., Hardcastle, M. J., Kraft, R. P., Evans, D. A., and Jarvis, M. (2015). The link between accretion mode and environment in radio-loud active galaxies. *MNRAS*, 453(3):2682–2706.

Intema, H. T., Jagannathan, P., Mooley, K. P., and Frail, D. A. (2017). The GMRT 150 MHz all-sky radio survey. First alternative data release TGSS ADR1. *A&A*, 598:A78.

Intema, H. T., van der Tol, S., Cotton, W. D., Cohen, A. S., van Bemmel, I. M., and Röttgering, H. J. A. (2009). Ionospheric calibration of low frequency radio interferometric observations using the peeling scheme. I. Method description and first results. *A&A*, 501(3):1185–1205.

Jaffe, W. J. (1977). Origin and transport of electrons in the halo radio source in the Coma cluster. *ApJ*, 212:1–7.

Jaffe, W. J. and Perola, G. C. (1973). Dynamical Models of Tailed Radio Sources in Clusters of Galaxies. *A&A*, 26:423.

Jarvis, M., Taylor, R., Agudo, I., Allison, J. R., Deane, R. P., Frank, B., Gupta, N., Heywood, I., Maddox, N., McAlpine, K., Santos, M., Scaife, A. M. M., Vaccari, M., Zwart, J. T. L., Adams, E., Bacon, D. J., Baker, A. J., Bassett, B. A., Best, P. N., Beswick, R., Blyth, S., Brown, M. L., Bruggen, M., Cluver, M., Colafrancesco, S., Cotter, G., Cress, C., Davé, R., Ferrari, C., Hardcastle, M. J., Hale, C. L., Harrison, I., Hatfield, P. W., Klockner, H. R., Kolwa, S., Malefahlo, E., Marubini, T., Mauch, T., Moodley, K., Morganti, R., Norris, R. P., Peters, J. A., Prand oni, I., Prescott, M., Oliver, S., Oozeer, N., Rottgering, H. J. A., Seymour, N., Simpson, C., Smirnov, O., and Smith, D. J. B. (2016). The MeerKAT International GHz Tiered Extragalactic Exploration (MIGHTEE) Survey. In *MeerKAT Science: On the Pathway to the SKA*, page 6.

Jetha, N. N., Ponman, T. J., Hardcastle, M. J., and Croston, J. H. (2007). Active galactic nuclei heating in the centres of galaxy groups: a statistical study. *MNRAS*, 376(1):193–204.

Johnson, R., Ponman, T. J., and Finoguenov, A. (2009). A statistical analysis of the Two-Dimensional XMM-Newton Group Survey: the impact of feedback on group properties. *MNRAS*, 395:1287–1308.

Jones, L. R., Ponman, T. J., Horton, A., Babul, A., Ebeling, H., and Burke, D. J. (2003). The nature and space density of fossil groups of galaxies. *MNRAS*, 343(2):627–638.

Juráňová, A., Werner, N., Gaspari, M., Lakhchaura, K., Nulsen, P. E. J., Sun, M., Canning, R. E. A., Allen, S. W., Simionescu, A., Oonk, J. B. R., Connor, T., and Donahue, M. (2019). Cooling in the X-ray halo of the rotating, massive early-type galaxy NGC 7049. *MNRAS*, 484:2886–2895.

Kalberla, P. M. W., Burton, W. B., Hartmann, D., Arnal, E. M., Bajaja, E., Morras, R., and Pöppel, W. G. L. (2005). The Leiden/Argentine/Bonn (LAB) Survey of Galactic HI. Final data release of the combined LDS and IAR surveys with improved stray-radiation corrections. *A&A*, 440:775–782.

Kale, R. and Dwarakanath, K. S. (2012). Multi-frequency Studies of Radio Relics in the Galaxy Clusters A4038, A1664, and A786. *ApJ*, 744(1):46.

Kang, H., Ryu, D., and Jones, T. W. (2012). Diffusive Shock Acceleration Simulations of Radio Relics. *ApJ*, 756(1):97.

Kang, H., Ryu, D., and Jones, T. W. (2017). Shock Acceleration Model for the Toothbrush Radio Relic. *ApJ*, 840(1):42.

Kauffmann, G., Heckman, T. M., Tremonti, C., Brinchmann, J., Charlot, S., White, S. D. M., Ridgway, S. E., Brinkmann, J., Fukugita, M., Hall, P. B., Ivezić, Ž., Richards, G. T., and Schneider, D. P. (2003). The host galaxies of active galactic nuclei. *MNRAS*, 346(4):1055–1077.

Kelly, B. C. (2007). Some Aspects of Measurement Error in Linear Regression of Astronomical Data. *ApJ*, 665(2):1489–1506.

Kempner, J. C. and David, L. P. (2004). A Chandra view of the multiple merger in Abell 2744. *MNRAS*, 349(2):385–392.

Kettula, K., Finoguenov, A., Massey, R., Rhodes, J., Hoekstra, H., Taylor, J. E., Spinelli, P. F., Tanaka, M., Ilbert, O., Capak, P., McCracken, H. J., and Koekemoer, A. (2013). Weak Lensing Calibrated M-T Scaling Relation of Galaxy Groups in the COSMOS Field^{sstarf}. *ApJ*, 778(1):74.

Kettula, K., Giodini, S., van Uitert, E., Hoekstra, H., Finoguenov, A., Lerchster, M., Erben, T., Heymans, C., Hildebrandt, H., Kitching, T. D., Mahdavi, A., Mellier, Y., Miller, L., Mirkazemi, M., Van Waerbeke, L., Coupon, J., Egami, E., Fu, L., Hudson, M. J., Kneib, J. P., Kuijken, K., McCracken, H. J., Pereira, M. J., Rowe, B., Schrabback, T., Tanaka, M., and Velander, M. (2015). CFHTLenS: weak lensing calibrated scaling relations for low-mass clusters of galaxies. *MNRAS*, 451(2):1460–1481.

Kim, D.-W., Anderson, C., Burke, D., D'Abrusco, R., Fabbiano, G., Fruscione, A., Lauer, J., McCollough, M., Morgan, D., Mossman, A., O'Sullivan, E., Paggi, A., Vrtilek, S., and Trinchieri, G. (2019). Chandra Early-type Galaxy Atlas. *ApJ*, 241(2):36.

Kirkpatrick, C. C., Clerc, N., Finoguenov, A., Damsted, S., Ider Chitham, J., Kukkola, A. E., Gueguen, A., Furnell, K., Rykoff, E., Comparat, J., Saro, A., Capasso, R., Padilla, N., Erfanianfar, G., Mamon, G. A., Collins, C., Merloni, A., Brownstein, J. R., and Schneider, D. P. (2021). SPIDERS: an overview of the largest catalogue of spectroscopically confirmed x-ray galaxy clusters. *MNRAS*, 503(4):5763–5777.

Klein, M., Grandis, S., Mohr, J. J., Paulus, M., Abbott, T. M. C., Annis, J., Avila, S., Bertin, E., Brooks, D., Buckley-Geer, E., Rosell, A. C., Kind, M. C., Carretero, J., Castander, F. J., Cunha, C. E., D'Andrea, C. B., da Costa, L. N., De Vicente, J., Desai, S., Diehl, H. T., Dietrich, J. P., Doel, P., Evrard, A. E., Flaugher, B., Fosalba, P., Frieman, J., García-Bellido, J., Gaztanaga, E., Giles, P. A., Gruen, D., Gruendl, R. A., Gschwend, J., Gutierrez, G., Hartley, W. G., Hollowood, D. L., Honscheid, K., Hoyle, B., James, D. J., Jeltema, T., Kuehn, K., Kuropatkin, N., Lima, M., Maia, M. A. G., March, M., Marshall, J. L., Menanteau, F., Miquel, R., Ogando, R. L. C., Plazas, A. A., Romer, A. K., Roodman, A., Sanchez, E., Scarpine, V., Schindler, R., Serrano, S., Sevilla-Noarbe, I., Smith, M., Smith, R. C., Soares-Santos, M., Sobreira, F., Suchyta, E., Swanson, M. E. C., Tarle, G., Thomas, D., Vikram, V., and DES Collaboration (2019). A new RASS galaxy cluster catalogue with low contamination extending to z $\sim$ 1 in the DES overlap region. *MNRAS*, 488(1):739–769.

Klein, M., Mohr, J. J., Desai, S., Israel, H., Allam, S., Benoit-Lévy, A., Brooks, D., Buckley-Geer, E., Carnero Rosell, A., Carrasco Kind, M., Cunha, C. E., da Costa, L. N., Dietrich, J. P., Eifler, T. F., Evrard, A. E., Frieman, J., Gruen, D., Gruendl, R. A., Gutierrez, G., Honscheid, K., James, D. J., Kuehn, K., Lima, M., Maia, M. A. G., March, M., Melchior, P., Menanteau, F., Miquel, R., Plazas, A. A., Reil, K., Romer, A. K., Sanchez, E., Santiago, B., Scarpine, V., Schubnell, M., Sevilla-Noarbe, I., Smith, M., Soares-Santos, M., Sobreira, F., Suchyta, E., Swanson, M. E. C., Tarle, G., and DES Collaboration (2018). A multicomponent matched filter cluster confirmation tool for eROSITA: initial application to the RASS and DES-SV data sets. *MNRAS*, 474(3):3324–3343.

Klein, M., Oguri, M., Mohr, J. J., Grandis, S., Ghirardini, V., Liu, T., Liu, A., and Bulbul, E. (2021). The eROSITA Final Equatorial-Depth Survey (eFEDS): Optical confirmation, redshifts, and properties of the cluster and group catalog. *A&A*, page (accepted).

Klein, U. and Fletcher, A. (2015). *Galactic and Intergalactic Magnetic Fields*.

Koens, L. A., Maughan, B. J., Jones, L. R., Ebeling, H., Horner, D. J., Perlman, E. S., Phillipps, S., and Scharf, C. A. (2013). The WARPS Survey - VIII. Evolution of the galaxy cluster X-ray Luminosity Function. *MNRAS*, 435(4):3231–3242.

Kolokythas, K., O'Sullivan, E., Intema, H., Raychaudhury, S., Babul, A., Giacintucci, S., and Gitti, M. (2019). The complete local volume groups sample - III. Characteristics of group central radio galaxies in the Local Universe. *MNRAS*, 489(2):2488–2504.

Kolokythas, K., O'Sullivan, E., Raychaudhury, S., Giacintucci, S., Gitti, M., and Babul, A. (2018). The Complete Local-volume Groups Sample - II. A study of the central radio galaxies in the high-richness sub-sample. *MNRAS*, 481(2):1550–1577.

Laigle, C., Davidzon, I., Ilbert, O., Devriendt, J., Kashino, D., Pichon, C., Capak, P., Arnouts, S., de la Torre, S., Dubois, Y., Gozaliasl, G., Le Borgne, D., Lilly, S., McCracken, H. J., Salvato, M., and Slyz, A. (2019). Horizon-AGN virtual observatory - 1. SED-fitting performance and forecasts for future imaging surveys. *MNRAS*, 486(4):5104–5123.

Laine, S., van der Marel, R. P., Lauer, T. R., Postman, M., O'Dea, C. P., and Owen, F. N. (2003). Hubble Space Telescope Imaging of Brightest Cluster Galaxies. *AJ*, 125(2):478–505.

Lakhchaura, K., Werner, N., Sun, M., Canning, R. E. A., Gaspari, M., Allen, S. W., Connor, T., Donahue, M., and Sarazin, C. (2018). Thermodynamic properties, multiphase gas, and AGN feedback in a large sample of giant ellipticals. *MNRAS*, 481(4):4472–4504.

Large, M. I., Mathewson, D. S., and Haslam, C. G. T. (1959). A High-Resolution Survey of the Coma Cluster of Galaxies at 408 Mc./s. *Nature*, 183(4676):1663–1664.

LaRoque, S. J., Bonamente, M., Carlstrom, J. E., Joy, M. K., Nagai, D., Reese, E. D., and Dawson, K. S. (2006). X-Ray and Sunyaev-Zel'dovich Effect Measurements of the Gas Mass Fraction in Galaxy Clusters. *ApJ*, 652:917–936.

Lauer, T. R., Postman, M., Strauss, M. A., Graves, G. J., and Chisari, N. E. (2014). Brightest Cluster Galaxies at the Present Epoch. *ApJ*, 797(2):82.

Leauthaud, A., Finoguenov, A., Kneib, J.-P., Taylor, J. E., Massey, R., Rhodes, J., Ilbert, O., Bundy, K., Tinker, J., George, M. R., Capak, P., Koekemoer, A. M., Johnston, D. E., Zhang, Y.-Y., Cappelluti, N., Ellis, R. S., Elvis, M., Giodini, S., Heymans, C., Le Fèvre, O., Lilly, S., McCracken, H. J., Mellier, Y., Réfrégier, A., Salvato, M., Scoville, N., Smoot, G., Tanaka, M., Van Waerbeke, L., and Wolk, M. (2010). A Weak Lensing Study of X-ray Groups in the Cosmos Survey: Form and Evolution of the Mass-Luminosity Relation. *ApJ*, 709(1):97–114.

Ledlow, M. J., Owen, F. N., and Eilek, J. A. (2002). Rich-cluster and non-cluster radio galaxies and the /(P, D) diagram for a large number of FR I and FR II sources. *New A Rev.*, 46(2-7):343–347.

Li, Y., Bryan, G. L., and Quataert, E. (2019). The Fate of Asymptotic Giant Branch Winds in Massive Galaxies and the Intracluster Medium. *ApJ*, 887(1):41.

Li, Y., Ruszkowski, M., and Tremblay, G. (2018). The Effects of Ram Pressure on the Cold Clouds in the Centers of Galaxy Clusters. 854(2):91.

Lilly, S. and Zcosmos Team (2005). The zCOSMOS Redshift Survey. *The Messenger*, 121:42–45.

Lilly, S. J., Le Fèvre, O., Renzini, A., Zamorani, G., Scodeggio, M., Contini, T., Carollo, C. M., Hasinger, G., Kneib, J. P., Iovino, A., Le Brun, V., Maier, C., Mainieri, V., Mignoli, M., Silverman, J., Tasca, L. A. M., Bolzonella, M., Bongiorno, A., Bottini, D., Capak, P., Caputi, K., Cimatti, A., Cucciati, O., Daddi, E., Feldmann, R., Franzetti, P., Garilli, B., Guzzo, L., Ilbert, O., Kampczyk, P., Kovac, K., Lamareille, F., Leauthaud, A., Le Borgne, J. F., McCracken, H. J., Marinoni, C., Pello, R., Ricciardelli, E., Scarlata, C., Vergani, D., Sanders, D. B., Schinnerer, E., Scoville, N., Taniguchi, Y., Arnouts, S., Aussel, H., Bardelli, S., Brusa, M., Cappi, A., Ciliegi, P., Finoguenov, A., Foucaud, S., Franceschini, A., Halliday, C., Impey, C., Knobel, C., Koekemoer, A., Kurk, J., Maccagni, D., Maddox, S., Marano, B., Marconi, G., Meneux, B., Mobasher, B., Moreau, C., Peacock, J. A., Porciani, C., Pozzetti, L., Scaramella, R., Schiminovich, D., Shopbell, P., Smail, I., Thompson, D., Tresse, L., Vettolani, G., Zanichelli, A., and Zucca, E. (2007). zCOSMOS: A Large VLT/VIMOS Redshift Survey Covering $0 < z < 3$ in the COSMOS Field. *ApJS*, 172(1):70–85.

Lin, Y.-T. and Mohr, J. J. (2007). Radio Sources in Galaxy Clusters: Radial Distribution, and 1.4 GHz and K-band Bivariate Luminosity Function. *ApJS*, 170(1):71–94.

Lin, Y.-T., Mohr, J. J., and Stanford, S. A. (2003). Near-Infrared Properties of Galaxy Clusters: Luminosity as a Binding Mass Predictor and the State of Cluster Baryons. *ApJ*, 591(2):749–763.

Liu, A., Bulbul, E., Ghirardini, V., Liu, T., Klein, M., Clerc, N., Özsoy, Y., and Ramos-Ceja, M. E. (2021). The eROSITA Final Equatorial-Depth Survey (eFEDS): The Catalogof Galaxy Clusters and Groups. *A&A*, page (submitted).

Liu, A., Zhai, M., and Tozzi, P. (2019a). On the origin of central abundance drops in the intracluster medium of galaxy groups and clusters. *MNRAS*, 485(2):1651–1664.

Liu, F. S., Mao, S., Deng, Z. G., Xia, X. Y., and Wen, Z. L. (2009). Major dry mergers in early-type brightest cluster galaxies. *MNRAS*, 396(4):2003–2010.

Liu, F. S., Xia, X. Y., Mao, S., Wu, H., and Deng, Z. G. (2008). Photometric properties and scaling relations of early-type Brightest Cluster Galaxies. *MNRAS*, 385(1):23–39.

Liu, W., Sun, M., Nulsen, P., Clarke, T., Sarazin, C., Forman, W., Gaspari, M., Giacintucci, S., Lal, D. V., and Edge, T. (2019b). AGN feedback in galaxy group 3C 88: cavities, shock, and jet reorientation. *MNRAS*, 484(3):3376–3392.

Loi, F., Murgia, M., Govoni, F., Vacca, V., Bonafede, A., Ferrari, C., Prandoni, I., Feretti, L., Giovannini, G., and Li, H. (2019). Rotation measure synthesis applied to synthetic SKA images of galaxy clusters. *MNRAS*, 490(4):4841–4857.

Lovisari, L., Forman, W. R., Jones, C., Ettori, S., Andrade-Santos, F., Arnaud, M., Démoclès, J., Pratt, G. W., Randall, S., and Kraft, R. (2017). X-Ray Morphological Analysis of the Planck ESZ Clusters. *ApJ*, 846(1):51.

Lovisari, L., Reiprich, T. H., and Schellenberger, G. (2015). Scaling properties of a complete X-ray selected galaxy group sample. *A&A*, 573:A118.

Lovisari, L., Schellenberger, G., Sereno, M., Ettori, S., Pratt, G. W., Forman, W. R., Jones, C., Andrade-Santos, F., Randall, S., and Kraft, R. (2020). X-Ray Scaling Relations for a Representative Sample of Planck-selected Clusters Observed with XMM-Newton. *ApJ*, 892(2):102.

Macario, G., Venturi, T., Brunetti, G., Dallacasa, D., Giacintucci, S., Cassano, R., Bardelli, S., and Athreya, R. (2010). The very steep spectrum radio halo in Abell 697. *A&A*, 517:A43.

Machalski, J., Chyzy, K. T., and Jamrozy, M. (2004). Giant Radio Sources in View of the Dynamical Evolution of FRII-type Population. I. The Observational Data and Basic Physical Parameters of Sources Derived from the Analytical Model. *Acta Astron.*, 54:249–279.

Mack, K. H., Klein, U., O'Dea, C. P., Willis, A. G., and Saripalli, L. (1998). Spectral indices, particle ages, and the ambient medium of giant radio galaxies. *A&A*, 329:431–442.

Mahajan, S., Mamon, G. A., and Raychaudhury, S. (2011). The velocity modulation of galaxy properties in and near clusters: quantifying the decrease in star formation in backsplash galaxies. *MNRAS*, 416(4):2882–2902.

Mahdavi, A. and Geller, M. J. (2001). The L_X-σ Relation for Galaxies and Clusters of Galaxies. *ApJ*, 554(2):L129–L132.

Main, R. A., McNamara, B. R., Nulsen, P. E. J., Russell, H. R., and Vantyghem, A. N. (2017). A relationship between halo mass, cooling, active galactic nuclei heating and the co-evolution of massive black holes. *MNRAS*, 464(4):4360–4382.

Makarov, D., Prugniel, P., Terekhova, N., Courtois, H., and Vauglin, I. (2014). HyperLEDA. III. The catalogue of extragalactic distances. *A&A*, 570:A13.

Malarecki, J. M., Jones, D. H., Saripalli, L., Staveley-Smith, L., and Subrahmanyan, R. (2015). Giant radio galaxies - II. Tracers of large-scale structure. *MNRAS*, 449(1):955–986.

Mamon, G. A. (1992). Are Cluster Ellipticals the Products of Mergers? *ApJ*, 401:L3.

Mamon, G. A., Biviano, A., and Boué, G. (2013). MAMPOSSt: Modelling Anisotropy and Mass Profiles of Observed Spherical Systems - I. Gaussian 3D velocities. *MNRAS*, 429(4):3079–3098.

Mandal, S., Intema, H. T., Shimwell, T. W., van Weeren, R. J., Botteon, A., Röttgering, H. J. A., Hoang, D. N., Brunetti, G., de Gasperin, F., Giacintucci, S., Hoekstra, H., Stroe, A., Brüggen, M., Cassano, R., Shulevski, A., Drabent, A., and Rafferty, D. (2019). Ultra-steep spectrum emission in the merging galaxy cluster Abell 1914. *A&A*, 622:A22.

Maraston, C. (2005). Evolutionary population synthesis: models, analysis of the ingredients and application to high-z galaxies. *MNRAS*, 362:799–825.

Markevitch, M. (2010). Intergalactic shock fronts. *arXiv e-prints*, page arXiv:1010.3660.

Markevitch, M., Govoni, F., Brunetti, G., and Jerius, D. (2005). Bow Shock and Radio Halo in the Merging Cluster A520. *ApJ*, 627(2):733–738.

Markevitch, M. and Vikhlinin, A. (2007). Shocks and cold fronts in galaxy clusters. *Physics Reports*, 443(1):1–53.

Markevitch, M., Vikhlinin, A., Forman, W. R., and Sarazin, C. L. (1999). Mass Profiles of the Typical Relaxed Galaxy Clusters A2199 and A496. *ApJ*, 527(2):545–553.

Mathews, W. G. (1989). On the Global Ecology of Elliptical Galaxies. *AJ*, 97:42.

Mathews, W. G. (1990). *The Ins and Outs of Gas Flows in Elliptical Galaxies*, volume 160, page 265.

McCarthy, I. G., Schaye, J., Ponman, T. J., Bower, R. G., Booth, C. M., Dalla Vecchia, C., Crain, R. A., Springel, V., Theuns, T., and Wiersma, R. P. C. (2010). The case for AGN feedback in galaxy groups. *MNRAS*, 406(2):822–839.

McCourt, M., O'Leary, R. M., Madigan, A.-M., and Quataert, E. (2015). Magnetized gas clouds can survive acceleration by a hot wind. 449(1):2.

McDonald, M., Gaspari, M., McNamara, B. R., and Tremblay, G. R. (2018). Revisiting the Cooling Flow Problem in Galaxies, Groups, and Clusters of Galaxies. *ApJ*, 858:45.

McDonald, M., McNamara, B. R., Voit, G. M., Bayliss, M., Benson, B. A., Brodwin, M., Canning, R. E. A., Florian, M. K., Garmire, G. P., Gaspari, M., Gladders, M. D., Hlavacek-Larrondo, J., Kara, E., Reichardt, C. L., Russell, H. R., Saro, A., Sharon, K., Somboonpanyakul, T., Tremblay, G. R., and van Weeren, R. J. (2019). Anatomy of a Cooling Flow: The Feedback Response to Pure Cooling in the Core of the Phoenix Cluster. *ApJ*, 885(1):63.

McDonald, M., Swinbank, M., Edge, A. C., Wilner, D. J., Veilleux, S., Benson, B. A., Hogan, M. T., Marrone, D. P., McNamara, B. R., Wei, L. H., Bayliss, M. B., and Bautz, M. W. (2014). The State of the Warm and Cold Gas in the Extreme Starburst at the Core of the Phoenix Galaxy Cluster (SPT-CLJ2344-4243). *ApJ*, 784:18.

McDonald, M., Veilleux, S., Rupke, D. S. N., and Mushotzky, R. (2010). On the Origin of the Extended Hα Filaments in Cooling Flow Clusters. *ApJ*, 721:1262–1283.

McNamara, B. R. and Nulsen, P. E. (2012). Mechanical feedback from active galactic nuclei in galaxies, groups and clusters. *New Journal of Physics*, 14(5):55023.

McNamara, B. R. and Nulsen, P. E. J. (2007). Heating Hot Atmospheres with Active Galactic Nuclei. *ARA&A*, 45:117–175.

McNamara, B. R. and Nulsen, P. E. J. (2012). Mechanical feedback from active galactic nuclei in galaxies, groups and clusters. *New Journal of Physics*, 14(5):055023.

McNamara, B. R., Nulsen, P. E. J., Wise, M. W., Rafferty, D. A., Carilli, C., Sarazin, C. L., and Blanton, E. L. (2005). The heating of gas in a galaxy cluster by X-ray cavities and large-scale shock fronts. *Nature*, 433(7021):45–47.

McNamara, B. R., Russell, H. R., Nulsen, P. E. J., Hogan, M. T., Fabian, A. C., Pulido, F., and Edge, A. C. (2016). A Mechanism for Stimulating AGN Feedback by Lifting Gas in Massive Galaxies. *ApJ*, 830:79.

McNamara, B. R., Wise, M., Nulsen, P. E. J., David, L. P., Sarazin, C. L., Bautz, M., Markevitch, M., Vikhlinin, A., Forman, W. R., Jones, C., and Harris, D. E. (2000). [ITAL]Chandra[/ITAL] X-Ray Observations of the Hydra A Cluster: An Interaction between the Radio Source and the X-Ray–emitting Gas. *ApJ*, 534(2):L135–L138.

Merloni, A. and Heinz, S. (2007). Measuring the kinetic power of active galactic nuclei in the radio mode. *MNRAS*, 381(2):589–601.

Merloni, A., Körding, E., Heinz, S., Markoff, S., Di Matteo, T., and Falcke, H. (2006). Why the fundamental plane of black hole activity is not simply a distance driven artifact. *New A*, 11(8):567–576.

Merloni, A., Predehl, P., Becker, W., Böhringer, H., Boller, T., Brunner, H., Brusa, M., Dennerl, K., German eROSITA Consortium, t., and et al. (2012). eROSITA Science Book: Mapping the Structure of the Energetic Universe. *ArXiv e-prints*.

Mittal, R., Hudson, D. S., Reiprich, T. H., and Clarke, T. (2009). AGN heating and ICM cooling in the HIFLUGCS sample of galaxy clusters. *A&A*, 501(3):835–850.

Mittal, R., Hudson, D. S., Reiprich, T. H., and Clarke, T. (2009). AGN heating and ICM cooling in the HIFLUGCS sample of galaxy clusters. *A&A*, 501:835–850.

Mohan, N. and Rafferty, D. (2015a). PyBDSF: Python Blob Detection and Source Finder.

Mohan, N. and Rafferty, D. (2015b). PyBDSF: Python Blob Detection and Source Finder.

Mohr, J. J., Mathiesen, B., and Evrard, A. E. (1999). Properties of the Intracluster Medium in an Ensemble of Nearby Galaxy Clusters. *ApJ*, 517:627–649.

Molendi, S. and Pizzolato, F. (2001). Is the Gas in Cooling Flows Multiphase? *ApJ*, 560(1):194–200.

Moravec, E., Gonzalez, A. H., Stern, D., Clarke, T., Brodwin, M., Decker, B., Eisenhardt, P. R. M., Mo, W., Pope, A., Stanford, S. A., and Wylezalek, D. (2020). The Massive and Distant Clusters of WISE Survey. VII. The Environments and Properties of Radio Galaxies in Clusters at z $\sim$ 1. *ApJ*, 888(2):74.

Moretti, A., Guzzo, L., Campana, S., Lazzati, D., Panzera, M. R., Tagliaferri, G., Arena, S., Braglia, F., Dell'Antonio, I., and Longhetti, M. (2004). The Brera Multi-scale Wavelet HRI Cluster Survey. I. Selection of the sample and number counts. *A&A*, 428:21–37.

Morganti, R., Fogasy, J., Paragi, Z., Oosterloo, T., and Orienti, M. (2013). Radio Jets Clearing the Way Through a Galaxy: Watching Feedback in Action. *Science*, 341(6150):1082–1085.

Narayan, R. and Medvedev, M. V. (2001). Thermal Conduction in Clusters of Galaxies. *ApJL*, 562(2):L129–L132.

Narayan, R. and Yi, I. (1995). Advection-dominated Accretion: Underfed Black Holes and Neutron Stars. *ApJ*, 452:710.

Nipoti, C. and Binney, J. (2005). Time variability of active galactic nuclei and heating of cooling flows. *MNRAS*, 361:428–436.

Noble, A. G., Webb, T. M. A., Yee, H. K. C., Muzzin, A., Wilson, G., van der Burg, R. F. J., Balogh, M. L., and Shupe, D. L. (2016). The Phase Space of z$\sim$1.2 SpARCS Clusters: Using Herschel to Probe Dust Temperature as a Function of Environment and Accretion History. *ApJ*, 816(2):48.

Nolting, C., Jones, T. W., O'Neill, B. J., and Mendygral, P. J. (2019). Interactions between Radio Galaxies and Cluster Shocks. I. Jet Axes Aligned with Shock Normals. *ApJ*, 876(2):154.

Nulsen, P. E. J., Jones, C., Forman, W. R., David, L. P., McNamara, B. R., Rafferty, D. A., Bîrzan, L., and Wise, M. W. (2007). AGN Heating Through Cavities and Shocks. In Böhringer, H., Pratt, G. W., Finoguenov, A., and Schuecker, P., editors, *Heating versus Cooling in Galaxies and Clusters of Galaxies*, page 210.

Nulsen, P. E. J., McNamara, B. R., David, L. P., and Wise, M. W. (2005). X-Ray Cavities and Cooling Flows. *Highlights of Astronomy*, 13:307.

Nulsen, P. E. J., McNamara, B. R., Wise, M. W., and David, L. P. (2005). The Cluster-Scale AGN Outburst in Hydra A. *ApJ*, 628(2):629–636.

O'Dea, C. P. and Owen, F. N. (1985). The global properties of a representative sample of 51 narrow-angle-tail radio sources in the directions of Abell clusters. *AJ*, 90:954–972.

Offringa, A., McKinley, B., Hurley-Walker, N., Briggs, F., Wayth, R., Kaplan, D., Bell, M., Feng, L., Neben, A., Hughes, J., Rhee, J., Murphy, T., Bhat, N., Bernardi, G., Bowman, J., Cappallo, R., Corey, B., Deshpande, A., Emrich, D., Ewall-Wice, A., Gaensler, B., Goeke, R., Greenhill, L., Hazelton, B., Hindson, L., Johnston-Hollitt, M., Jacobs, D., Kasper, J., Kratzenberg, E., Lenc, E., Lonsdale, C., Lynch, M., McWhirter, S., Mitchell, D., Morales, M., Morgan, E., Kudryavtseva, N., Oberoi, D., Ord, S., Pindor, B., Procopio, P., Prabu, T., Riding, J., Roshi, D., Shankar, N. U., Srivani, K., Subrahmanyan, R., Tingay, S., Waterson, M., Webster, R., Whitney, A., Williams, A., and Williams, C. (2014). WSCLEAN: an implementation of a fast, generic wide-field imager for radio astronomy. *MNRAS*, 444(1):606–619.

Offringa, A. R. (2016). Compression of interferometric radio-astronomical data. *A&A*, 595:A99.

Olivares, V., Salomé, P., Combes, F., Hamer, S., Guillard, P., Lehnert, M. D., Polles, F., Beckmann, R. S., Dubois, Y., Donahue, M., Edge, A., Fabian, A. C., McNamara, B., Rose, T., Russell, H., Tremblay, G., Vantyghem, A., Canning, R. E. A., Ferland, G., Godard, B., Hogan, M., Peirani, S., and Pineau des Forets, G. (2019). Ubiquitous cold and massive filaments in cool core clusters. 631:A22.

O'Neill, B. J., Jones, T. W., Nolting, C., and Mendygral, P. J. (2019). Shocked Narrow-angle Tail Radio Galaxies: Simulations and Emissions. *ApJ*, 887(1):26.

O'Sullivan, E., Giacintucci, S., David, L. P., Gitti, M., Vrtilek, J. M., Raychaudhury, S., and Ponman, T. J. (2011a). Heating the Hot Atmospheres of Galaxy Groups and Clusters with Cavities: The Relationship between Jet Power and Low-frequency Radio Emission. *ApJ*, 735(1):11.

O'Sullivan, E., Giacintucci, S., David, L. P., Gitti, M., Vrtilek, J. M., Raychaudhury, S., and Ponman, T. J. (2011b). Heating the Hot Atmospheres of Galaxy Groups and Clusters with Cavities: The Relationship between Jet Power and Low-frequency Radio Emission. *ApJ*, 735:11–+.

O'Sullivan, E., Giacintucci, S., David, L. P., Vrtilek, J. M., and Raychaudhury, S. (2011c). A deep Chandra observation of the poor cluster AWM 4 - II. The role of the radio jets in enriching the intracluster medium. *MNRAS*, 411:1833–1842.

O'Sullivan, E., Ponman, T. J., Kolokythas, K., Raychaudhury, S., Babul, A., Vrtilek, J. M., David, L. P., Giacintucci, S., Gitti, M., and Haines, C. P. (2017). The Complete Local Volume Groups Sample - I. Sample selection and X-ray properties of the high-richness subsample. *MNRAS*, 472(2):1482–1505.

O'Sullivan, E., Worrall, D. M., Birkinshaw, M., Trinchieri, G., Wolter, A., Zezas, A., and Giacintucci, S. (2011d). Interaction between the intergalactic medium and central radio source in the NGC 4261 group of galaxies. *MNRAS*, 416(4):2916–2931.

Owen, F. N., Eilek, J. A., and Kassim, N. E. (2000). M87 at 90 Centimeters: A Different Picture. *ApJ*, 543(2):611–619.

Owen, F. N., O'Dea, C. P., Inoue, M., and Eilek, J. A. (1985). VLA observations of the multiple jet galaxy 3C 75. *ApJ*, 294:L85–L88.

Owen, F. N. and Rudnick, L. (1976). Radio sources with wide-angle tails in Abell clusters of galaxies. *ApJ*, 205:L1–L4.

Padovani, P., Alexander, D. M., Assef, R. J., De Marco, B., Giommi, P., Hickox, R. C., Richards, G. T., Smolčić, V., Hatziminaoglou, E., Mainieri, V., and Salvato, M. (2017). Active galactic nuclei: what's in a name? *A&A Rev.*, 25(1):2.

Panagoulia, E. K., Fabian, A. C., and Sanders, J. S. (2014). A volume-limited sample of X-ray galaxy groups and clusters - I. Radial entropy and cooling time profiles. *MNRAS*, 438:2341–2354.

Pandge, M. B., Kale, R., Dabhade, P., Mahato, M., and Raychaudhury, S. (2022). Giant Metrewave Radio Telescope unveils steep-spectrum antique filaments in the galaxy cluster Abell 725. *MNRAS*, 509(2):1837–1847.

Pasini, T., Brüggen, M., de Gasperin, F., Bîrzan, L., O'Sullivan, E., Finoguenov, A., Jarvis, M., Gitti, M., Brighenti, F., Whittam, I. H., Collier, J. D., Heywood, I., and Gozaliasl, G. (2020). The relation between the diffuse X-ray luminosity and the radio power of the central AGN in galaxy groups. *MNRAS*, 497(2):2163–2174.

Pasini, T., Brüggen, M., Hoang, D. N., Ghirardini, V., Bulbul, E., Klein, M., Liu, A., Shimwell, T. W., Hardcastle, M. J., Williams, W. L., Botteon, A., Gastaldello, F., van Weeren, R. J., Merloni, A., de Gasperin, F., Bahar, Y. E., Pacaud, F., and Ramos-Ceja, M. (2022a). The eROSITA Final Equatorial-Depth Survey (eFEDS). LOFAR view of brightest cluster galaxies and AGN feedback. *A&A*, 661:A13.

Pasini, T., Edler, H. W., Brüggen, M., de Gasperin, F., Botteon, A., Rajpurohit, K., van Weeren, R. J., Gastaldello, F., Gaspari, M., Brunetti, G., Cuciti, V., Nanci, C., di Gennaro, G., Rossetti, M., Hoang, D. D. D. N., and Riseley, C. J. (2022b). Particle re-acceleration and diffuse radio sources in the galaxy cluster Abell 1550. *arXiv e-prints*, page arXiv:2205.12281.

Pasini, T., Finoguenov, A., Brüggen, M., Gaspari, M., de Gasperin, F., and Gozaliasl, G. (2021a). Radio galaxies in galaxy groups: kinematics, scaling relations, and AGN feedback. *MNRAS*, 505(2):2628–2637.

Pasini, T., Gitti, M., Brighenti, F., O'Sullivan, E., Gastaldello, F., Temi, P., and Hamer, S. L. (2021b). A First Chandra View of the Cool Core Cluster A1668: Offset Cooling and AGN Feedback Cycle. *ApJ*, 911(1):66.

Pasini, T., Gitti, M., Brighenti, F., Temi, P., Amblard, A., Hamer, S. L., Ettori, S., O'Sullivan, E., and Gastaldello, F. (2019). A BCG with Offset Cooling: Is the AGN Feedback Cycle Broken in A2495? *ApJ*, 885(2):111.

Peterson, J. R. and Fabian, A. C. (2006). X-ray spectroscopy of cooling clusters. *Physics Reports*, 427(1):1–39.

Peterson, J. R., Paerels, F. B. S., Kaastra, J. S., Arnaud, M., Reiprich, T. H., Fabian, A. C., Mushotzky, R. F., Jernigan, J. G., and Sakelliou, I. (2001). X-ray imaging-spectroscopy of Abell 1835. *A&A*, 365:L104–L109.

Petrosian, V. (2001). On the Nonthermal Emission and Acceleration of Electrons in Coma and Other Clusters of Galaxies. *ApJ*, 557:560–572.

Pfrommer, C., Enßlin, T. A., and Springel, V. (2008). Simulating cosmic rays in clusters of galaxies - II. A unified scheme for radio haloes and relics with predictions of the γ-ray emission. *MNRAS*, 385(3):1211–1241.

Planck Collaboration, Ade, P. A. R., Aghanim, N., Arnaud, M., Ashdown, M., Aumont, J., Baccigalupi, C., Banday, A. J., Barreiro, R. B., Barrena, R., Bartlett, J. G., Bartolo, N., Battaner, E., Battye, R., Benabed, K., Benoît, A., Benoit-Lévy, A., Bernard, J. P., Bersanelli, M., Bielewicz, P., Bikmaev, I., Böhringer, H., Bonaldi, A., Bonavera, L., Bond, J. R., Borrill, J., Bouchet, F. R., Bucher, M., Burenin, R., Burigana, C., Butler, R. C., Calabrese, E., Cardoso, J. F., Carvalho, P., Catalano, A., Challinor, A., Chamballu, A., Chary, R. R., Chiang, H. C., Chon, G., Christensen, P. R., Clements, D. L., Colombi, S., Colombo, L. P. L., Combet, C., Comis, B., Couchot, F., Coulais, A., Crill, B. P., Curto, A., Cuttaia, F., Dahle, H., Danese, L., Davies, R. D., Davis, R. J., de Bernardis, P., de Rosa, A., de Zotti, G., Delabrouille, J., Désert, F. X., Dickinson, C., Diego, J. M., Dolag, K., Dole, H., Donzelli, S., Doré, O., Douspis, M., Ducout, A., Dupac, X., Efstathiou, G., Eisenhardt, P. R. M., Elsner, F., Enßlin, T. A., Eriksen, H. K., Falgarone, E., Fergusson, J., Feroz, F., Ferragamo, A., Finelli, F., Forni, O., Frailis, M., Fraisse, A. A., Franceschi, E., Frejsel, A., Galeotta, S., Galli, S., Ganga, K., Génova-Santos, R. T., Giard, M., Giraud-Héraud, Y., Gjerløw, E., González-Nuevo, J., Górski, K. M., Grainge, K. J. B., Gratton, S., Gregorio, A., Gruppuso, A., Gudmundsson, J. E., Hansen, F. K., Hanson, D., Harrison, D. L., Hempel, A., Henrot-Versillé, S., Hernández-Monteagudo, C., Herranz, D., Hildebrandt, S. R., Hivon, E., Hobson, M., Holmes, W. A., Hornstrup, A., Hovest, W., Huffenberger, K. M., Hurier, G., Jaffe, A. H., Jaffe, T. R., Jin, T., Jones, W. C., Juvela, M., Keihänen, E., Keskitalo, R., Khamitov, I., Kisner, T. S., Kneissl, R., Knoche, J., Kunz, M., Kurki-Suonio, H., Lagache, G., Lamarre, J. M., Lasenby, A., Lattanzi, M., Lawrence, C. R., Leonardi, R., Lesgourgues, J., Levrier, F., Liguori, M., Lilje, P. B., Linden-Vørnle, M., López-Caniego, M., Lubin, P. M., Macías-Pérez, J. F., Maggio, G., Maino, D., Mak, D. S. Y., Mandolesi, N., Mangilli, A., Martin, P. G., Martínez-González, E., Masi, S., Matarrese, S., Mazzotta, P., McGehee, P., Mei, S., Melchiorri, A., Melin, J. B., Mendes, L., Mennella, A., Migliaccio, M., Mitra, S., Miville-Deschênes, M. A., Moneti, A., Montier, L., Morgante, G., Mortlock, D., Moss, A., Munshi, D., Murphy, J. A., Naselsky, P., Nastasi, A., Nati, F., Natoli, P., Netterfield, C. B., Nørgaard-Nielsen, H. U., Noviello, F., Novikov, D., Novikov, I., Olamaie, M., Oxborrow, C. A., Paci, F., Pagano, L., Pajot, F., Paoletti, D., Pasian, F., Patanchon, G., Pearson, T. J., Perdereau, O., Perotto, L., Perrott, Y. C., Perrotta, F., Pettorino, V., Piacentini, F., Piat, M., Pierpaoli, E., Pietrobon, D., Plaszczynski, S., Pointecouteau, E., Polenta, G., Pratt, G. W., Prézeau, G., Prunet, S., Puget, J. L., Rachen, J. P., Reach, W. T., Rebolo, R., Reinecke, M., Remazeilles, M., Renault, C., Renzi, A., Ristorcelli, I., Rocha, G., Rosset, C., Rossetti, M., Roudier, G., Rozo, E., Rubiño-Martín, J. A., Rumsey, C., Rusholme, B., Rykoff, E. S., Sandri, M., Santos, D., Saunders, R. D. E., Savelainen, M., Savini, G., Schammel, M. P., Scott, D., Seiffert, M. D., Shellard, E. P. S., Shimwell, T. W., Spencer, L. D., Stanford, S. A., Stern, D., Stolyarov, V., Stompor, R., Streblyanska, A., Sudiwala, R., Sunyaev, R., Sutton, D., Suur-Uski, A. S., Sygnet, J. F., Tauber, J. A., Terenzi, L., Toffolatti, L., Tomasi, M., Tramonte, D., Tristram, M., Tucci, M., Tuovinen, J., Umana, G., Valenziano, L., Valiviita, J., Van Tent, B., Vielva, P., Villa, F., Wade, L. A., Wandelt, B. D., Wehus, I. K., White, S. D. M., Wright, E. L., Yvon, D., Zacchei, A., and Zonca, A. (2016). Planck 2015 results. XXVII. The second Planck catalogue of Sunyaev-Zeldovich sources. *A&A*, 594:A27.

Ponman, T. J., Allan, D. J., Jones, L. R., Merrifield, M., McHardy, I. M., Lehto, H. J., and Luppino, G. A. (1994). A possible fossil galaxy group. *Nature*, 369(6480):462–464.

Pope, E. C. D., Babul, A., Pavlovski, G., Bower, R. G., and Dotter, A. (2010). Mass transport by buoyant bubbles in galaxy clusters. *MNRAS*, 406:2023–2037.

Prasad, D., Sharma, P., and Babul, A. (2015). Cool Core Cycles: Cold Gas and AGN Jet Feedback in Cluster Cores. *ApJ*, 811(2):108.

Predehl, P., Andritschke, R., Arefiev, V., Babyshkin, V., Batanov, O., Becker, W., Böhringer, H., Bogomolov, A., Boller, T., Borm, K., Bornemann, W., Bräuninger, H., Brüggen, M., Brunner, H., Brusa, M., Bulbul, E., Buntov, M., Burwitz, V., Burkert, W., Clerc, N., Churazov, E., Coutinho, D., Dauser, T., Dennerl, K., Doroshenko, V., Eder, J., Emberger, V., Eraerds, T., Finoguenov, A., Freyberg, M., Friedrich, P., Friedrich, S., Fürmetz, M., Georgakakis, A., Gilfanov, M., Granato, S., Grossberger, C., Gueguen, A., Gureev, P., Haberl, F., Hälker, O., Hartner, G., Hasinger, G., Huber, H., Ji, L., Kienlin, A. v., Kink, W., Korotkov, F., Kreykenbohm, I., Lamer, G., Lomakin, I., Lapshov, I., Liu, T., Maitra, C., Meidinger, N., Menz, B., Merloni, A., Mernik, T., Mican, B., Mohr, J., Müller, S., Nandra, K., Nazarov, V., Pacaud, F., Pavlinsky, M., Perinati, E., Pfeffermann, E., Pietschner, D., Ramos-Ceja, M. E., Rau, A., Reiffers, J., Reiprich, T. H., Robrade, J., Salvato, M., Sanders, J., Santangelo, A., Sasaki, M., Scheuerle, H., Schmid, C., Schmitt, J., Schwope, A., Shirshakov, A., Steinmetz, M., Stewart, I., Strüder, L., Sunyaev, R., Tenzer, C., Tiedemann, L., Trümper, J., Voron, V., Weber, P., Wilms, J., and Yaroshenko, V. (2021). The eROSITA X-ray telescope on SRG. *A&A*, 647:A1.

Pulido, F. A., McNamara, B. R., Edge, A. C., Hogan, M. T., Vantyghem, A. N., Russell, H. R., Nulsen, P. E. J., Babyk, I., and Salomé, P. (2018). The Origin of Molecular Clouds in Central Galaxies. *ApJ*, 853(2):177.

Qiu, Y., Bogdanović, T., Li, Y., McDonald, M., and McNamara, B. R. (2020). The formation of dusty cold gas filaments from galaxy cluster simulations. *Nature Astronomy*, 4:900–906.

Rafferty, D. A., McNamara, B. R., Nulsen, P. E. J., and Wise, M. W. (2006). The Feedback-regulated Growth of Black Holes and Bulges through Gas Accretion and Starbursts in Cluster Central Dominant Galaxies. *ApJ*, 652(1):216–231.

Rajpurohit, K., Hoeft, M., van Weeren, R. J., Rudnick, L., Röttgering, H. J. A., Forman, W. R., Brüggen, M., Croston, J. H., Andrade-Santos, F., Dawson, W. A., Intema, H. T., Kraft, R. P., Jones, C., and Jee, M. J. (2018). Deep VLA Observations of the Cluster 1RXS J0603.3+4214 in the Frequency Range of 1-2 GHz. *ApJ*, 852(2):65.

Rajpurohit, K., Hoeft, M., Vazza, F., Rudnick, L., van Weeren, R. J., Wittor, D., Drabent, A., Brienza, M., Bonnassieux, E., Locatelli, N., Kale, R., and Dumba, C. (2020). New mysteries and challenges from the Toothbrush relic: wideband observations from 550 MHz to 8 GHz. *A&A*, 636:A30.

Rajpurohit, K., Hoeft, M., Wittor, D., van Weeren, R. J., Vazza, F., Rudnick, L., Rajpurohit, S., Forman, W. R., Riseley, C. J., Brienza, M., Bonafede, A., Rajpurohit, A. S., Domínguez-Fernández, P., Eilek, J., Bonnassieux, E., Brüggen, M., Loi, F., Röttgering, H. J. A., Drabent, A., Locatelli, N., Botteon, A., Brunetti, G., and Clarke, T. E. (2022a). Turbulent magnetic fields in the merging galaxy cluster MACS J0717.5+3745. *A&A*, 657:A2.

Rajpurohit, K., van Weeren, R. J., Hoeft, M., Vazza, F., Brienza, M., Forman, W., Wittor, D., Domínguez-Fernández, P., Rajpurohit, S., Riseley, C. J., Botteon, A., Osinga, E., Brunetti, G., Bonnassieux, E., Bonafede, A., Rajpurohit, A. S., Stuardi, C., Drabent, A., Brüggen, M., Dallacasa, D., Shimwell, T. W., Röttgering, H. J. A., Gasperin, F. d., Miley, G. K., and Rossetti, M. (2022b). Deep Low-frequency Radio Observations of A2256. I. The Filamentary Radio Relic. *ApJ*, 927(1):80.

Rajpurohit, K., Vazza, F., van Weeren, R. J., Hoeft, M., Brienza, M., Bonnassieux, E., Riseley, C. J., Brunetti, G., Bonafede, A., Brüggen, M., Formann, W. R., Rajpurohit, A. S., Röttgering, H. J. A., Drabent, A., Domínguez-Fernández, P., Wittor, D., and Andrade-Santos, F. (2021). Dissecting nonthermal emission in the complex multiple-merger galaxy cluster Abell 2744: Radio and X-ray analysis. *A&A*, 654:A41.

Randall, S. W., Nulsen, P. E. J., Jones, C., Forman, W. R., Bulbul, E., Clarke, T. E., Kraft, R., Blanton, E. L., David, L., Werner, N., Sun, M., Donahue, M., Giacintucci, S., and Simionescu, A. (2015). A Very Deep Chandra Observation of the Galaxy Group NGC 5813: AGN Shocks, Feedback, and Outburst History. *ApJ*, 805(2):112.

Rasia, E., Borgani, S., Murante, G., Planelles, S., Beck, A. M., Biffi, V., Ragone-Figueroa, C., Granato, G. L., Steinborn, L. K., and Dolag, K. (2015). Cool Core Clusters from Cosmological Simulations. *ApJ*, 813(1):L17.

Rau, U. and Cornwell, T. J. (2011). A multi-scale multi-frequency deconvolution algorithm for synthesis imaging in radio interferometry. *A&A*, 532:A71.

Revaz, Y., Combes, F., and Salomé, P. (2008). Formation of cold filaments in cooling flow clusters. *A&A*, 477(3):L33–L36.

Rhee, J., Smith, R., Choi, H., Yi, S. K., Jaffé, Y., Candlish, G., and Sánchez-Jánssen, R. (2017). Phase-space Analysis in the Group and Cluster Environment: Time Since Infall and Tidal Mass Loss. *ApJ*, 843(2):128.

Rodriguez-Gomez, V., Genel, S., Vogelsberger, M., Sijacki, D., Pillepich, A., Sales, L. V., Torrey, P., Snyder, G., Nelson, D., Springel, V., Ma, C.-P., and Hernquist, L. (2015). The merger rate of galaxies in the Illustris simulation: a comparison with observations and semi-empirical models. *MNRAS*, 449(1):49–64.

Roettiger, K., Burns, J. O., and Stone, J. M. (1999). A Cluster Merger and the Origin of the Extended Radio Emission in Abell 3667. *ApJ*, 518(2):603–612.

Roger, R. S., Costain, C. H., and Bridle, A. H. (1973). The low-frequency spectra of nonthermal radio sources. *AJ*, 78:1030.

Rose, T., Edge, A. C., Combes, F., Gaspari, M., Hamer, S., Nesvadba, N., Peck, A. B., Sarazin, C., Tremblay, G. R., Baum, S. A., Bremer, M. N., McNamara, B. R., O'Dea, C., Oonk, J. B. R., Russell, H., Salomé, P., Donahue, M., Fabian, A. C., Ferland, G., Mittal, R., and Vantyghem, A. (2019). Constraining cold accretion on to supermassive black holes: molecular gas in the cores of eight brightest cluster galaxies revealed by joint CO and CN absorption. *MNRAS*, 489(1):349–365.

Rossetti, M., Gastaldello, F., Ferioli, G., Bersanelli, M., De Grandi, S., Eckert, D., Ghizzardi, S., Maino, D., and Molendi, S. (2016). Measuring the dynamical state of Planck SZ-selected clusters: X-ray peak - BCG offset. *MNRAS*, 457(4):4515–4524.

Rossetti, M. and Molendi, S. (2010). Cool core remnants in galaxy clusters. *A&A*, 510:A83.

Rottgering, H., Wieringa, M., Hunstead, R., and Ekers, R. (1997). The extended radio emission in the luminous X-ray cluster A3667. *MNRAS*, 290(4):577–584.

Sabater, J., Best, P., Hardcastle, M., Shimwell, T., Tasse, C., Williams, W., Brüggen, M., Cochrane, R., Croston, J., de Gasperin, F., Duncan, K., Gürkan, G., Mechev, A., Morabito, L., Prandoni, I., Röttgering, H., Smith, D., Harwood, J., Mingo, B., Mooney, S., and Saxena, A. (2019). The LoTSS view of radio AGN in the local Universe. The most massive galaxies are always switched on. *A&A*, 622:A17.

Sabater, J., Best, P. N., and Argudo-Fernández, M. (2013). Effect of the interactions and environment on nuclear activity. *MNRAS*, 430(1):638–651.

Salomé, P. and Combes, F. (2003). Cold molecular gas in cooling flow clusters of galaxies. *A&A*, 412:657–667.

Sanders, J. S., Dennerl, K., Russell, H. R., Eckert, D., Pinto, C., Fabian, A. C., Walker, S. A., Tamura, T., ZuHone, J., and Hofmann, F. (2020). Measuring bulk flows of the intracluster medium in the Perseus and Coma galaxy clusters using XMM-Newton. *A&A*, 633:A42.

Sanderson, A. J. R., Edge, A. C., and Smith, G. P. (2009). LoCuSS: the connection between brightest cluster galaxy activity, gas cooling and dynamical disturbance of X-ray cluster cores. *MNRAS*, 398(4):1698–1705.

Saro, A., Mohr, J. J., Bazin, G., and Dolag, K. (2013). Toward Unbiased Galaxy Cluster Masses from Line-of-sight Velocity Dispersions. *ApJ*, 772(1):47.

Sądowski, A. and Gaspari, M. (2017). Kinetic and radiative power from optically thin accretion flows. *MNRAS*, 468:1398–1404.

Schellenberger, G., David, L. P., Vrtilek, J., O'Sullivan, E., Lim, J., Forman, W., Sun, M., Combes, F., Salome, P., Jones, C., Giacintucci, S., Edge, A., Gastaldello, F., Temi, P., Brighenti, F., and Bardelli, S. (2020). Atacama Compact Array Measurements of the Molecular Mass in the NGC 5044 Cooling-flow Group. *ApJ*, 894(1):72.

Schinnerer, E., Sargent, M. T., Bondi, M., Smolčić, V., Datta, A., Carilli, C. L., Bertoldi, F., Blain, A., Ciliegi, P., Koekemoer, A., and Scoville, N. Z. (2010). The VLA-COSMOS Survey. IV. Deep Data and Joint Catalog. *ApJS*, 188(2):384–404.

Schinnerer, E., Smolčić, V., Carilli, C. L., Bondi, M., Ciliegi, P., Jahnke, K., Scoville, N. Z., Aussel, H., Bertoldi, F., Blain, A. W., Impey, C. D., Koekemoer, A. M., Le Fevre, O., and Urry, C. M. (2007). The VLA-COSMOS Survey. II. Source Catalog of the Large Project. *ApJS*, 172(1):46–69.

Shakura, N. I. and Sunyaev, R. A. (1973). Reprint of 1973A&A....24..337S. Black holes in binary systems. Observational appearance. *A&A*, 500:33–51.

Sharma, R. S., Choi, E., Somerville, R. S., Snyder, G. F., Kocevski, D. D., Moster, B. P., Naab, T., Narayanan, D., Ostriker, J. P., and Rosario, D. J. (2021). The Connection between Mergers and AGN Activity in Simulated and Observed Massive Galaxies. *arXiv e-prints*, page arXiv:2101.01729.

Shen, L., Miller, N. A., Lemaux, B. C., Tomczak, A. R., Lubin, L. M., Rumbaugh, N., Fassnacht, C. D., Becker, R. H., Gal, R. R., Wu, P.-F., and Squires, G. (2017). The properties of radio galaxies and the effect of environment in large-scale structures at z $\sim$ 1. *MNRAS*, 472(1):998–1022.

Shen, S., Yang, X., Mo, H., van den Bosch, F., and More, S. (2014). The Statistical Nature of the Brightest Group Galaxies. *ApJ*, 782(1):23.

Shimwell, T. W., Brown, S., Feain, I. J., Feretti, L., Gaensler, B. M., and Lage, C. (2014). Deep radio observations of the radio halo of the bullet cluster 1E 0657-55.8. *MNRAS*, 440(4):2901–2915.

Shimwell, T. W., Hardcastle, M. J., Tasse, C., Best, P. N., Röttgering, H. J. A., Williams, W. L., Botteon, A., Drabent, A., Mechev, A., Shulevski, A., van Weeren, R. J., Bester, L., Brüggen, M., Brunetti, G., Callingham, J. R., Chyży, K. T., Conway, J. E., Dijkema, T. J., Duncan, K., de Gasperin, F., Hale, C. L., Haverkorn, M., Hugo, B., Jackson, N., Mevius, M., Miley, G. K., Morabito, L. K., Morganti, R., Offringa, A., Oonk, J. B. R., Rafferty, D., Sabater, J., Smith, D. J. B., Schwarz, D. J., Smirnov, O., O'Sullivan, S. P., Vedantham, H., White, G. J., Albert, J. G., Alegre, L., Asabere, B., Bacon, D. J., Bonafede, A., Bonnassieux, E., Brienza, M., Bilicki, M., Bonato, M., Calistro Rivera, G., Cassano, R., Cochrane, R., Croston, J. H., Cuciti, V., Dallacasa, D., Danezi, A., Dettmar, R. J., Di Gennaro, G., Edler, H. W., Enßlin, T. A., Emig, K. L., Franzen, T. M. O., García-Vergara, C., Grange, Y. G., Gürkan, G., Hajduk, M., Heald, G., Heesen, V., Hoang, D. N., Hoeft, M., Horellou, C., Iacobelli, M., Jamrozy, M., Jelić, V., Kondapally, R., Kukreti, P., Kunert-Bajraszewska, M., Magliocchetti, M., Mahatma, V., Małek, K., Mandal, S., Massaro, F., Meyer-Zhao, Z., Mingo, B., Mostert, R. I. J., Nair, D. G., Nakoneczny, S. J., Nikiel-Wroczyński, B., Orrú, E., Pajdosz-Śmierciak, U., Pasini, T., Prandoni, I., van Piggelen, H. E., Rajpurohit, K., Retana-Montenegro, E., Riseley, C. J., Rowlinson, A., Saxena, A., Schrijvers, C., Sweijen, F., Siewert, T. M., Timmerman, R., Vaccari, M., Vink, J., West, J. L., Wołowska, A., Zhang, X., and Zheng, J. (2022). The LOFAR Two-metre Sky Survey. V. Second data release. *A&A*, 659:A1.

Shimwell, T. W., Luckin, J., Brüggen, M., Brunetti, G., Intema, H. T., Owers, M. S., Röttgering, H. J. A., Stroe, A., van Weeren, R. J., Williams, W. L., Cassano, R., de Gasperin, F., Heald, G. H., Hoang, D. N., Hardcastle, M. J., Sridhar, S. S., Sabater, J., Best, P. N., Bonafede, A., Chyży, K. T., Enßlin, T. A., Ferrari, C., Haverkorn, M., Hoeft, M., Horellou, C., McKean, J. P., Morabito, L. K., Orrù, E., Pizzo, R., Retana-Montenegro, E., and White, G. J. (2016). A plethora of diffuse steep spectrum radio sources in Abell 2034 revealed by LOFAR. *MNRAS*, 459(1):277–290.

Shimwell, T. W., Markevitch, M., Brown, S., Feretti, L., Gaensler, B., Johnston-Hollitt, M., Lage, C., and Srinivasan, R. (2015). Another shock for the Bullet cluster, and the source of seed electrons for radio relics. *MNRAS*, 449(2):1486–1494.

Shimwell, T. W., Röttgering, H. J. A., Best, P. N., Williams, W. L., Dijkema, T. J., de Gasperin, F., Hardcastle, M. J., Heald, G. H., Hoang, D. N., Horneffer, A., Intema, H., Mahony, E. K., Mandal, S., Mechev, A. P., Morabito, L., Oonk, J. B. R., Rafferty, D., Retana-Montenegro, E., Sabater, J., Tasse, C., van Weeren, R. J., Brüggen, M., Brunetti, G., Chyży, K. T., Conway, J. E., Haverkorn, M., Jackson, N., Jarvis, M. J., McKean, J. P., Miley, G. K., Morganti, R., White, G. J., Wise, M. W., van Bemmel, I. M., Beck, R., Brienza, M., Bonafede, A., Calistro Rivera, G., Cassano, R., Clarke, A. O., Cseh, D., Deller, A., Drabent, A., van Driel, W., Engels, D., Falcke, H., Ferrari, C., Fröhlich, S., Garrett, M. A., Harwood, J. J., Heesen, V., Hoeft, M., Horellou, C., Israel, F. P., Kapińska, A. D., Kunert- Bajraszewska, M., McKay, D. J., Mohan, N. R., Orrú, E., Pizzo, R. F., Prandoni, I., Schwarz, D. J., Shulevski, A., Sipior, M., Smith, D. J. B., Sridhar, S. S., Steinmetz, M., Stroe, A., Varenius, E., van der Werf, P. P., Zensus, J. A., and Zwart, J. T. L. (2017). The LOFAR Two-metre Sky Survey. I. Survey description and preliminary data release. *A&A*, 598:A104.

Shimwell, T. W., Tasse, C., Hardcastle, M. J., Mechev, A. P., Williams, W. L., Best, P. N., Röttgering, H. J. A., Callingham, J. R., Dijkema, T. J., de Gasperin, F., Hoang, D. N., Hugo, B., Mirmont, M., Oonk, J. B. R., Prandoni, I., Rafferty, D., Sabater, J., Smirnov, O., van Weeren, R. J., White, G. J., Atemkeng, M., Bester, L., Bonnassieux, E., Brüggen, M., Brunetti, G., Chyży, K. T., Cochrane, R., Conway, J. E., Croston, J. H., Danezi, A., Duncan, K., Haverkorn, M., Heald, G. H., Iacobelli, M., Intema, H. T., Jackson, N., Jamrozy, M., Jarvis, M. J., Lakhoo, R., Mevius, M., Miley, G. K., Morabito, L., Morganti, R., Nisbet, D., Orrú, E., Perkins, S., Pizzo, R. F., Schrijvers, C., Smith, D. J. B., Vermeulen, R., Wise, M. W., Alegre, L., Bacon, D. J., van Bemmel, I. M., Beswick, R. J., Bonafede, A., Botteon, A., Bourke, S., Brienza, M., Calistro Rivera, G., Cassano, R., Clarke, A. O., Conselice, C. J., Dettmar, R. J., Drabent, A., Dumba, C., Emig, K. L., Enßlin, T. A., Ferrari, C., Garrett, M. A., Génova-Santos, R. T., Goyal, A., Gürkan, G., Hale, C., Harwood, J. J., Heesen, V., Hoeft, M., Horellou, C., Jackson, C., Kokotanekov, G., Kondapally, R., Kunert-Bajraszewska, M., Mahatma, V., Mahony, E. K., Mandal, S., McKean, J. P., Merloni, A., Mingo, B., Miskolczi, A., Mooney, S., Nikiel-Wroczyński, B., O'Sullivan, S. P., Quinn, J., Reich, W., Roskowiński, C., Rowlinson, A., Savini, F., Saxena, A., Schwarz, D. J., Shulevski, A., Sridhar, S. S., Stacey, H. R., Urquhart, S., van der Wiel, M. H. D., Varenius, E., Webster, B., and Wilber, A. (2019). The LOFAR Two-metre Sky Survey. II. First data release. *A&A*, 622:A1.

Sijacki, D., Vogelsberger, M., Genel, S., Springel, V., Torrey, P., Snyder, G. F., Nelson, D., and Hernquist, L. (2015). The Illustris simulation: the evolving population of black holes across cosmic time. *MNRAS*, 452(1):575–596.

Slee, O. B., Roy, A. L., Murgia, M., Andernach, H., and Ehle, M. (2001). Four Extreme Relic Radio Sources in Clusters of Galaxies. *AJ*, 122(3):1172–1193.

Smirnov, O. M. and Tasse, C. (2015). Radio interferometric gain calibration as a complex optimization problem. *MNRAS*, 449(3):2668–2684.

Smolčić, V., Finoguenov, A., Zamorani, G., Schinnerer, E., Tanaka, M., Giodini, S., and Scoville, N. (2011). On the occupation of X-ray-selected galaxy groups by radio active galactic nuclei since z = 1.3. *MNRAS*, 416(1):L31–L35.

Smolčić, V., Novak, M., Delvecchio, I., Ceraj, L., Bondi, M., Delhaize, J., Marchesi, S., Murphy, E., Schinnerer, E., Vardoulaki, E., and Zamorani, G. (2017). The VLA-COSMOS 3 GHz Large Project: Cosmic evolution of radio AGN and implications for radio-mode feedback since z 5. *A&A*, 602:A6.

Smolčić, V., Schinnerer, E., Finoguenov, A., Sakelliou, I., Carilli, C. L., Botzler, C. S., Brusa, M., Scoville, N., Ajiki, M., Capak, P., Guzzo, L., Hasinger, G., Impey, C., Jahnke, K., Kartaltepe, J. S., McCracken, H. J., Mobasher, B., Murayama, T., Sasaki, S. S., Shioya, Y., Taniguchi, Y., and Trump, J. R. (2007). A Wide-Angle Tail Radio Galaxy in the COSMOS Field: Evidence for Cluster Formation. *ApJS*, 172(1):295–313.

Soker, N. (2016). The jet feedback mechanism (JFM) in stars, galaxies and clusters. *New A Rev.*, 75:1–23.

Soker, N. and Pizzolato, F. (2005). Feedback Heating with Slow Jets in Cooling Flow Clusters. *ApJ*, 622:847–852.

Spergel, D. N., Bean, R., Doré, O., Nolta, M. R., Bennett, C. L., Dunkley, J., Hinshaw, G., Jarosik, N., Komatsu, E., Page, L., Peiris, H. V., Verde, L., Halpern, M., Hill, R. S., Kogut, A., Limon, M., Meyer, S. S., Odegard, N., Tucker, G. S., Weiland, J. L., Wollack, E., and Wright, E. L. (2007). Three-Year Wilkinson Microwave Anisotropy Probe (WMAP) Observations: Implications for Cosmology. *ApJ*, 170(2):377–408.

Springel, V., Frenk, C. S., and White, S. D. M. (2006). The large-scale structure of the Universe. *Nature*, 440(7088):1137–1144.

Stott, J. P., Collins, C. A., Sahlén, M., Hilton, M., Lloyd-Davies, E., Capozzi, D., Hosmer, M., Liddle, A. R., Mehrtens, N., Miller, C. J., Romer, A. K., Stanford, S. A., Viana, P. T. P., Davidson, M., Hoyle, B., Kay, S. T., and Nichol, R. C. (2010). The XMM Cluster Survey: The Build-up of Stellar Mass in Brightest Cluster Galaxies at High Redshift. *ApJ*, 718(1):23–30.

Stott, J. P., Edge, A. C., Smith, G. P., Swinbank, A. M., and Ebeling, H. (2008). Near-infrared evolution of brightest cluster galaxies in the most X-ray luminous clusters since z = 1. *MNRAS*, 384(4):1502–1510.

Stuardi, C., Bonafede, A., Wittor, D., Vazza, F., Botteon, A., Locatelli, N., Dallacasa, D., Golovich, N., Hoeft, M., van Weeren, R. J., Brüggen, M., and de Gasperin, F. (2019). Particle re-acceleration and Faraday-complex structures in the RXC J1314.4-2515 galaxy cluster. *MNRAS*, 489(3):3905–3926.

Subrahmanyan, R., Saripalli, L., Safouris, V., and Hunstead, R. W. (2008). On the Relationship between a Giant Radio Galaxy MSH 05-22 and the Ambient Large-Scale Galaxy Structure. *ApJ*, 677(1):63–78.

Subramanian, K. (2016). The origin, evolution and signatures of primordial magnetic fields. *Reports on Progress in Physics*, 79(7):076901.

Sun, M. (2009). Every BCG with a Strong Radio Agn has an X-Ray Cool Core: Is the Cool Core-Noncool Core Dichotomy Too Simple? *ApJ*, 704:1586–1604.

Sun, M. (2012). Hot gas in galaxy groups: recent observations. *New Journal of Physics*, 14(4):045004.

Sun, M., Jones, C., Forman, W., Vikhlinin, A., Donahue, M., and Voit, M. (2007). X-Ray Thermal Coronae of Galaxies in Hot Clusters: Ubiquity of Embedded Mini-Cooling Cores. *ApJ*, 657(1):197–231.

Sun, M., Voit, G. M., Donahue, M., Jones, C., Forman, W., and Vikhlinin, A. (2009). Chandra Studies of the X-Ray Gas Properties of Galaxy Groups. *ApJ*, 693(2):1142–1172.

Sutherland, R. S. and Dopita, M. A. (1993). Cooling functions for low-density astrophysical plasmas. *ApJS*, 88:253–327.

Tasse, C. (2014a). Applying Wirtinger derivatives to the radio interferometry calibration problem. *arXiv e-prints*, page arXiv:1410.8706.

Tasse, C. (2014b). Nonlinear Kalman filters for calibration in radio interferometry. *A&A*, 566:A127.

Tasse, C., Hugo, B., Mirmont, M., Smirnov, O., Atemkeng, M., Bester, L., Hardcastle, M. J., Lakhoo, R., Perkins, S., and Shimwell, T. (2018). Faceting for direction-dependent spectral deconvolution. *A&A*, 611:1–15.

Tasse, C., Hugo, B., Mirmont, M., Smirnov, O., Atemkeng, M., Bester, L., Hardcastle, M. J., Lakhoo, R., Perkins, S., and Shimwell, T. (2018). Faceting for direction-dependent spectral deconvolution. *A&A*, 611:A87.

Tasse, C., Shimwell, T., Hardcastle, M. J., O'Sullivan, S. P., van Weeren, R., Best, P. N., Bester, L., Hugo, B., Smirnov, O., Sabater, J., Calistro-Rivera, G., de Gasperin, F., Morabito, L. K., Röttgering, H., Williams, W. L., Bonato, M., Bondi, M., Botteon, A., Brüggen, M., Brunetti, G., Chyży, K. T., Garrett, M. A., Gürkan, G., Jarvis, M. J., Kondapally, R., Mandal, S., Prandoni, I., Repetti, A., Retana-Montenegro, E., Schwarz, D. J., Shulevski, A., and Wiaux, Y. (2021a). The LOFAR Two-meter Sky Survey: Deep Fields Data Release 1. I. Direction-dependent calibration and imaging. *A&A*, 648:A1.

Tasse, C., Shimwell, T., Hardcastle, M. J., O'Sullivan, S. P., van Weeren, R., Best, P. N., Bester, L., Hugo, B., Smirnov, O., Sabater, J., Calistro-Rivera, G., de Gasperin, F., Morabito, L. K., Röttgering, H., Williams, W. L., Bonato, M., Bondi, M., Botteon, A., Brüggen, M., Brunetti, G., Chyży, K. T., Garrett, M. A., Gürkan, G., Jarvis, M. J., Kondapally, R., Mandal, S., Prandoni, I., Repetti, A., Retana-Montenegro, E., Schwarz, D. J., Shulevski, A., and Wiaux, Y. (2021b). The LOFAR Two-meter Sky Survey: Deep Fields Data Release 1. I. Direction-dependent calibration and imaging. *A&A*, 648:A1.

Temi, P., Amblard, A., Gitti, M., Brighenti, F., Gaspari, M., Mathews, W. G., and David, L. (2018). ALMA Observations of Molecular Clouds in Three Group-centered Elliptical Galaxies: NGC 5846, NGC 4636, and NGC 5044. *ApJ*, 858:17.

Teyssier, R. (2002). Cosmological hydrodynamics with adaptive mesh refinement. A new high resolution code called RAMSES. *A&A*, 385:337–364.

Tremblay, G. R., Combes, F., Oonk, J. B. R., Russell, H. R., McDonald, M. A., Gaspari, M., Husemann, B., Nulsen, P. E. J., McNamara, B. R., Hamer, S. L., O'Dea, C. P., Baum, S. A., Davis, T. A., Donahue, M., Voit, G. M., Edge, A. C., Blanton, E. L., Bremer, M. N., Bulbul, E., Clarke, T. E., David, L. P., Edwards, L. O. V., Eggerman, D., Fabian, A. C., Forman, W., Jones, C., Kerman, N., Kraft, R. P., Li, Y., Powell, M., Randall, S. W., Salomé, P., Simionescu, A., Su, Y., Sun, M., Urry, C. M., Vantyghem, A. N., Wilkes, B. J., and ZuHone, J. A. (2018). A Galaxy-scale Fountain of Cold Molecular Gas Pumped by a Black Hole. *ApJ*, 865:13.

Truong, N., Pillepich, A., and Werner, N. (2021). Correlations between supermassive black holes and hot gas atmospheres in IllustrisTNG and X-ray observations. *MNRAS*, 501(2):2210–2230.

Ubertosi, F., Gitti, M., Torresi, E., Brighenti, F., and Grandi, P. (2021). A Chandra study of Abell 795 - a sloshing cluster with a FR0 radio galaxy at its center. *MNRAS*.

van der Tol, S., Veenboer, B., and Offringa, A. R. (2018). Image Domain Gridding: a fast method for convolutional resampling of visibilities. *A&A*, 616:A27.

Van Dokkum, P. G. and Franx, M. (1995). Dust in the Cores of Early-Type Galaxies. *AJ*, 110:2027.

van Haarlem, M. P., Wise, M. W., Gunst, A. W., Heald, G., McKean, J. P., Hessels, J. W. T., de Bruyn, A. G., Nijboer, R., Swinbank, J., Fallows, R., Brentjens, M., Nelles, A., Beck, R., Falcke, H., Fender, R., Hörandel, J., Koopmans, L. V. E., Mann, G., Miley, G., Röttgering, H., Stappers, B. W., Wijers, R. A. M. J., Zaroubi, S., van den Akker, M., Alexov, A., Anderson, J., Anderson, K., van Ardenne, A., Arts, M., Asgekar, A., Avruch, I. M., Batejat, F., Bähren, L., Bell, M. E., Bell, M. R., van Bemmel, I., Bennema, P., Bentum, M. J., Bernardi, G., Best, P., Bîrzan, L., Bonafede, A., Boonstra, A. J., Braun, R., Bregman, J., Breitling, F., van de Brink, R. H., Broderick, J., Broekema, P. C., Brouw, W. N., Brüggen, M., Butcher, H. R., van Cappellen, W., Ciardi, B., Coenen, T., Conway, J., Coolen, A., Corstanje, A., Damstra, S., Davies, O., Deller, A. T., Dettmar, R. J., van Diepen, G., Dijkstra, K., Donker, P., Doorduin, A., Dromer, J., Drost, M., van Duin, A., Eislöffel, J., van Enst, J., Ferrari, C., Frieswijk, W., Gankema, H., Garrett, M. A., de Gasperin, F., Gerbers, M., de Geus, E., Grießmeier, J. M., Grit, T., Gruppen, P., Hamaker, J. P., Hassall, T., Hoeft, M., Holties, H. A., Horneffer, A., van der Horst, A., van Houwelingen, A., Huijgen, A., Iacobelli, M., Intema, H., Jackson, N., Jelic, V., de Jong, A., Juette, E., Kant, D., Karastergiou, A., Koers, A., Kollen, H., Kondratiev, V. I., Kooistra, E., Koopman, Y., Koster, A., Kuniyoshi, M., Kramer, M., Kuper, G., Lambropoulos, P., Law, C., van Leeuwen, J., Lemaitre, J., Loose, M., Maat, P., Macario, G., Markoff, S., Masters, J., McFadden, R. A., McKay-Bukowski, D., Meijering, H., Meulman, H., Mevius, M., Middelberg, E., Millenaar, R., Miller-Jones, J. C. A., Mohan, R. N., Mol, J. D., Morawietz, J., Morganti, R., Mulcahy, D. D., Mulder, E., Munk, H., Nieuwenhuis, L., van Nieuwpoort, R., Noordam, J. E., Norden, M., Noutsos, A., Offringa, A. R., Olofsson, H., Omar, A., Orrú, E., Overeem, R., Paas, H., Pand ey-Pommier, M., Pandey, V. N., Pizzo, R., Polatidis, A., Rafferty, D., Rawlings, S., Reich, W., de Reijer, J. P., Reitsma, J., Renting, G. A., Riemers, P., Rol, E., Romein, J. W., Roosjen, J., Ruiter, M., Scaife, A., van der Schaaf, K., Scheers, B., Schellart, P., Schoenmakers, A., Schoonderbeek, G., Serylak, M., Shulevski, A., Sluman, J., Smirnov, O., Sobey, C., Spreeuw, H., Steinmetz, M., Sterks, C. G. M., Stiepel, H. J., Stuurwold, K., Tagger, M., Tang, Y., Tasse, C., Thomas, I., Thoudam, S., Toribio, M. C., van der Tol, B., Usov, O., van Veelen, M., van der Veen, A. J., ter Veen, S., Verbiest, J. P. W., Vermeulen, R., Vermaas, N., Vocks, C., Vogt, C., de Vos, M., van der Wal, E., van Weeren, R., Weggemans, H., Weltevrede, P., White, S., Wijnholds, S. J., Wilhelmsson, T., Wucknitz, O., Yatawatta, S., Zarka, P., Zensus, A., and van Zwieten, J. (2013). LOFAR: The LOw-Frequency ARray. *A&A*, 556:A2.

van Weeren, R., Shimwell, T., Botteon, A., Brunetti, G., Brüggen, M., Boxelaar, J., Cassano, R., Di Gennaro, G., Andrade-Santos, F., Bonnassieux, E., Bonafede, A., Cuciti, V., Dallacasa, D., de Gasperin, F., Gastaldello, F., Hardcastle, M., Hoeft, M., Kraft, R., Mandal, S., Rossetti, M., Röttgering, H., Tasse, C., and Wilber, A. (2021). LOFAR observations of galaxy clusters in HETDEX. Extraction and self-calibration of individual LOFAR targets. *A&A*, 651:A115.

van Weeren, R. J., Andrade-Santos, F., Dawson, W. A., Golovich, N., Lal, D. V., Kang, H., Ryu, D., Brìggen, M., Ogrean, G. A., Forman, W. R., Jones, C., Placco, V. M., Santucci, R. M., Wittman, D., Jee, M. J., Kraft, R. P., Sobral, D., Stroe, A., and Fogarty, K. (2017). The case for electron re-acceleration at galaxy cluster shocks. *Nature Astronomy*, 1:0005.

van Weeren, R. J., Brunetti, G., Brüggen, M., Andrade-Santos, F., Ogrean, G. A., Williams, W. L., Röttgering, H. J. A., Dawson, W. A., Forman, W. R., de Gasperin, F., Hardcastle, M. J., Jones, C., Miley, G. K., Rafferty, D. A., Rudnick, L., Sabater, J., Sarazin, C. L., Shimwell, T. W., Bonafede, A., Best, P. N., Bîrzan, L., Cassano, R., Chyży, K. T., Croston, J. H., Dijkema, T. J., Enßlin, T., Ferrari, C., Heald, G., Hoeft, M., Horellou, C., Jarvis, M. J., Kraft, R. P., Mevius, M., Intema, H. T., Murray, S. S., Orrú, E., Pizzo, R., Sridhar, S. S., Simionescu, A., Stroe, A., van der Tol, S., and White, G. J. (2016). LOFAR, VLA, and Chandra Observations of the Toothbrush Galaxy Cluster. *ApJ*, 818(2):204.

van Weeren, R. J., de Gasperin, F., Akamatsu, H., Brüggen, M., Feretti, L., Kang, H., Stroe, A., and Zandanel, F. (2019). Diffuse Radio Emission from Galaxy Clusters. *Space Sci. Rev.*, 215(1):16.

van Weeren, R. J., Hoeft, M., Röttgering, H. J. A., Brüggen, M., Intema, H. T., and van Velzen, S. (2011). A double radio relic in the merging galaxy cluster ZwCl 0008.8+5215. *A&A*, 528:A38.

van Weeren, R. J., Röttgering, H. J. A., Bagchi, J., Raychaudhury, S., Intema, H. T., Miniati, F., Enßlin, T. A., Markevitch, M., and Erben, T. (2009a). Radio observations of ZwCl 2341.1+0000: a double radio relic cluster. *A&A*, 506(3):1083–1094.

van Weeren, R. J., Röttgering, H. J. A., Brüggen, M., and Cohen, A. (2009b). A search for steep spectrum radio relics and halos with the GMRT. *A&A*, 508(1):75–92.

van Weeren, R. J., Röttgering, H. J. A., Brüggen, M., and Hoeft, M. (2010). Particle Acceleration on Megaparsec Scales in a Merging Galaxy Cluster. *Science*, 330(6002):347.

van Weeren, R. J., Röttgering, H. J. A., Intema, H. T., Rudnick, L., Brüggen, M., Hoeft, M., and Oonk, J. B. R. (2012a). The "toothbrush-relic": evidence for a coherent linear 2-Mpc scale shock wave in a massive merging galaxy cluster? *A&A*, 546:A124.

van Weeren, R. J., Röttgering, H. J. A., Intema, H. T., Rudnick, L., Brüggen, M., Hoeft, M., and Oonk, J. B. R. (2012b). The "toothbrush-relic": evidence for a coherent linear 2-Mpc scale shock wave in a massive merging galaxy cluster? *A&A*, 546:A124.

van Weeren, R. J., Williams, W. L., Hardcastle, M. J., Shimwell, T. W., Rafferty, D. A., Sabater, J., Heald, G., Sridhar, S. S., Dijkema, T. J., Brunetti, G., Brüggen, M., Andrade-Santos, F., Ogrean, G. A., Röttgering, H. J. A., Dawson, W. A., Forman, W. R., de Gasperin, F., Jones, C., Miley, G. K., Rudnick, L., Sarazin, C. L., Bonafede, A., Best, P. N., Bîrzan, L., Cassano, R., Chyży, K. T., Croston, J. H., Ensslin, T., Ferrari, C., Hoeft, M., Horellou, C., Jarvis, M. J., Kraft, R. P., Mevius, M., Intema, H. T., Murray, S. S., Orrú, E., Pizzo, R., Simionescu, A., Stroe, A., van der Tol, S., and White, G. J. (2016). LOFAR FACET CALIBRATION. *Astrophys. J. Suppl. Ser.*, 223(1):2.

Vantyghem, A. N., McNamara, B. R., Russell, H. R., Main, R. A., Nulsen, P. E. J., Wise, M. W., Hoekstra, H., and Gitti, M. (2014). Cycling of the powerful AGN in MS 0735.6+7421 and the duty cycle of radio AGN in clusters. *MNRAS*, 442(4):3192–3205.

Vazza, F. and Brüggen, M. (2014). Do radio relics challenge diffusive shock acceleration? *MNRAS*, 437(3):2291–2296.

Vazza, F., Brüggen, M., Wittor, D., Gheller, C., Eckert, D., and Stubbe, M. (2016). Constraining the efficiency of cosmic ray acceleration by cluster shocks. *MNRAS*, 459(1):70–83.

Vazza, F., Locatelli, N., Rajpurohit, K., Banfi, S., Domínguez-Fernández, P., Wittor, D., Angelinelli, M., Inchingolo, G., Brienza, M., Hackstein, S., Dallacasa, D., Gheller, C., Brüggen, M., Brunetti, G., Bonafede, A., Ettori, S., Stuardi, C., Paoletti, D., and Finelli, F. (2021). Magnetogenesis and the Cosmic Web: A Joint Challenge for Radio Observations and Numerical Simulations. *Galaxies*, 9(4):109.

Vazza, F., Roediger, E., and Brüggen, M. (2012). Turbulence in the ICM from mergers, cool-core sloshing, and jets: results from a new multi-scale filtering approach. *A&A*, 544:A103.

Vikhlinin, A., Kravtsov, A., Forman, W., Jones, C., Markevitch, M., Murray, S. S., and Van Speybroeck, L. (2006). Chandra Sample of Nearby Relaxed Galaxy Clusters: Mass, Gas Fraction, and Mass-Temperature Relation. *ApJ*, 640(2):691–709.

Vikhlinin, A., Kravtsov, A. V., Burenin, R. A., Ebeling, H., Forman, W. R., Hornstrup, A., Jones, C., Murray, S. S., Nagai, D., Quintana, H., and Voevodkin, A. (2009). Chandra Cluster Cosmology Project III: Cosmological Parameter Constraints. *ApJ*, 692(2):1060–1074.

Voit, G. M., Donahue, M., Bryan, G. L., and McDonald, M. (2015). Regulation of star formation in giant galaxies by precipitation, feedback and conduction. *Nature*, 519:203–206.

Voit, G. M., Kay, S. T., and Bryan, G. L. (2005). The baseline intracluster entropy profile from gravitational structure formation. *MNRAS*, 364:909–916.

Voit, G. M., Ma, C. P., Greene, J., Goulding, A., Pandya, V., Donahue, M., and Sun, M. (2018). A General Precipitation-limited L $_X$-T-R Relation among Early-type Galaxies. *ApJ*, 853(1):78.

Von Der Linden, A., Best, P. N., Kauffmann, G., and White, S. D. M. (2007). How special are brightest group and cluster galaxies? *MNRAS*, 379(3):867–893.

Wen, Z. L. and Han, J. L. (2013). Substructure and dynamical state of 2092 rich clusters of galaxies derived from photometric data. *MNRAS*, 436(1):275–293.

Werner, N., Oonk, J. B. R., Sun, M., Nulsen, P. E. J., Allen, S. W., Canning, R. E. A., Simionescu, A., Hoffer, A., Connor, T., Donahue, M., Edge, A. C., Fabian, A. C., von der Linden, A., Reynolds, C. S., and Ruszkowski, M. (2014). The origin of cold gas in giant elliptical galaxies and its role in fuelling radio-mode AGN feedback. *MNRAS*, 439(3):2291–2306.

White, R. L., Becker, R. H., Helfand, D. J., and Gregg, M. D. (1997). A Catalog of 1.4 GHz Radio Sources from the FIRST Survey. *ApJ*, 475(2):479–493.

White, S. D. M. and Frenk, C. S. (1991a). Galaxy Formation through Hierarchical Clustering. *ApJ*, 379:52.

White, S. D. M. and Frenk, C. S. (1991b). Galaxy formation through hierarchical clustering. *ApJ*, 379:52–79.

Wilber, A., Brüggen, M., Bonafede, A., Savini, F., Shimwell, T., van Weeren, R. J., Rafferty, D., Mechev, A. P., Intema, H., Andrade-Santos, F., Clarke, A. O., Mahony, E. K., Morganti, R., Prandoni, I., Brunetti, G., Röttgering, H., Mandal, S., de Gasperin, F., and Hoeft, M. (2018). LOFAR discovery of an ultra-steep radio halo and giant head-tail radio galaxy in Abell 1132. *MNRAS*, 473(3):3536–3546.

Williams, W. L., van Weeren, R. J., Röttgering, H. J. A., Best, P., Dijkema, T. J., de Gasperin, F., Hardcastle, M. J., Heald, G., Prand oni, I., Sabater, J., Shimwell, T. W., Tasse, C., van Bemmel, I. M., Brüggen, M., Brunetti, G., Conway, J. E., Enßlin, T., Engels, D., Falcke, H., Ferrari, C., Haverkorn, M., Jackson, N., Jarvis, M. J., Kapińska, A. D., Mahony, E. K., Miley, G. K., Morabito, L. K., Morganti, R., Orrú, E., Retana-Montenegro, E., Sridhar, S. S., Toribio, M. C., White, G. J., Wise, M. W., and Zwart, J. T. L. (2016a). LOFAR 150-MHz observations of the Boötes field: catalogue and source counts. *MNRAS*, 460(3):2385–2412.

Williams, W. L., van Weeren, R. J., Röttgering, H. J. A., Best, P., Dijkema, T. J., de Gasperin, F., Hardcastle, M. J., Heald, G., Prand oni, I., Sabater, J., Shimwell, T. W., Tasse, C., van Bemmel, I. M., Brüggen, M., Brunetti, G., Conway, J. E., Enßlin, T., Engels, D., Falcke, H., Ferrari, C., Haverkorn, M., Jackson, N., Jarvis, M. J., Kapińska, A. D., Mahony, E. K., Miley, G. K., Morabito, L. K., Morganti, R., Orrú, E., Retana-Montenegro, E., Sridhar, S. S., Toribio, M. C., White, G. J., Wise, M. W., and Zwart, J. T. L. (2016b). LOFAR 150-MHz observations of the Boötes field: catalogue and source counts. *MNRAS*, 460(3):2385–2412.

Willis, J. P., Pacaud, F., Valtchanov, I., Pierre, M., Ponman, T., Read, A., Andreon, S., Altieri, B., Quintana, H., Dos Santos, S., Birkinshaw, M., Bremer, M., Duc, P. A., Galaz, G., Gosset, E., Jones, L., and Surdej, J. (2005). The XMM Large-Scale Structure survey: an initial sample of galaxy groups and clusters to a redshift z < 0.6*. *MNRAS*, 363(2):675–691.

Willott, C. J., Rawlings, S., Blundell, K. M., and Lacy, M. (1999). The emission line-radio correlation for radio sources using the 7C Redshift Survey. *MNRAS*, 309(4):1017–1033.

Willson, M. A. G. (1970). Radio observations of the cluster of galaxies in Coma Berenices - the 5C4 survey. *MNRAS*, 151:1.

Wittor, D., Ettori, S., Vazza, F., Rajpurohit, K., Hoeft, M., and Domínguez-Fernández, P. (2021). Exploring the spectral properties of radio relics - I: integrated spectral index and Mach number. *MNRAS*, 506(1):396–414.

Wittor, D. and Gaspari, M. (2020). Dissecting the turbulent weather driven by mechanical AGN feedback. *MNRAS*, 498(4):4983–5002.

Wu, X.-P., Xue, Y.-J., and Fang, L.-Z. (1999). The L_X-T and L_X-σ Relationships for Galaxy Clusters Revisited. *ApJ*, 524(1):22–30.

Yang, H. Y. K., Gaspari, M., and Marlow, C. (2019). The Impact of Radio AGN Bubble Composition on the Dynamics and Thermal Balance of the Intracluster Medium. *ApJ*, 871(1):6.

Yang, H. Y. K. and Reynolds, C. S. (2016). Interplay Among Cooling, AGN Feedback, and Anisotropic Conduction in the Cool Cores of Galaxy Clusters. *ApJ*, 818(2):181.

Yuan, Z. S., Han, J. L., and Wen, Z. L. (2016). Radio luminosity function of brightest cluster galaxies. *MNRAS*, 460(4):3669–3678.

Zhang, Y. Y., Andernach, H., Caretta, C. A., Reiprich, T. H., Böhringer, H., Puchwein, E., Sijacki, D., and Girardi, M. (2011). HIFLUGCS: Galaxy cluster scaling relations between X-ray luminosity, gas mass, cluster radius, and velocity dispersion. *A&A*, 526:A105.

ZuHone, J. A., Markevitch, M., and Johnson, R. E. (2010). Stirring up the pot: Can Cooling flows in galaxy clusters be quenched by gas sloshing? *ApJ*, 717(2):908–928.